

Properties of small-scale turbulence in Rayleigh-Bénard convection

by

Shashwat Bhattacharya



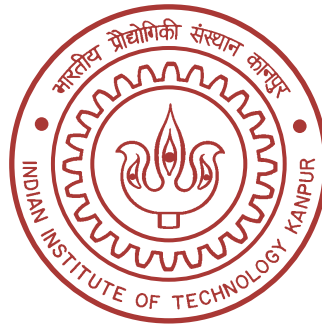
**DEPARTMENT OF MECHANICAL ENGINEERING
INDIAN INSTITUTE OF TECHNOLOGY KANPUR**

February, 2021

Properties of small-scale turbulence in Rayleigh-Bénard convection

A Thesis Submitted
in Partial Fulfilment of the Requirements
for the Degree of
Doctor of Philosophy

by
Shashwat Bhattacharya



to the
DEPARTMENT OF MECHANICAL ENGINEERING
INDIAN INSTITUTE OF TECHNOLOGY KANPUR
February, 2021

CERTIFICATE



It is certified that the work contained in the thesis titled “**Properties of small-scale turbulence in Rayleigh-Bénard convection**”, by **Shashwat Bhattacharya**, has been carried out under my supervision and that this work has not been submitted elsewhere for a degree.

A handwritten signature in black ink, appearing to read 'Meh V'.

Prof. Mahendra K. Verma
(Thesis supervisor)
Department of Physics
IIT Kanpur
Kanpur-208016
India

February, 2021

Declaration

This is to certify that the thesis titled Properties of small-scale turbulence in Rayleigh-Bénard convection has been authored by me. It presents the research conducted by me under the supervision of Prof. Mahendra K. Verma. To the best of my knowledge, it is an original work, both in terms of research content and narrative, and has not been submitted elsewhere, in part or in full, for a degree. Further, due credit has been attributed to the relevant state-of-the-art and collaborations (if any) with appropriate citations and acknowledgements, in line with established norms and practices.



Signature

Name: Shashwat Bhattacharya

Programme: PhD

Department: Mechanical Engineering
Indian Institute of Technology Kanpur
Kanpur 208016

Synopsis

Name	: Shashwat Bhattacharya
Roll No.	: 16205274
Degree for which submitted	: Doctor of Philosophy
Department	: Mechanical Engineering
Title of the Thesis	: Properties of small-scale turbulence in Rayleigh-Bénard convection
Thesis Supervisor	: Prof. Mahendra Kumar Verma
Month and year of submission	: February, 2021

Buoyancy-driven convection is encountered in many engineering applications and natural phenomena, and hence has been a topic of research for more than a century. Researchers often focus on a simplified model of convection, *Rayleigh-Bénard convection* (RBC), where a fluid is enclosed between two horizontal walls with the bottom wall kept at a higher temperature than the top wall [1, 2, 3, 4]. RBC is governed by two dimensionless parameters: the Rayleigh number (Ra), which is the ratio of the buoyancy and the dissipative forces, and the Prandtl number (Pr), which is the ratio of kinematic viscosity to thermal diffusivity. Important response parameters of RBC are the Nusselt number (Nu), which is a measure of the global heat flux, and the Reynolds number (Re), which is a measure of the large-scale velocity (U) and hence the intensity of turbulence. Researchers also study the small-scale statistics of RBC, namely, the spectra of kinetic energy and entropy, velocity and temperature structure functions, and the viscous and thermal dissipation rates.

The energetics of three-dimensional homogeneous and isotropic turbulence (HIT) away from walls is reasonably well-understood and was described by Kolmogorov [5,

[1] Chandrasekhar, S. *Hydrodynamic and Hydromagnetic Stability* (Dover publications, Oxford, 1981).

[2] Ahlers, G., Grossmann, S. & Lohse, D. *Rev. Mod. Phys.* **81**, 503–537 (2009).

[3] Chillà, F. & Schumacher, J. *Eur. Phys. J. E* **35**, 58 (2012).

[4] Verma, M. K. *Physics of Buoyant Flows: From Instabilities to Turbulence* (World Scientific, Singapore, 2018).

[5] Kolmogorov, A. N. *Dokl Acad Nauk SSSR* **30**, 301–305 (1941).

[6], reviewed in Ref. [7]. However, in RBC, the physics becomes more involved due to the presence of walls, their associated boundary layers, and buoyancy [2, 3, 4, 8]. There has been a long-standing debate on whether thermal convection follows Bolgiano-Obukhov phenomenology [9, 10], similar to stably-stratified turbulence, or Kolmogorov’s phenomenology [5, 6], similar to homogeneous isotropic turbulence; see Refs. [8, 11, 12] for a detailed review. Although it has recently been shown that the kinetic energy spectrum of thermal convection exhibits Kolmogorov-like scaling [11, 12, 13, 14], the behavior of the structure functions of convection is still not conclusive [8, 15]. Further, the walls bring about spatial inhomogeneity in the viscous and thermal dissipation rates in RBC, causing them to scale differently in the bulk and in the boundary layers of the RBC cell [2, 3, 16]. It is generally assumed that the dissipation rates in the bulk scale similarly as in HIT [17, 18]; however, a few studies indicate that this may not be the case [19, 20, 21, 22, 23].

The overall aim of this thesis is to address the aforementioned gaps in the energetics of RBC. We employ direct numerical simulations to comprehensively study the properties of small-scale turbulence in RBC and their impact on the scaling of Reynolds and Nusselt numbers. We analyze the velocity structure functions of RBC and show that they are similar to those of HIT for small and moderate Prandtl numbers. We explore the Prandtl number dependence on the amplitudes of the kinetic energy spectrum, structure functions, and the statistics of the local heat flux, which has not been done before. Further, we study the scaling relations and relative strengths of the viscous and thermal dissipation rates in the bulk and boundary layers to understand the effects of walls on the statistics of RBC. To get conclusive results, we determine the

-
- [6] Kolmogorov, A. N. *Dokl Acad Nauk SSSR* **32**, 16–18 (1941)
 - [7] Sreeivasan, K. R. & Antonia, R. A. *Annu. Rev. Fluid Mech.* **29**, 435–472 (1997)
 - [8] Lohse, D. & Xia, K.-Q. *Annu. Rev. Fluid Mech.* **42**, 335–364 (2010).
 - [9] Bolgiano, R. J. *Geophys. Res.* **64**, 2226–2229 (1959).
 - [10] Obukhov, A. M. *Dokl Acad Nauk SSSR* **125**, 1246 (1959).
 - [11] Kumar, A., Chatterjee, A. G. & Verma, M. K. *Phys. Rev. E* **90**, 023016 (2014).
 - [12] Verma, M. K., Kumar, A. & Pandey, A. *New J. Phys.* **19**, 025012 (2017)
 - [13] Mishra, P. K. & Verma, M. K. *Phys. Rev. E* **81**, 056316 (2010)
 - [14] Bhattacharjee, J. K., *Phys. Lett. A* **379**, 696–699 (2015)
 - [15] Ching, E. S. C. *Statistics and Scaling in Turbulent Rayleigh-Bénard Convection* (Springer, Berlin, 2013).
 - [16] Silano, G., Sreenivasan, K. R. & Verzicco, R. J. *Fluid Mech.* **526**, 409–446 (2010)
 - [17] Grossmann, S. & Lohse, D. J. *Fluid Mech.* **407**, 27–56 (2000).
 - [18] Grossmann, S. & Lohse, D. *Phys. Rev. Lett.* **86**, 3316–3319 (2001).
 - [19] Verzicco, R. & Camussi, R. J. *Fluid Mech.* **477**, 19–49 (2003)
 - [20] He, X., Tong, P. & Xia, K. Q. *Phys. Rev. Lett.* **98**, 144501 (2007)
 - [21] Emran, M. S. & Schumacher, J. J. *Fluid Mech.* **611**, 13–34 (2008)
 - [22] Pandey A., Kumar, A., Chatterjee, A. G. & Verma, M. K. *Phys. Rev. E* **94**, 053106 (2016)
 - [23] Pandey A. & Verma, M. K. *Phys. Fluids* **28**, 095105 (2016)

boundary layer thicknesses for every set of governing parameters and compute the scaling of the dissipation rates, for the first time, over the entire bulk and boundary layer volumes. Finally, we use the results of our above studies to enhance the well-known Grossmann and Lohse’s model [17, 18] that predicts the Nusselt and Reynolds numbers for a given set of governing parameters.

A brief outline of the thesis is as follows. In Chapter 1, we introduce RBC and present its governing equations and their nondimensionalization. We discuss the response parameters of RBC and introduce the concepts of boundary layers. We review the past theoretical, numerical, and experimental works on structure functions, spectral quantities, local heat fluxes, and dissipation rates of RBC. We also review past research on the dependence of Re and Nu on the governing parameters of RBC.

In Chapter 2, we discuss the details of our numerical simulations of RBC using finite-difference solver SARAS [24] and finite-volume solver OpenFOAM [25]. We explain the computations of the structure functions using fastSF [26] and the spectral quantities using the pseudo-spectral code TARANG [27]. Finally, we detail the procedure for the computations of global quantities, boundary layer thicknesses, and the dissipation rates using our numerical data.

In Chapter 3, we compute the velocity structure functions of RBC for $Pr = 1$ and show that they scale similar to those of HIT [28]. The scaling exponents are found to be in agreement with the predictions of She and Leveque [29], similar to HIT. Our results are consistent with the previous studies that reported Kolmogorov-like kinetic energy spectrum in RBC [11, 12]. We also show that in RBC, the kinetic energy flux in the intermediate scales is less than the viscous dissipation rate, unlike in homogeneous isotropic turbulence, due to multiscale kinetic energy injection.

In Chapter 4, we analyze the Prandtl number dependence of spectra and fluxes of kinetic energy and entropy of turbulent thermal convection using our simulation data [30]. We show that the magnitudes of the kinetic energy fluxes and spectra and those of structure functions increase with the decrease of Pr , thus indicating stronger

[24] Verma, M. K. *et al.* *S. N. Comput. Sci.* **1**, 178 (2020).

[25] Jasak, H., Jemcov, A., Tukovic, Z. *et al.* in *International Workshop on Coupled Methods in Numerical Dynamics* **1000**, 1–20 (2007).

[26] Sadhukhan, S., Bhattacharya, S. & Verma, M. K. *J. Open Source Softw.* **6**, 2185 (2021).

[27] Verma, M. K. *et al.* *Pramana-J. Phys.* **81**, 617–629 (2013).

[28] Bhattacharya, S., Sadhukhan, S., Guha, A. & Verma, M. K. *Phys. Fluids* **31**, 115107 (2019).

[29] She, Z.-S. & Leveque, E. *Phys. Rev. Lett.* **72**, 336–339 (1994).

[30] Bhattacharya, S., Verma, M. K. & Samtaney, R. under review in *Phys. Rev. Fluids* (2021).

nonlinearity for flows with small Prandtl numbers. Consistent with these observations, the kinetic energy injection rates and the dissipation rates too increase with the decrease of Pr. On the other hand, the amplitudes of the entropy spectrum do not vary significantly with Pr. For small Prandtl numbers, most of the kinetic energy is injected at large scales, whereas for large Prandtl numbers, the energy injection is somewhat homogeneously distributed over different scales. Further, the tail of the probability distributions of the local heat flux grows with the increase of Pr, indicating increased fluctuations in the local heat flux with Pr.

In Chapter 5, we study the scaling relations of viscous dissipation rates in the bulk and boundary layers of the convection cell for $Pr = 1$ and 6.8 [31]. We show that contrary to the general belief, viscous dissipation rate dominates in the bulk rather than in the boundary layers. The thickness of the viscous boundary layers, δ_u , is observed to deviate marginally from the widely-held assumption of $\delta_u \sim Re^{-1/2}$ [32]. The bulk dissipation is similar to HIT where it follows a log-normal distribution; however, it differs from U^3/d by a factor of $Ra^{-0.18}$, where d is the distance between the thermal plates. The dissipation rates in the boundary layers are rarer but more intense with stretched exponential distribution.

In Chapter 6, we obtain the scaling relations of thermal dissipation rates in the bulk and boundary layers of the convection cell for $Pr = 1$ and 100 [33]. We show that unlike viscous dissipation rate, the thermal dissipation rate dominates in the boundary layers by a factor of approximately 3. The thermal dissipation rate in the bulk differs from $U\Delta^2/d$ (as in homogeneous isotropic turbulence) by a factor of $Ra^{-\alpha}$, where Δ is the temperature difference between the thermal plates, and $\alpha = 0.22$ for $Pr = 1$ and 0.25 for $Pr = 100$. Both bulk and boundary layer dissipation rates follow stretched exponential distributions.

In Chapter 7, we extend Grossmann and Lohse's (GL) model for the predictions of Reynolds and Nusselt numbers in RBC [34]. Towards this objective, we use functional forms for the prefactors of the dissipation rates in the bulk and the boundary layers. The functional forms arise due to inhibition of nonlinear interactions in the presence of walls and buoyancy compared to homogeneous isotropic turbulence, along with a deviation of viscous boundary layer profile from Prandtl-Blasius theory (as discussed

[31] Bhattacharya, S., Pandey, A., Kumar, A. & Verma, M. K. *Phys. Fluids* **30**, 031702 (2018).

[32] Landau, L. D. & Lifshitz, E. M. *Fluid Mechanics* (Elsevier, Oxford, 1987).

[33] Bhattacharya, S., Samtaney, R. & Verma, M. K. *Phys. Fluids* **31**, 075104 (2019).

[34] Bhattacharya, S., Verma, M. K. & Samtaney, R. *Phys. Fluids* **33**, 015113, (2021)

in Chapters 5 and 6). We perform 60 numerical runs on a three-dimensional unit box for a range of Rayleigh numbers (Ra) and Prandtl numbers (Pr) and determine the aforementioned functional forms using machine learning. The revised predictions are in better agreement with the past experimental and numerical results than those of the GL model, especially for extreme Prandtl numbers.

In Chapter 8, we present the important conclusions from our present work. Further, we discuss the scope of future research based on the results of this work.

Acknowledgements

February, 2021

Shashwat Bhattacharya

I would like to express my sincere gratitude to my thesis supervisor, Prof. Mahendra Kumar Verma, for his continuous support, guidance, and patience throughout my Ph.D. days. I learned many important concepts on turbulence and high-performance computing from him. His encouragement as well as constructive criticisms helped me a lot in my work. In our regular evening walks, we used to exchange many ideas on our research work; these discussions proved to be very useful for my research. I am also indebted to Prof. Anirban Guha, who was my co-supervisor till he left IIT Kanpur to join University of Dundee. I learned the concepts of advanced fluid dynamics and hydrodynamic stability from Prof. Guha, and physics of turbulence and high-performance computing from Prof. Verma.

I would extend my deepest gratitude to our collaborator, Prof. Ravi Samtaney of King Abdullah University of Science and Technology (KAUST), Saudi Arabia. His wealth of knowledge on computational fluid dynamics and turbulent flows proved to be very helpful during my research work. I would also like to thank him for providing access to Shaheen II, one of the fastest supercomputers of the world. Most of the simulations for my thesis were performed in Shaheen II under the projects k1052 and k1416. I would also like to thank my other collaborators, Dr. Ambrish Pandey and Dr. Abhishek Kumar, who were also my seniors. Their continuous guidance and moral support helped me a lot in the initial phase of my PhD.

I am also grateful to various instructors during my coursework; their teachings proved to be highly beneficial for my research. I learned important concepts of advanced mathematical methods from Prof. Anurag Gupta, and heat and mass transfer from Prof. P. S. Ghoshdastidar and Prof. Jishnu Bhattacharya. I would like to extend my thanks to Prof. Malay K. Das for helpful discussions on applied numerical methods and fluid dynamics. Many thanks to Prof. Syed Fahad Anwer and Prof. Rodion Stepanov for their immense help in developing our inhouse finite difference code SARAS. I am also highly grateful to Prof. Jörg Schumacher, Prof. K. R. Sreenivasan, Prof. Pranav Joshi, Prof. Arnab Bhattacharya, Prof. Supratik Banerjee, Prof. Anikesh Pal, Prof. Pankaj Mishra, and Prof. Franck Plunian for useful discussions.

I am thankful to Manmohan Debvanshi and Roshan Bhaskaran for helping in lab-related issues. Special thanks to Manmohan for helping me in handling various administrative matters. I thank Mr. Vishal Garg, and Mr. Vivek Garg for their help in computer-related problems. I would like to acknowledge all staff members of the department of Mechanical Engineering, IIT Kanpur for their kind support. I would like to thank all the teaching and non-teaching staff of IIT Kanpur.

Further, I would like to thank all my present lab mates for all their help and support during my PhD days. My PhD thesis required the usage of the finite difference code SARAS, of which Roshan Samuel, one of my labmates, is the lead developer. I am very grateful to him for developing such a fast and efficient code. Many thanks to Shadab Alam, Roshan Samuel, Shubhadeep Sadhukhan, Soumaydeep Chatterjee, Ali Asad, Mohammad Anas, Ali Asad, Dr. Sonakshi Sachdev, Rohit Jayaram, and Aryan Sharma for fruitful discussions. My special thanks to Shubhadeep Sadhukhan for his involvement in developing a parallel code to compute structure functions of turbulence; this code was also used in my thesis. I thank Anando Gopal Chatterjee for his help in computation-related issues. I am also thankful to my senior Dr. Manohar Sharma, for his encouragement and useful discussions on turbulence-related problems. I am also thankful to Dr. Akanksha Gupta for useful discussions related to two-dimensional turbulence.

I thank the anonymous referees and editors of the various journals for their constructive criticism on our work. I am thankful to Indian Space Research Organization, Science and Engineering Research Board (SERB), Department of Science and Technology (DST), IIT Kanpur, and the Russian Science Foundation Russia for funding our research work. I also thank ICTS Bangalore as well as the organizers for European Turbulence Conference 2019, and International Conference on Rayleigh-Bénard Turbulence 2018 for organizing conferences on various fields of turbulence. These conferences provided me with an opportunity to interact with many experts in turbulence.

My stay in IIT Kanpur was highly enjoyable due to the company of some very good friends. Apart from my labmates, I thank my other friends – Narendra Pratap, Ghulam Sarwar, Manoj Sharma, Shubhro Sen, Abhishek Singh, Ambuj Gautam, Rohitashwa Chattopadhyay, Samrat Mandal, Akanksha Gupta, and Vinay Tripathi – for making my stay in IITK memorable.

Last but not the least, I would like to thank my parents for their constant encour-

agement and support. Due to Covid 19 pandemic, I had to carry out my last 10 months of my PhD work from home. I am very grateful to my parents for all their help and support, especially during my work from home.

Chapter 3 consists of the reprint of the manuscript [Bhattacharya et al. \(2019a\)](#), inserted with the permission of AIP Publishing. Chapter 5 consists of the reprint of the manuscript [Bhattacharya et al. \(2018\)](#), inserted with the permission of AIP Publishing. Chapter 6 consists of the reprint of the manuscript [Bhattacharya et al. \(2019b\)](#), inserted with the permission of AIP Publishing. Chapter 7 consists of the reprint of the manuscript [Bhattacharya et al. \(2021b\)](#), inserted with the permission of AIP Publishing. The relevant permissions are attached at the end of the thesis.

February, 2021

Shashwat Bhattacharya

To my family and teachers...

List of Publications

- **In peer-reviewed journals**

1. **Bhattacharya, S.***, Pandey, A., Kumar, A. & Verma, M. K. Complexity of viscous dissipation in turbulent thermal convection, *Phys. Fluids*. **30**, 031702 (2018).
2. **Bhattacharya, S.***, Samtaney, R. & Verma, M. K. Scaling and spatial intermittency of thermal dissipation in turbulent convection, *Phys. Fluids*. **31**, 075104 (2019).
3. **Bhattacharya, S.***, Sadhukhan, S., Guha, A. & Verma, M. K. Similarities between the structure functions of thermal convection and hydrodynamic turbulence, *Phys. Fluids*. **31**, 115107 (2019).
4. Verma, M. K.* , Samuel, R., Chatterjee, S., **Bhattacharya, S.** & Asad, A. Challenges in Fluid Flow Simulations Using Exascale Computing, *S. N. Comput. Sci.* **1**, 178 (2020).
5. **Bhattacharya, S.***, Verma, M. K. & Samtaney, R. Revisiting Reynolds and Nusselt numbers in turbulent thermal convection, *Phys. Fluids*. **33**, 015113 (2021).
6. Sadhukhan, S*., **Bhattacharya, S.** & Verma, M. K. fastSF: A parallel code for computing the structure functions of turbulence, *J. Open Source Softw.* **6**, 2185 (2021).
7. **Bhattacharya, S.***, Verma, M. K. & Samtaney, R. Prandtl number dependence of the small-scale properties in Rayleigh-Bénard convection, *Phys. Rev. Fluids* **6**, 063501 (2021).

- **Under review in journals**

1. Samuel, R.* , **Bhattacharya, S.**, Asad, A., Chatterjee, S., Verma, M. K., Samtaney, R. & Anwer, S. F. SARAS: A general-purpose PDE solver for fluid dynamics, *J. Open Source Softw.* (under review).

*Corresponding author

Contents

Acknowledgements	xi
List of Publications	xvii
List of Figures	xxiii
List of Tables	xxvii
1 Introduction	1
1.1 Thermal convection	1
1.2 Governing equations and non-dimensional parameters	3
1.3 Important diagnostics of RBC	6
1.3.1 Global quantities: Nusselt and Reynolds numbers	6
1.3.2 Viscous and thermal dissipation rates	8
1.3.3 Structure functions	8
1.3.4 Spectral quantities	9
1.4 Viscous and thermal boundary layers	12
1.5 Phenomenology of turbulent RBC	14
1.5.1 Homogeneous and isotropic hydrodynamic turbulence	14
1.5.2 Passive scalar turbulence	15

CONTENTS

1.5.3	Buoyancy-driven turbulence	16
1.6	Scaling of viscous and thermal dissipation rates	21
1.7	Scaling of Nusselt and Reynolds numbers	24
1.8	Statistics of local heat fluxes	27
1.9	Problems addressed in the thesis	28
1.10	Outline of the thesis	29
2	Numerical methods	33
2.1	Simulations of RBC	33
2.1.1	Finite volume method: OpenFOAM	34
2.1.2	Finite difference method: SARAS	35
2.2	Post-processing of the simulation data	38
2.2.1	Structure functions	38
2.2.2	Energy and entropy spectra and fluxes	41
2.2.3	Global quantities	43
2.2.4	Boundary layer thicknesses	44
2.2.5	Dissipation rates	45
3	Velocity structure functions of turbulent RBC	49
3.1	Introduction	49
3.2	A summary of our results	50
3.3	Published manuscript	51
4	Behavioural changes in turbulent RBC with Prandtl number	65
4.1	Introduction	65
4.2	Details of our numerical simulations	66
4.3	Variation of spectral quantities with Prandtl number	67
4.3.1	Kinetic energy spectra and fluxes	67
4.3.2	Energy flux and viscous dissipation in thermal convection	70
4.3.3	Entropy spectra and fluxes	72
4.4	Structure functions	75

CONTENTS

4.5	Prandtl number dependence of local heat flux	77
4.6	Summary and conclusions	80
5	Scaling and spatial distribution of viscous dissipation	83
5.1	Introduction	83
5.2	A summary of our results	84
5.3	Published manuscript	85
6	Scaling and spatial distribution of thermal dissipation	93
6.1	Introduction	93
6.2	A summary of our results	94
6.3	Published manuscript	94
7	Revisiting Reynolds and Nusselt numbers in turbulent convection	103
7.1	Introduction	103
7.2	A summary of our results	104
7.3	Published manuscript	105
8	Summary and conclusions	121
8.1	Conclusions of the thesis	121
8.2	Scope of future work	124
	Bibliography	127

List of Figures

1.1	Schematic of Rayleigh-Bénard convection showing heated bottom wall, cold top wall, and convective motion of the fluid.	2
1.2	For horizontal rigid and conducting walls: (a) Typical velocity profile u showing the viscous boundary layers (shaded region) formed near the horizontal walls, and (b) the temperature profile T showing the thermal boundary layers (shaded region) near the horizontal walls.	13
2.1	Schematic for computing the velocity structure functions. The velocity difference $\delta\mathbf{u}(\mathbf{l})$ is computed by taking the difference between two points with the same indices in the pink and the green subdomains. For example, $\mathbf{u}(\mathbf{l}) - \mathbf{u}(0,0) = \mathbf{u}_B - \mathbf{u}_A$, where B and A are the origins of the green and the pink subdomains. This feature enables vectorization of the computation. This figure is taken from Ref. (Sadhukhan et al., 2021).	40
2.2	For $Ra = 10^7$ and $Pr = 1$ simulated using SARAS: (a) viscous boundary layer thickness near the bottom wall, and (b) thermal boundary layer thickness near the bottom wall.	44

LIST OF FIGURES

4.1 For $Ra = 10^7$ and $Pr = 0.02, 0.1, 1, 6.8,$ and 100 : (a) Integral kinetic energy spectrum, $\sum_k^\infty E_u(k')$ vs. wavenumber k , (b) kinetic energy flux, $\Pi_u(k)$, vs. k , (c) energy injection rate due to buoyancy, $\mathcal{F}_B(k)$, vs. k , and (d) $d_k\Pi_u(k)/\Pi_u(k)$ vs. k . The amplitudes of the energy spectrum and flux decrease with Pr . For $Pr \leq 1$, the energy spectrum exhibits Kolmogorov's scaling. 68

4.2 (a) For $Ra = 10^7$ and $Pr = 0.02$ (green), 0.1 (red), 1 (black), 6.8 (brown), and 100 (purple): Plots of the cumulative kinetic energy injection by buoyancy $\sum_k^\infty \mathcal{F}_B(k')$ (solid curves) and the viscous dissipation rate ϵ_u (dashed curves) vs. k . (b) Plots of ϵ_u and maximum kinetic energy flux $\Pi_{u,max}$ vs. k . The cumulative energy injection and dissipation rates decrease with the increase of Pr , similar to the energy spectrum and flux. The difference between the kinetic energy flux and the dissipation rate increases as Pr is increased. 71

4.3 For $Pr = 0.02, 0.1, 1, 6.8,$ and 100 , plots of $\tilde{\epsilon}_u = \epsilon_u/(U^3/d)$ vs. Ra . For small Pr , $\epsilon_u \sim U^3/d$ as in hydrodynamic turbulence. However, ϵ_u has an additional Ra dependence for larger Prandtl numbers. 72

4.4 For $Ra = 10^7$ and $Pr = 1, 6.8,$ and 100 : (a) Entropy spectrum E_θ (with dual branches) and (b) entropy flux Π_θ vs. k . The amplitudes of the entropy spectrum do not vary with Pr , but the amplitudes of the entropy flux decrease with increase of Pr 73

4.5 For $Ra = 10^7$ and $Pr = 0.02$ and 0.1 : Semi-log plots of (a) normalized entropy spectrum kE_θ and (b) entropy flux Π_θ vs. k . The lower branch of the entropy spectrum and the entropy flux fit well with exponential function. The magnitudes of both the entropy spectra and the fluxes do not vary significantly with Pr for this regime. 74

LIST OF FIGURES

4.6	For $Pr = 0.02, 0.1, 1, 6.8,$ and 100 : longitudinal velocity structure functions of orders (a) 2, (b) 3, (c) 5, and (d) 7 vs. l . The amplitudes of the structure functions decrease with the increase of Pr	76
4.7	For $Pr = 0.02, 0.1,$ and 1 : The scaling exponents ζ_q for the velocity structure functions vs. order q . The exponents match closely with the predictions of She and Leveque (SL94). The figure also exhibits the extrapolated ζ_q 's for K41 ($q/3$) and Bolgiano-Obukhov (BO59) ($3q/5$).	77
4.8	For $Ra = 10^7$: The probability distribution functions (PDFs) of normalized local convective heat flux in the (a) x direction, (b) y direction, and (c) z direction for different Pr . The fluctuations of the local heat flux increase with Pr	78
4.9	For $Ra = 10^7$: The probability distribution functions (PDFs) of the local convective heat flux normalized with their respective standard deviations ($\sigma_x, \sigma_y, \sigma_z$) in the (a) x direction, (b) y direction, and (c) z direction. The normalized PDFs for different Prandtl numbers collapse into one curve.	79
5.1	Schematic of a cubical RBC cell with no-slip boundaries depicting the bulk (brown) and the viscous boundary layer (gray) regions. This figure is adapted from Bhattacharya et al. (2018)	84

List of Tables

1.1	Prandtl numbers of typical fluids	5
4.1	Details of our data obtained direct numerical simulations of RBC performed in a cubical box for $Ra = 10^7$: the Prandtl number (Pr), the grid size, the ratio of the Kolmogorov length scale (for $Pr \leq 1$) or the Batchelor length scale (for $Pr > 1$) to the mesh width ($\eta/\Delta x$), the number of grid points in viscous and thermal boundary layers (N_{VBL} and N_{TBL} respectively), the Nusselt number (Nu), the Nusselt number computed using the viscous dissipation rate (Nu_u), the Nusselt number computed using the thermal dissipation rate (Nu_T), the number of non-dimensional time units (t_{ND}), and snapshots over which the quantities are averaged.	66
4.2	For $Pr = 0.02$ to 100 and $Ra = 10^7$: Standard deviations (σ_x , σ_y , and σ_z) of the local heat fluxes $u_x T$, $u_y T$, and $u_z T$ respectively, and the number of snapshots over which the PDFs of the above quantities are averaged. The standard deviations increase with Pr	78

Chapter 1

Introduction

1.1 Thermal convection

Thermal convection is the transfer of heat in a fluid due to its bulk movement. There are two types of convection - forced convection and buoyancy-driven (natural) convection ([Kays and Crawford, 1993](#); [Bejan, 2013](#)). In forced convection, the fluid motion is generated through external means such as pumps and fans. On the other hand, in buoyancy-driven convection, the fluid motion is brought about by buoyancy forces that are generated due to density differences in different parts of the fluid. The temperature variations in the fluid induce such density differences.

Typical applications involving forced convection are heat exchangers, cooling fans, and air conditioning systems. Buoyancy-driven convection is encountered in natural phenomena such as atmospheric flows, the earth's mantle, and solar turbulence. It is also encountered in many engineering applications such as heat sinks in electronic circuits, solar thermal collectors, chimneys, natural draft cooling towers, and thermal furnaces. An important advantage of natural convection in engineering is that no mechanical equipments such as pumps or fans are involved; this saves energy consumption and maintenance costs.

In this thesis, we analyze *Rayleigh-Bénard convection* (RBC), a paradigm for many flows involving buoyancy-driven convection. RBC consists of a fluid enclosed between two horizontal walls, with the bottom wall kept at a higher temperature than the top

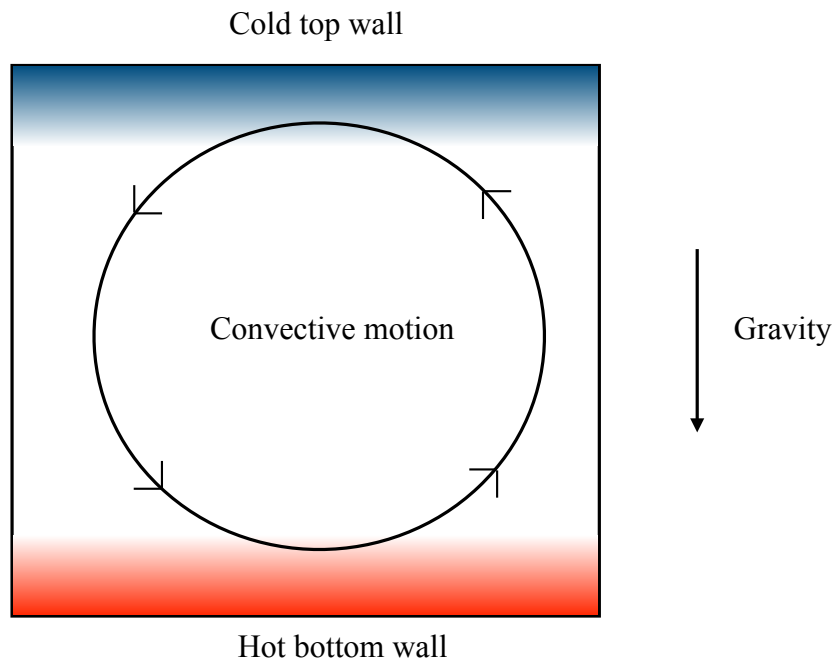


FIGURE 1.1: Schematic of Rayleigh-Bénard convection showing heated bottom wall, cold top wall, and convective motion of the fluid.

wall. This arrangement leads to an unstable configuration with hot and light fluid at the bottom, and cold and dense fluid at the top, giving rise to the convective motion of the fluid (see Fig. 1.1) *.

In this chapter, we discuss the basic framework of RBC. We start with the governing equations and then discuss the important diagnostic tools for studying RBC. We review the past theoretical, experimental, and numerical studies on the small-scale and the global properties of RBC related to the thesis. We identify the gaps in these studies and formulate problems which we address in this thesis. Finally, we provide an outline of the subsequent chapters of my thesis.

[*] An opposite configuration comprising of cold bottom wall and hot top wall leads to a stable system that needs external force to sustain convective motion. Such a system is called a *stably-stratified system*.

1.2 Governing equations and non-dimensional parameters

We consider RBC under the Boussinesq approximation in which the variations of density are neglected except in the buoyancy term in the governing equations (Chandrasekhar, 1981; Ahlers et al., 2009a; Chillà and Schumacher, 2012). Additionally, the fluid properties such as thermal diffusivity (κ), kinematic viscosity (ν), and thermal expansivity (α) are treated as constants. The viscous dissipation term is dropped from the temperature equation as it is small compared to the other terms. The above approximations simplify the physics but provide a fairly accurate description for many convective flows encountered in nature and industries (Kays and Crawford, 1993; Bejan, 2013).

The governing equations of RBC are as follows (Chandrasekhar, 1981; Bhattacharjee, 1987; Ahlers et al., 2009b; Chillà and Schumacher, 2012; Verma, 2018):

$$\frac{\partial \mathbf{u}}{\partial t} + (\mathbf{u} \cdot \nabla) \mathbf{u} = -\frac{\nabla p}{\rho_0} + \alpha g T \hat{z} + \nu \nabla^2 \mathbf{u}, \quad (1.1)$$

$$\frac{\partial T}{\partial t} + (\mathbf{u} \cdot \nabla) T = \kappa \nabla^2 T, \quad (1.2)$$

$$\nabla \cdot \mathbf{u} = 0, \quad (1.3)$$

where \mathbf{u} and p respectively are the velocity and pressure fields, T is the temperature field, ρ_0 is the mean density of the fluid, and g is the acceleration due to gravity. In any buoyancy-driven convection, T is an active scalar as it influences the velocity field through the buoyancy term, $\alpha g T \hat{z}$.

The governing equations of RBC can also be written in terms of θ , the fluctuation of the temperature field from the pure conduction state. When there is no convection, the temperature field (T_c) is a function of only the vertical coordinate z and is given by

$$T_c(z) = T_b - \frac{\Delta}{d} z, \quad (1.4)$$

where T_b is the temperature of the bottom wall, and Δ and d are respectively the temperature difference and the distance between the horizontal walls. The temperature fluctuation is given by

$$\theta(x, y, z) = T(x, y, z) - T_c(z). \quad (1.5)$$

In terms of θ , the governing equations of RBC become

$$\frac{\partial \mathbf{u}}{\partial t} + (\mathbf{u} \cdot \nabla) \mathbf{u} = -\frac{\nabla \sigma}{\rho_0} + \alpha g \theta \hat{z} + \nu \nabla^2 \mathbf{u}, \quad (1.6)$$

$$\frac{\partial \theta}{\partial t} + (\mathbf{u} \cdot \nabla) \theta = \frac{\Delta}{d} u_z + \kappa \nabla^2 \theta, \quad (1.7)$$

$$\nabla \cdot \mathbf{u} = 0, \quad (1.8)$$

where

$$\sigma = p + \alpha g \left(\int^z T_c(z') dz' \right) \quad (1.9)$$

is the modified pressure field (Chandrasekhar, 1981; Verma, 2018).

In numerical and experimental fluid dynamics, it is a standard practice to present data in terms of dimensionless parameters. The governing equations of RBC can be nondimensionalized by appropriate rescaling of variables, thus reducing the number of parameters in the system and making the subsequent analysis simpler. In numerical simulations, it is customary to employ the free-fall velocity ($\sqrt{\alpha g \Delta d}$) as the velocity scale, d as the length scale, and Δ as the temperature scale. The nondimensionalized variables are (Verzicco and Camussi, 1997, 1999; Emran and Schumacher, 2008)

$$\mathbf{u}' = \frac{\mathbf{u}}{\sqrt{\alpha g \Delta d}}, \quad \nabla' = \nabla d, \quad T' = \frac{T}{\Delta}, \quad t' = \frac{\sqrt{\alpha g \Delta d}}{d} t, \quad p' = \frac{p}{\rho_0 \alpha g \Delta d}. \quad (1.10)$$

The governing equations [Eqs. (1.1) to (1.3)] in terms of the nondimensional variables become

$$\frac{\partial \mathbf{u}'}{\partial t'} + \mathbf{u}' \cdot \nabla' \mathbf{u}' = -\nabla' p' + T' \hat{z} + \sqrt{\frac{\text{Pr}}{\text{Ra}}} \nabla'^2 \mathbf{u}', \quad (1.11)$$

$$\frac{\partial T'}{\partial t'} + \mathbf{u}' \cdot \nabla' T' = \frac{1}{\sqrt{\text{RaPr}}} \nabla'^2 T', \quad (1.12)$$

$$\nabla' \cdot \mathbf{u}' = 0, \quad (1.13)$$

where Ra and Pr are Rayleigh and Prandtl numbers respectively. Ra and Pr are the governing parameters of RBC and are given by

$$\text{Ra} = \frac{\alpha g \Delta d^3}{\nu \kappa}, \quad \text{Pr} = \frac{\nu}{\kappa}. \quad (1.14)$$

The Rayleigh number is the ratio of the buoyancy and the dissipative forces. For the

TABLE 1.1: Prandtl numbers of typical fluids

Fluid	Prandtl number	Fluid	Prandtl number
Sun	$\sim 10^{-7}$	Air	0.7
Liquid sodium	0.005	Water	6.8
Mercury	0.02	<i>n</i> -butanol	50
Mixtures of noble gases	0.16 to 0.7	Engine oil	100 to 40,000
Helium	0.7	Earth's mantle	$\sim 10^{25}$

same fluid, Ra depends on the imposed temperature difference between the thermal walls. The Prandtl number is a property of the fluid and is the ratio of the kinematic viscosity and the thermal diffusivity. Typical values of Pr are provided in Table 1.1 (Kays and Crawford, 1993; Coulson and Richardson, 1999; Bejan, 2013; Schumacher and Sreenivasan, 2020).

At small Rayleigh numbers, the heat is transferred purely via conduction. Above a certain critical Rayleigh number (Ra_c), the Rayleigh-Bénard system becomes unstable to small perturbations. The critical Rayleigh number is of the order of 10^3 , with its exact value depending on the geometry of the system and the boundary conditions. For example, for a fluid enclosed between two rigid infinite walls, $Ra_c \approx 1708$ (Chandrasekhar, 1981).

Once the flow becomes unstable, primary convective rolls are generated. As Ra is increased, these rolls become unstable and lead to the generation of secondary rolls. These secondary rolls, in turn, create time-dependent patterns and chaos (Ecke et al., 1991; Paul et al., 2011). For moderate and large- Pr RBC ($Pr \gtrsim 1$), the generation of secondary rolls starts at $Ra \approx 20Ra_c$ (Paul et al., 2011). On the other hand, small- Pr RBC ($Pr \ll 1$) tends to be more unstable than large- Pr convection due to the presence of vortical modes (Pal et al., 2009; Mishra et al., 2010). The generation of secondary rolls in small- Pr RBC occurs at a much lower Rayleigh number – almost at the critical Rayleigh number (Ra_c) itself (Nandukumar and Pal, 2016).

At larger Rayleigh numbers, in the regimes governed by $Ra \gtrsim 10^6 Pr$ (Pandey and Verma, 2016; Pandey et al., 2016a), the flow becomes turbulent and consists of eddies of different scales. The kinetic and thermal energies are transferred from one eddy to another via strong nonlinear interactions. The scales of turbulent RBC can be classified as large or small. The large scales of the flow are of the order of the cell's size. Most of the kinetic and thermal energies are contained in the large scales of the

flow, which dominate the transport of heat and momentum. The small scales comprise of the inertial and the dissipative ranges. Most of the viscous and thermal dissipation occur in the dissipative range (Sreenivasan and Antonia, 1997). The inertial range lies between the large and dissipative scales. This thesis deals with studies on the inertial scale turbulence of RBC, though we call it small-scale in order to contrast with large scales.

1.3 Important diagnostics of RBC

Turbulent Rayleigh-Bénard convection is examined using various diagnostic tools. These tools are the global and local heat fluxes, large-scale velocity, viscous and thermal dissipation rates, the spectra and fluxes of kinetic energy and entropy, and the velocity and temperature structure functions. In this section, we briefly discuss these diagnostic tools.

1.3.1 Global quantities: Nusselt and Reynolds numbers

In RBC, there is a net heat transport from the bottom wall to the top wall; the heat flux is quantified by a nondimensional number, the Nusselt number (Nu). The Nusselt number is the ratio of the total heat flux to the conduction heat flux. At any height z , the Nusselt number is given by

$$\text{Nu} = \frac{\langle u_z T \rangle_A - \kappa \frac{\partial \langle T \rangle_A}{\partial z}}{\kappa \Delta / d}, \quad (1.15)$$

where $\langle \rangle_A$ represents averaging over a horizontal cross-section (Siggia, 1994; Ahlers et al., 2009b). On the right-hand side (RHS) of Eq. (1.15), the first term is the convective heat flux, and the second term is the conduction heat flux. Under a steady state, the Nusselt number is independent of z (Ahlers et al., 2009b; Chillà and Schumacher, 2012). Vertical averaging of Eq. (1.15) yields

$$\text{Nu} = 1 + \frac{\langle u_z T \rangle}{\kappa \Delta / d}. \quad (1.16)$$

In the above relation, $\langle \rangle$ represents the volume average. Since hot plumes ascend and cold plumes descend, u_z and T are positively correlated. Hence, the quantity $\langle u_z T \rangle$

is positive, and the Nusselt number is always greater than or equal to 1. Note that $\text{Nu} = 1$ represents pure conduction.

In RBC, the large-scale velocity is quantified by the Reynolds number (Re), which is computed as[†]

$$\text{Re} = \frac{Ud}{\nu}, \quad (1.17)$$

where U is the large-scale velocity. There are various definitions of U . In numerical studies, U is generally taken to be the root mean square (RMS) velocity (Ahlers et al., 2009b), which is calculated as follows:

$$U_{\text{rms}} = \sqrt{\langle u_x^2 + u_y^2 + u_z^2 \rangle}. \quad (1.18)$$

In experiments, the large scale velocity is often taken as the maximum horizontal or vertical velocity or is based on the peak frequency in the power spectra of the velocity or temperature cross-correlation functions (Ahlers et al., 2009b). Reynolds number is also a measure of the intensity of turbulence in an RBC system.

Apart from the Reynolds number, the Peclét number (Pe) is also used to quantify the large-scale velocity. Peclét number is the ratio of the nonlinear term and the viscous term of the thermal energy equation [Eq. (1.2)], and is given by

$$\text{Pe} = \frac{Ud}{\kappa}. \quad (1.19)$$

The Reynolds and Nusselt numbers are functions of the governing parameters: the Rayleigh and Prandtl numbers. Both Reynolds and Nusselt numbers increase with Rayleigh number. The dependence of Re and Nu on Ra and Pr is reviewed in detail in Sec. 1.7 and is further explored in Chapter 7 of this thesis.

[†] Eq. (1.17) represents the ratio of the nonlinear term, $\mathbf{u} \cdot \nabla \mathbf{u}$, and the viscous term, $\nu \nabla^2 \mathbf{u}$, for hydrodynamic turbulence. In RBC, we get a correction of $\text{Ra}^{-0.14}$. See Sec. 1.6 for discussion.

1.3.2 Viscous and thermal dissipation rates

In RBC, the kinetic energy of the flow gets dissipated at small scales due to viscosity. This phenomenon is quantified by the viscous dissipation rate, which is given by

$$\epsilon_u = \frac{\nu}{2} \left\langle \left(\frac{\partial u_i}{\partial x_j} + \frac{\partial u_j}{\partial x_i} \right)^2 \right\rangle, \quad (1.20)$$

where $i = (x, y, z)$ is the i th component of the velocity field. Similarly, the dissipation of thermal energy is quantified by the thermal dissipation rate, which is given by

$$\epsilon_T = \kappa \langle |\nabla T|^2 \rangle. \quad (1.21)$$

Both the viscous and thermal dissipation rates are positive quantities and are associated with the irreversibilities of the flow.

The viscous and thermal dissipation rates in RBC are related to the global heat transport (Nu) by the following exact relations derived by [Shraiman and Siggia \(1990\)](#):

$$\epsilon_u = \frac{\nu^3}{d^4} (\text{Nu} - 1) \frac{\text{Ra}}{\text{Pr}^2}, \quad (1.22)$$

$$\epsilon_T = \frac{\kappa \Delta^2}{d^2} \text{Nu}. \quad (1.23)$$

The above relations play an important role in our analysis in Chapters 5, 6, and 7 of this thesis.

1.3.3 Structure functions

Structure function is an important diagnostics tool that describes turbulence ([Kolmogorov, 1941a,b](#)). Structure functions quantify the dynamics of turbulent flows at different scales in the real space. The velocity and temperature structure functions are defined as follows.

Let \mathbf{r} and $\mathbf{r} + \mathbf{l}$ be two points in the fluid. The difference between the velocity fields at these two points is $\delta \mathbf{u} = \mathbf{u}(\mathbf{r} + \mathbf{l}) - \mathbf{u}(\mathbf{r})$. The difference in the parallel components of the velocity field along \mathbf{l} is $\delta u = \delta \mathbf{u} \cdot \hat{\mathbf{l}}$. The corresponding difference in the perpendicular component is $\delta u_{\perp} = |\delta \mathbf{u} - \delta u \hat{\mathbf{l}}|$. Assuming statistical homogeneity, we

define the longitudinal velocity structure functions of order q as (Kolmogorov, 1941a,b; Lesieur, 2008; Frisch, 1995)

$$S_q^u(\mathbf{l}) = \langle (\delta u)^q \rangle = \langle [\{ \mathbf{u}(\mathbf{r} + \mathbf{l}) - \mathbf{u}(\mathbf{r}) \} \cdot \hat{\mathbf{l}}]^q \rangle, \quad (1.24)$$

and the transverse velocity structure functions of order q as

$$S_q^{u\perp}(\mathbf{l}) = \langle (\delta u_\perp)^q \rangle = \langle |\delta \mathbf{u} - \delta u \hat{\mathbf{l}}|^q \rangle. \quad (1.25)$$

Here, $\langle \cdot \rangle$ denotes ensemble averaging. In this thesis, we consider only the longitudinal velocity structure functions, which, henceforth, will be referred to as simply velocity structure functions for brevity. For this component, an exact relation exists for the third-order pertaining to homogeneous isotropic turbulence (Kolmogorov, 1941a,b); see Sec. 1.5.1. This relation will be of relevance to our studies (Chapters 3 and 4).

Similar to velocity structure functions, we can define the structure functions for the temperature field as (Sreenivasan, 1991; Warhaft, 2000; Yeung, 2002)

$$S_q^T(\mathbf{l}) = \langle (\delta T)^q \rangle = \langle [T(\mathbf{r} + \mathbf{l}) - T(\mathbf{r})]^q \rangle. \quad (1.26)$$

We will discuss these quantities in Sec. 1.5 and Chapters 3 and 4.

1.3.4 Spectral quantites

We now describe the important spectral quantities used for analyzing the statistics of turbulence in thermal convection. Like structure functions, these quantities help to quantify the dynamics of turbulent flows at different scales.

To compute the spectral quantities, we need to represent the fluid flow in spectral space. Towards this objective, the velocity and temperature fields are expressed as a sum of basis functions. For rigid (no-slip) walls, the expansion of the fields is complex and involves the usage of Chebyshev polynomials (Canuto et al., 1988; Boyd, 2013). On the other hand, for stress-free (free-slip) walls, the expansion of velocity and temperature fields is simpler, involving Fourier basis functions, or more specifically, sine and cosine basis functions (see Chapter 2, Sec. 2.2.2 for details). It is to be noted that for turbulent flows with rigid walls, the near-wall structures are very small compared to the box size and contribute mostly to the dissipative scales. The properties in

the inertial range are not affected by these structures. Hence, even for flows bounded by rigid walls, the spectral quantities computed using Fourier expansion describe the inertial-range turbulence with reasonable accuracy (Verma, 2018).

Spectral quantities are expressed in terms of *wavenumbers*. A wavenumber vector is given by $\mathbf{k} = (k_x, k_y, k_z)$, where

$$k_x = \frac{l\pi}{L_x}, \quad k_y = \frac{m\pi}{L_y}, \quad k_z = \frac{n\pi}{L_z}. \quad (1.27)$$

Here, L_x , L_y , and L_z are respectively the length, width, and height of the convection cell. l , m , and n are positive integers for impenetrable and stress-free walls. Wavenumbers are inverse of length scales; large wavenumbers correspond to small length scales.

Typical spectral quantities are the kinetic energy and entropy spectra, kinetic energy and entropy fluxes, kinetic energy and entropy injection spectra, and the kinetic energy and entropy dissipation spectra. The kinetic energy spectrum is the kinetic energy contained in a wavenumber shell of radius k and of unit thickness (Frisch, 1995; Pope, 2000; Davidson, 2004; Lesieur, 2008). It is defined as

$$E_u(k, t) = \frac{1}{2} \sum_{k \leq |\mathbf{k}'| < k+1} |\mathbf{u}(\mathbf{k}', t)|^2, \quad (1.28)$$

where $\mathbf{u}(\mathbf{k})$ is the Fourier transform of the velocity field. The evolution of kinetic energy spectrum is given by the variable energy flux equation, which is as follows (Frisch, 1995; Lesieur, 2008; Khatri et al., 2018; Verma, 2019b):

$$\frac{\partial}{\partial t} E_u(k, t) = -\frac{d}{dk} \Pi_u(k, t) + \mathcal{F}_B(k, t) - D(k, t). \quad (1.29)$$

In the above equation, $\Pi_u(k, t)$, $\mathcal{F}_B(k, t)$, and $D(k, t)$ are the kinetic energy flux, modal kinetic energy injection rate, and modal kinetic energy dissipation rate respectively. In the following, we explain these quantities in more detail.

The kinetic energy flux quantifies the cascade of kinetic energy from large scales to smaller scales by nonlinear interactions between different velocity modes. The flux is computed as follows (Kraichnan, 1959; Dar et al., 2001; Verma, 2004):

$$\Pi_u(k_0, t) = \sum_{k \geq k_0} \sum_{p < k_0} \delta_{\mathbf{k}, \mathbf{p}+\mathbf{q}} \Im([\mathbf{k} \cdot \mathbf{u}(\mathbf{q}, t)][\mathbf{u}^*(\mathbf{k}, t) \cdot \mathbf{u}(\mathbf{p}, t)]). \quad (1.30)$$

In thermal convection, the kinetic energy is injected by buoyancy. The energy injection spectrum $\mathcal{F}_B(k)$ is given by (Frisch, 1995; Lesieur, 2008)

$$\mathcal{F}_B(k, t) = \sum_{|\mathbf{k}|=k} \text{Re}\{\mathbf{u}(\mathbf{k}, t) \cdot \mathbf{f}^*(\mathbf{k}, t)\} = \alpha g \sum_{|\mathbf{k}|=k} \text{Re}\{u_z(\mathbf{k}, t)\theta^*(\mathbf{k}, t)\}. \quad (1.31)$$

where $\mathbf{f} = \alpha g \theta \hat{\mathbf{z}}$ is the buoyancy term in the momentum equation [Eq. (1.6)] and "*" represents the complex conjugate. The kinetic energy gets dissipated predominantly at small scales due to viscosity. This phenomenon is quantified by the viscous dissipation spectrum, $D(k, t)$, which is given by (Frisch, 1995; Lesieur, 2008)

$$D(k, t) = 2\nu k^2 E_u(k, t), \quad (1.32)$$

with the total viscous dissipation rate being $\epsilon_u = \sum_0^\infty D(k)$. Recall that in real space, ϵ_u is given by Eq. (1.20).

For a steady state, the variable energy flux equation [Eq. (1.29)] reduces to

$$\frac{d}{dk} \Pi_u(k) = \mathcal{F}_B(k) - D(k). \quad (1.33)$$

The above equation implies that for a steady state, the total kinetic energy injection rate $\sum_0^\infty \mathcal{F}_B(k)$ equals the total viscous dissipation rate ϵ_u (Frisch, 1995; Lesieur, 2008).

The entropy spectrum [$E_\theta(k)$] is the entropy ($\theta^2/2$) contained in a wavenumber shell of radius k and of unit thickness. It is given by

$$E_\theta(k, t) = \frac{1}{2} \sum_{k \leq |\mathbf{k}'| < k+1} |\theta(\mathbf{k}', t)|^2. \quad (1.34)$$

Similar to the kinetic energy spectrum, the time evolution of the entropy spectrum is given by the variable entropy flux equation (Frisch, 1995; Lesieur, 2008; Verma, 2019b), which is given by

$$\frac{\partial}{\partial t} E_\theta(k, t) = -\frac{d}{dk} \Pi_\theta(k, t) + \mathcal{F}_\theta(k, t) - D_\theta(k, t), \quad (1.35)$$

where $\Pi_\theta(k, t)$ is the entropy flux (which quantifies the transfer of entropy among different scales), and $\mathcal{F}_\theta(k, t)$ and $D_\theta(k, t)$ are respectively the modal injection and dissipation rates of entropy. The above quantities are given by (Frisch, 1995; Lesieur, 2008;

Verma, 2019b)

$$\Pi_\theta(k_0, t) = \sum_{k \geq k_0} \sum_{p < k_0} \delta_{\mathbf{k}, \mathbf{p} + \mathbf{q}} \Im([\mathbf{k} \cdot \mathbf{u}(\mathbf{q})][\theta^*(\mathbf{k}, t)\theta(\mathbf{p}, t)]). \quad (1.36)$$

$$\mathcal{F}_\theta(k) = \frac{\Delta}{d} \sum_{|\mathbf{k}|=k} \text{Re}\{u_z(\mathbf{k})\theta^*(\mathbf{k})\}, \quad (1.37)$$

$$D_\theta(k) = 2\kappa k^2 E_\theta(k). \quad (1.38)$$

For a steady state, Eq. (1.35) reduces to

$$\frac{d}{dk} \Pi_\theta(k) = \mathcal{F}_\theta(k) - D_\theta(k). \quad (1.39)$$

The above equation implies that for a steady state, the total entropy injection rate $\sum_0^\infty \mathcal{F}_\theta(k)$ equals the total entropy dissipation rate ϵ_θ (Frisch, 1995; Lesieur, 2008). The kinetic energy and entropy spectra are directly related to the structure functions (Frisch, 1995; Davidson, 2004; Ching, 2013).

In the next section, we discuss the typical spatial distribution of velocity and temperature fields in an RBC cell.

1.4 Viscous and thermal boundary layers

In this section, we introduce the concepts of viscous and thermal boundary layers in RBC and discuss the velocity and temperature profiles typically encountered in these regions.

For turbulent convection with rigid walls, the velocity on a wall is zero due to no-slip boundary conditions. The flow in the bulk is dominated by a large-scale circulation (LSC). Hence, the wall-parallel velocity field rises from zero on the wall to the LSC's velocity over a very short distance, which is typically less than 5% of the domain's dimension (Verzicco and Camussi, 2003; Breuer et al., 2004; Scheel et al., 2012; Shi et al., 2012). This small region adjacent to the wall is called the *viscous boundary layer*, or *kinetic boundary layer*. The region between the viscous boundary layers is called *turbulent bulk*. Figure 1.2(a) exhibits the profile of the area-averaged wall-parallel velocity field, showing the viscous boundary layers (shaded region) near the walls. Note that for 3D RBC confined by six rigid walls, there will be a total of six viscous boundary layers.

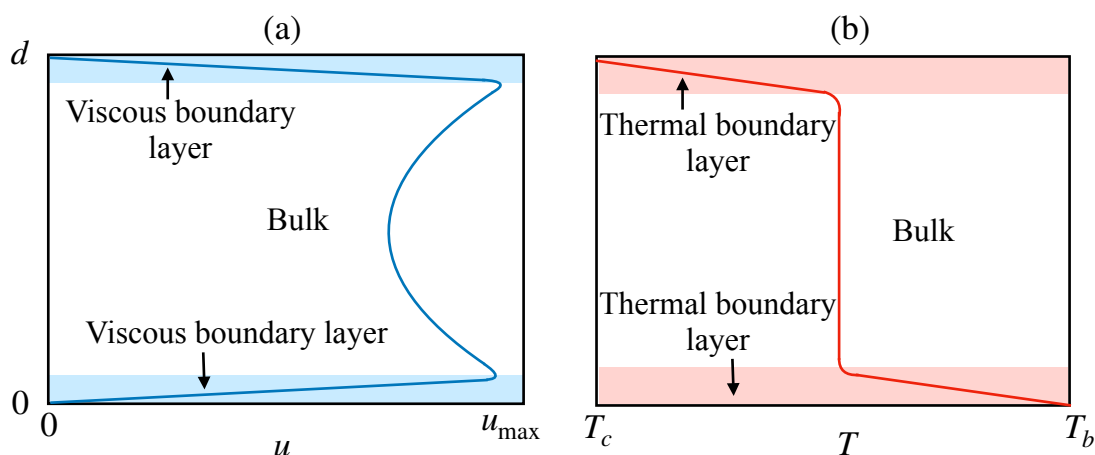


FIGURE 1.2: For horizontal rigid and conducting walls: (a) Typical velocity profile u showing the viscous boundary layers (shaded region) formed near the horizontal walls, and (b) the temperature profile T showing the thermal boundary layers (shaded region) near the horizontal walls.

For pure conduction, the temperature of the fluid drops linearly from T_b at the bottom wall to T_c at the top wall. For turbulent convection, however, the bulk is roughly at the same temperature of $(T_b + T_c)/2$. Thus, the temperature falls steeply from T_b to $(T_b + T_c)/2$ over a short distance near the bottom wall and from $(T_b + T_c)/2$ to T_c near the top wall [Fig. 1.2(b)]. These regimes in which the temperature varies steeply are called *thermal boundary layers*. The thermal boundary layers are formed near only the horizontal conducting walls (Ahlers et al., 2009b; Chillà and Schumacher, 2012).

The thickness of the thermal boundary layers, δ_T , is given by the following exact relation (Malkus, 1954; Siggia, 1994; Ahlers et al., 2009b):

$$\delta_T = \frac{d}{2\text{Nu}}. \quad (1.40)$$

For large Reynolds numbers, the viscous boundary layer thickness, δ_u , can be estimated as

$$\delta_u \sim \frac{d}{\sqrt{\text{Re}}}, \quad (1.41)$$

similar to the boundary layer thickness over a flat plate (Landau and Lifshitz, 1987; Shishkina et al., 2010, 2013). However, as we will show later in Sec. 1.7 and in Chapters 5 and 7, the viscous boundary layer thickness differs from Eq. (1.41), albeit marginally.

The boundary layers bring about interesting subtleties in the scaling of the dissipation rates and the large-scale quantities that will be discussed later in this chapter (Sec. 1.6).

1.5 Phenomenology of turbulent RBC

In this section, we review the small-scale statistics of turbulent RBC. We discuss the current understanding of the scaling of the spectral quantities and structure functions of RBC.

1.5.1 Homogeneous and isotropic hydrodynamic turbulence

Before going further into the details of turbulence in RBC, we briefly discuss the celebrated Kolmogorov's theory (Kolmogorov, 1941a,b) of hydrodynamic turbulence. The turbulence in such a system is statistically homogeneous and isotropic in the inertial range. In this system, the kinetic energy $[(1/2)\langle |\mathbf{u}|^2 \rangle]$ is supplied at large length scales, which cascades to intermediate scales or the inertial range and then to the dissipative scales. Kolmogorov's theory assumes that in the inertial range, no kinetic energy is injected, and the viscous dissipation rate is negligible. This leads to the kinetic energy flux Π_u being constant in the inertial range and equal to the total viscous dissipation rate ϵ_u . Kolmogorov (1941a,b) analytically derived the following relation for the third-order longitudinal velocity structure function of such a flow:

$$S_3^u(l) = -\frac{4}{5}\epsilon_u l. \quad (1.42)$$

For any order q , one expects, using dimensional analysis, that in the inertial range,

$$S_q^u(l) \sim l^{q/3}. \quad (1.43)$$

However, results from several experimental and numerical studies show deviations from the exponent $q/3$ for $q \neq 3$. These deviations arise due to intermittency effects. Among many models, such as β model, multifractal model, and log-normal model (Frisch, 1995; Sreenivasan and Antonia, 1997; Verma, 2005), the model by She

and Leveque (1994) provides the best fit function to the scaling exponent (ζ_q) of the velocity structure function, which is given by

$$\zeta_q = \frac{q}{9} + 2 \left(1 - \left(\frac{2}{3} \right)^{q/3} \right). \quad (1.44)$$

According to Kolmogorov's theory, the mechanisms of kinetic energy forcing and dissipation do not affect the physics of the inertial range; hence the kinetic energy spectrum depends only on the wavenumber k and the inertial range kinetic energy flux Π_u (Kolmogorov, 1941a,b; Frisch, 1995). Using this assumption and noting that $\Pi_u = \epsilon_u$, dimensional analysis leads to the well-known $k^{-5/3}$ relation for the kinetic energy spectrum in the inertial range:

$$E_u(k) = K_{K_0} \epsilon_u^{2/3} k^{-5/3}, \quad (1.45)$$

where K_{K_0} is the Kolmogorov constant.

1.5.2 Passive scalar turbulence

Obukhov (1949) and Corrsin (1951) described homogeneous and isotropic turbulence with a passive scalar θ . For such flows, the third-order velocity structure function and the kinetic energy spectrum follow Kolmogorov's relations given by Eqs. (1.42) and (1.45) because passive scalars do not influence the fluid flow. Further, Obukhov and Corrsin's theory assumes that the scalar energy $[(1/2)\langle\theta^2\rangle]$ is injected at large scales, cascades down to the intermediate and then to the dissipative scales. Similar to the kinetic energy flux, the scalar flux Π_θ is also constant in the inertial range and equals the scalar dissipation rate ϵ_θ . Using dimensional analysis, the following could be extrapolated for the scalar energy spectrum $[E_\theta(k)]$ and the structure functions $[S_q^\theta(l)]$ of passive scalar turbulence (Obukhov, 1949; Corrsin, 1951; Sreenivasan, 1991):

$$E_\theta(k) = K_{OC} \epsilon_\theta \epsilon_u^{-1} k^{-5/3}, \quad (1.46)$$

$$S_q^\theta(l) \sim l^{q/3}, \quad (1.47)$$

where K_{OC} is the Obukhov-Corrsin constant. It is to be noted that the above relations are only approximate. There are intermittency corrections similar to that of She-

Leveque's relation for homogeneous isotropic turbulence (Frisch, 1995; Falkovich et al., 2001)

The phenomenology governing homogeneous isotropic turbulence with passive scalar is known as Kolmogorov-Obukhov (KO) phenomenology in the literature (Lesieur, 2008; Verma, 2019b; Sadhukhan et al., 2019).

1.5.3 Buoyancy-driven turbulence

The energetics becomes more involved in buoyancy-driven turbulence compared to homogeneous isotropic hydrodynamic turbulence. In such flows, buoyancy acts at all scales, including the inertial range, and alters the scaling of the structure functions and the spectra of kinetic energy and entropy (Bolgiano, 1959; Obukhov, 1959; Procaccia and Zeitak, 1989; L'vov and Falkovich, 1992; Lohse and Xia, 2010). In the following, we discuss the phenomenology of buoyancy-driven flows. We also review the results of experiments and numerical simulations of such flows.

A. Stably-stratified turbulence

For stably-stratified turbulence, Bolgiano (1959) and Obukhov (1959) proposed that below a certain wavenumber k_B in the inertial range, where the buoyancy forces are strong, the kinetic energy spectrum follows a steeper scaling compared to homogeneous isotropic turbulence. This is due to kinetic energy being converted to potential energy by buoyancy in this subrange. As a consequence, the kinetic energy flux decreases with wavenumber k , unlike Kolmogorov's constant kinetic energy flux. The energy and entropy spectra in such systems are given by

$$E_u(k) = c_1 \epsilon_\theta^{2/5} (\alpha g)^{4/5} k^{-11/5}, \quad (1.48)$$

$$E_\theta(k) = c_2 \epsilon_\theta^{4/5} (\alpha g)^{-2/5} k^{-7/5}, \quad (1.49)$$

$$\Pi_u(k) = c_3 \epsilon_\theta^{3/5} (\alpha g)^{6/5} k^{-4/5}, \quad (1.50)$$

$$\Pi_\theta(k) = \epsilon_\theta. \quad (1.51)$$

where c_1 , c_2 , and c_3 are constants (Bolgiano, 1959; Obukhov, 1959). Above the Bolgiano wavenumber k_B , the buoyancy forces are weak, resulting in KO scaling of the kinetic energy and entropy spectra given by Eqs. (1.45) and (1.46).

An extension of the Bolgiano-Obukhov (BO) theory to velocity and temperature structure functions yields (Lohse and Xia, 2010)

$$S_u^q(l) \sim l^{3q/5}, \quad (1.52)$$

$$S_\theta^q(l) \sim l^{q/5}. \quad (1.53)$$

The aforementioned relations are for $l > l_B$, the Bolgiano length scale. Below this length scale, the KO relations of $S_u^q(l) \sim l^{q/3}$ and $S_\theta^q(l) \sim l^{q/3}$ are expected. Thus, when l_B is small, BO scaling becomes more prominent.

BO scaling of the energy and entropy spectra has been reported in the numerical studies of stably-stratified turbulence under moderate stratification[‡] (see, for example, Kimura and Herring, 1996; Kumar et al., 2014; Kumar and Verma, 2015). For weakly stratified turbulence, KO scaling has been reported because the buoyancy forces are weak (Kumar et al., 2014; Kumar and Verma, 2015). BO scaling has again not been observed for strongly-stratified turbulence. This is because in this regime, the anisotropy induced by buoyancy becomes strong, and the flow becomes quasi-two dimensional, giving rise to different physics (refer to Lindborg, 2006; Brethouwer et al., 2007; Bartello and Tobias, 2013, for further details).

B. Energy and entropy spectra of RBC

Using theoretical arguments, Procaccia and Zeitak (1989), L'vov (1991), L'vov and Falkovich (1992), and Rubinstein (1994) proposed the applicability of BO scaling to RBC as well. Researchers have attempted to confirm the above theory with the help of experiments and numerical simulations, as well as using theoretical arguments. In the following, we discuss the numerical and experimental results on the scaling of kinetic energy and entropy spectra of RBC.

Many researchers have earlier reported BO scaling for moderate and large-Pr RBC (see, for example, Wu et al., 1990; Chillà et al., 1993; Kerr, 1996; Ashkenazi and Steinberg, 1999b; Niemela et al., 2000; Shang and Xia, 2001; Zhou and Xia, 2001). However, BO scaling was not observed in the early studies of small-Pr RBC (Cioni et al., 1995; Takeshita et al., 1996; Camussi and Verzicco, 1998; Horanyi et al., 1999; Mishra and

[‡] In stably-stratified turbulence, the strength of stratification is given by the Richardson number (Ri), which is the ratio of the buoyancy and nonlinear terms. The regimes of $Ri \ll 1$, $Ri \sim 1$, and $Ri \gg 1$ respectively correspond to weak, moderate, and strong stratification (Verma et al., 2017).

Verma, 2010). In a critical review, Lohse and Xia (2010) raised doubts on BO phenomenology in RBC.

More recently, using phenomenological arguments and numerical simulations, Kumar et al. (2014) and Verma et al. (2017) argued for Kolmogorov's scaling in the kinetic energy spectrum of RBC. They suggested that since hot plumes ascend and cold plumes descend, u_z and θ are positively correlated, that is,

$$\langle u_z \theta \rangle > 0 \implies \sum \text{Re}[\theta(k) u_z^*(k)] > 0.$$

Although the above relation does not imply that $\text{Re}[\theta(k) u_z^*(k)] > 0$, the latter turns out to be true for most cases (Kumar et al., 2014). Using this condition, Kumar et al. (2014) and Verma et al. (2017) argued that the kinetic energy injection spectrum, $\mathcal{F}_B(k)$, is positive in the inertial range. They further supported their argument with their numerical data for $\text{Pr} = 1$ RBC, using which they showed that $\mathcal{F}_B(k) > 0$ in the inertial range. Thus, assuming negligible dissipation in the inertial range, the variable energy flux equation for RBC becomes

$$\frac{\partial \Pi_u}{\partial k} \approx \mathcal{F}_B(k) > 0. \quad (1.54)$$

The above equation shows that the kinetic energy flux is a non-decreasing function of k . Using this condition, Kumar et al. (2014) and Verma et al. (2017) ruled out BO scaling in RBC, as BO scaling predicts $\Pi_u(k)$ to be a decreasing function of k (given by $\Pi_u(k) \sim k^{-4/5}$).

Further, Kumar et al. (2014) and Verma et al. (2017) also showed that $\mathcal{F}_B(k)$ is strong only at large scales and drops sharply as $\sim k^{-5/3}$, implying that $\mathcal{F}_B(k) \approx 0$ the inertial range. Hence, Eq. (1.54) becomes

$$\frac{\partial \Pi_u}{\partial k} \approx 0, \quad (1.55)$$

which gives $\Pi_u(k) = \text{constant}$. The constancy of kinetic energy flux gives rise to Kolmogorov-like ($\sim k^{-5/3}$) kinetic energy spectrum in RBC.

Subsequent works on small and moderate-Pr convection, conducted by Schumacher et al. (2015), Bhattacharjee (2015), Frick et al. (2015), Kumar and Verma (2015, 2018), and Shestakov et al. (2017), also reported Kolmogorov scaling of the kinetic energy spectrum. However, large-Pr convection was shown to exhibit a much steeper ki-

netic energy spectrum ($E_u(k) \sim k^{-13/3}$) due to strong viscous dissipation (see [Pandey et al., 2014, 2016b](#), for details).

In the numerical studies of [Mishra and Verma \(2010\)](#), [Pandey et al. \(2014\)](#), [Kumar et al. \(2014\)](#), and [Verma et al. \(2017\)](#), the entropy spectrum of RBC was reported to exhibit two branches. The upper branch was observed to scale as $\sim k^{-2}$, while the lower branch did not exhibit any clear scaling. [Mishra and Verma \(2010\)](#) and [Pandey et al. \(2014\)](#) explained the upper branch in terms of the temperature modes $\theta(0, 0, 2k_z)$, which are approximately equal to $-1/(2k_z\pi)$ when the thermal boundary layer thickness is very small compared to the domain size. The temperature modes of both the branches were shown to yield the constant entropy flux. For small Prandtl number ($Pr = 0.02$), the upper branch was not very prominent ([Mishra and Verma, 2010](#)). This is because the thermal boundary layers for small-Pr convection occupy a significant proportion of the total volume of the domain. As a result, many of the $\theta(0, 0, 2k_z) = -1/(2k_z\pi)$ modes are absent and hence the k^{-2} branch is less conspicuous for such a case.

C. Structure functions of RBC

Unlike the energy and entropy spectra, the behavior of the structure functions of RBC is not yet conclusive. In the following, we present the past experimental and numerical results on the structure functions of RBC.

[Benzi et al. \(1994a,b\)](#) simulated both 2D and 3D RBC using Lattice Boltzmann method and computed the velocity and temperature structure functions up to the sixth order. They could not observe any discernible scaling for the structure functions due to short inertial range. They derived a relationship between the velocity and temperature structure functions and suggested BO scaling based on the above relationship. [Ching \(2000\)](#) computed the velocity and temperature structure functions using the experimental data of [Heslot et al. \(1987\)](#) and [Sano et al. \(1989\)](#) and observed two distinct scaling regimes separated by the Bolgiano-length scale, which is suggestive of BO scaling. However, [Ching \(2000\)](#) also observed the scaling exponents to deviate marginally from those predicted by the BO theory.

Several researchers computed structure functions separately at the cell-center and near the walls and obtained KO scaling at the cell-center and BO scaling near the walls. [Calzavarini et al. \(2002\)](#) computed third-order structure functions using their lattice

Boltzmann simulation data and suggested BO scaling near the walls and KO scaling at the cell center. Sun et al. (2006) carried out experiments that involved high-resolution multipoint measurements of temperature and velocity fields in water. Their exponents of velocity structure functions computed at the cell center fit well with the She-Leveque model [Eq. (1.44)], with the lower orders following Kolmogorov scaling and higher orders deviating from it. Using refined similarity hypothesis, Ching et al. (2013) derived power-law relations for conditional velocity and temperature structure functions computed at given values of the locally averaged thermal dissipation rate. They further computed the conditional temperature structure functions up to the fourth-order using the experimental data of He and Tong (2009). Based on the observed power-law scaling, they too concluded BO scaling near walls and KO scaling at the cell center. The above studies attributed KO scaling in the bulk to the large value of local l_B , which is of the same order as the cell size. Since l_B is small near the walls, it is argued that the structure functions in those regions follow BO scaling.

In yet another set of studies described in the following, the results of the structure functions are different from those mentioned above. Ching (2007) computed the structure functions of plume velocity using the experimental data of Castaing et al. (1989) and Shang et al. (2003) and found them to scale similar to the temperature structure functions. This does not agree with BO scaling where the velocity and temperature structure functions scale differently [Eqs. (1.52) and (1.53)]. Kunnen et al. (2008) conducted direct numerical simulations of RBC and reported the velocity structure functions to follow BO scaling for Rayleigh number $Ra = 10^8$ and Kolmogorov scaling for higher Ra . Ching and Cheng (2008) calculated temperature structure functions using shell model of homogeneous RBC and found them to deviate significantly from BO scaling for $q > 4$. Kaczorowski and Xia (2013) conducted direct numerical simulations (DNS) of RBC and found that the velocity structure functions computed at the cell center approach Kolmogorov scaling for lower orders.

From the conflicting nature of the results from past studies, it is clear that the behaviour of the structure functions of turbulent convection has not yet been clearly established as to whether they follow KO or BO scaling. This is because in the studies mentioned above, the inertial range was not wide enough to get a conclusive answer. Further, the above studies did not take into account that in thermal convection, buoyancy injects kinetic energy into the system at all scales, unlike flows governed by BO phenomenology, where buoyancy depletes kinetic energy from the system. Based on

Kolmogorov-like phenomenology of RBC described by [Kumar et al. \(2014\)](#) and [Verma et al. \(2017\)](#), we expect the velocity structure functions of RBC to be similar to those of homogeneous isotropic turbulence.

There are other interesting topics on spectral quantities and structure functions that are yet to be explored. Currently, the literature on the structure functions of RBC is restricted to $\text{Pr} < 7$. The behavior of structure functions at larger Prandtl numbers is yet to be reported. Further, past research on the structure functions and the energy and entropy spectra was conducted for fixed sets of governing parameters. A comprehensive study on the behavior of these quantities under variations in Ra and Pr is still missing in the literature.

1.6 Scaling of viscous and thermal dissipation rates

In this section, we review the literature on the statistics of viscous and thermal dissipation rates in RBC.

For homogeneous isotropic turbulence with passive scalar, the viscous and scalar dissipation rates can be estimated as

$$\epsilon_u \sim \frac{U^3}{L}, \quad \epsilon_\theta \sim \frac{U\Theta^2}{L}, \quad (1.56)$$

where L and Θ are large-scale length and scalar fields respectively ([McComb, 1990](#); [Frisch, 1995](#); [Lesieur, 2008](#)). However, the scaling of the dissipation rates is different for RBC, where boundary layers near the walls play an important role and T is an *active* scalar. Note that for RBC, the large-scale length and scalar (temperature) fields are taken respectively as the distance d and the temperature difference Δ between the conducting plates. Using scaling arguments and Eqs. (1.22) and (1.23) that relate the dissipation rates to the global heat flux, [Pandey and Verma \(2016\)](#) and [Pandey et al. \(2016a\)](#) deduced that for $\text{Pr} \sim 1$, the global dissipation rates in RBC scale as

$$\epsilon_u \sim \frac{U^3}{d} \text{Ra}^{-0.2}, \quad \epsilon_T \sim \frac{U\Delta^2}{d} \text{Ra}^{-0.2}, \quad (1.57)$$

instead of U^3/d and $U\Delta^2/d$. [Pandey and Verma \(2016\)](#) and [Pandey et al. \(2016a\)](#) attributed the additional Ra dependence in the above relations to suppression of nonlin-

ear interactions due to the presence of walls. They showed that in RBC, the ratio of the nonlinear term, $\mathbf{u} \cdot \nabla \mathbf{u}$, to the viscous term, $\nu \nabla^2 \mathbf{u}$, scales as $(Ud/\nu)\text{Ra}^{-0.14}$ instead of Ud/ν as in homogeneous isotropic turbulence. [Verma \(2018\)](#) argued that some Fourier modes that are otherwise present in homogeneous isotropic turbulence are absent in wall-bounded RBC, resulting in the breaking of several channels of nonlinear interactions and energy cascades.

The walls also bring about spatial inhomogeneity in the viscous and thermal dissipation rates. The scaling of the dissipation rates is expected to be different in bulk and boundary layers of RBC. [Grossmann and Lohse \(2000, 2001\)](#) argued that the viscous and thermal dissipation rates in the bulk, represented respectively as $\epsilon_{u,\text{bulk}}$ and $\epsilon_{T,\text{bulk}}$, scale as U^3/d and $U\Delta^2/d$, similar to homogeneous isotropic turbulence. Later studies, however, observed deviations in the scaling of bulk dissipation rates; they are described as follows.

Using their numerical data, [Verzicco and Camussi \(2003\)](#) computed the viscous dissipation rate averaged over a subvolume at the cell-center occupying 4% of the total cell volume. The above dissipation rate, normalized with U^3/d , was observed to be a decreasing function of Ra instead of being a constant, implying that $\epsilon_{u,\text{bulk}} \neq U^3/d$. A similar additional Ra dependence was also observed for thermal dissipation rate by [Emran and Schumacher \(2008\)](#), who used their numerical data to compute the thermal dissipation rate averaged over a subvolume inside the bulk occupying one-third of the total volume of the cell. They reported the above dissipation rate normalized with $U\Delta^2/d$ to decrease with Ra, again indicating that $\epsilon_{T,\text{bulk}} \neq U\Delta^2/d$. [He et al. \(2007\)](#) and [He and Tong \(2009\)](#) used their experimental data to measure the thermal dissipation rate in the cell-center and observed a correction of $\text{Ra}^{-0.33}$ in the scaling of the thermal dissipation rate. Although all the results described above suggest that the scaling of the dissipation rates has an additional Ra dependence, there were some limitations in these studies that are discussed at the end of this section.

In so far as the spatial distribution of the dissipation rates in RBC are concerned, it is generally believed that most of the dissipation occurs near the boundaries ([Puthenveetil and Arakeri, 2005](#); [Puthenveetil et al., 2005](#)). Interestingly, however, numerical studies of three-dimensional RBC, conducted by [Verzicco and Camussi \(2003\)](#) and [Silano et al. \(2010\)](#), have revealed that although the thermal dissipation rate dominates in the boundary layers for a wide range of Ra and Pr, the viscous dissipation rate dominates in the bulk for large Rayleigh numbers ($\text{Ra} > 10^8$). Numerical studies conducted

by [Kumar et al. \(2014\)](#) and [Verma et al. \(2017\)](#) on the viscous dissipation spectrum of RBC revealed that significant dissipation also occurs at large scales in addition to the dissipative scales, implying that the viscous dissipation rate is strong in the bulk. However, for two-dimensional RBC, [Zhang et al. \(2017\)](#) reported both viscous and thermal dissipation rates to dominate in the boundary layers for even large Rayleigh numbers ($\sim 10^{10}$).

Since the boundary layers occupy a very small volume compared to the bulk, both thermal and viscous dissipation rates are more intense in the boundary layers. This feature has been observed in the spatial profiles of the local dissipation rates reported in the experiments of [He et al. \(2007, 2011\)](#) and [He and Tong \(2009\)](#), and several numerical simulations ([Shishkina and Wagner, 2005](#); [Emran and Schumacher, 2008](#); [Silano et al., 2010](#); [Scheel et al., 2013](#); [Scheel and Schumacher, 2016, 2017](#); [Zhang et al., 2017](#)). [Emran and Schumacher \(2008\)](#) and [Scheel et al. \(2013\)](#) computed the probability distribution functions (PDFs) of thermal dissipation rates in the bulk and in the boundary layers and reported the PDFs for both subvolumes to be stretched exponentials, similar to passive scalar dissipation ([Chertkov et al., 1998](#)). They further observed that the tails of the PDFs of the boundary layers are wider than those of the bulk, implying that extreme events occur more frequently in the boundary layers. [Scheel et al. \(2013\)](#) and [Zhang et al. \(2017\)](#) observed the viscous dissipation rate in the boundary layers to follow stretched exponential as well. The above studies also revealed that the fluctuations of the dissipation rates increase with Rayleigh numbers.

The above numerical and experimental studies have some caveats that are described below. In the experiments of [He et al. \(2007\)](#) and [He and Tong \(2009\)](#), the thermal dissipation rates were measured only at selected points in the bulk and in the boundary layers. Ideally, since the dissipation rates vary throughout the domain, they should be measured at many points and then averaged for accurate results. However, this process is very difficult in experiments. In the scaling analysis conducted by [Verzicco and Camussi \(2003\)](#), [Emran and Schumacher \(2008\)](#), and [Scheel and Schumacher \(2017\)](#), the bulk was taken as a sub-region in the center of the cell. This may affect the accuracy of their results on scaling of the bulk dissipation rate because the dissipation rates are expected to vary throughout the bulk. Further, for computing the relative strengths of the dissipation rates in the bulk and boundary layers, [Silano et al. \(2010\)](#) fixed the boundary layer thickness at 1/50 of the cell depth for all Pr and Ra. Again, this approach may not be very accurate because the boundary layer thicknesses vary

with Ra and Pr.

1.7 Scaling of Nusselt and Reynolds numbers

In this section, we review the studies on the dependence of the Nusselt and Reynolds numbers on Ra and Pr.

One of the earliest theories explaining the scaling of Nu is that of [Davis \(1922b,a\)](#), in which it was deduced that $Nu \sim Ra^{1/4}$ for small Rayleigh numbers. Later, [Malkus \(1954\)](#) proposed the marginal stability theory according to which the the heat transport is independent of the cell-height d . This assumption yielded $Nu \sim Ra^{1/3}$.

[Kraichnan \(1962\)](#) suggested that for small Prandtl numbers, where the viscous boundary layer is thinner compared to the thermal boundary layer, the velocity profile is logarithmic for very large Rayleigh numbers (called the ultimate regime). Under this assumption, [Kraichnan \(1962\)](#) deduced that

$$Nu \sim \begin{cases} (RaPr)^{1/2}(\ln Ra)^{-3/2}, & Pr \leq 0.15, \\ Ra^{1/2}Pr^{-1/4}(\ln Ra)^{-1/2}, & 0.15 < Pr \leq 1, \end{cases} \quad (1.58)$$

$$Re \sim \begin{cases} (Ra/Pr)^{1/2}(\ln Ra)^{-3/2}, & Pr \leq 0.15, \\ Ra^{1/2}Pr^{-3/4}(\ln Ra)^{-1/2}, & 0.15 < Pr \leq 1, \end{cases} \quad (1.59)$$

[Spiegel \(1971\)](#) proposed that for large Rayleigh numbers, the kinematic viscosity and the thermal diffusivity do not influence the heat flux. This assumption leads to $Nu \sim Ra^{1/2}$, similar to the arguments of [Kraichnan \(1962\)](#). Subsequently, [Castaing et al. \(1989\)](#) argued that $Nu \sim Ra^{2/7}$ and $Re \sim Ra^{3/7}$ based on the existence of a mixing zone in the central region of the RBC cell where hot rising plumes meet mildly warm fluid. [Castaing et al. \(1989\)](#) also deduced that $Re^\omega \sim Ra^{1/2}$, where Re^ω is Reynolds number based on the frequency ω of torsional azimuthal oscillations of the large scale wind in RBC. Later, [Shraiman and Siggia \(1990\)](#) derived that $Nu \sim Ra^{2/7}Pr^{-1/7}$ and $Re \sim Ra^{3/7}Pr^{-5/7}$ (with logarithmic corrections) using the properties of boundary layers.

Some researchers have analytically derived bounds on the exponent for Nusselt number's scaling. [Constantin and Doering \(1999\)](#) and [Ierley and Kerswell \(2006\)](#) de-

duced that in the limit of infinite Prandtl number, $Nu \leq cRa^{1/3}$ (with logarithmic corrections) for rigid walls, where c is a constant. For stress-free walls, [Ierley and Kerswell \(2006\)](#) and [Whitehead and Doering \(2011, 2012\)](#) deduced that $Nu \leq cRa^{5/12}$ (again, with logarithmic corrections), where c is again a constant.

Many experiments and simulations of RBC have been performed to obtain the scaling of Nu and Re . These studies also revealed a power-law scaling of Nu and Re as $Nu \sim Ra^\alpha Pr^\beta$ and $Re \sim Ra^\gamma Pr^\delta$. For the scaling of Nu , the exponent α ranges from 0.25 for $Pr \ll 1$ (see, for example, [Rossby, 1969](#); [Cioni et al., 1997](#); [Verzicco and Camussi, 1997](#); [Scheel and Schumacher, 2016, 2017](#)) to approximately 0.3 for $Pr \gtrsim 1$ (see, for example, [Castaing et al., 1989](#); [Kerr, 1996](#); [Niemela et al., 2000](#); [Xia et al., 2002](#); [Funkschilling et al., 2005](#); [Sameen et al., 2008, 2009](#); [Vishnu and Sameen, 2020](#)). α also depends on the regime of Ra as well: for example, for $Pr \sim 1$, α varies from 0.3 for moderate Ra to 0.35 for very large Ra ($\sim 10^{15}$) ([Zhu et al., 2018](#); [Iyer et al., 2020](#)). The exponent β ranges from approximately zero for $Pr \gtrsim 1$ (see, for example, [Ashkenazi and Steinberg, 1999a](#); [Ahlers and Xu, 2001](#); [Xia et al., 2002](#); [Silano et al., 2010](#)) to 0.15 for $Pr \ll 1$ ([Verzicco and Camussi, 1999](#); [Schmalzl et al., 2002](#); [Petschel et al., 2013](#)). Thus, Nu has a relatively weaker dependence on Pr .

For the scaling of Re , the exponent γ was observed to be approximately 0.4 for $Pr \ll 1$ (see, for example, [Cioni et al., 1997](#); [Verzicco and Camussi, 1999](#); [Kerr and Herring, 2000](#); [Scheel and Schumacher, 2016, 2017](#)), between 0.45 and 0.5 for $Pr \sim 1$ (see, for example, [Xin and Xia, 1997](#); [Niemela et al., 2001](#); [Brown et al., 2005](#); [Emran and Schumacher, 2008](#); [Verma et al., 2012](#); [Kaczorowski and Xia, 2013](#)), and 0.6 for $Pr \gg 1$ (see, for example, [Lam et al., 2002](#); [Horn et al., 2013](#); [Pandey et al., 2014, 2016b](#); [Shishkina et al., 2017](#)). The exponent δ has been observed to range from -0.7 for $Pr \lesssim 1$ ([Verzicco and Camussi, 1999](#)) to -0.95 for $Pr \gg 1$ ([Lam et al., 2002](#); [Silano et al., 2010](#)). For a more detailed review on the past experiments and simulations on Nu and Re scaling, refer to [Ahlers et al. \(2009a\)](#), [Chillà and Schumacher \(2012\)](#), and [Verma \(2018\)](#).

The ultimate regime, characterized by $Nu \sim Ra^{1/2}$, has been observed in simulations of RBC with periodic boundary conditions ([Verma et al., 2012](#); [Lohse and Toschi, 2003](#)), in free convection with density gradient ([He et al., 2012](#); [Pawar and Arakeri, 2016a,b](#)), and in convection with only lateral walls ([Schmidt et al., 2012](#)). Using numerical simulations, [Calzavarini et al. \(2005\)](#) showed that $Re \sim Pr^{1/2}$ and $Nu \sim Pr^{1/2}$ for convection with periodic walls. However, [Calzavarini et al. \(2006\)](#) and [Doering \(2019\)](#)

raised doubts on the ultimate scaling observed in RBC with periodic walls because of the presence of elevator modes in the system. Some experiments and simulations of RBC with non-periodic walls and very large Ra ($\sim 10^{15}$) have reported a possible transition to the ultimate regime (see, for example, [Chavanne et al., 1997](#); [Roche et al., 2001](#); [Ahlers et al., 2009a](#); [He et al., 2012](#); [Ahlers et al., 2017](#)). However, other studies involving experiments and simulations of very large Ra convection, notably those of [Glazier et al. \(1999\)](#), [Niemela et al. \(2000\)](#), and [Iyer et al. \(2020\)](#), argued against any transition to the ultimate regime.

The above studies show that the scaling of Re and Nu depends on the regime of Ra and Pr , highlighting the need for a unified model that encompasses all the regimes. [Grossmann and Lohse \(2000, 2001, 2002, 2003\)](#) constructed one such model, henceforth referred to as GL model. To derive this model, [Grossmann and Lohse \(2000, 2001\)](#) substituted the bulk and the boundary layer contributions of viscous and thermal dissipation rates in the exact relations of [Shraiman and Siggia \(1990\)](#). The bulk and the boundary layer contributions were written in terms of Re , Nu , Ra , and Pr using the properties of boundary layers (Prandtl-Blasius theory) and those of hydrodynamic and passive scalar turbulence in the bulk. Finally, using additional crossover functions, [Grossmann and Lohse \(2001\)](#) obtained a system of equations for Re and Nu in terms of Ra , Pr , and several coefficients that were determined using inputs from experimental data ([Stevens et al., 2013](#)). The predictions of [Kraichnan \(1962\)](#), [Castaing et al. \(1989\)](#), and [Shraiman and Siggia \(1990\)](#) were shown to be limiting cases of the GL model.

The GL model has been quite successful in predicting large scale velocity and heat transport in many experiments and simulations. However, it does not capture large Pr convection very accurately ([Verma, 2018](#)) and has been reported to under-predict the Reynolds number ([Ahlers et al., 2009b](#)). Note that the scaling exponent for Re has a longer range (0.40 to 0.60) compared to that for Nu (0.25 to 0.35); hence the predictions for Re are more sensitive to modeling parameters. Further, the GL model is based on certain assumptions that are not valid for RBC. For example, the model assumes that the viscous and the thermal dissipation rate in the bulk scales similar to those of homogeneous isotropic turbulence. However, as explained in Sec. 1.6, numerical and experimental studies have observed deviations from the above relations ([Verzicco and Camussi, 2003](#); [He et al., 2007](#); [Emran and Schumacher, 2008](#); [He and Tong, 2009](#)). Moreover, recent studies have revealed that the viscous boundary layer thickness in

RBC deviates from $\text{Re}^{-1/2}$, contrary to the assumptions of the GL model (Breuer et al., 2004; Scheel et al., 2012; Shi et al., 2012).

We conclude this section by briefly describing a recent work by Pandey and Verma (2016) and Pandey et al. (2016a), who developed an analytical relation for the Peclét number by estimating the relative strengths of the various terms of the momentum equation [Eq. (1.6)]. Their predictions of Pe match well with the past experiments and numerical simulations and were shown to be better than those of the GL model (Verma, 2018). They also explained the deviation of the Nusselt number from Kraichnan's prediction of $\text{Nu} \sim \text{Ra}^{1/2}$ to the experimentally and numerically observed scaling of $\text{Nu} \sim \text{Ra}^{0.3}$ based on correlations

1.8 Statistics of local heat fluxes

The local convective heat fluxes in the x , y , and z directions are given by $u_x T$, $u_y T$, and $u_z T$ respectively. Even though there is a net heat flow from the bottom wall to the top wall (as discussed in Sec. 1.3.1), there can be local heat fluxes in the downward direction as well as in the horizontal directions (Shang et al., 2003; Shishkina and Wagner, 2007; Kaczorowski and Xia, 2013; Pharasi et al., 2016). The positive vertical heat fluxes dominate the negative ones, leading to a net vertical heat flux. Similar asymmetry has been observed in many other systems, for example, in wave turbulence (Falcon et al., 2008). The positive and negative horizontal heat fluxes, on the other hand, are symmetric and cancel each other. Hence, there is no heat flow in the horizontal directions.

Past analyses on the local heat fluxes have revealed some interesting statistics as described below. Shang et al. (2003) computed the PDFs of the local heat fluxes measured at the cell center and near one sidewall of their experimental setup of RBC. They observed the vertical heat flux measured near the sidewall to exhibit stronger asymmetry and fluctuations compared to that measured in the cell center.

Shishkina and Wagner (2007) computed the vertical local heat fluxes using their numerical data for a fixed $\text{Pr} = 0.7$ and Ra spanning from 10^6 to 10^8 . They observed the asymmetry in the vertical heat flux to increase with Ra . Similar observations were reported in the numerical analysis of RBC by Kaczorowski and Xia (2013) and Pharasi et al. (2016). The variations of the heat flux with Pr are yet to be studied.

1.9 Problems addressed in the thesis

In this thesis, we attempt to fill some of the gaps in RBC described in Sections. 1.5 to 1.8.

As discussed earlier, there have been long-standing debates on whether RBC follows Kolmogorov phenomenology, as in homogeneous isotropic turbulence, or Bolgiano-Obukhov phenomenology, as in stably-stratified turbulence. Although the kinetic energy spectrum and flux were shown to exhibit Kolmogorov-like scaling by [Kumar et al. \(2014\)](#) and [Verma et al. \(2017\)](#), the behavior of the velocity structure functions remains inconclusive. In this thesis, we show that the velocity structure functions of RBC scale similar to those of homogeneous isotropic turbulence and hence reinforce the arguments of [Kumar et al. \(2014\)](#) and [Verma et al. \(2017\)](#). We use the data from high-resolution direct numerical simulation of RBC for large Rayleigh numbers so as to obtain a wide inertial range and hence a conclusive scaling of the structure functions. We also analyze, for the first time, the velocity structure functions of RBC for $Pr \gg 1$.

As mentioned at the end of Sec. 1.5.3, previous studies focussed on the small-scale statistics of turbulence in different regimes of Ra and Pr . However, a comparative study for the whole range of Pr was missing. In this thesis, we address the Pr dependence of the spectra and fluxes of kinetic energy and entropy along with the velocity structure functions. We also study, for the first time, the Pr dependence of the statistics of the local heat flux of RBC.

In RBC, the walls and their associated boundary layers modify the statistics of viscous and thermal dissipation rates compared to homogeneous isotropic turbulence ([Pandey et al., 2016a](#); [Pandey and Verma, 2016](#)); hence, it is important to analyze and quantify their scaling and relative strengths in the boundary layers and in the bulk of RBC. However, a comprehensive discussion on these topics has been missing (see Sec. 1.6). In this thesis, we carry out a detailed numerical analysis of the relative strengths of the dissipation rates in the entire volume of the bulk and boundary layers of RBC. We compute the boundary layer thicknesses for every set of governing parameters and hence determine the bulk and boundary layer subvolumes in which we compute the dissipation rates. This way, we study the variations of the boundary layer thicknesses with Ra and Pr .

An outcome of these studies has been the enhancement of the well-known GL model that provides more accurate predictions of Nu and Re for a given set of governing parameters.

1.10 Outline of the thesis

The outline of the rest of the thesis is as follows.

- In Chapter 2, we discuss the details of our numerical simulations of RBC using finite-difference solver SARAS (Anderson, 1995; Verma et al., 2020; Samuel et al., 2020) and finite-volume solver OpenFOAM (Jasak et al., 2007). We explain the computations of the structure functions using fastSF (Sadhukhan et al., 2021) and the spectral quantities using the pseudo-spectral code TARANG (Verma et al., 2013; Chatterjee et al., 2018). Finally, we detail the procedure for the computations of global quantities, boundary layer thicknesses, and the dissipation rates using numerical data.
- In Chapter 3, we compute the velocity structure functions of RBC for $Pr = 1$ and show that they scale similar to those of homogeneous isotropic turbulence. The scaling exponents are found to be in agreement with the predictions of She and Leveque [Eq. (1.44)], a model for homogeneous isotropic turbulence. Our results are consistent with the previous studies that reported Kolmogorov-like kinetic energy spectrum in RBC (Kumar et al., 2014; Verma et al., 2017). We also show that in RBC, the kinetic energy flux in the intermediate scales is less than the total viscous dissipation rate, unlike in homogeneous isotropic turbulence, due to multiscale kinetic energy injection.
- In Chapter 4, we analyze the Prandtl number dependence of spectra and fluxes of kinetic energy and entropy of turbulent thermal convection using simulation data. We show that the magnitudes of the kinetic energy fluxes and spectra and those of structure functions increase with the decrease of Pr , thus indicating an increase of nonlinearity for flows with small Prandtl numbers. Consistent with these observations, the kinetic energy injection rates and the dissipation rates too increase with the decrease of Pr . On the other hand, the amplitudes of the entropy spectrum do not vary significantly with Pr . For small Prandtl numbers,

most of the kinetic energy is injected at large scales, whereas for large Prandtl numbers, the energy injection is somewhat homogeneously distributed over different scales. Further, the tail of the probability distributions of the local heat flux grows with the increase of Pr, indicating increased fluctuations in the local heat flux with Pr.

- In Chapter 5, we study the scaling relations of viscous dissipation rates in the bulk and boundary layers of RBC for $\text{Pr} = 1$ and 6.8. We show that contrary to the general belief, viscous dissipation rate dominates in the bulk rather than in the boundary layers. The thickness of the viscous boundary layers, δ_u , is observed to deviate marginally from the widely-held assumption of $\delta_u \sim \text{Re}^{-1/2}$. The bulk dissipation is similar to homogeneous isotropic turbulence where it follows a log-normal distribution; however, it differs from U^3/d by an additional factor of $\text{Ra}^{-0.18}$, where d is the distance between the thermal plates. The dissipation rates in the boundary layers are rarer but more intense with stretched exponential distribution.
- In Chapter 6, we obtain the scaling relations of thermal dissipation rates in the bulk and boundary layers of RBC for $\text{Pr} = 1$ and 100. We show that unlike viscous dissipation rate, the thermal dissipation rate dominates in the boundary layers by a factor of approximately 3. The thermal dissipation rate in the bulk differs from $U\Delta^2/d$ (as in homogeneous isotropic turbulence) by an additional factor of $\text{Ra}^{-\alpha}$, where Δ is the temperature difference between the thermal plates, and $\alpha = 0.22$ for $\text{Pr} = 1$ and 0.25 for $\text{Pr} = 100$. Both bulk and boundary layer dissipation rates follow stretched exponential distributions.
- In Chapter 7, we extend [Grossmann and Lohse's](#) (GL) model for the predictions of Reynolds and Nusselt numbers in RBC. Towards this objective, we use functional forms for the prefactors of the dissipation rates in the bulk and the boundary layers. The functional forms arise due to i) additional Ra dependence on the scaling of the bulk dissipation rates compared to homogeneous isotropic turbulence (as discussed in Chapters 5 and 6), and ii) a deviation of viscous boundary layer profile from Prandtl-Blasius theory. We perform 60 numerical runs on a three-dimensional unit box for a range of Rayleigh numbers (Ra) and Prandtl numbers (Pr) and determine the aforementioned functional forms using machine learning. The revised predictions are in better agreement with the past numerical and experimental results than those of the GL model, especially for extreme

Prandtl numbers.

- In Chapter 8, we conclude the present study. We also discuss the scope of future work arising from our study.

Chapter 2

Numerical methods

In this chapter, we detail the numerical methods employed in our present work. We perform our simulations of Rayleigh-Bénard convection (RBC) using a finite-volume code OpenFOAM (Jasak et al., 2007) and a finite-difference code SARAS (Verma et al., 2020; Samuel et al., 2020). We also employ a pseudo-spectral code TARANG (Verma et al., 2013; Chatterjee et al., 2018) to compute the spectra and fluxes of kinetic energy and entropy, and a parallel code fastSF (Sadhukhan et al., 2021) to compute the structure functions. We use Python scripts to compute the global quantities, boundary layer thicknesses, and dissipation rates, primarily using Python's "NumPy" (van der Walt et al., 2011) and "SciPy" (Virtanen et al., 2020) libraries.

This chapter is organized as follows. We provide the details of the simulations of RBC using finite-difference and finite-volume methods in Sec. 2.1. In Sec. 2.2, we present the methods employed in the computation of the structure functions, spectral quantities, large-scale quantities, boundary layer thicknesses, and the dissipation rates using the data from our numerical simulations.

2.1 Simulations of RBC

In this section, we discuss the details of the numerical methods used in our simulations of RBC. In the initial years of my doctoral work, we used the open-source finite volume solver OpenFOAM (Jasak et al., 2007) for our simulations. Later, an in-house finite dif-

ference code, SARAS, was developed by [Samuel et al. \(2020\)](#) and used for subsequent simulations.

2.1.1 Finite volume method: OpenFOAM

The *finite volume method* (FVM) is an important technique employed in computational fluid dynamics (CFD). In this method, the spatial domain is discretized into a finite number of control volumes. The governing partial differential equations of fluid flow are expressed in their integral forms. Using divergence theorem, the volume integrals containing the divergence terms are converted to surface integrals that are computed as fluxes at each control volume's surfaces. An important advantage of this method is that the conservation quantities at the discretized level is enforced because the flux leaving a given control volume equals that entering the adjacent control volume ([Ferziger and Peric, 2001](#)). Another advantage of FVM is that it can be easily employed for complex geometries ([Moukalled et al., 2016](#)). In this subsection, we detail our simulations of RBC using OpenFOAM, an open-source finite volume solver ([Jasak et al., 2007](#)).

We numerically solve the non-dimensional governing equations of RBC [Eqs. (1.11) to (1.13)] in a three-dimensional unit box. We employ Gaussian finite-volume integration for the computations of the derivative terms (pressure gradient, nonlinear, and laplacian terms) of the governing equations. Gaussian integration involves interpolating the field values from cell-center to nodes and then to cell-faces, following which the values are summed over all the faces ([Moukalled et al., 2016](#)). Linear interpolation is employed for our cases. For time-stepping, we employ the second-order Crank-Nicolson scheme ([Crank and Nicolson, 1947](#)). The solver uses PISO (Pressure-Implicit with Splitting of Operators) algorithm ([Issa, 1985](#)) for solving the discretized governing equations of fluid flow.

We varied the Rayleigh number (Ra) from 10^6 to 10^8 and the Prandtl number (Pr) from 1 to 100. We employ no-slip boundary conditions on all the walls by setting $u_x = u_y = u_z = 0$ on each wall. We impose isothermal boundary conditions on the horizontal walls by setting the temperature (in its non-dimensional form) on the bottom wall to 1 and on the top wall to 0. On each sidewall, we set $\nabla T \cdot \hat{n} = 0$ (adiabatic boundary conditions), where \hat{n} is the unit vector normal to the wall. All our runs involve a non-uniform mesh of 256^3 grid resolution. The mesh width is minimum near the boundaries and maximum in the cell center, with an expansion ratio of 2.

Hence, the mesh width is 0.0027 near the boundaries and $2 \times 0.0027 = 0.0054$ in the cell center. With this grid configuration, we ensure the required number of points in the boundary layers to satisfy the resolution criterion of [Grötzbach \(1983\)](#). We choose a constant value for the time step (Δt) for each run; $\Delta t = 0.001$ free-fall time unit for all the runs with the exception of $Ra = 2 \times 10^6$, $Pr = 100$ for which $\Delta t = 0.0005$ free-fall time unit. The solution files are saved after the simulation progresses every one free-fall time. More parameter-specific details and the validations of our simulations are described in Chapters 5 and 6.

There were a few problems in using OpenFOAM. Being a finite-volume solver, it is more computationally intensive than solvers employing the finite difference method. Simulations of RBC for $Ra > 10^8$ or $Pr < 1$ required a grid resolution of more than 256^3 . However, employing OpenFOAM for such a high-resolution simulation was turning out to be very expensive. It is to be noted that our analysis is restricted to RBC in a cubical cell that can easily be simulated using a finite-difference solver with comparable accuracy but with less computational resources ([Ferziger and Peric, 2001](#)). Hence, once the finite difference code SARAS was developed in our group by [Samuel et al. \(2020\)](#) during the later years of my doctoral work, all the subsequent high-resolution simulations were performed using SARAS. We will describe SARAS in detail in the next subsection.

2.1.2 Finite difference method: SARAS

The *finite difference method* (FDM) is another popular technique employed in CFD. It is simple to incorporate in regular geometries (cuboid, cylinder, sphere, etc.), is computationally efficient, and provides accurate solutions for these geometries ([Anderson, 1995](#); [Ferziger and Peric, 2001](#)). In FDM, the spatial domain is discretized into a finite number of points. The values of the velocity, pressure, and temperature fields are considered only at these discrete points ([Anderson, 1995](#); [Ferziger and Peric, 2001](#)). The governing partial differential equations of the fluid flow are converted to algebraic equations by approximating derivatives with finite differences. The solution at each point is obtained by numerically solving the above algebraic equations. In the following, we describe the method of simulation of RBC using the finite difference code SARAS that was developed by [Samuel et al. \(2020\)](#) and reviewed by [Verma et al. \(2020\)](#).

SARAS uses a staggered grid configuration ([Ferziger and Peric, 2001](#)) for storing

the velocity, pressure, and temperature fields. In this arrangement, the velocity fields are stored on the face-centers, whereas the scalar fields (pressure and temperature) are stored in the cell-centers. Equations (1.11) to (1.13) are spatially discretized using the second-order central difference scheme. According to this scheme, the partial derivative of a field, $f(x, y, z)$, with respect to, say, x , is given by

$$\frac{\partial f(x, y, z)}{\partial x} = \frac{f(x + \Delta x, y, z) - f(x - \Delta x, y, z)}{2\Delta x}, \quad (2.1)$$

where Δx is the mesh-width in the x direction. The function f can be velocity or temperature field.

Using SARAS, we solve the non-dimensional equations [Eqs. (1.11) to (1.13)] of RBC. The computation procedure is as follows. Let the velocity, temperature, and pressure field at time $t = t^{(n)}$ be $\mathbf{u}^{(n)}$, $T^{(n)}$, and $p^{(n)}$, respectively. The corresponding fields at the next time-step, $t^{(n+1)}$, namely $\mathbf{u}^{(n+1)}$, $T^{(n+1)}$ and $p^{(n+1)}$, are calculated as described below (also, refer to [Patankar and Spalding, 1972](#); [Ferziger and Peric, 2001](#), for details).

An intermediate velocity field using the known values $\mathbf{u}^{(n)}$, $T^{(n)}$, and $p^{(n)}$ is calculated as

$$\mathbf{u}^\# = \mathbf{u}^{(n)} + \Delta t \left[\sqrt{\frac{\text{Pr}}{\text{Ra}}} \nabla^2 \left(\frac{\mathbf{u}^{(n)} + \mathbf{u}^\#}{2} \right) + T^{(n)} \hat{\mathbf{z}} - \mathbf{u}^{(n)} \cdot \nabla \mathbf{u}^{(n)} - \nabla p^{(n)} \right], \quad (2.2)$$

where Δt is the timestep. In the above equation, the viscous term $\nabla^2 \mathbf{u}$ is handled semi-implicitly with equal contribution from $\mathbf{u}^{(n)}$ and $\mathbf{u}^\#$. Equation (2.2) can be rearranged as

$$\mathbf{u}^\# - \Delta t \sqrt{\frac{\text{Pr}}{\text{Ra}}} \frac{\nabla^2 \mathbf{u}^\#}{2} = \mathbf{u}^{(n)} + \Delta t \left(\sqrt{\frac{\text{Pr}}{\text{Ra}}} \frac{\nabla^2 \mathbf{u}^{(n)}}{2} + T^{(n)} \hat{\mathbf{z}} - \mathbf{u}^{(n)} \cdot \nabla \mathbf{u}^{(n)} - \nabla p^{(n)} \right). \quad (2.3)$$

The above equation is solved iteratively using the Gauss-Jacobi method ([Kreyszig, 2011](#)).

The intermediate field $\mathbf{u}^\#$ may not satisfy the continuity equation; hence it requires an appropriate correction. This correction is derived by the assuming the fol-

lowing expression for $\mathbf{u}^{(n+1)}$ (Patankar, 1980; Anderson, 1995):

$$\mathbf{u}^{(n+1)} = \mathbf{u}^{(n)} + \Delta t \left[\sqrt{\frac{\text{Pr}}{\text{Ra}}} \nabla^2 \left(\frac{\mathbf{u}^{(n)} + \mathbf{u}^\#}{2} \right) + T^{(n)} \hat{z} - \mathbf{u}^{(n)} \cdot \nabla \mathbf{u}^{(n)} - \nabla p^{(n+1)} \right]. \quad (2.4)$$

Subtracting Eq. (2.2) from Eq. (2.4), we get

$$\mathbf{u}^{(n+1)} - \mathbf{u}^\# = -\Delta t (\nabla p^\#), \quad (2.5)$$

where $p^\# = p^{(n+1)} - p^{(n)}$ is a pressure correction term. Taking the divergence Eq. (2.5) and noting that $\nabla \cdot \mathbf{u}^{(n+1)} = 0$ due to the incompressibility condition, we get the following Poisson equation for the pressure correction term:

$$\nabla^2 p^\# = \frac{\nabla \cdot \mathbf{u}^\#}{\Delta t}. \quad (2.6)$$

SARAS uses *geometric multigrid method* (Wesseling, 1992) to solve the above pressure Poisson equation. Using the above pressure correction, the velocity and pressure fields at time $t^{(n+1)}$ are obtained as

$$p^{(n+1)} = p^{(n)} + p^\#, \quad (2.7)$$

$$\mathbf{u}^{(n+1)} = \mathbf{u}^\# - \Delta t (\nabla p^\#). \quad (2.8)$$

The temperature field is updated by handling the diffusion term, $\nabla^2 T$, similar to velocity field in Eq. (2.3) and iteratively solving the following equation using the Gauss-Jacobi method:

$$T^{(n+1)} - \Delta t \frac{1}{\sqrt{\text{RaPr}}} \frac{\nabla^2 T^{(n+1)}}{2} = T^{(n)} + \Delta t \left(\frac{1}{\sqrt{\text{RaPr}}} \frac{\nabla^2 T^{(n)}}{2} - \mathbf{u}^{(n)} \cdot \nabla T^{(n)} \right). \quad (2.9)$$

Now, we detail the simulation parameters for our present studies. The simulations are performed in a cubical box of unit dimensions. We vary the Rayleigh number from 5×10^5 to 5×10^9 and the Prandtl number from 0.02 to 100. We impose no-slip boundary conditions on all walls, adiabatic boundary conditions on sidewalls, and isothermal boundary conditions on the top and bottom walls. We vary the grid size from 257^3 to 1025^3 , depending on the parameters. The grid sizes are chosen in such a way that the viscous and thermal boundary layers contain the required number of

grid-points to satisfy the resolution criterion of [Grötzbach \(1983\)](#) and [Verzicco and Camussi \(2003\)](#). The time step Δt is determined by fixing the maximum Courant number at 0.2. The maximum Courant number is given by

$$C = \frac{u_{x,\max}\Delta x}{\Delta t} + \frac{u_{y,\max}\Delta y}{\Delta t} + \frac{u_{z,\max}\Delta z}{\Delta t}, \quad (2.10)$$

where $u_{x,\max}$, $u_{y,\max}$, and $u_{z,\max}$ are respectively the maximum values of the x , y , and z components of velocities, and Δx , Δy , and Δz are the respective mesh widths in the x , y , and z directions. Note that we use a uniform grid, hence Δx , Δy and Δz are equal.

We start a simulation on a coarse grid of 64^3 for $Ra = 4000$, and unit Prandtl number with $\mathbf{u} = 0$ and $T = 0$ as initial conditions. Upon reaching a steady-state, we successively increase the grid resolution and the intensity of turbulence (by increasing Ra or decreasing Pr) till we reach the required grid size and the governing parameters. After that, we run the simulations further for 3 to 101 free-fall time (depending on parameters) after attaining a steady-state. More parameter-specific details and the validations of our simulations are described in Chapters 4 and 7.

2.2 Post-processing of the simulation data

In this section, we present the numerical methods employed in the post-processing of our simulation data. We describe the methods used to compute the structure functions, kinetic energy and entropy spectra and fluxes, the global quantities, boundary layer thicknesses and the dissipation rates.

2.2.1 Structure functions

Structure functions are two-point statistical quantities; thus, an accurate computation of these quantities requires averaging over many points. However, incorporation of a large number of points makes the computations very expensive and challenging. Therefore, we require an efficient parallel code for accurate computation of structure functions. In this subsection, we describe the design of fastSF, a parallel C++ code developed by us to compute the structure functions for a given velocity or scalar field on Cartesian grids of a 2D or 3D box ([Sadhukhan et al., 2021](#)). This code uses Message

Passing Interface (MPI) for parallelization.

Typical computations of structure functions involve running six nested for loops: the outer three loops describing the position vector \mathbf{r} and the inner three loops describing $\mathbf{r} + \mathbf{l}$. Such an algorithm is used for computing the structure functions of RBC in Chapter 3. On the other hand, *fastSF*, which is used for computing the structure functions in Chapter 4, has a more efficient algorithm as described below. The velocity difference, $\delta\mathbf{u}(\mathbf{l})$, is computed by taking the difference between two points with the same indices in two equal-sized subdomains generated by the position vector \mathbf{l} (see Fig. 2.1 for an illustration). This feature enables vectorization and loops over l , thus requiring only three loops instead of six. In the following, we provide the algorithm for velocity structure function computation.

Pseudo-code

Data: Velocity field \mathbf{u} in domain (L_x, L_y, L_z) ; number of processors P .

Procedure:

- Divide \mathbf{l} 's among various processors. The process of data division among the processors has been described later in this section.
- For every processor:
 - for $\mathbf{l} = (l_x, l_y, l_z)$ assigned to the processor:
 - * Compute $\delta\mathbf{u}(l_x, l_y, l_z)$ by taking the difference between two points with the same indices in pink and green subdomains as shown in Fig. 2.1. This feature enables vectorized subtraction operation.
 - * $\delta u(l_x, l_y, l_z) = \delta\mathbf{u} \cdot \hat{\mathbf{l}}$ (Vectorized).
 - * for order q :
 - $S_q^u(l_x, l_y, l_z) = \text{Average of } (\delta u)^q$ (Vectorized).
 - Send the values of $S_q^u(l_x, l_y, l_z)$, q , l_x , l_y , and l_z to the root process.
- The root process stores $S_q^u(l_x, l_y, l_z)$.
- Stop

Since $S_q^u(\mathbf{l})$ is important for intermediate scales (inertial range) only, we vary \mathbf{l} up to half the domain size, that is, up to $(L_x/2, L_y/2, L_z/2)$, to save computational cost.

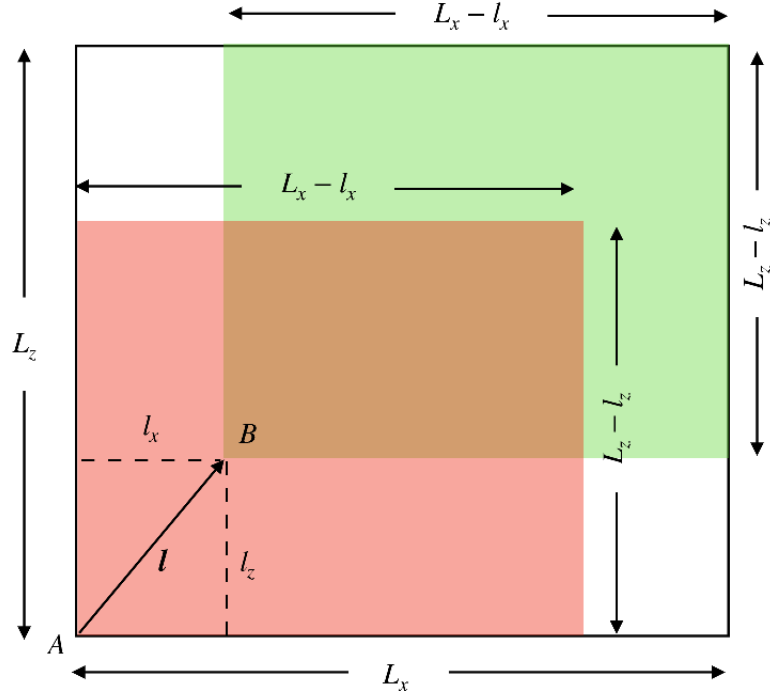


FIGURE 2.1: Schematic for computing the velocity structure functions. The velocity difference $\delta \mathbf{u}(\mathbf{l})$ is computed by taking the difference between two points with the same indices in the pink and the green subdomains. For example, $\mathbf{u}(\mathbf{l}) - \mathbf{u}(0,0) = \mathbf{u}_B - \mathbf{u}_A$, where B and A are the origins of the green and the pink subdomains. This feature enables vectorization of the computation. This figure is taken from Ref. (Sadhukhan et al., 2021).

The \mathbf{l} 's are divided among MPI processors along x and y directions. Each MPI processor computes the structure functions for the points assigned to it and has access to the entire input data. After computing the structure function for a given \mathbf{l} , each processor communicates the result to the root process, which stores the $S_q^u(\mathbf{l})$ and $S_q^{u\perp}(\mathbf{l})$ arrays.

It is clear from Fig. 2.1 that the sizes of the pink or green subdomains are $(L_x - l_x)(L_y - l_y)(L_z - l_z)$, which are function of \mathbf{l} 's. This function decreases with increasing \mathbf{l} leading to larger computational costs for small l and less cost of larger l . Hence, a straightforward division of the domain among the processors along x and y directions will lead to a load imbalance. Therefore, we assign both large and small \mathbf{l} 's to each processor to achieve equal load distribution. We illustrate the above idea using the

following example.

Consider a one-dimensional domain of size $L = 15$, for which the possible l 's are

$$l = \{0, 1, 2, 3 \dots 15\}.$$

We need to compute the structure functions for l ranging from 0 to 7. We divide the task among four processors, with two l 's assigned to each processor. The following distribution of l 's ensures equal load distribution:

$$\text{Processor 0: } l = \{0, 7\}, \quad \sum(L - l) = (15 - 0) + (15 - 7) = 23,$$

$$\text{Processor 1: } l = \{1, 6\}, \quad \sum(L - l) = (15 - 1) + (15 - 6) = 23,$$

$$\text{Processor 2: } l = \{2, 5\}, \quad \sum(L - l) = (15 - 2) + (15 - 5) = 23,$$

$$\text{Processor 3: } l = \{3, 4\}, \quad \sum(L - l) = (15 - 3) + (15 - 4) = 23.$$

Similarly, if two processors are used, then the following distribution results in load balance.

$$\text{Processor 0: } l = \{0, 7, 2, 5\},$$

$$\text{Processor 1: } l = \{1, 6, 3, 4\}.$$

This idea of load distribution has been implemented in our program and has been extended to higher dimensions. `fastSF` is scalable over many processors as a result of the above load-balancing strategy along with vectorization ([Sadhukhan et al., 2021](#)).

The scaling of the velocity structure functions is analyzed in detail in Chapters 3 and 4.

2.2.2 Energy and entropy spectra and fluxes

We employ the pseudo-spectral code TARANG ([Chatterjee et al., 2018](#); [Verma et al., 2013](#)) to compute the spectra and fluxes of kinetic energy and entropy. TARANG is an object-oriented parallel code written in C++ and used for simulating flows involving fluids, RBC, and magnetohydrodynamics. The code also has functions to carry out important diagnostics such as computation of energy and entropy spectra and fluxes, shell-to-shell energy transfer, ring energy spectra, etc. (see, for example, [Nath et al.,](#)

2016; Gupta et al., 2019; Sharma et al., 2019). However, TARANG in its present form can solve only for periodic and free-slip boundary conditions but cannot simulate no-slip conditions. Thus, we do not use TARANG for our simulations as our subsequent analysis requires the presence of viscous boundary layers that are formed only near no-slip walls.

TARANG can, however, be used as a post-processing tool to accurately compute the inertial-range spectra and fluxes of kinetic energy and entropy using the data generated from simulations involving no-slip walls. This is done by approximating the velocity field using free-slip conditions and employing Fourier (sine and cosine) expansion of the field. Note that the viscous boundary layer thickness is very small compared to the domain size, and the small-scale structures in the boundary layers do not affect the inertial-range properties (Verma, 2018, 2019b). Hence, even for flows bounded by rigid walls, the inertial-range spectra and fluxes can be computed by TARANG using Fourier expansion with reasonable accuracy.

To satisfy the free-slip boundary conditions, we expand the velocity field as follows (Verma, 2018).

$$u_x(x, y, z) = \sum_{k_x, k_y, k_z} \hat{u}_x(k_x, k_y, k_z) 8 \sin(k_x x) \cos(k_y y) \cos(k_z z), \quad (2.11)$$

$$u_y(x, y, z) = \sum_{k_x, k_y, k_z} \hat{u}_y(k_x, k_y, k_z) 8 \cos(k_x x) \sin(k_y y) \cos(k_z z), \quad (2.12)$$

$$u_z(x, y, z) = \sum_{k_x, k_y, k_z} \hat{u}_z(k_x, k_y, k_z) 8 \cos(k_x x) \cos(k_y y) \sin(k_z z), \quad (2.13)$$

where $k_x = l\pi$, $k_y = m\pi$, and $k_z = n\pi$; l , m , and n are positive integers. For the field θ , the fluctuation of temperature from conduction profile, the boundary conditions are as follows. θ is zero on the horizontal walls, and $\nabla\theta \cdot \hat{n} = 0$ on the sidewalls. To satisfy these boundary conditions, θ is expanded using sin and cos basis function as follows.

$$\theta(x, y, z) = \sum_{k_x, k_y, k_z} \hat{\theta}(k_x, k_y, k_z) 8 \cos(k_x x) \cos(k_y y) \sin(k_z z). \quad (2.14)$$

We also compute the spectral quantities using the data obtained from numerical simulations of RBC conducted earlier by Verma et al. (2017) and Chatterjee et al. (2018)*. The simulation for generating the above data was conducted using TARANG,

[*] I was not involved with this simulation as it was conducted before the start of my doctoral work.

employing free-slip boundary conditions on the horizontal walls ($u_z = 0, \partial u_x / \partial z = \partial u_y / \partial z = 0$) and periodic boundary conditions on the vertical walls. To satisfy these boundary conditions, the velocity and temperature fields are expanded using the following basis functions:

$$u_x(x, y, z) = \sum_{k_x, k_y, k_z} \hat{u}_x(k_x, k_y, k_z) 2 \exp(ik_x x + ik_y y) \cos(k_z z), \quad (2.15)$$

$$u_y(x, y, z) = \sum_{k_x, k_y, k_z} \hat{u}_y(k_x, k_y, k_z) 2 \exp(ik_x x + ik_y y) \cos(k_z z), \quad (2.16)$$

$$u_z(x, y, z) = \sum_{k_x, k_y, k_z} \hat{u}_z(k_x, k_y, k_z) 2 \exp(ik_x x + ik_y y) \sin(k_z z), \quad (2.17)$$

$$\theta(x, y, z) = \sum_{k_x, k_y, k_z} \hat{\theta}(k_x, k_y, k_z) 2 \exp(ik_x x + ik_y y) \sin(k_z z), \quad (2.18)$$

where $k_x = 2l\pi, k_y = 2m\pi$, and $k_z = n\pi$; l and m are positive or negative integers, but n is a positive integer.

Having computed the Fourier transforms of the velocity and temperature fields, the spectra and fluxes of kinetic energy and entropy are computed using Eqs. (1.28), (1.30), (1.34) and (1.36). These quantities will be studied in detail in Chapter 4.

2.2.3 Global quantities

In this subsection, we discuss the procedure for computing the global quantities: namely the Reynolds number and the Nusselt number. The Reynolds number is based on the root mean square velocity in our present work. Using our simulation data of nondimensional velocity field, we compute the nondimensional root mean square velocity using the following formula employing Simpson's 1/3 rule for integration:

$$U_{\text{rms}} = \sqrt{\int_0^1 \int_0^1 \int_0^1 (u_x^2 + u_y^2 + u_z^2) dx dy dz}. \quad (2.19)$$

Using the value of U_{rms} , we calculate the Reynolds number in its nondimensional form as

$$\text{Re} = \sqrt{\frac{\text{Ra}}{\text{Pr}}} U_{\text{rms}}. \quad (2.20)$$

To compute the Nusselt number, we first numerically evaluate the average of the

vertical heat flux ($\langle u_z T \rangle$) using the nondimensional vertical velocity and temperature fields as follows:

$$\langle u_z T \rangle = \int_0^1 \int_0^1 \int_0^1 u_z T dx dy dz. \quad (2.21)$$

We employ Simpson's 1/3 rule for the above integration. After obtaining the average vertical heat flux, the Nusselt number in its nondimensional form is computed as

$$\text{Nu} = 1 + \sqrt{\text{RaPr}} \langle u_z T \rangle. \quad (2.22)$$

2.2.4 Boundary layer thicknesses

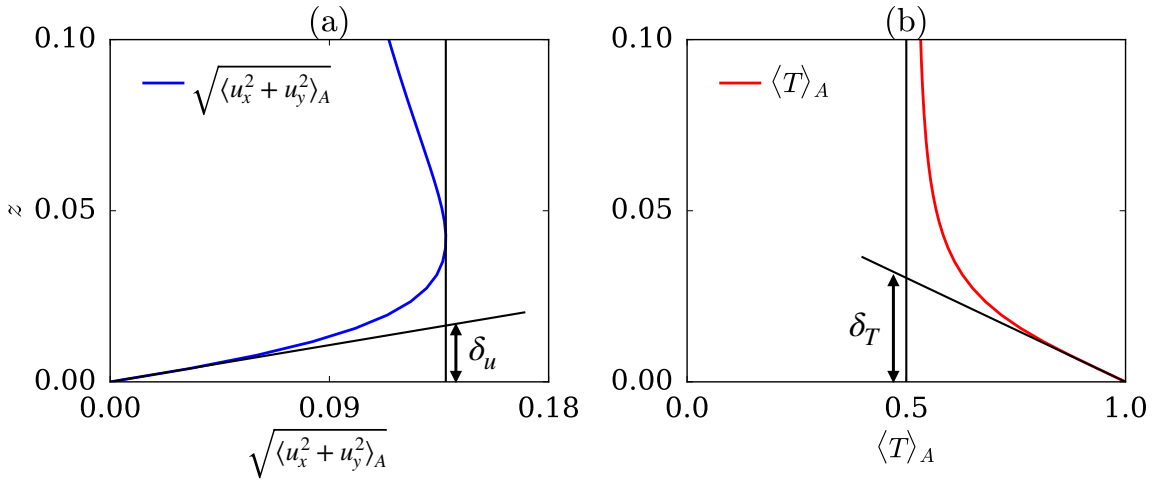


FIGURE 2.2: For $\text{Ra} = 10^7$ and $\text{Pr} = 1$ simulated using SARAS: (a) viscous boundary layer thickness near the bottom wall, and (b) thermal boundary layer thickness near the bottom wall.

In this subsection, we explain the method of computing the boundary layer thicknesses.

To compute the thickness of the viscous boundary layer formed near a wall, we first calculate the root mean square of the wall-parallel velocity over every plane parallel to the wall. For example, near the bottom wall, we compute the root mean square of the wall-parallel velocity ($\sqrt{\langle u_x^2 + u_y^2 \rangle_A}$) over every horizontal plane. The viscous boundary layer thickness, δ_u , is then computed as the depth where a linear fit of the above wall-parallel velocity profile near the wall intersects with the tangent to the same velocity profile at its local maximum. See Fig. 2.2(a) for an illustration of the computation of the viscous boundary layer thickness near the bottom wall.

For computing the thermal boundary layer thickness, we compute the temperature profile $\langle T \rangle_A$ averaged over every horizontal plane. The thermal boundary layer thickness, δ_T , is then computed as the depth where a linear fit of the temperature profile near the wall intersects with the mean temperature $T = 0.5$. See Fig. 2.2(b) for an illustration.

The above-described methods are standard procedures for computing the boundary layer thicknesses (Scheel et al., 2012; Ahlers et al., 2009b; Breuer et al., 2004; Wagner et al., 2012).

2.2.5 Dissipation rates

The local viscous and thermal dissipation rates per unit volume, denoted as $\epsilon_u(\mathbf{r})$ and $\epsilon_T(\mathbf{r})$, are calculated as follows:

$$\epsilon_u(\mathbf{r}) = \frac{1}{2} \sqrt{\frac{\text{Pr}}{\text{Ra}}} \left(\frac{\partial u_i}{\partial x_j} + \frac{\partial u_j}{\partial x_i} \right)^2 \quad (2.23)$$

$$\epsilon_T(\mathbf{r}) = \frac{1}{\sqrt{\text{RaPr}}} |\nabla T|^2, \quad (2.24)$$

where u_i and u_j are the i th and the j th components of velocity respectively. The gradients are computed using the second-order central difference method. The dissipation rates averaged over the entire volume are obtained as follows:

$$\epsilon_u = \int_0^1 \int_0^1 \int_0^1 \epsilon_u(\mathbf{r}) dx dy dz, \quad (2.25)$$

$$\epsilon_T = \int_0^1 \int_0^1 \int_0^1 \epsilon_T(\mathbf{r}) dx dy dz, \quad (2.26)$$

The above integrations are performed using Simpson's 1/3 rule. The total viscous and thermal dissipation rates, \tilde{D}_u and \tilde{D}_T respectively, are the products of the volume-averaged dissipation rates and the total volume of the RBC cell. Note that ϵ_u and ϵ_T are dissipation rates per unit volume.

In this thesis, we analyze the scaling and relative strengths of the dissipation rates in the bulk and in the boundary layers. Let $\delta_{u,TW}$ and $\delta_{u,SW}$ respectively be the thicknesses of the viscous boundary layers near the thermal plates and the sidewalls. Here, the subscripts TW and SW refer to thermal walls and sidewalls respectively. The total

viscous and thermal dissipation rates in the bulk are computed as

$$\tilde{D}_{u,\text{bulk}} = \int_{\delta_{u,\text{TW}}}^{1-\delta_{u,\text{TW}}} \int_{\delta_{u,\text{SW}}}^{1-\delta_{u,\text{SW}}} \int_{\delta_{u,\text{SW}}}^{1-\delta_{u,\text{SW}}} \epsilon_u(\mathbf{r}) dx dy dz, \quad (2.27)$$

$$\tilde{D}_{T,\text{bulk}} = \int_{\delta_T}^{1-\delta_T} \int_0^1 \int_0^1 \epsilon_T(\mathbf{r}) dx dy dz. \quad (2.28)$$

Having computed the total viscous dissipation rates in the bulk, we compute the total dissipation rates in the boundary layers by subtracting the bulk dissipation rates from the total dissipation rates:

$$\tilde{D}_{u,\text{BL}} = \tilde{D}_u - \tilde{D}_{u,\text{bulk}}, \quad (2.29)$$

$$\tilde{D}_{T,\text{BL}} = \tilde{D}_T - \tilde{D}_{T,\text{bulk}}. \quad (2.30)$$

Finally, we compute the average dissipation rates in the bulk and in the boundary layers. Towards this objective, we calculate the volumes of the bulk and the boundary layer regions:

$$V_{\text{bulk},u} = (1 - 2\delta_{u,\text{TW}})(1 - 2\delta_{u,\text{SW}})^2, \quad (2.31)$$

$$V_{\text{BL},u} = 1 - V_{\text{bulk},u}, \quad (2.32)$$

$$V_{\text{bulk},T} = 1 - 2\delta_{T,\text{TW}}, \quad (2.33)$$

$$V_{\text{BL},T} = 1 - V_{\text{bulk},T}, \quad (2.34)$$

where the subscripts u and T represent the viscous and thermal profiles respectively. Using the values of the subvolumes thus obtained, we compute the average dissipation rates in the bulk and boundary layers as

$$\epsilon_{u,\text{bulk}} = \tilde{D}_{u,\text{bulk}}/V_{\text{bulk},u}, \quad \epsilon_{u,\text{BL}} = \tilde{D}_{u,\text{BL}}/V_{\text{BL},u}, \quad (2.35)$$

$$\epsilon_{T,\text{bulk}} = \tilde{D}_{T,\text{bulk}}/V_{\text{bulk},T}, \quad \epsilon_{T,\text{BL}} = \tilde{D}_{T,\text{BL}}/V_{\text{BL},T}. \quad (2.36)$$

The following pseudocode summarizes the computation procedure of the dissipation rates in the bulk and boundary layers.

Pseudo-code

Data: Velocity field $\mathbf{u}(\mathbf{r})$, Temperature field $T(\mathbf{r})$.

Procedure

- Obtain $\delta_{u,SW}$, $\delta_{u,TW}$, and δ_T using the method described in Sec. 2.2.4.

- $\epsilon_u(\mathbf{r}) = \frac{1}{2} \sqrt{\frac{\text{Pr}}{\text{Ra}}} \left(\frac{\partial u_i}{\partial x_j} + \frac{\partial u_j}{\partial x_i} \right)^2$, $\epsilon_T(\mathbf{r}) = \frac{1}{\sqrt{\text{RaPr}}} |\nabla T|^2$.

- $\tilde{D}_u = \int_0^1 \int_0^1 \int_0^1 \epsilon_u(\mathbf{r}) dx dy dz$,

$$\tilde{D}_T = \int_0^1 \int_0^1 \int_0^1 \epsilon_T(\mathbf{r}) dx dy dz \text{ (Simpson's rule).}$$

- $\tilde{D}_{u,\text{bulk}} = \int_{\delta_{u,TW}}^{1-\delta_{u,TW}} \int_{\delta_{u,SW}}^{1-\delta_{u,SW}} \int_{\delta_{u,SW}}^{1-\delta_{u,SW}} \epsilon_u(\mathbf{r}) dx dy dz$,

$$\tilde{D}_{T,\text{bulk}} = \int_{\delta_T}^{1-\delta_T} \int_0^1 \int_0^1 \epsilon_T(\mathbf{r}) dx dy dz \text{ (Simpson's rule)}$$

- $\tilde{D}_{u,\text{BL}} = \tilde{D}_u - \tilde{D}_{u,\text{bulk}}$,

$$\tilde{D}_{T,\text{BL}} = \tilde{D}_T - \tilde{D}_{T,\text{bulk}}.$$

- $V_{\text{bulk},u} = (1 - 2\delta_{u,TW})(1 - 2\delta_{u,SW})^2$, $V_{\text{BL},u} = 1 - V_{\text{bulk},u}$

$$V_{\text{bulk},T} = 1 - 2\delta_{T,TW}, \quad V_{\text{BL},T} = 1 - V_{\text{bulk},T}.$$

- $\epsilon_{u,\text{bulk}} = \tilde{D}_{u,\text{bulk}} / V_{\text{bulk},u}$, $\epsilon_{u,\text{BL}} = \tilde{D}_{u,\text{BL}} / V_{\text{BL},u}$,

$$\epsilon_{T,\text{bulk}} = \tilde{D}_{T,\text{bulk}} / V_{\text{bulk},T}, \quad \epsilon_{T,\text{BL}} = \tilde{D}_{T,\text{BL}} / V_{\text{BL},T}.$$

- Stop.

The scaling of the dissipation rates in the bulk and boundary layers will be discussed in detail in Chapters 5, 6, and 7.

Chapter 3

Velocity structure functions of turbulent RBC

3.1 Introduction

An important topic of research in Rayleigh-Bénard convection (RBC) is the behavior of the structure functions and the kinetic energy and entropy spectra in the inertial range. As discussed in the introductory chapter (Sec. 1.5.3), there has been a long-standing debate on whether RBC follows Kolmogorov-like phenomenology, as in homogeneous isotropic turbulence, or Bolgiano-Obukhov phenomenology, as in stably-stratified turbulence. Recently, [Kumar et al. \(2014\)](#) and [Verma et al. \(2017\)](#) used phenomenological arguments and numerical simulations to show that the kinetic energy spectrum of RBC is Kolmogorov-like ($k^{-5/3}$). However, the behavior of the velocity structure functions remains inconclusive as researchers reported conflicting results (see Sec. 1.5.3.C for a detailed discussion). In this chapter, we compute the velocity structure functions of RBC using data from high-resolution direct numerical simulations for large Rayleigh numbers. We obtain a wide inertial range and hence conclusively show that the velocity structure functions of RBC scale similar to those of homogeneous isotropic turbulence, consistent with the results of [Kumar et al. \(2014\)](#) and [Verma et al. \(2017\)](#) for the kinetic energy spectrum.

The results presented in this chapter have been published in *Physics of Fluids* ([Bhat-](#)

tacharya et al., 2019a). A summary of our results is as follows.

3.2 A summary of our results

We analyze the velocity structure functions of RBC using two sets of numerical data. The first dataset was generated by Verma et al. (2017) using the pseudo-spectral code TARANG on a 4096^3 grid for $Ra = 1.1 \times 10^{11}$ and $Pr = 1$. The convection cell of the first dataset consists of free-slip horizontal walls and periodic sidewalls. The second dataset was generated by Kumar and Verma (2018) using OpenFOAM on a 256^3 grid for $Ra = 1.1 \times 10^8$ and $Pr = 1$. All the walls of the convection cell of the second dataset have no-slip boundary conditions imposed on them.

We compute the velocity structure functions $S_q^u(l)$ for $q = 2$ to 10 and obtain their scaling exponents ζ_q for every order. ζ_q 's are called intermittency exponents. We show that the third-order structure functions, computed using both sets of data, scale according to Kolmogorov's theory [$S_3^u(l) \sim -l$] as in homogeneous isotropic turbulence. Our results are consistent with Kolmogorov's energy spectrum observed in turbulent convection. The intermittency exponents of the structure functions of RBC match well with She and Leveque (1994)'s predictions for homogeneous isotropic turbulence. We also demonstrate that the structure functions show extended self-similarity.

We further compute the probability distribution function (PDF) of velocity increments [$\delta u = \{\mathbf{u}(\mathbf{r} + \mathbf{l}) - \mathbf{u}(\mathbf{r})\} \cdot \mathbf{l}/|\mathbf{l}|$] for different values of the separation distance l . We show that for small l , the PDFs are non-Gaussian with wide tails. With increasing l , the PDFs become closer to Gaussian. The tails of the PDFs follow a stretched exponential, with the stretching exponent increasing with l , as is observed in homogeneous isotropic turbulence (Donzis et al., 2008).

We compute the inertial-range kinetic energy flux, Π_u , using the third-order structure functions and show that $\Pi_u \neq \epsilon_u$; instead, it is two to three times less than ϵ_u for our cases. This is unlike in homogeneous isotropic turbulence, where the flux equals the dissipation rate. Using phenomenological arguments and our simulation data, we have shown that this difference arises due to non-zero, albeit weak, buoyancy present in the inertial range. In the next chapter, we show that this factor increases with the increase of Prandtl number.

3.3 Published manuscript

The details of our numerical simulations and the results are presented in the attached published manuscript ([Bhattacharya et al., 2019a](#)).

Similarities between the structure functions of thermal convection and hydrodynamic turbulence

Cite as: Phys. Fluids 31, 11 51 07 (2019); doi: 10.1063/1.5119905

Submitted: 14 July 2019 • Accepted: 27 October 2019 •

Published Online: 13 November 2019



Shashwat Bhattacharya,^{1,a)} Shubhadeep Sadhukhan,² Anirban Guha,³ and Mahendra K. Verma²

AFFILIATIONS

¹Department of Mechanical Engineering, Indian Institute of Technology Kanpur, Kanpur 208016, India

²Department of Physics, Indian Institute of Technology Kanpur, Kanpur 208016, India

³School of Science and Engineering, University of Dundee, Dundee DD1 4HN, Scotland, United Kingdom

^{a)}Electronic mail: shabhattach@iitk.ac.in

ABSTRACT

In this paper, we analyze the scaling of velocity structure functions of turbulent thermal convection. Using high-resolution numerical simulations, we show that the structure functions scale similar to those of hydrodynamic turbulence, with the scaling exponents in agreement with the predictions of She and Leveque [“Universal scaling laws in fully developed turbulence,” Phys. Rev. Lett. 72, 336–339 (1994)]. The probability distribution functions of velocity increments are non-Gaussian with wide tails in the dissipative scales and become close to Gaussian in the inertial range. The tails of the probability distribution follow a stretched exponential. We also show that in thermal convection, the energy flux in the inertial range is less than the viscous dissipation rate. This is unlike in hydrodynamic turbulence where the energy flux and the dissipation rate are equal.

Published under license by AIP Publishing. <https://doi.org/10.1063/1.5119905>

I. INTRODUCTION

Turbulence remains largely an unsolved problem for scientists and engineers even today. The energetics of three-dimensional homogeneous and isotropic turbulence is, however, well understood and was explained by Kolmogorov.^{1,2} Here, the energy supplied at large scales cascades down to intermediate scales and then to dissipative scales. The rate of energy supply equals the energy flux, Π_u , and the viscous dissipation rate ϵ_u . Kolmogorov showed that such flows exhibit the following property:^{1–3}

$$\left\langle \left[\{ \mathbf{u}(\mathbf{r} + \mathbf{l}) - \mathbf{u}(\mathbf{r}) \} \cdot \hat{\mathbf{l}} \right]^3 \right\rangle = -\frac{4}{5} \Pi_u l, \quad (1)$$

$$\Pi_u = \epsilon_u,$$

for $\eta \ll l \ll L$, where L is the length scale at which energy is supplied and is of the order of the domain size, and η is the dissipative scale, called Kolmogorov length scale. In Eq. (1), $\langle \cdot \rangle$ represents the ensemble average, and $\mathbf{u}(\mathbf{r})$ and $\mathbf{u}(\mathbf{r} + \mathbf{l})$ are the velocity fields at positions \mathbf{r} and $\mathbf{r} + \mathbf{l}$, respectively. The left-hand side of Eq. (1), denoted as $S_3^u(l)$, is the third-order velocity structure

function. For any order q , one expects that, using dimensional analysis, $S_q^u(l) = \langle [\{ \mathbf{u}(\mathbf{r} + \mathbf{l}) - \mathbf{u}(\mathbf{r}) \} \cdot \hat{\mathbf{l}}]^q \rangle \sim l^{q/3}$. Using the theory of Obukhov⁴ and Corrsin⁵ on turbulence with passive scalar θ , dimensional analysis yields $S_q^\theta(l) \sim l^{q/3}$, where $S_q^\theta(l) = \langle \{ \theta(\mathbf{r} + \mathbf{l}) - \theta(\mathbf{r}) \}^q \rangle$ is the structure function for the passive scalar. The aforementioned relations for S_q^u and S_q^θ are known as Kolmogorov-Obukhov (KO) scaling in the literature. In reality, however, the exponents deviate from $q/3$ (other than for 3) due to intermittency effects. The velocity structure functions scale as $S_q^u(l) \sim l^{\zeta_q}$, where the exponents ζ_q fit well with the model of She and Leveque.⁶

The scaling of structure functions of turbulent convection, however, remains an unsolved problem and hence is the theme of this paper. We focus on Rayleigh-Bénard Convection (RBC) that deals with a fluid enclosed between two horizontal plates, with the bottom plate kept at a higher temperature than the top plate. In thermal convection, complications arise due to anisotropy introduced by gravity and also because the temperature T is an active scalar.

For stably stratified turbulence, Bolgiano⁷ and Obukhov⁸ predicted the kinetic energy spectrum $E_u(k)$ and the thermal energy

spectrum $E_T(k)$ to scale as $k^{-11/5}$ and $k^{-7/5}$, respectively, where $k \sim 1/l$ is the wavenumber. An extension of Bolgiano-Obukov (BO) theory to structure functions gives $S_q^u(l) \sim l^{3q/5}$ and $S_q^T(l) \sim l^{q/5}$, where S_q^T is the temperature structure function. BO scaling occurs above the Bolgiano length scale l_B , where the buoyancy forces are dominant. Evidences of BO scaling have been observed in recent studies of stably stratified^{9,10} and rotating stratified turbulence.¹¹ Using theoretical arguments, Procaccia and Zeitak,¹² L'vov,¹³ L'vov and Falkovich,¹⁴ and Rubinstein¹⁵ proposed the applicability of BO scaling to RBC as well. Researchers have attempted to confirm the above theory with the help of experiments and numerical simulations as well as using theoretical arguments.

Benzi *et al.*^{16,17} simulated both 2D and 3D RBC using the lattice Boltzmann method and computed velocity and temperature structure functions up to the sixth order. They could not observe any discernible scaling for the structure functions due to short inertial range. They found them, however, to be self-similar for a wide range of l , a phenomenon known as extended self-similarity (ESS).^{18,19} Furthermore, they claimed BO scaling from the relationship between the velocity and the temperature structure functions. Ching²⁰ computed temperature and velocity structure functions of thermal convection using the experimental data of Heslot, Castaing, and Libchaber²¹ and Sano, Wu, and Libchaber²² as well as the numerical data of Benzi *et al.*²³ Although Ching²⁰ observed two distinct scaling regimes separated by the Bolgiano scale, the scaling exponents deviated from BO theory.

Many researchers obtained KO scaling in the bulk and attributed it to the large value of local l_B , which is of the same order as the box size. Since l_B is small near the walls, it is argued that the structure functions in those regions follow BO scaling. Using the third-order structure functions calculated using their lattice Boltzmann simulation data, Calzavarini, Toschi, and Tripicciono²⁴ claimed BO scaling near the walls and KO scaling at the cell center. High-resolution multipoint measurements of velocity and temperature fields in water were conducted by Sun, Zhou, and Xia.²⁵ Their exponents of velocity structure functions computed at the cell center fit well with the She-Leveque model, with the lower orders following Kolmogorov scaling. Using the refined similarity hypothesis, Ching *et al.*²⁶ derived power-law relations for conditional velocity and temperature structure functions computed at the given values of the locally averaged thermal dissipation rate. Ching *et al.*²⁶ further computed the conditional temperature structure functions up to the fourth order using the experimental data of He and Tong.²⁷ Based on the observed power-law scaling, they concluded BO scaling near walls and KO scaling at the cell center.

Using the experimental data of Castaing *et al.*²⁸ and Shang *et al.*,²⁹ Ching³⁰ computed the structure functions of plume velocity and found them to scale similar to the temperature structure functions. This is unlike the case of velocity structure functions in BO scaling, where they scale differently from the temperature structure functions. Kunnen *et al.*³¹ conducted direct numerical simulations (DNS) of RBC in a grid resolution of $129 \times 257 \times 257$. The velocity structure functions computed by them follow BO scaling for Rayleigh number $Ra = 10^8$ and Kolmogorov scaling for higher Ra . Ching and Cheng³² calculated temperature structure functions using the shell model of homogeneous RBC and found them to deviate significantly from BO scaling for $q > 4$. Kaczorowski and Xia³³ conducted direct numerical simulations (DNS) of RBC in grids

ranging from 64^3 to 770^3 and found that the velocity structure functions computed at the cell center approach Kolmogorov scaling for lower orders.

From the conflicting nature of past results, it is clear that the behavior of the structure functions of turbulent convection has not yet been clearly established. Lohse and Xia³⁴ reviewed the experimental, numerical, and theoretical results of past works critically and raised doubts on the applicability of BO scaling in RBC. Recently, using phenomenological arguments and numerical simulations, Kumar, Chatterjee, and Verma⁹ and Verma, Kumar, and Pandey¹⁰ showed the Kolmogorov energy spectrum in RBC. Using energetics arguments, they derived that the energy cascade rate in turbulent convection is constant, leading to Kolmogorov scaling. Their predictions are being accepted and acknowledged by several groups as is evident from recent literature.^{35–41} However, some researchers still believe that BO scaling is applicable to RBC.^{11,42–44} In this paper, using numerical simulations, we reinforce the results of Kumar, Chatterjee, and Verma⁹ and Verma, Kumar, and Pandey¹⁰ by showing that the velocity structure functions of thermal convection scale similarly as those of 3D hydrodynamic turbulence. We further show that although the energy flux in turbulent convection is constant similar to hydrodynamic turbulence, it differs from the viscous dissipation rate. We will discuss the scaling of temperature structure functions in a future work.

The outline of this paper is as follows: In Sec. II, we describe the governing equations of RBC. In Sec. III, we discuss the phenomenology of turbulent convection and derive the scaling of third-order structure functions. In Sec. IV, we briefly discuss the simulation details and the procedure employed to calculate the velocity structure functions. In Sec. V, we present the scaling of the structure functions and discuss the nature of the probability distribution functions (PDFs) of velocity increments. Furthermore, we compare the energy flux and viscous dissipation rate in RBC and show that the flux is less than the dissipation rate. Finally, we conclude in Sec. VI.

II. GOVERNING EQUATIONS

In RBC, under the Boussinesq approximation,^{45,46} we assume the kinematic viscosity ν , thermal diffusivity κ , and thermal expansion coefficient α to be constants. Furthermore, the density of the fluid is taken to be constant, except for the buoyancy term in the momentum equation. The temperature field T can be split as

$$T(x, y, z) = T_c(z) + \theta(x, y, z), \quad (2)$$

where $T_c(z)$ is the conduction temperature profile and $\theta(x, y, z)$ is the deviation of temperature from the conduction state. Furthermore, the temperature fluctuation θ is related to the density fluctuation ρ as^{45,47}

$$\rho = -\rho_0 \alpha \theta,$$

where ρ_0 is the mean fluid density. The governing equations of RBC are as follows:

$$\frac{\partial \mathbf{u}}{\partial t} + (\mathbf{u} \cdot \nabla) \mathbf{u} = -\frac{\nabla \sigma}{\rho_0} + \alpha g \theta \hat{z} + \nu \nabla^2 \mathbf{u}, \quad (3)$$

$$\frac{\partial \theta}{\partial t} + (\mathbf{u} \cdot \nabla) \theta = \frac{\Delta}{d} u_z + \kappa \nabla^2 \theta, \quad (4)$$

$$\nabla \cdot \mathbf{u} = 0, \quad (5)$$

where \mathbf{u} and σ are the velocity and the pressure fields, respectively, and Δ and d are the temperature difference and distance, respectively, between the top and the bottom plates.

Using d as the length scale, $\sqrt{\alpha g \Delta d}$ as the velocity scale, and Δ as the temperature scale, we nondimensionalize Eqs. (3)–(5), which yields

$$\frac{\partial \mathbf{u}}{\partial t} + \mathbf{u} \cdot \nabla \mathbf{u} = -\nabla \sigma + \theta \hat{z} + \sqrt{\frac{\text{Pr}}{\text{Ra}}} \nabla^2 \mathbf{u}, \quad (6)$$

$$\frac{\partial \theta}{\partial t} + \mathbf{u} \cdot \nabla \theta = u_z + \frac{1}{\sqrt{\text{Ra Pr}}} \nabla^2 \theta, \quad (7)$$

$$\nabla \cdot \mathbf{u} = 0, \quad (8)$$

where $\text{Ra} = \alpha g \Delta d^3 / (\nu \kappa)$ is the Rayleigh number and $\text{Pr} = \nu / \kappa$ is the Prandtl number. The Rayleigh and Prandtl numbers are the main governing parameters of RBC.

In Sec. III, we construct a phenomenology for the structure functions of turbulent convection.

III. PHENOMENOLOGY FOR TURBULENT CONVECTION BASED ON HYDRODYNAMIC TURBULENCE

A. Energy fluxes and spectra in hydrodynamic turbulence and thermal convection

For 3D hydrodynamic turbulence, the energy cascade rate Π_u in turbulent flows is constant in the inertial range ($\eta \ll l \ll L$). Dimensional analysis gives the following relation for the energy spectrum $E_u(k)$:

$$E_u(k) = K_{\text{KO}} (\Pi_u)^{2/3} k^{-5/3}, \quad (9)$$

where K_{KO} is the Kolmogorov constant. The aforementioned $k^{-5/3}$ spectrum is known as Kolmogorov's spectrum. In this section, we briefly describe the phenomenological arguments of Kumar, Chatterjee, and Verma,⁹ Verma, Kumar, and Pandey,¹⁰ and Verma⁴⁷ according to which the energy spectrum in turbulent convection follows Kolmogorov scaling with constant energy flux, contrary to the arguments of L'vov¹³ and L'vov and Falkovich,¹⁴ who proposed Bolgiano-Obukhov scaling with variable flux.

In all turbulent flows, the following equation can be derived using Eq. (3) (see Refs. 3, 47, and 48):

$$\frac{\partial}{\partial t} E_u(k, t) = -\frac{\partial}{\partial k} \Pi_u(k, t) + \hat{\mathcal{F}}(k, t) - \hat{D}_u(k, t), \quad (10)$$

where $\hat{\mathcal{F}}(k, t)$ is the energy feed due to forcing and $\hat{D}_u(k)$ is the dissipation rate of kinetic energy. For a steady state, we have $\frac{\partial}{\partial t} E_u(k, t) \approx 0$ that modifies Eq. (10) to

$$\frac{d}{dk} \Pi_u(k) = \hat{\mathcal{F}}(k) - \hat{D}_u(k). \quad (11)$$

Now, we will separately consider hydrodynamic turbulence and RBC and show that the flux is constant for both the cases. However, there is a difference between the two fluxes, as shown below.

1. Hydrodynamic turbulence

The forcing in hydrodynamic turbulence is supplied at small wavenumbers. In the inertial range, $\hat{\mathcal{F}}(k) = 0$ and $\hat{D}_u(k)$ is negligible. This results in the following^{1-3,48} equation:

$$\frac{d}{dk} \Pi_u(k) = 0, \quad \Rightarrow \Pi_u(k) = \text{constant}. \quad (12)$$

Note that in hydrodynamic turbulence, the forcing injection $\mathcal{F}(k)$ is modeled numerically in many ways (refer to Ref. 49 for details).

Let us consider a small wavenumber k_0 that lies in the inertial range and is slightly larger than the forcing wavenumber. Integration of Eq. (11) from 0 to k_0 yields

$$\Pi_u(k_0) - \Pi_u(0) = \int_0^{k_0} \hat{\mathcal{F}}(k) dk - \int_0^{k_0} \hat{D}_u(k) dk. \quad (13)$$

Note that $\int_0^{k_0} \hat{\mathcal{F}}(k) dk$ is the total energy injection rate for hydrodynamic turbulence. Since $\Pi_u(0) = 0$ and the dissipation at small wavenumbers is negligible, we obtain

$$\Pi_u(k_0) \approx \int_0^{k_0} \hat{\mathcal{F}}(k) dk. \quad (14)$$

Now, integration of Eq. (11) from k_0 to ∞ yields

$$\Pi_u(\infty) - \Pi_u(k_0) = \int_{k_0}^{\infty} \hat{\mathcal{F}}(k) dk - \int_{k_0}^{\infty} \hat{D}_u(k) dk. \quad (15)$$

Since $\Pi_u(\infty) = 0$ and $\hat{\mathcal{F}}(k) = 0$ for $k \in [k_0, \infty)$, we get

$$\Pi_u(k_0) = \int_{k_0}^{\infty} \hat{D}_u(k) dk \approx \int_0^{\infty} \hat{D}_u(k) dk = \epsilon_u. \quad (16)$$

Note that k_0 is small and $\hat{D}_u(k)$ is small in the forcing band. Therefore, the lower limit of the aforementioned integration has been replaced with 0. Thus, using Eqs. (14) and (16), we deduce that in hydrodynamic turbulence, the energy flux in the inertial range is constant and is approximately equal to the dissipation rate ϵ_u and the total energy injection rate.

2. Thermal convection

In turbulent convection, the energy is injected into the system by buoyancy. We denote this energy feed as $\hat{\mathcal{F}}_B(k)$. Note that we do not inject energy externally in convection as we do in hydrodynamic turbulence. Furthermore, unlike hydrodynamic turbulence, $\hat{\mathcal{F}}_B(k)$ acts at all scales in thermal convection. Replacing $\hat{\mathcal{F}}(k)$ with $\hat{\mathcal{F}}_B(k)$, we rewrite Eq. (11) as

$$\frac{d}{dk} \Pi_u(k) = \hat{\mathcal{F}}_B(k) - \hat{D}_u(k). \quad (17)$$

Since hot plumes ascend and the cold plumes descend, u_z and θ are positively correlated, which means that^{9,10}

$$\langle \theta(\mathbf{r}) u_z(\mathbf{r}) \rangle > 0.$$

Using this condition, Kumar, Chatterjee, and Verma⁹ and Verma, Kumar, and Pandey¹⁰ claimed that $\hat{\mathcal{F}}_B(k) > 0$, that is, buoyancy feeds energy to the system. Hence, $\frac{d}{dk} \Pi_u(k) > 0$ in the steady state from Eq. (17). It is important to note that in stably stratified flows, buoyancy depletes energy from the system. Thus, for such flows, $\hat{\mathcal{F}}_B < 0$, resulting in $\frac{d}{dk} \Pi_u(k) < 0$. This means that the flux decreases with wavenumber in the inertial range; this is an important ingredient of Bolgiano-Obukhov scaling.^{7,8} Since the flux does not decrease with wavenumber in thermal convection, Bolgiano-Obukhov scaling is ruled out.

Furthermore, in turbulent convection, Pandey and Verma⁵⁰ and Pandey *et al.*⁵¹ showed that buoyancy is strong only at large scales and is weak in the inertial range. Nath *et al.*⁵² showed that the distribution of velocity field in turbulent convection is nearly

isotropic similar to hydrodynamic turbulence, again indicating weak buoyancy.

Based on the above observations, Kumar, Chatterjee, and Verma⁹ and Verma, Kumar, and Pandey¹⁰ argued that $\hat{\mathcal{F}}_B$ does not bring about a noticeable increase in $\Pi_u(k)$ (see Fig. 1). Therefore, $\hat{\mathcal{F}}_B \approx \hat{D}_u \approx 0$, which reduces Eq. (17) to

$$\frac{d}{dk}\Pi_u(k) \approx 0, \Rightarrow \Pi_u(k) \approx \text{constant}. \quad (18)$$

Thus, it can be inferred from Eq. (18) that Kolmogorov’s theory of hydrodynamic turbulence is also applicable to thermal convection. Integrating Eq. (17) from 0 to a small wavenumber k_0 lying in the inertial range yields

$$\Pi_u(k_0) - \Pi_u(0) = \int_0^{k_0} \hat{\mathcal{F}}_B(k)dk - \int_0^{k_0} \hat{D}_u(k)dk. \quad (19)$$

Since $\Pi_u(0) = 0$ and the dissipation rate is negligible at small wavenumbers, the above equation reduces to

$$\Pi_u(k_0) \approx \int_0^{k_0} \hat{\mathcal{F}}_B(k)dk. \quad (20)$$

Since $\hat{\mathcal{F}}_B(k)$ is strong at large scales, we deduce from Eq. (20) that a large part of energy is injected by buoyancy at large scales that contributes to the energy flux in the inertial range; this feature is similar to hydrodynamic turbulence.

There is, however, a difference between the energetics of RBC and that of 3D turbulence. Integrating Eq. (17) from k_0 to ∞ yields

$$\Pi_u(\infty) - \Pi_u(k_0) = \int_{k_0}^{\infty} \hat{\mathcal{F}}_B(k)dk - \int_{k_0}^{\infty} \hat{D}_u(k)dk. \quad (21)$$

Since $\Pi_u(\infty) = 0$, the above equation becomes

$$\Pi_u(k_0) = \int_{k_0}^{\infty} \hat{D}_u(k)dk - \int_{k_0}^{\infty} \hat{\mathcal{F}}_B(k)dk. \quad (22)$$

Since k_0 is small compared to the dissipation range wavenumbers, we can write

$$\int_{k_0}^{\infty} \hat{D}_u(k)dk \approx \int_0^{\infty} \hat{D}_u(k)dk = \epsilon_u.$$

Now, $\int_{k_0}^{\infty} \hat{\mathcal{F}}_B(k)dk$ is the energy injected by buoyancy at small scales. It must be noted that $\int_{k_0}^{\infty} \hat{\mathcal{F}}_B(k)dk > 0$ in RBC because $\hat{\mathcal{F}}_B(k)$, albeit weak, is positive and adds up to a significant amount when

integrated over the inertial and dissipation range (see Sec. V C). Therefore,

$$\Pi_u(k_0) \approx \epsilon_u - \int_{k_0}^{\infty} \hat{\mathcal{F}}_B(k)dk < \epsilon_u. \quad (23)$$

Equation (23) clearly shows that unlike in hydrodynamic turbulence, the energy flux in the inertial range is smaller than the dissipation rate due to the energy injected by buoyancy at small scales. Recall that in hydrodynamic turbulence, no energy is injected in these regimes. In Sec. V C, using the results of numerical simulations of turbulent convection, we show that the energy flux is smaller than the dissipation rate by a factor of two to three for our selected cases. Note that this factor likely depends on Ra, Pr, type of boundary conditions, etc. A careful study of the spectra and fluxes of thermal convection for different regimes of Ra and Pr needs to be carried out to ascertain how this factor depends on the aforementioned parameters.

In Subsection III B, following the procedure of Kolmogorov,^{1,2} we derive the relation for the third-order velocity structure functions of turbulent convection.

B. Velocity structure functions of turbulent convection

Sun, Zhou, and Xia²⁵ and Zhou, Sun, and Xia⁵³ performed experiments of turbulent thermal convection and observed isotropy in regions away from walls. Using detailed numerical simulations, Nath *et al.*⁵² computed the modal energy of the inertial-range Fourier modes of turbulent convection as a function of polar angle Θ (angle between the buoyancy direction and the wavenumber) and found it to be approximately independent of Θ . Thus, they showed that turbulent convection is nearly isotropic. In Sec. V A, we compute the second-order velocity structure functions as functions of l and Θ (Θ is the angle between the buoyancy direction and l) using our numerical data and show that they are nearly independent of Θ . This again shows near-isotropy in thermal convection. We believe that isotropy is related to the fact that in turbulent convection, buoyancy “effectively” injects energy at large scales, but it is weak in the inertial range.

Furthermore, at high Rayleigh numbers, the boundary layers are very thin, with the boundary layer thickness $\delta_u \ll d$, where d is the domain height. Therefore, for simplification, we neglect the effects of boundary layers and consider the system to be homogeneous. In the Appendix, we show that in turbulent thermal convection, the planar structure functions and those computed in the

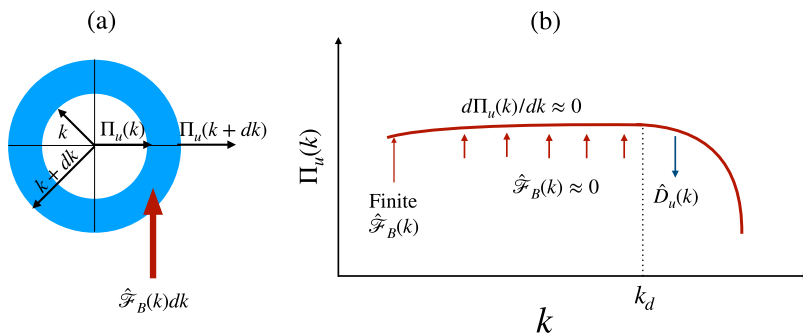


FIG. 1. For RBC: (a) A schematic diagram of a wavenumber shell of radius k showing the buoyant energy feed $\hat{\mathcal{F}}_B$ and the kinetic energy flux $\Pi_u(k)$. (b) Schematic plot of $\Pi_u(k)$ vs k . $\Pi_u(k) \approx \text{constant}$ in the inertial range because of weak $\hat{\mathcal{F}}_B$. Viscous dissipation $\hat{D}_u(k)$ is dominant for $k > k_d$.

entire domain exhibit somewhat similar scaling; this result also validates the assumptions of approximate homogeneity and isotropy for turbulent convection. Using the assumptions of homogeneity, isotropy, and steady state and following similar lines of arguments as Kolmogorov,^{1,2} we derive the relation for the third-order structure function for turbulent convection in the following discussion.

For homogeneous and incompressible turbulent flows, the temporal evolution of the second-order velocity correlation function can be written as follows:¹⁻³

$$\frac{\partial}{\partial t} \left[\frac{1}{2} \langle u_i(\mathbf{r}) u_i(\mathbf{r} + \mathbf{l}) \rangle \right] = T_u(\mathbf{l}) + \mathcal{F}_B(\mathbf{l}) - D_u(\mathbf{l}), \quad (24)$$

where

$$T_u(\mathbf{l}) = \frac{1}{4} \nabla_l \cdot \langle [u(\mathbf{r} + \mathbf{l}) - u(\mathbf{r})]^2 [\mathbf{u}(\mathbf{r} + \mathbf{l}) - \mathbf{u}(\mathbf{r})] \rangle,$$

$$\mathcal{F}_B(\mathbf{l}) = \langle F_i(\mathbf{r}) u_i(\mathbf{r} + \mathbf{l}) \rangle,$$

$$D_u(\mathbf{l}) = \nu \nabla^2 \langle u_i(\mathbf{r}) u_i(\mathbf{r} + \mathbf{l}) \rangle.$$

Here, $T_u(\mathbf{l})$ is the nonlinear energy transfer at scale \mathbf{l} , $\mathcal{F}_B(\mathbf{l})$ is the force correlation at \mathbf{l} , and $D_u(\mathbf{l})$ is the corresponding dissipation rate. The symbol ∇^2 represents the Laplacian at $\mathbf{r} + \mathbf{l}$. Under a steady state, the left-hand side of Eq. (24) disappears. Furthermore, we focus on the inertial range where $D_u(\mathbf{l}) \approx 0$ that yields

$$\mathcal{F}_B(\mathbf{l}) \approx -T_u(\mathbf{l}). \quad (25)$$

Now, $\mathcal{F}_B(\mathbf{l})$ can be expanded as Fourier series as follows:

$$\mathcal{F}_B(\mathbf{l}) = \sum_{\mathbf{k}} \hat{\mathcal{F}}_B(\mathbf{k}) \exp(i\mathbf{k} \cdot \mathbf{l}). \quad (26)$$

Following Verma, Kumar, and Pandey,¹⁰ we model $\hat{\mathcal{F}}_B(\mathbf{k})$ as³

$$\hat{\mathcal{F}}_B(\mathbf{k}) = \frac{A}{2} (\delta_{\mathbf{k}, \mathbf{k}_0} + \delta_{\mathbf{k}, -\mathbf{k}_0}) + Bk^{-5/3}. \quad (27)$$

Substitution of Eq. (27) into Eq. (26) yields

$$\begin{aligned} \mathcal{F}_B(\mathbf{l}) &= A \cos(\mathbf{k}_0 \cdot \mathbf{l}) + \int Bk^{-5/3} \exp(i\mathbf{k} \cdot \mathbf{l}) d\mathbf{k} \\ &\approx A + DBl^{2/3}. \end{aligned} \quad (28)$$

This is because $\mathbf{k}_0 \cdot \mathbf{l} \approx 0$ since turbulent convection is essentially forced by large-scale plumes.¹⁰ Here, B is a small constant. Now, for an isotropic flow, $T_u(\mathbf{l}) = T_u(l)$ and is related to the third-order structure function $S_3^u(l)$ as (see Ref. 3)

$$T_u(l) = \frac{1}{12} \frac{1}{l^2} \frac{d}{dl} \left[\frac{1}{l} \frac{d}{dl} \{ l^4 S_3^u(l) \} \right]. \quad (29)$$

Combining Eqs. (25), (28), and (29), we get

$$-\frac{1}{12} \frac{1}{l^2} \frac{d}{dl} \left[\frac{1}{l} \frac{d}{dl} \{ l^4 S_3^u(l) \} \right] = A + DBl^{2/3}. \quad (30)$$

Integrating the above expression twice and noting that $S_3^u(0) = 0$, we obtain the following relation:

$$S_3^u(l) = -\frac{4}{5} (Al + D'Bl^{5/3}). \quad (31)$$

Now, we assume that the large-scale buoyant energy feed at $k = k_0$ equals the energy flux Π_u and that B is small. Therefore, we have $A \approx \Pi_u$, and

$$S_3^u(l) = -\frac{4}{5} \Pi_u l. \quad (32)$$

Thus, the scaling of the third-order structure functions of RBC is similar to those of 3D hydrodynamic turbulence, except that $\epsilon_u S_3^u(l)$ is replaced by Π_u . Note that $\Pi_u < \epsilon_u$ for RBC. We will verify the above relation in Sec. V using numerical simulations.

It is important to note that for hydrodynamic turbulence, $\hat{\mathcal{F}}(k)$ is provided at small wavenumbers and is equal to the viscous dissipation rate ϵ_u . Inverse Fourier transform of $\hat{\mathcal{F}}(k)$ results in a constant value of $\mathcal{F}(l)$ that equals ϵ_u . Using the same procedure as shown above, one can derive that $S_3^u(l) = -(4/5)\epsilon_u l$. Note that in RBC, ϵ_u of the above $S_3^u(l)$ is replaced by Π_u . We also remark that our arguments are consistent with the results of Kunnen and Clercx,⁵⁴ who computed the scale-by-scale energy budget in direct numerical simulations of RBC and showed that $S_3^u(l) \neq -(4/5)\epsilon_u l$ for convective turbulence.

Finally, as mentioned previously, it must be noted that Eq. (32) has been derived under the assumption of homogeneity and isotropy, which may not be the case for all regimes of turbulent convection. For example, Nath *et al.*⁵² have shown that anisotropy is stronger for large Prandtl numbers. Thus, we cannot make the assumption of isotropy in this regime.

In Sec. IV, we discuss the numerical techniques involved in the computation of the structure functions.

IV. NUMERICAL METHODS

We use two sets of numerical data to compute the velocity structure functions, each set having different boundary conditions. The first set is the data of Verma, Kumar, and Pandey,¹⁰ who performed direct numerical simulations (DNS) of RBC on a 4096^3 grid. The grid corresponds to a cube of unit dimension. The Rayleigh and Prandtl numbers were chosen as 1.1×10^{11} and unity, respectively. The simulation was performed using a pseudospectral code.^{55,56} Free-slip and isothermal boundary conditions were employed at the top and bottom plates, and periodic boundary conditions were employed at the side walls. For details, refer to Ref. 10.

The second set of data is that of Kumar and Verma.⁵⁷ This simulation was performed using a finite volume solver⁵⁸ on a nonuniform 256^3 grid that corresponds to a cube of unit dimension. The Rayleigh and Prandtl numbers were chosen as 1×10^8 and unity, respectively. No-slip boundary conditions were imposed at all the walls; such realistic boundary conditions capture the wall effects. Isothermal boundary conditions were imposed at the top and bottom plates and adiabatic boundary conditions at the side walls. For spatial discretization schemes, time-marching method, and the validation of the code, see Refs. 57, 59, and 60. We interpolate the velocity fields to a uniform 256^3 grid.

We compute the velocity structure functions in the entire domain using a combination of shared (OpenMP) and distributed memory [Message Passing Interface (MPI)] parallelization (see Ref. 61). The computations involve running six nested for loops: the outer three loops describing the position vector \mathbf{r} and the inner three loops describing $\mathbf{r} + \mathbf{l}$. To save computational resources, we condense our free-slip data to 512^3 grid. Note that we are interested only in scales pertaining to the inertial range and not the dissipative scales. After the aforementioned coarsening, we are still able to resolve scales above 6η and capture the inertial range very well in addition to avoiding unnecessary computational costs. The number

of MPI nodes used was equal to the number of grid points in the x -direction, while the number of OpenMP threads used was 32.

In Sec. V, we will discuss the numerical results.

V. NUMERICAL RESULTS

In this section, for turbulent thermal convection, we describe the scaling of the velocity structure functions, the probability distribution functions of velocity increments, and the difference between the energy flux and viscous dissipation rate.

A. Structure functions

Before computing the structure functions, we first numerically compute the viscous dissipation rate ϵ_u using the velocity field data of our free-slip and no-slip cases. We use the relation

$$\epsilon_u = \langle 2\nu S_{ij}S_{ij} \rangle \quad (33)$$

to compute the viscous dissipation rate, where S_{ij} is the strain rate tensor, and $\langle \cdot \rangle$ represents the volume average. Furthermore, we compute the Kolmogorov length scale η and the Nusselt number Nu using the following relations:^{3,34,62}

$$\eta = \left(\frac{\nu^3}{\epsilon_u} \right)^{1/4}, \quad (34)$$

$$\text{Nu} = 1 + \frac{\langle u_z \theta \rangle}{\kappa \Delta d^{-1}}. \quad (35)$$

In Table I, we list the values of Nu, ν , ϵ_u , and η for both free-slip and no-slip data. Clearly, η is larger for the no-slip case because of lower Ra. Furthermore, we remark that the viscous boundary layers are thin for our data, with $\delta_u = 0$ for the free-slip simulation and $\delta_u \approx 2\eta$ for the no-slip simulation.⁵⁹ Thus, most of the flow resides in the bulk.

Next, we validate the assumption of isotropy in turbulent convection. Using both sets of data, we compute the second-order velocity structure functions in the entire domain as functions of l and Θ , where Θ is the angle between the buoyancy direction and l . Figures 2(a) and 2(b) exhibit the polar plots $S_2^u(l, \Theta)$, with l spanning the inertial-dissipation range ($0 < l/\eta < 210$ for the free-slip case and $0 < l/\eta < 40$ for the no-slip case). Figures 2(a) and 2(b) clearly show that the structure functions are nearly independent of Θ , thereby demonstrating near-isotropy in the inertial-dissipation range.

Now, we compute the magnitude of S_q^u as a function of l in the entire domain, with q ranging from 2 to 10. Figure 3 exhibits the plots of structure functions of orders 2, 3, 6, 8, and 10 vs l/η for both sets of data. Contrary to the results of Benzi *et al.*,^{16,17} we observe a discernible scaling range for the third order structure function. The range is found to be $32 < l/\eta < 200$ for the free-slip data and $19 < l/\eta$

TABLE I. For the two simulations of RBC: Rayleigh number Ra, Nusselt number Nu, kinematic viscosity ν , viscous dissipation rate ϵ_u , and Kolmogorov length scale η .

Case	Ra	Nu	ν	ϵ_u	η
Free-slip	1.1×10^{11}	582	3.02×10^{-6}	2.59×10^{-3}	3.21×10^{-4}
No-slip	1.0×10^8	32.8	1.00×10^{-4}	3.18×10^{-3}	4.21×10^{-3}

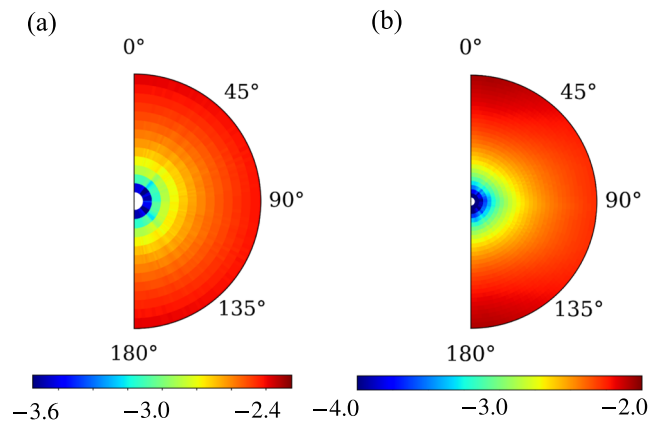


FIG. 2. For the (a) free-slip and (b) no-slip simulations of RBC: Polar (l, Θ) plots of the logarithms of second-order velocity structure functions, where Θ is the angle between the buoyancy-direction and l . l spans the inertial-dissipation range: $0 < l/\eta < 210$ for the free-slip data and $0 < l/\eta < 40$ for the no-slip data. The structure functions are nearly independent of Θ , thus demonstrating near-isotropy in the inertial-dissipation range.

< 40 for the no-slip data. The range is much smaller for the no-slip case because of the higher value of η . Note that the length scales in the inertial range are much larger than the boundary layer thickness.

We compute the scaling exponents ζ_q and the prefactor \mathcal{A} by fitting the relation $S_q^u(l) = \mathcal{A}l^{\zeta_q}$ to our data within the scaling range. Table II lists \mathcal{A} and ζ_q for both sets of data. Note that $\zeta_3 = 0.97$ and 0.98 for the free-slip and the no-slip cases, respectively, which are close to Kolmogorov scaling of $S_3^u \sim l$. From Table II and Figs. 3 and 4, we observe that for lower orders, the scaling exponents ζ_q for free-slip and no-slip boundary conditions are nearly equal, and they are close to $q/3$, which is a generalization of Kolmogorov's theory of turbulence. For $q = 2$, $\zeta_2 \approx 2q/3$ that yields $k^{-5/3}$ energy spectrum. These results are consistent with the Kolmogorov energy spectrum in thermal convection observed by Kumar, Chatterjee, and Verma,⁹ Verma, Kumar, and Pandey,¹⁰ and Kumar and Verma.⁵⁷ Our results are also consistent with those of Sun, Zhou, and Xia²⁵ and Kaczorowski and Xia,³³ who reported Kolmogorov scaling of the structure functions of RBC computed at the cell center. On the other hand, our results are contrary to those of Benzi *et al.*,^{16,17} Calzavarini, Toschi, and Tripiccone,²⁴ and Kunnen *et al.*³¹ (for $\text{Ra} = 10^8$), who deduced Bolgiano-Obukhov scaling based on their simulations. However, it must be noted that Kunnen *et al.*³¹ could not observe Bolgiano-Obukhov scaling for $\text{Ra} > 10^8$; rather, they reported Kolmogorov scaling, similar to our results. We will discuss more on Bolgiano-Obukhov scaling later in this section.

As illustrated in Table II and Fig. 4, higher order ζ_q 's for the free-slip data are marginally lower than those for the no-slip data. Also, for higher order structure functions, ζ_q deviates from $q/3$ due to intermittency. To explain intermittency effects in hydrodynamic turbulence, She and Leveque⁶ proposed the following model for ζ_q :

$$\zeta_q = \frac{q}{9} + 2 \left(1 - \left(\frac{2}{3} \right)^{q/3} \right). \quad (36)$$

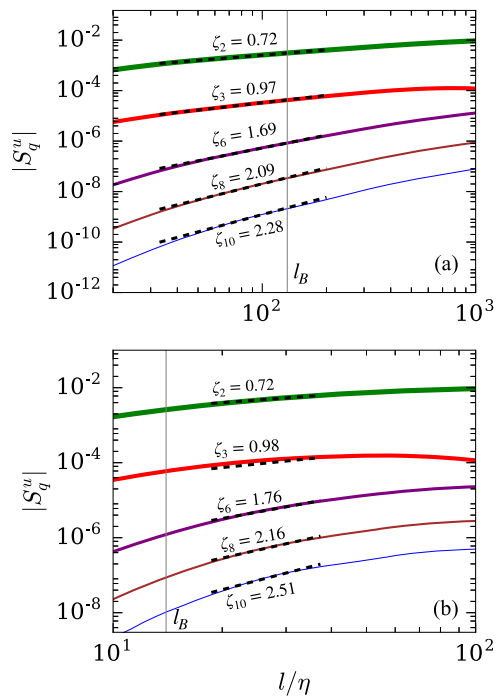


FIG. 3. For (a) the free-slip and (b) no-slip simulations of RBC: plots of $|S_q^u|$ with decreasing line thickness for $q = 2$ (green), 3 (red), 6 (purple), 8 (brown), and 10 (blue) vs l/η . The vertical solid gray line marks the Bolgiano length scale.

Interestingly, the aforementioned equation describes ζ_q calculated using our RBC data quite well [see Figs. 4(a) and 4(b)]. These results demonstrate similarities between ζ_q scaling in convection and in hydrodynamic turbulence, consistent with earlier results.^{9,10,47} Our results also match with the experimental work of Sun, Zhou, and Xia,²⁵ who observed the scaling exponents of structure functions calculated at the cell-center to fit with the model of She-Leveque.

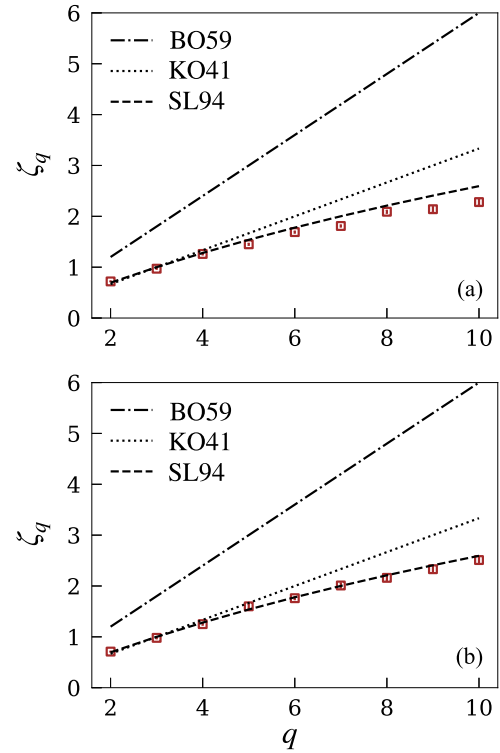


FIG. 4. For (a) the free-slip and (b) no-slip simulations of RBC: plots of ζ_q (squares) vs q . ζ_q matches closely with the predictions of She and Leveque⁵ (dashed line). The figures also contain the prediction of Kolmogorov $\zeta_q = q/3$ (dotted line) and the prediction of Bolgiano-Obukhov $\zeta_q = 3q/5$ (chained line).

In Fig. 5, we plot the logarithms of S_2^u , S_6^u , S_8^u , and S_{10}^u vs $\log_{10} |S_3^u|$ for both free-slip and no-slip cases and observe the structure functions to be self-similar, that is,

$$S_q^u \sim (S_3^u)^{\beta(q,3)}, \quad (37)$$

TABLE II. For the free-slip and no-slip simulations of RBC: prefactor \mathcal{A} and the scaling exponent ζ_q for the structure functions computed by fitting the relation $|S_q^u(l)| = \mathcal{A}l^{\zeta_q}$ to our data.

q	Free-slip simulation ($Ra = 1.1 \times 10^{11}$)		No-slip simulation ($Ra = 1.0 \times 10^8$)	
	\mathcal{A}	ζ_q	\mathcal{A}	ζ_q
2	$(2.8 \pm 0.1) \times 10^{-2}$	0.70 ± 0.01	$(2.3 \pm 0.1) \times 10^{-2}$	0.71 ± 0.01
3	$(9.3 \pm 0.5) \times 10^{-4}$	0.97 ± 0.01	$(8.5 \pm 0.5) \times 10^{-4}$	0.98 ± 0.02
4	$(2.0 \pm 0.1) \times 10^{-3}$	1.26 ± 0.02	$(1.6 \pm 0.1) \times 10^{-3}$	1.25 ± 0.02
5	$(1.5 \pm 0.1) \times 10^{-4}$	1.45 ± 0.02	$(2.6 \pm 0.2) \times 10^{-4}$	1.60 ± 0.04
6	$(1.8 \pm 0.1) \times 10^{-4}$	1.69 ± 0.02	$(2.6 \pm 0.2) \times 10^{-4}$	1.76 ± 0.03
7	$(2.1 \pm 0.1) \times 10^{-5}$	1.81 ± 0.02	$(7.6 \pm 0.8) \times 10^{-5}$	2.01 ± 0.05
8	$(2.7 \pm 0.3) \times 10^{-5}$	2.09 ± 0.03	$(6.0 \pm 0.6) \times 10^{-5}$	2.16 ± 0.05
9	$(3.9 \pm 0.7) \times 10^{-6}$	2.14 ± 0.05	$(2.6 \pm 0.4) \times 10^{-5}$	2.33 ± 0.07
10	$(3.1 \pm 0.5) \times 10^{-6}$	2.28 ± 0.05	$(2.1 \pm 0.3) \times 10^{-5}$	2.51 ± 0.07

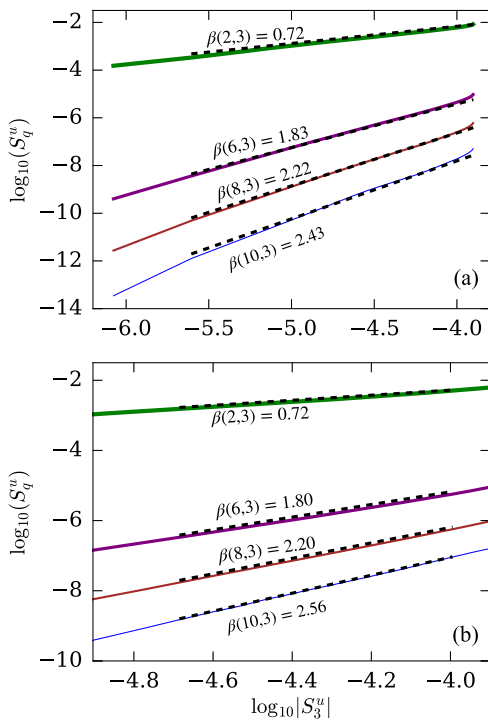


FIG. 5. For (a) the free-slip and (b) no-slip simulations of RBC: plots of S_q^u vs S_3^u . This extended self-similarity goes beyond the inertial range.

where $\beta(q, 3) = \zeta_q/\zeta_3$. The computed values of the exponent $\beta(q, 3)$ are also shown in Fig. 5. This scaling occurs for l/η ranging from 12 to 530 for the free-slip case and 9–45 for the no-slip case. The range of S_q^u vs S_3^u plots of Fig. 5 is wider than that of S_q^u plots of Fig. 3 (in Fig. 5, the range extends well beyond the inertial range to the dissipative scales). This is called extended self-similarity (ESS).^{18,19} ESS has been observed in previous studies of convection.^{16,17,34} Note that ESS was first reported by Benzi *et al.*¹⁸ in hydrodynamic turbulence.

According to Pope,⁶² the upper limit of the inertial range can be estimated by $l_{EI}^p \approx L/6$ and the lower limit $l_{DI}^p \approx 60\eta$. Going by this estimate, $l_{EI}^p = 530\eta$ for our free-slip data. Note that the upper and the lower limits of the power-law range of the structure functions for our free-slip data are of the same order of magnitude as Pope's estimate. For the no-slip case, because of the large value of η and the dissipative nature of the OpenFOAM solver, $l_{DI}^p (= 60\eta)$ is greater than $l_{EI}^p (= 40\eta)$. Therefore, Pope's estimate for the lower limit does not hold for the no-slip case; this is expected because Pope's estimates are expected to work for homogeneous and isotropic turbulence or periodic boundary condition.

An important point to note is that ζ_q curve does not fit with $\zeta_q = 3q/5$, which is a generalization of the Bolgiano-Obukhov (BO) model. As discussed in Sec. III A 2, Kumar, Chatterjee, and Verma⁹ and Verma, Kumar, and Pandey¹⁰ have argued against the Bolgiano-Obukhov (BO) model for RBC based on energy flux arguments. This result is contrary to some of the earlier works^{12–14,16,17,20,31} that argue in favor of the Bolgiano-Obukhov model. Note that the Bolgiano

length computed using $l_B = \text{Nu}^{1/2}/(\text{PrRa})^{1/4}$ is approximately 130η and 14η for the free-slip and no-slip boundary conditions, respectively. They are marked as vertical lines in Fig. 3. We do not discuss l_B in detail because the Bolgiano-Obukhov (BO) model has been shown to be inapplicable for RBC^{9,10,47} (see Sec. III A 2).

In the Appendix, we compute the planar structure functions for several horizontal cross sections. We observe that these structure functions are somewhat similar to those described above, with a difference that planar structure functions exhibit relatively higher fluctuations. This is due to lesser averaging for the planar structure function.

In Subsection V B, we describe the probability distribution function (PDF) for the velocity difference between two points.

B. Probability distribution function for velocity increments

For different values of l/η , we compute the probability distribution functions (PDFs) of velocity increments, $\delta u = \{\mathbf{u}(\mathbf{r} + \mathbf{l}) - \mathbf{u}(\mathbf{r})\} \cdot \hat{\mathbf{l}}$, using the free-slip and the no-slip data. Figure 6(a) exhibits the PDFs of δu for the free-slip data. For small l , the PDFs are non-Gaussian with wide tails. The tails fit with a stretched exponential curve given by $P(\delta u) \sim \exp(-m|\delta u^*|^\alpha)$, where $\delta u^* = \delta u/\sqrt{\langle \delta u^2 \rangle}$. We observe that the stretching exponent $\alpha = 0.8, 1.0$, and 1.8 for $l/\eta = 12, 62$, and 170 , respectively. Thus, the PDFs become closer to Gaussian (represented by the dashed black curve) as l increases. This is expected

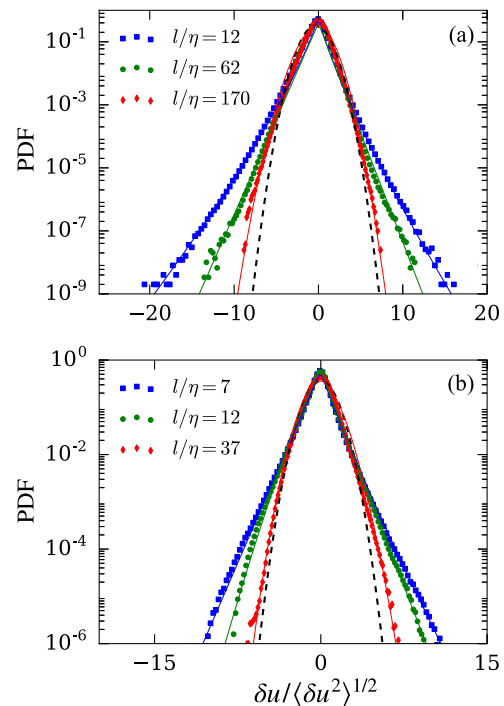


FIG. 6. For (a) the free-slip and (b) no-slip simulations of RBC: probability distribution functions of δu for various l/η (as shown in legends). The tails fit well with the stretched exponential (solid curves). The dashed black curves represent the standard Gaussian distribution.

since the velocities at two largely separated points become independent of each other. Our results are similar to those observed in hydrodynamic turbulence (see Refs. 63 and 64).

Figure 6(b) exhibits the PDFs of δu calculated using the no-slip data. Clearly, the tails are narrower compared to the free-slip case. This is because of the weaker velocity fluctuations owing to the lower Rayleigh number. Moreover, the presence of viscous boundary layers also reduces the fluctuations. Pandey *et al.*⁶⁵ showed that for the same parameters, the large scale velocity and heat flux are less for convection with no-slip walls than with free-slip walls. Similar to the free-slip case, the tails of the PDFs fit well with a stretched exponential. For $l/\eta = 7, 12,$ and 37 , α' 's are 0.9, 1.0, and 1.7, respectively, for the left tail and 1.0, 1.2, and 1.9, respectively, for the right tail. The PDFs become close to Gaussian at large scales, similar to the free-slip case.

C. Buoyancy forcing, energy flux, and viscous dissipation rate

In this section, we provide a numerical demonstration that the energy flux and the viscous dissipation rate differ in RBC.

Using the third-order velocity structure functions, we calculate the energy flux Π_u using Eq. (32) as

$$\Pi_u = -\frac{5}{4} \frac{S_3^u}{l}. \quad (38)$$

We list the values of the energy flux in Table III. We also compute the Fourier transform of our velocity and temperature field data and compute the spectral energy flux using the following relation:^{55,56}

$$\Pi_u(k_0) = \sum_{k \geq k_0} \sum_{p < k_0} \delta_{\mathbf{k}, \mathbf{p}+\mathbf{q}} \mathcal{J}([\mathbf{k} \cdot \mathbf{u}(\mathbf{q})][\mathbf{u}^*(\mathbf{k}) \cdot \mathbf{u}(\mathbf{p})]). \quad (39)$$

We plot the flux [computed using Eq. (39)] against k in Fig. 7. We observe the value of the flux to be almost constant in the inertial range, and it closely matches with that computed using Eq. (38). In Table III, we also list the values of ϵ_u computed in Sec. V A.

From Table III, we observe that $\epsilon_u \approx 2\Pi_u$ for the free-slip case and $\approx 3\Pi_u$ for the no-slip case. This is unlike in 3D hydrodynamic turbulence in which the flux and viscous dissipation rate are equal. Our results are consistent with our arguments in Sec. III A 2 where we show that the difference between the flux and the viscous dissipation rate arises due to nonzero buoyancy in the inertial range.

Using the values of $\Pi_u(k)$ computed using Eq. (39), we numerically compute $\frac{d}{dk}\Pi_u(k)$ using the central-difference method. We also compute the energy spectrum $E_u(k)$ and obtain the spectrum of viscous dissipation using the relation $\hat{D}_u(k) = 2\nu k^2 E_u(k)$. Using the values of the dissipation spectrum and $\frac{d}{dk}\Pi_u(k)$ and assuming steady

TABLE III. For the two simulations of RBC: energy flux Π_u computed using the third-order structure functions, viscous dissipation rate ϵ_u , and the Kolmogorov constant K_{KO} .

Case	Π_u	ϵ_u	K_{KO}
Free-slip	$(1.29 \pm 0.06) \times 10^{-3}$	2.59×10^{-3}	1.59 ± 0.09
No-slip	$(1.09 \pm 0.03) \times 10^{-3}$	3.18×10^{-3}	1.53 ± 0.04

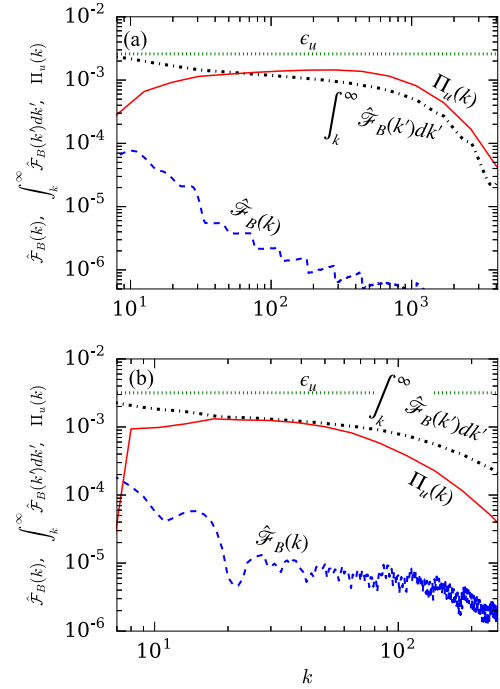


FIG. 7. For (a) the free-slip and (b) no-slip simulations of RBC: the spectra of buoyancy forcing $\hat{\mathcal{F}}_B(k)$ (dashed blue lines), its integral $\int_k^\infty \hat{\mathcal{F}}_B(k')dk'$ (chained black lines), and the kinetic energy flux $\Pi_u(k)$ (solid red lines). $\hat{\mathcal{F}}_B(k)$ is weak in the inertial range. $\Pi_u(k)$ is of the same order as $\int_k^\infty \hat{\mathcal{F}}_B(k')dk'$ and is less than the viscous dissipation rate ϵ_u (dotted green lines).

state, we compute $\hat{\mathcal{F}}_B(k)$ using Eq. (17),

$$\hat{\mathcal{F}}_B(k) = \frac{d}{dk}\Pi_u(k) + \hat{D}_u(k).$$

We plot the values of $\Pi_u(k)$, $\hat{\mathcal{F}}_B(k)$, and $\int_k^\infty \hat{\mathcal{F}}_B(k')dk'$ in Fig. 7(a) for the free-slip case and in Fig. 7(b) for the no-slip case. In each of the plots, we also draw a horizontal line denoting the viscous dissipation rate. As shown in Figs. 7(a) and 7(b), in the inertial range,

$$\Pi_u \sim \int_k^\infty \hat{\mathcal{F}}_B(k')dk'$$

and is approximately $\epsilon_u/2$ for the free-slip case and $\epsilon_u/3$ for the no-slip case. In addition, $\hat{\mathcal{F}}_B(k')$ in the inertial range is weak, consistent with our previous arguments.

In Fig. 8, we plot the cumulative buoyant energy forcing $\int_0^k \hat{\mathcal{F}}_B(k')dk'$, the cumulative viscous dissipation rate $\int_0^k \hat{D}_u(k')dk'$, and the energy flux $\Pi_u(k)$ against k for both sets of data. The plots clearly show that the cumulative buoyant energy forcing at small wavenumbers contributes to the energy flux in the inertial range, consistent with our arguments in Sec. III A 2. For the free-slip data, $\int_0^k \hat{\mathcal{F}}_B(k')dk'$ remains close to the flux until $k = 200$, after which it deviates from $\Pi_u(k)$. Similar behavior is also observed for the no-slip data, but with the threshold wavenumber $k = 18$. Above these wavenumbers, $\int_0^k \hat{\mathcal{F}}_B(k')dk'$ increases slowly and merges with the

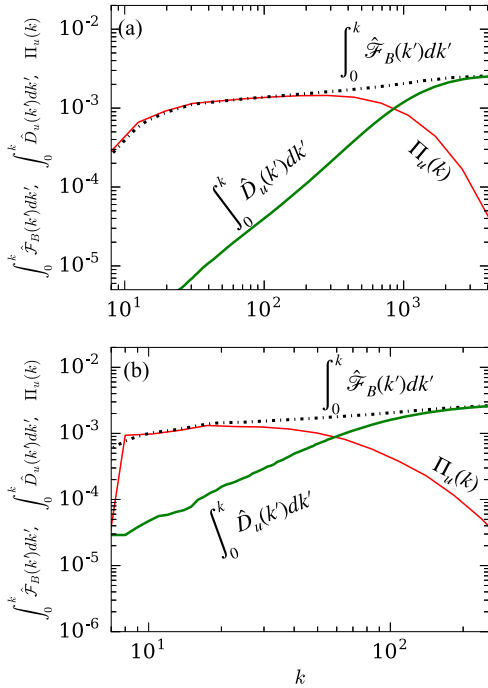


FIG. 8. For (a) the free-slip and (b) no-slip simulations of RBC: the spectra of cumulative buoyancy forcing $\int_0^k \hat{\mathcal{F}}_B(k')dk'$ (chained black lines), kinetic energy flux $\Pi_u(k)$ (solid red lines), and cumulative dissipation rate $\int_0^k \hat{D}_u(k')dk'$ (thick green lines). The cumulative buoyancy forcing at small wavenumbers contributes mainly to the flux in the inertial range.

cumulative dissipation rate $\int_0^k \hat{D}_u(k')dk'$ at dissipation wavenumbers. It is clear that $\int_0^k \hat{\mathcal{F}}_B(k')dk'$ at small wavenumbers (which contributes to the inertial range energy flux) is, respectively, 1/2 and 1/3 of the total energy injection rate $[\int_0^\infty \hat{\mathcal{F}}_B(k')dk']$ for the free-slip and the no-slip data.

Finally, we compute the Kolmogorov constant K_{KO} by first calculating the constant C using the following relation involving the second-order structure function and the energy flux:

$$S_2^u(l) = C(\Pi_u)^{2/3} l^{2/3}. \quad (40)$$

After this, we compute the Kolmogorov constant using⁶²

$$K_{KO} = \frac{55}{72} C. \quad (41)$$

We list the values of Kolmogorov constant for both free-slip and no-slip cases in Table III. Interestingly, K_{KO} of Table III is quite close to that for hydrodynamic turbulence.³

VI. CONCLUSIONS

Using the numerical data of thermal convection, we compute the velocity structure functions S_q^u for $q = 2-10$. The first dataset¹⁰ was generated with free-slip boundary conditions for $Ra = 1.1 \times 10^{11}$ and $Pr = 1$, and the second set⁵⁷ with no-slip boundary conditions with $Ra = 1 \times 10^8$ and $Pr = 1$. We calculate the scaling exponent ζ_q from S_q^u .

We show that the third-order structure functions, computed using both sets of data, scale according to Kolmogorov's theory [$S_3^u = -(4/5)\Pi_u l$]. Our results are consistent with Kolmogorov's energy spectrum observed in turbulent convection. The exponents of the structure functions of thermal convection match well with the predictions of She-Leveque. We demonstrate that the structure functions show extended self-similarity.

We also calculate the probability distribution function (PDF) of velocity increments for different values of the separation distance l . We show that for small l , the PDFs are non-Gaussian with wide tails. With increasing l , the PDFs become closer to Gaussian. The tails of the PDFs follow a stretched exponential, and the stretching exponent increases with l . Note that the PDFs of hydrodynamic turbulence show similar behavior.

We compute the energy flux Π_u using the third-order structure functions and show that $\Pi_u \neq \epsilon_u$; instead, it is two to three times less than ϵ_u for our cases. This is unlike in hydrodynamic turbulence where flux equals the dissipation rate. Using phenomenological arguments, we have shown that this difference arises due to nonzero, albeit weak, buoyancy present in the inertial range.

In summary, the scaling behavior of velocity structure functions of turbulent convection shows similarities with those of 3D hydrodynamic turbulence. We do not analyze the temperature structure functions in this paper. Some of the notable works on temperature structure functions of turbulent convection include those of Ching²⁰ and Ching *et al.*²⁶ We will discuss the scaling of temperature structure functions in a future work.

ACKNOWLEDGMENTS

We are grateful to A. Kumar and A. Chatterjee for sharing their numerical data with us. We acknowledge R. Samuel and M. Sharma for their contributions in the development of the code to calculate structure functions. We thank S. Chakraborty and S. Vashishtha for useful discussions. Our numerical simulations were performed on Shaheen II at KAUST Supercomputing Laboratory, Saudi Arabia, under project No. k1052. This work was supported by Research Grant No. PLANEX/PHY/2015239 from Indian Space Research Organisation, India, and the Department of Science and Technology, India (Grant No. INT/RUS/RSF/P-03) for the Indo-Russian project.

APPENDIX: EXTENT OF HOMOGENEITY IN TURBULENT CONVECTION

For very high Rayleigh number RBC, the boundary layers are quite thin. Hence, the flow, mostly residing in the bulk, is nearly homogeneous. However, for relatively smaller Ra (around 10^8), there can be some inhomogeneity due to plumes and large-scale structures. To test the extent of inhomogeneity, we compute the third-order velocity structure functions for three horizontal slices of the free-slip and no-slip flow profiles detailed in the main text. The three slices are at $z = 0.25, 0.5$, and 0.75 . Note that the $z = 0.5$ corresponds to the midplane.

Figure 9 exhibits the plots of $|S_3^u(l)|$ vs l/η for the three planes. For the free-slip data with higher Ra [Fig. 9(a)], $|S_3^u(l)| \sim l^3$, where $\zeta_3 \approx 1$ for $z = 0.25$ and 0.5 . However, for the $z = 0.75$ plane,

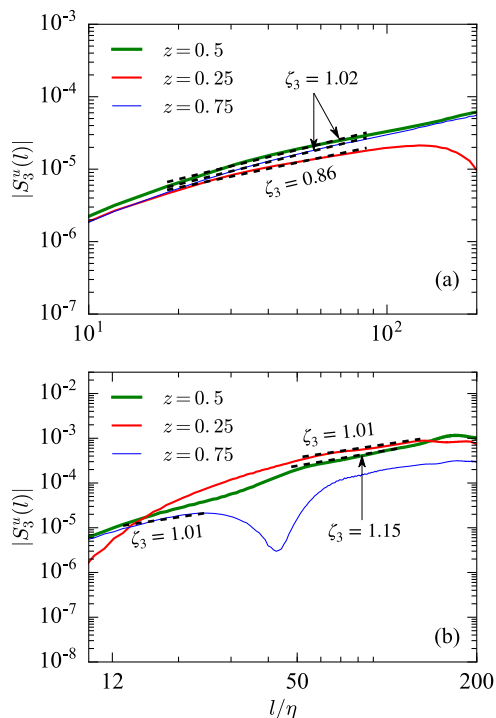


FIG. 9. Plots of the planar structure function $S_3^u(l)$ at $z = 0.25, 0.5$, and 0.75 for (a) the free-slip and (b) no-slip simulations. Despite some spatial inhomogeneity, especially for the no-slip boundary condition (b), there exists scaling range with the scaling exponent $\zeta_3 \sim 1$.

$\zeta_3 = 0.86$, which is slightly below unity. The upper and the lower limits of the scaling range are nearly the same as those for the structure functions computed in the entire domain [see Fig. 3(a)]. Thus, it is reasonable to assume the free-slip data to be homogeneous. However, we observe stronger spatial inhomogeneities for the no-slip data, as shown in Fig. 9(b). Here, the scaling regime of $|S_3^u(l)| \sim l^{\zeta_3}$ is observed for all three planes, with ζ_3 ranging from 1.02 to 1.15. However, the range of the scaling regime differs for the three planes. Note that the spatial inhomogeneities are stronger for no-slip boundary conditions due to the relatively stronger plumes for the no-slip boundaries.

As mentioned earlier, the observed inhomogeneity, which is more prominent for no-slip data, can be attributed to localized plumes. Thus, the structure functions are required to be averaged over more points to cancel out the effects of the plumes. That is why bulk structure functions are smoother than those for the planes, and they are closer to the predictions of She-Leveque.⁶

REFERENCES

- A. N. Kolmogorov, "Dissipation of energy in locally isotropic turbulence," *Dokl. Akad. Nauk SSSR* **32**, 16–18 (1941).
- A. N. Kolmogorov, "The local structure of turbulence in incompressible viscous fluid for very large Reynolds numbers," *Dokl. Akad. Nauk SSSR* **30**, 301–305 (1941).
- U. Frisch, *Turbulence: The Legacy of A. N. Kolmogorov* (Cambridge University Press, Cambridge, 1995).
- A. M. Obukhov, "Structure of the temperature field in a turbulent flow," *Isv. Geogr. Geophys. Ser.* **13**, 58–69 (1949).
- S. Corrsin, "On the spectrum of isotropic temperature fluctuations in an isotropic turbulence," *J. Appl. Phys.* **22**, 469–473 (1951).
- Z.-S. She and E. Leveque, "Universal scaling laws in fully developed turbulence," *Phys. Rev. Lett.* **72**, 336–339 (1994).
- R. Bolgiano, "Turbulent spectra in a stably stratified atmosphere," *J. Geophys. Res.* **64**, 2226–2229, <https://doi.org/10.1029/jz064i012p02226> (1959).
- A. M. Obukhov, "On influence of buoyancy forces on the structure of temperature field in a turbulent flow," *Dokl. Akad. Nauk SSSR* **125**, 1246 (1959).
- A. Kumar, A. G. Chatterjee, and M. K. Verma, "Energy spectrum of buoyancy-driven turbulence," *Phys. Rev. E* **90**, 023016 (2014).
- M. K. Verma, A. Kumar, and A. Pandey, "Phenomenology of buoyancy-driven turbulence: Recent results," *New J. Phys.* **19**, 025012 (2017).
- D. L. Rosenberg, A. G. Pouquet, R. Marino, and P. D. Mininni, "Evidence for Bolgiano-Obukhov scaling in rotating stratified turbulence using high-resolution direct numerical simulations," *Phys. Fluids* **27**, 055105 (2015).
- I. Procaccia and R. Zeitak, "Scaling exponents in nonisotropic convective turbulence," *Phys. Rev. Lett.* **62**, 2128–2131 (1989).
- V. S. L'vov, "Spectra of velocity and temperature-fluctuations with constant entropy flux of fully-developed free-convective turbulence," *Phys. Rev. Lett.* **67**, 687–690 (1991).
- V. S. L'vov and G. Falkovich, "Conservation laws and two-flux spectra of hydrodynamic convective turbulence," *Physica D* **57**, 85–95 (1992).
- R. Rubinstein, "Renormalization group theory of Bolgiano scaling in Boussinesq turbulence," Technical Report ICOM-94-8; CMOTT-94-2, 1994.
- R. Benzi, F. Massaioli, S. Succi, and R. Tripiccone, "Scaling behaviour of the velocity and temperature correlation functions in 3D convective turbulence," *Europhys. Lett.* **28**, 231–236 (1994).
- R. Benzi, R. Tripiccone, F. Massaioli, S. Succi, and S. Ciliberto, "On the scaling of the velocity and temperature structure functions in Rayleigh-Bénard convection," *Europhys. Lett.* **25**, 341–346 (1994).
- R. Benzi, S. Ciliberto, R. Tripiccone, C. Baudet, F. Massaioli, and S. Succi, "Extended self-similarity in turbulent flows," *Phys. Rev. E* **48**, R29–R32 (1993).
- S. Chakraborty, U. Frisch, and S. S. Ray, "Extended self-similarity works for the Burgers equation and why," *J. Fluid Mech.* **649**, 275–285 (2010).
- E. S. C. Ching, "Intermittency of temperature field in turbulent convection," *Phys. Rev. E* **61**, R33 (2000).
- F. Heslot, B. Castaing, and A. Libchaber, "Transitions to turbulence in helium gas," *Phys. Rev. A* **36**, 5870–5873 (1987).
- M. Sano, X.-Z. Wu, and A. Libchaber, "Turbulence in helium-gas free convection," *Phys. Rev. A* **40**, 6421–6430 (1989).
- R. Benzi, L. Biferale, S. Ciliberto, M. Struglia, and R. Tripiccone, "Generalized scaling in fully developed turbulence," *Physica D* **96**, 162–181 (1996).
- E. Calzavarini, F. Toschi, and R. Tripiccone, "Evidences of Bolgiano-Obukhov scaling in three-dimensional Rayleigh-Bénard convection," *Phys. Rev. E* **66**, 016304 (2002).
- C. Sun, Q. Zhou, and K.-Q. Xia, "Cascades of velocity and temperature fluctuations in buoyancy-driven thermal turbulence," *Phys. Rev. Lett.* **97**, 144504 (2006).
- E. S. C. Ching, Y.-K. Tsang, T. N. Fok, X. He, and P. Tong, "Scaling behavior in turbulent Rayleigh-Bénard convection revealed by conditional structure functions," *Phys. Rev. E* **87**, 013005 (2013).
- X. He and P. Tong, "Measurements of the thermal dissipation field in turbulent Rayleigh-Bénard convection," *Phys. Rev. E* **79**, 026306 (2009).
- B. Castaing, G. Gunaratne, L. P. Kadanoff, A. Libchaber, and F. Heslot, "Scaling of hard thermal turbulence in Rayleigh-Bénard convection," *J. Fluid Mech.* **204**, 1–30 (1989).
- X.-D. Shang, X.-L. Qiu, P. Tong, and K.-Q. Xia, "Measured local heat transport in turbulent Rayleigh-Bénard convection," *Phys. Rev. Lett.* **90**, 074501 (2003).
- E. S. C. Ching, "Scaling laws in the central region of confined turbulent thermal convection," *Phys. Rev. E* **75**, 056302 (2007).
- R. P. J. Kunnen, H. J. H. Clercx, B. J. Geurts, L. J. A. van Bokhoven, R. A. D. Akkermans, and R. Verzicco, "Numerical and experimental investigation of

- structure-function scaling in turbulent Rayleigh-Bénard convection,” *Phys. Rev. E* **77**, 016302 (2008).
- ³²E. S. C. Ching and W. C. Cheng, “Anomalous scaling and refined similarity of an active scalar in a shell model of homogeneous turbulent convection,” *Phys. Rev. E* **77**, 015303 (2008).
- ³³M. Kaczorowski and K.-Q. Xia, “Turbulent flow in the bulk of Rayleigh-Bénard convection: Small-scale properties in a cubic cell,” *J. Fluid Mech.* **722**, 596–617 (2013).
- ³⁴D. Lohse and K.-Q. Xia, “Small-scale properties of turbulent Rayleigh-Bénard convection,” *Annu. Rev. Fluid Mech.* **42**, 335–364 (2010).
- ³⁵T. Meuel, M. Coudert, P. Fischer, C. Bruneau, and H. Kellay, “Effects of rotation on temperature fluctuations in turbulent thermal convection on a hemisphere,” *Sci. Rep.* **8**, 16513 (2018).
- ³⁶A. Alexakis and L. Biferale, “Cascades and transitions in turbulent flows,” *Phys. Rep.* **767-769**, 1–101 (2018).
- ³⁷C. Bruneau, P. Fischer, Y.-L. Xiong, and H. Kellay, “Numerical simulations of thermal convection on a hemisphere,” *Phys. Rev. Fluids* **3**, 043502 (2018).
- ³⁸A. Shestakov, R. Stepanov, and P. Frick, “On cascade energy transfer in convective turbulence,” *J. Appl. Mech. Tech. Phys.* **58**, 1171 (2017).
- ³⁹S. S. Pawar and J. H. Arakeri, “Kinetic energy and scalar spectra in high Rayleigh number axially homogeneous buoyancy driven turbulence,” *Phys. Fluids* **28**, 065103 (2016).
- ⁴⁰J. K. Bhattacharjee, “Kolmogorov argument for the scaling of the energy spectrum in a stratified fluid,” *Phys. Lett. A* **379**, 696–699 (2015).
- ⁴¹J. Schumacher, P. Götzfried, and J. D. Scheel, “Enhanced enstrophy generation for turbulent convection in low-Prandtl-number fluids,” *Proc. Natl. Acad. Sci. U. S. A.* **112**, 9530 (2015).
- ⁴²K. Shrestha, G. Mompean, and E. Calzavarini, “Finite-volume versus streaming-based lattice Boltzmann algorithm for fluid-dynamics simulations: A one-to-one accuracy and performance study,” *Phys. Rev. E* **93**, 023306 (2016).
- ⁴³F. Rincon, T. Roudier, A. Schekochihin, and M. Rieutord, “Supergranulation and multiscale flows in the solar photosphere,” *Astron. Astrophys.* **599**, A69 (2017).
- ⁴⁴F. Rincon and M. Rieutord, “The Sun’s supergranulation,” *Living Rev. Sol. Phys.* **15**, 6 (2018).
- ⁴⁵S. Chandrasekhar, *Hydrodynamic and Hydromagnetic Stability* (Oxford University Press, Oxford, 2013).
- ⁴⁶F. Chillà and J. Schumacher, “New perspectives in turbulent Rayleigh-Bénard convection,” *Eur. Phys. J. E* **35**, 58 (2012).
- ⁴⁷M. K. Verma, *Physics of Buoyant Flows* (World Scientific, Singapore, 2018).
- ⁴⁸M. Lesieur, *Turbulence in Fluids* (Springer-Verlag, Dordrecht, 2008).
- ⁴⁹C. Canuto, M. Y. Hussaini, A. Quarteroni, and T. A. Zang, *Spectral Methods in Fluid Dynamics* (Springer-Verlag, Berlin, Heidelberg, 1988).
- ⁵⁰A. Pandey and M. K. Verma, “Scaling of large-scale quantities in Rayleigh-Bénard convection,” *Phys. Fluids* **28**, 095105 (2016).
- ⁵¹A. Pandey, A. Kumar, A. G. Chatterjee, and M. K. Verma, “Dynamics of large-scale quantities in Rayleigh-Bénard convection,” *Phys. Rev. E* **94**, 053106 (2016).
- ⁵²D. Nath, A. Pandey, A. Kumar, and M. K. Verma, “Near isotropic behavior of turbulent thermal convection,” *Phys. Rev. Fluids* **1**, 064302 (2016).
- ⁵³Q. Zhou, C. Sun, and K.-Q. Xia, “Experimental investigation of homogeneity, isotropy, and circulation of the velocity field in buoyancy-driven turbulence,” *J. Fluid Mech.* **598**, 361–372 (2008).
- ⁵⁴R. P. J. Kunnen and H. J. H. Clercx, “Probing the energy cascade of convective turbulence,” *Phys. Rev. E* **90**, 063018 (2014).
- ⁵⁵M. K. Verma, A. G. Chatterjee, R. K. Yadav, S. Paul, M. Chandra, and R. Samtaney, “Benchmarking and scaling studies of pseudospectral code Tarang for turbulence simulations,” *Pramana* **81**, 617–629 (2013).
- ⁵⁶A. G. Chatterjee, M. K. Verma, A. Kumar, R. Samtaney, B. Hadri, and R. Khurram, “Scaling of a fast Fourier transform and a pseudo-spectral fluid solver up to 196608 cores,” *J. Parallel Distrib. Comput.* **113**, 77–91 (2018).
- ⁵⁷A. Kumar and M. K. Verma, “Applicability of Taylor’s hypothesis in thermally driven turbulence,” *R. Soc. Open Sci.* **5**, 172152 (2018).
- ⁵⁸H. Jasak, A. Jemcov, Z. Tukovic *et al.*, “OpenFOAM: A C++ library for complex physics simulations,” in *International Workshop on Coupled Methods in Numerical Dynamics* (IUC, Dubrovnik, Croatia, 2007), Vol. 1000, pp. 1–20.
- ⁵⁹S. Bhattacharya, A. Pandey, A. Kumar, and M. K. Verma, “Complexity of viscous dissipation in turbulent thermal convection,” *Phys. Fluids* **30**, 031702 (2018).
- ⁶⁰S. Bhattacharya, R. Samtaney, and M. K. Verma, “Scaling and spatial intermittency of thermal dissipation in turbulent convection,” *Phys. Fluids* **31**, 075104 (2019).
- ⁶¹P. S. Pacheco, *An Introduction to Parallel Programming* (Morgan Kaufmann, Burlington, 2011).
- ⁶²S. B. Pope, *Turbulent Flows* (Cambridge University Press, Cambridge, 2000).
- ⁶³P. Kailasnath, K. R. Sreenivasan, and G. Stolovitzky, “Probability density of velocity increments in turbulent flows,” *Phys. Rev. Lett.* **68**, 2766–2769 (1992).
- ⁶⁴D. A. Donzis, P. K. Yeung, and K. R. Sreenivasan, “Dissipation and enstrophy in isotropic turbulence: Resolution effects and scaling in direct numerical simulations,” *Phys. Fluids* **20**, 045108 (2008).
- ⁶⁵A. Pandey, M. K. Verma, A. G. Chatterjee, and B. Dutta, “Similarities between 2D and 3D convection for large Prandtl number,” *Pramana* **87**, 13 (2016).

Chapter 4

Behavioural changes in turbulent RBC with Prandtl number

4.1 Introduction

In Chapter 3, we analyzed the structure functions of RBC for $Pr = 1$ and showed that they scale similar to those of homogeneous and isotropic turbulence. Our results thus reinforced the arguments of [Kumar et al. \(2014\)](#) and [Verma et al. \(2017\)](#) who showed Kolmogorov-like scaling of the energy spectrum of RBC. We also showed that for RBC, the inertial range kinetic energy flux is less than the viscous dissipation rate due to multiscale kinetic energy injection due to buoyancy. Note, however, that large- Pr RBC exhibits much steeper power-laws [$E_u(k) \sim k^{-13/3}$] as shown by [Pandey et al. \(2014\)](#).

So far, the analysis of the structure functions and the spectral quantities of RBC have been conducted for fixed sets of governing parameters. These studies do not provide us with a comprehensive understanding of the variations of the above small-scale statistics with Ra or Pr . In this chapter, we study the Pr dependence of the spectra and fluxes of kinetic energy and entropy and the velocity structure functions. We also study, for the first time, the variations of the local heat fluxes with Pr . The results of this work have been published in *Physical Review Fluids* ([Bhattacharya et al., 2021a](#)).

The outline of the chapter is as follows. We discuss the simulation details in Sec. 4.2. In Sec. 4.3, we obtain the Pr dependence on the spectral quantities using our

TABLE 4.1: Details of our data obtained direct numerical simulations of RBC performed in a cubical box for $Ra = 10^7$: the Prandtl number (Pr), the grid size, the ratio of the Kolmogorov length scale (for $Pr \leq 1$) or the Batchelor length scale (for $Pr > 1$) to the mesh width ($\eta/\Delta x$), the number of grid points in viscous and thermal boundary layers (N_{VBL} and N_{TBL} respectively), the Nusselt number (Nu), the Nusselt number computed using the viscous dissipation rate (Nu_u), the Nusselt number computed using the thermal dissipation rate (Nu_T), the number of non-dimensional time units (t_{ND}), and snapshots over which the quantities are averaged.

Pr	Grid size	$\eta/\Delta x$	N_{VBL}	N_{TBL}	Nu	Nu_u	Nu_T	t_{ND}	Snapshots
0.02	1025^3	1.45	7	48	10.3	11.0	10.8	3	31
0.1	513^3	1.52	6	20	13.9	14.0	13.9	33	66
1	257^3	2.31	5	9	16.3	16.3	16.4	101	101
6.8	257^3	2.33	6	9	15.9	15.8	16.0	101	101
100	257^3	2.30	7	9	16.8	16.7	16.6	101	101

simulation data. In Sec. 4.4, we discuss the scaling of velocity structure functions for different Pr. In Sec. 4.5, we study the probability distribution of the convective heat flux. We summarize our results in Sec. 4.6.

4.2 Details of our numerical simulations

We numerically solve Eqs. (1.11)-(1.13) for Pr from 0.02 to 100 for a fixed Rayleigh number of $Ra = 10^7$ to study Pr dependence of turbulent thermal convection. The simulations were performed on a cubical domain of unit dimension using the finite difference solver SARAS (Verma et al., 2020; Samuel et al., 2020). No-slip boundary conditions were imposed on all the walls, adiabatic boundary conditions on the sidewalls, and isothermal boundary conditions on the top and bottom walls. The maximum time for simulations ranges from 3 to 101 free-fall time (t_{ND}) after attaining a steady state. For discretization and time-marching schemes, refer to Chapter 2.

The grid resolutions were varied from 257^3 for $Pr = 100$ to 1025^3 for $Pr = 0.02$. The above grid resolutions ensure that the grid-spacing Δx is smaller than the Kolmogorov length scale $\eta = (\nu^3 \epsilon_u^{-1})^{1/4}$ for $Pr \leq 1$ and the Batchelor length scale $\eta_\theta = (\nu \kappa^2 \epsilon_u^{-1})^{1/4}$ for $Pr > 1$, indicating that the smallest scales of the simulations are adequately resolved. Further, we have a minimum of 7 points in the viscous and thermal

boundary layers, satisfying the resolution criterion of Grötzbach (1983) and Verzicco and Camussi (2003). We validate our simulations by computing the Nusselt number [see Chapter 2, Eq. (2.22)] for all our runs and ensuring that they are consistent with earlier results (Pandey et al., 2016a; Pandey and Verma, 2016; Scheel and Schumacher, 2017; Vishnu and Sameen, 2020). To verify whether the simulations are well resolved, we compute the Nusselt number using the total viscous and thermal dissipation rates by employing the exact relations of Shraiman and Siggia (1990) [Eqs. (1.22) and (1.23)]. The Nusselt numbers computed using the dissipation rates match closely with that computed using $\langle u_z T \rangle$. The simulation details are summarized in Table 4.1.

We use the pseudo-spectral code TARANG (Verma et al., 2013; Chatterjee et al., 2018) to compute the spectra and fluxes of kinetic energy and entropy and the parallel code fastSF (Sadhukhan et al., 2021) to compute the velocity structure functions. The readers are referred to Chapter 2 for details of the computation procedure.

In the next three sections, we present our numerical results.

4.3 Variation of spectral quantities with Prandtl number

In this section, we analyse the Pr dependence of the kinetic energy spectra, kinetic energy fluxes, energy injection rates, and dissipation rates using our numerical data.

4.3.1 Kinetic energy spectra and fluxes

We compute the kinetic energy spectrum ($E_u(k)$) and flux ($\Pi_u(k)$) for all our runs using Eqs. (1.28,1.30). Note that energy spectrum exhibits fluctuations at small and intermediate wavenumbers that produce large errors in the best-fit curves (Stepanov et al., 2014). To mitigate these errors, we employ best-fit curves for the *integral energy spectrum*, which is $\int_k^\infty E_u(k') dk' = \sum_k^\infty E_u(k')$. The integration process smoothens the curves significantly leading to a major reduction in fitting errors.

For the inertial-range spectral form of $E_u(k) \sim k^\alpha$, the integral $\sum_k^\infty E_u(k') \sim k^{\alpha+1}$, thus, the fit functions to the integral energy spectrum provides us the spectral index α . We plot $\sum_k^\infty E_u(k')$ and $\Pi_u(k)$ versus k in Fig. 4.1(a,b). The figure shows that For $\text{Pr} \leq 1$, $\sum_k^\infty E_u(k')$ scales as $k^{-2/3}$ for intermediate wavenumbers, which translates to

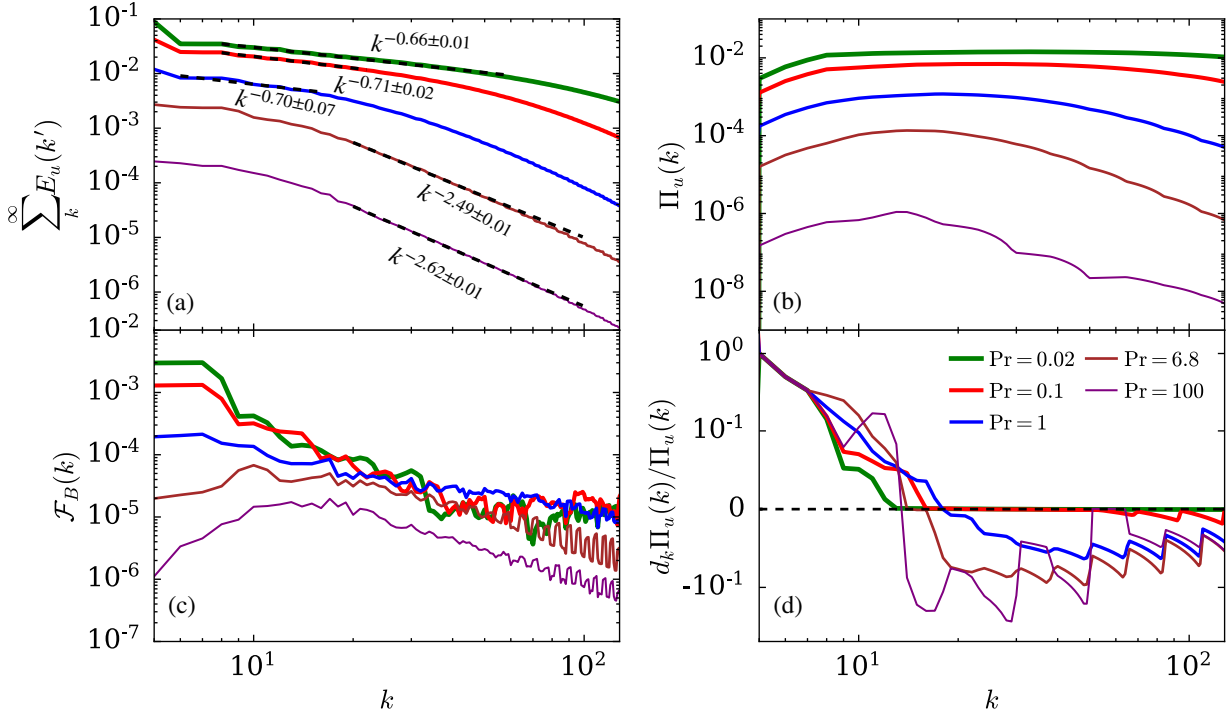


FIGURE 4.1: For $Ra = 10^7$ and $Pr = 0.02, 0.1, 1, 6.8,$ and 100 : (a) Integral kinetic energy spectrum, $\sum_k^\infty E_u(k')$ vs. wavenumber k , (b) kinetic energy flux, $\Pi_u(k)$, vs. k , (c) energy injection rate due to buoyancy, $\mathcal{F}_B(k)$, vs. k , and (d) $d_k \Pi_u(k) / \Pi_u(k)$ vs. k . The amplitudes of the energy spectrum and flux decrease with Pr . For $Pr \leq 1$, the energy spectrum exhibits Kolmogorov's scaling.

Kolmogorov's energy spectrum ($E_u(k) \sim k^{-5/3}$). The errors in the exponents obtained from the best fits range from 0.01 to 0.07. Further, consistent with the observed Kolmogorov's energy spectrum, $\Pi_u(k)$ is approximately constant over these wavenumbers. Our results, which are based on convection with no-slip walls, are consistent with earlier works on small and moderate Pr convection but with free-slip walls (Mishra and Verma, 2010; Kumar et al., 2014; Verma et al., 2017). These observations rule out Bolgiano-Obukhov scaling ($E_u(k) \sim k^{-11/5}$) for thermal convection. Earlier, based on positive kinetic-energy injection rate by buoyancy, Kumar et al. (2014) and Verma et al. (2017) had argued in favour of Kolmogorov's spectrum for turbulent convection.

For $Pr = 6.8$ and 100 , the kinetic energy flux $\Pi_u(k)$ decreases sharply with k in the inertial range. Thus, instead of Kolmogorov's spectrum, we obtain a much steeper energy spectrum: $\sum_k^\infty E_u(k') \sim k^{-2.49}$ for $Pr = 6.8$ and $\sim k^{-2.62}$ for $Pr = 100$, with an error of ± 0.01 in the exponents. These relations translate to $E_u(k) \sim k^{-3.49}$ for $Pr = 6.8$ and $\sim k^{-3.62}$ for $Pr = 100$. For $Pr \rightarrow \infty$, Pandey et al. (2014) derived that

$E_u(k) \sim k^{-13/3}$. Note that the energy spectra for $\text{Pr} = 6.8$ and 100 are quite close to the energy spectrum for $\text{Pr} \rightarrow \infty$, consistent with the earlier results on energy spectra and fluxes (Pandey et al., 2014, 2016b; Verma, 2018).

Now, we explore the Pr dependence of the amplitudes of the kinetic energy spectra and fluxes. Figure 4.1(a,b) shows that for the same Ra , convection with small Pr has more kinetic energy than that with large Pr . This is because the nonlinear interactions among the velocity modes for small- Pr convection are stronger than those for large- Pr convection. Further, for $\text{Pr} \leq 1$, the width of the wavenumbers' range over which Kolmogorov's scaling is observed decreases with the increase of Pr : $8 \leq k \leq 60$ for $\text{Pr} = 0.02$ and $6 \leq k \leq 17$ for $\text{Pr} = 1$. Note, however, that for large Prandtl numbers, power law regimes are observed at much larger wavenumbers.

Having analyzed the energy spectra and fluxes, we now examine the variations of the kinetic energy injection rates $\mathcal{F}_B(k)$ with Pr . We plot $\mathcal{F}_B(k)$ versus k for different Prandtl numbers in Fig. 4.1(c). These plots reveal that $\mathcal{F}_B(k)$ is positive for all Pr , implying that buoyancy feeds kinetic energy to the system. This observation is in agreement with the findings of Kumar et al. (2014) and Verma et al. (2017) for $\text{Pr} = 1$ and contradicts the earlier arguments favoring BO scaling in RBC (see, for example, Procaccia and Zeitak, 1989; L'vov, 1991; L'vov and Falkovich, 1992; Rubinstein, 1994; Ashkenazi and Steinberg, 1999b; Shang and Xia, 2001).

Figure 4.1(c) also shows that the kinetic energy injection is the strongest for $\text{Pr} = 0.02$ and becomes weaker as Pr increases, similar to the energy spectrum and flux. Further, for small Prandtl numbers, $\mathcal{F}_B(k)$ drops sharply with k compared to larger Prandtl numbers. This is because, in the limit of $\text{Pr} \rightarrow 0$, $\mathcal{F}_B(k)$ scales as $\text{Ra} \langle |u_z(k)|^2 \rangle / k^2$, which shows that $\mathcal{F}_B(k)$ decreases steeply with k (Mishra and Verma, 2010; Verma, 2018). Thus, for small and moderate Prandtl numbers, $\mathcal{F}_B(k)$ is small in the inertial range compared to the energy flux and cannot bring significant variations in $\Pi_u(k)$ in that regime. This results in Kolmogorov-like scaling of the kinetic energy spectrum for small and moderate- Pr convection, consistent with the arguments of earlier studies (Mishra and Verma, 2010; Kumar et al., 2014; Verma et al., 2017; Verma, 2019a).

In Fig. 4.1(d), we plot the normalized derivative of the kinetic energy flux, $d_k \Pi_u / \Pi_u(k)$, versus k for different Pr (d_k denotes the derivative with respect to k). Recall from Eq. (1.33) that $d_k \Pi_u(k) = \mathcal{F}_B(k) - D(k)$. Since energy is dissipated at small scales, $D(k)$ becomes stronger than $\mathcal{F}_B(k)$ at large wavenumbers, causing the kinetic energy flux to

be a decreasing function of k . As evident in Fig. 4.1(d), the crossover wavenumber at which the derivative of the flux changes sign decreases with increasing Pr: $k = 33$ for $\text{Pr} = 0.02$ and $k = 14$ for $\text{Pr} = 100$. This is expected; since Ra is constant in all the runs, the flow is more viscous for larger Pr. Hence, $D(k)$ is strong even at intermediate scales (Pandey et al., 2014). For $\text{Pr} = 6.8$ and 100, $D(k)$ exceeds $\mathcal{F}_B(k)$ by a significant amount at intermediate scales, resulting in $d_k \Pi_u(k) / \Pi_u(k) \lesssim -0.1$. Thus, $\Pi_u(k)$ decreases sharply with k for these Prandtl numbers in the intermediate scales, leading to a steeper energy spectrum compared to $k^{-5/3}$, consistent with the findings of Pandey et al. (2014, 2016b).

These results provide a comprehensive picture for the variations of kinetic energy spectra and fluxes of thermal convection with Pr. In the next subsection, we discuss how the strength of the nonlinear interactions in RBC vary with Pr.

4.3.2 Energy flux and viscous dissipation in thermal convection

In 3D hydrodynamic turbulence, the kinetic energy flux in the inertial range matches with the total dissipation rate. This is not the case in turbulent thermal convection because buoyancy feeds energy at all scales, including the dissipation range. Consequently, $\Pi_u < \epsilon_u$. In Chapter 3, we showed that for $\text{Pr} = 1$, the inertial-range kinetic energy flux is approximately one-third of the total dissipation rate. In this subsection, we will describe these quantities for various Prandtl numbers.

We numerically compute $\sum_k^\infty \mathcal{F}_B(k')$ for various Prandtl numbers using our data and plot them versus k in Fig. 4.2(a). In the same figure, we also plot ϵ_u for comparison. In Fig. 4.2(b), we plot the total viscous dissipation along with the maximum inertial range kinetic energy flux versus Pr. The figures show that the amplitudes of $\sum_k^\infty \mathcal{F}_B(k')$, as well as ϵ_u , decrease with the increase of Pr, consistent with the fact that the nonlinear interactions among the velocity modes decrease with increasing Pr. Our data shows that the total viscous dissipation rate decreases as $\text{Pr}^{-0.37}$ for $\text{Pr} < 1$, and as $\text{Pr}^{-0.51}$ for $\text{Pr} \geq 1$.

Further, for $\text{Pr} = 0.02$ and 0.1, $\sum_k^\infty \mathcal{F}_B(k')$ decreases steeply with k at small wavenumbers and becomes a few orders of magnitude less than ϵ_u in the intermediate scales, thus indicating that most of the energy is injected at large scales. As a result, the kinetic energy flux in the inertial range almost equals the total dissipation rate, similar

4.3 Variation of spectral quantities with Prandtl number

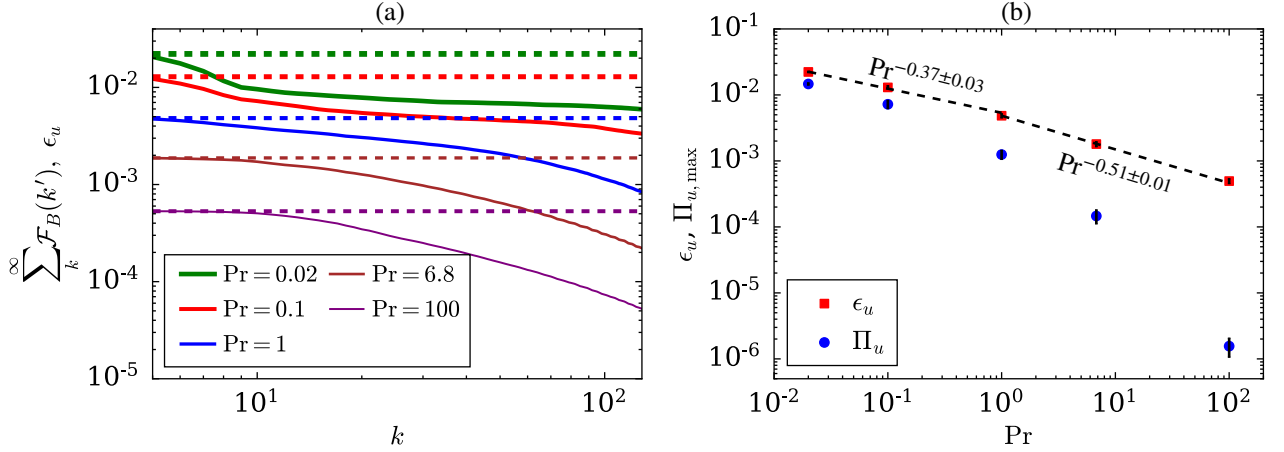


FIGURE 4.2: (a) For $Ra = 10^7$ and $Pr = 0.02$ (green), 0.1 (red), 1 (black), 6.8 (brown), and 100 (purple): Plots of the cumulative kinetic energy injection by buoyancy $\sum_k \mathcal{F}_B(k')$ (solid curves) and the viscous dissipation rate ϵ_u (dashed curves) vs. k . (b) Plots of ϵ_u and maximum kinetic energy flux $\Pi_{u,\max}$ vs. k . The cumulative energy injection and dissipation rates decrease with the increase of Pr , similar to the energy spectrum and flux. The difference between the kinetic energy flux and the dissipation rate increases as Pr is increased.

to 3D hydrodynamic turbulence. As Pr is increased, the decrease of $\sum_k \mathcal{F}_B(k')$ with k becomes progressively less sharp. Hence, for larger Prandtl numbers, only a small fraction of the total energy is injected at large scales, and significant amount of kinetic energy is injected in the inertial and dissipation ranges. Therefore, the inertial-range flux is much less than ϵ_u . For example, for $Pr = 100$, the inertial-range kinetic energy flux is about three orders of magnitude smaller than the dissipation rate. Figure 4.2(b) clearly contrasts the inertial-range kinetic energy flux and ϵ_u for large Prandtl numbers.

Now, we compare the scaling of ϵ_u in RBC and homogeneous isotropic turbulence. As mentioned in Sec. 1.6, ϵ_u for the latter scales as

$$\epsilon_u \approx U^3/d,$$

where U is the large scale velocity (for example, the root mean square velocity), and d is the size of the domain. However, Pandey and Verma (2016) and Pandey et al. (2016a) showed that in thermal convection for $Pr = 1$,

$$\epsilon_u \sim (U^3/d)Ra^{-0.2},$$

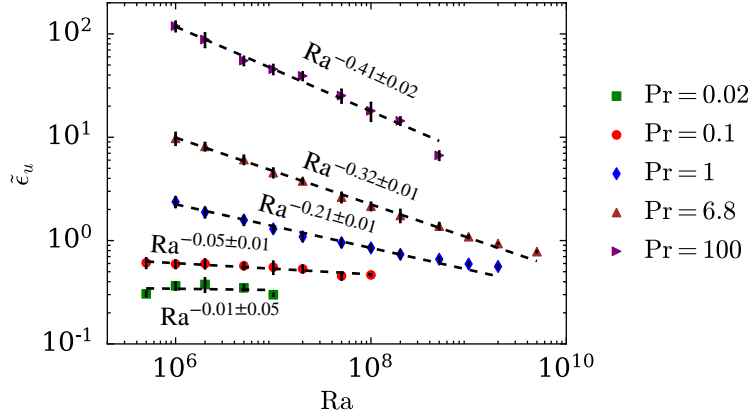


FIGURE 4.3: For $\text{Pr} = 0.02, 0.1, 1, 6.8$, and 100 , plots of $\tilde{\epsilon}_u = \epsilon_u / (U^3/d)$ vs. Ra . For small Pr , $\epsilon_u \sim U^3/d$ as in hydrodynamic turbulence. However, ϵ_u has an additional Ra dependence for larger Prandtl numbers.

instead of U^3/d . The additional Ra dependence was attributed to multiscale forcing by buoyancy and to the suppression of nonlinear interactions due to the presence of walls. Motivated by these observations, we investigate the scaling of viscous dissipation rate for various Prandtl numbers. Towards this objective, we use additional datasets that include simulations for Ra ranging from 5×10^5 to 2×10^9 and Pr ranging from 0.02 to 100 . We compute $\tilde{\epsilon}_u = \epsilon_u / (U^3/d)$ for all the data points and plot them versus Ra in Fig. 4.3. We also plot the best-fit curves for our data on the same figure.

Figure 4.3 shows that for $\text{Pr} = 0.02$, $\tilde{\epsilon}_u$ is constant as in hydrodynamic turbulence. However, for larger Pr , ϵ_u decreases with Ra with slopes getting steeper with the increase of Pr . For $\text{Pr} = 100$, $\tilde{\epsilon}_u$ decreases sharply as $\text{Ra}^{-0.41}$. The strong Ra dependence for large Pr is due to strong viscous dissipation in such flows.

4.3.3 Entropy spectra and fluxes

In this section, we compute the nondimensionalized entropy spectra, $E_\theta(k)$, and entropy fluxes, $\Pi_\theta(k)$, of RBC using our data for different Pr , with $\text{Ra} = 10^7$. We plot the entropy spectra and fluxes for $\text{Pr} = 1, 6.8$, and 100 in Fig. 4.4(a,b), and for $\text{Pr} = 0.02$ and 0.1 in Fig. 4.5(a,b). The figures show that the nondimensional entropy is approximately the same for all Prandtl numbers, unlike the kinetic energy spectrum that decreases with the increase of Pr . The entropy flux, however, decreases with the increase of Pr because the entropy flux is proportional to the velocity fluctuations (see Eq. (1.36)),

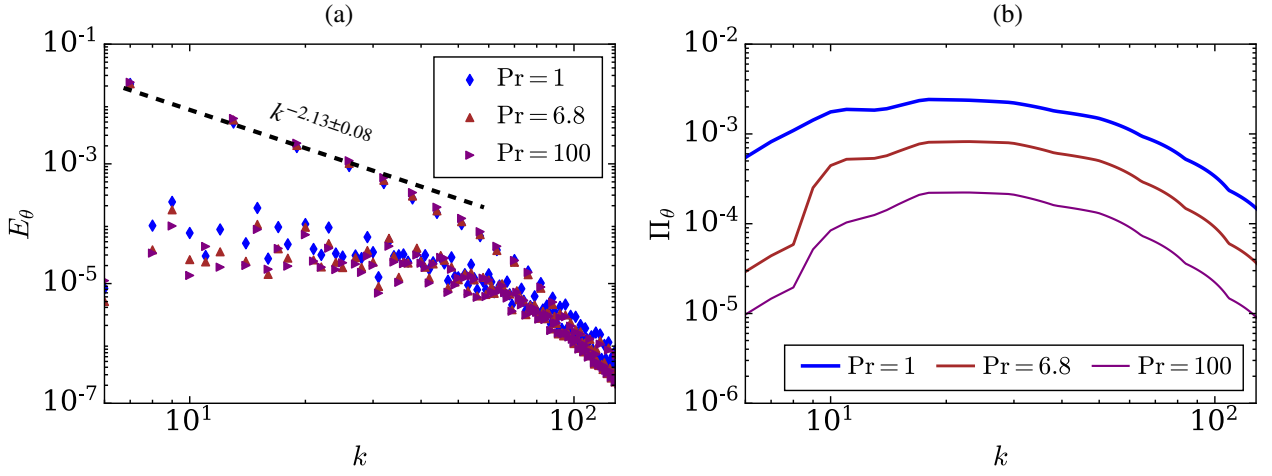


FIGURE 4.4: For $Ra = 10^7$ and $Pr = 1, 6.8,$ and 100 : (a) Entropy spectrum E_θ (with dual branches) and (b) entropy flux Π_θ vs. k . The amplitudes of the entropy spectrum do not vary with Pr , but the amplitudes of the entropy flux decrease with increase of Pr .

which are strong for flows with small Pr . The entropy spectrum exhibits dual branch for $Pr = 1, 6.8,$ and 100 , with the upper branch scaling as $\sim k^{-2.13 \pm 0.08}$. [Mishra and Verma \(2010\)](#) and [Pandey et al. \(2014\)](#) explained this branch in terms of the temperature modes $\theta(0, 0, 2n)$, which are approximately equal to $-1/(2n\pi)$ for thin thermal boundary layers (n being an integer). The lower branch, which is constituted by the remaining modes, does not exhibit any clear scaling. The temperature modes of both the branches yield the constant entropy flux (see Fig. 4.4(b)).

For $Pr = 0.02$ and 0.1 , the entropy spectrum again has two branches; however, the upper branch is not very prominent because of thick thermal boundary layers. For small- Pr convection, the nonlinear term of the θ -equation [Eq. (1.7)] is small compared to the diffusive term, similar to the momentum equation for laminar flows. Following the arguments of [Martínez et al. \(1997\)](#) and [Verma et al. \(2018\)](#) for energy spectrum of laminar flows, we propose that the entropy spectrum for small- Pr convection is of the following exponential form:

$$E_\theta(k) \sim k^{-1}(k/k_c) \exp(-k/k_c), \quad (4.1)$$

where k_c is the wavenumber beyond which the thermal energy dissipation becomes dominant.

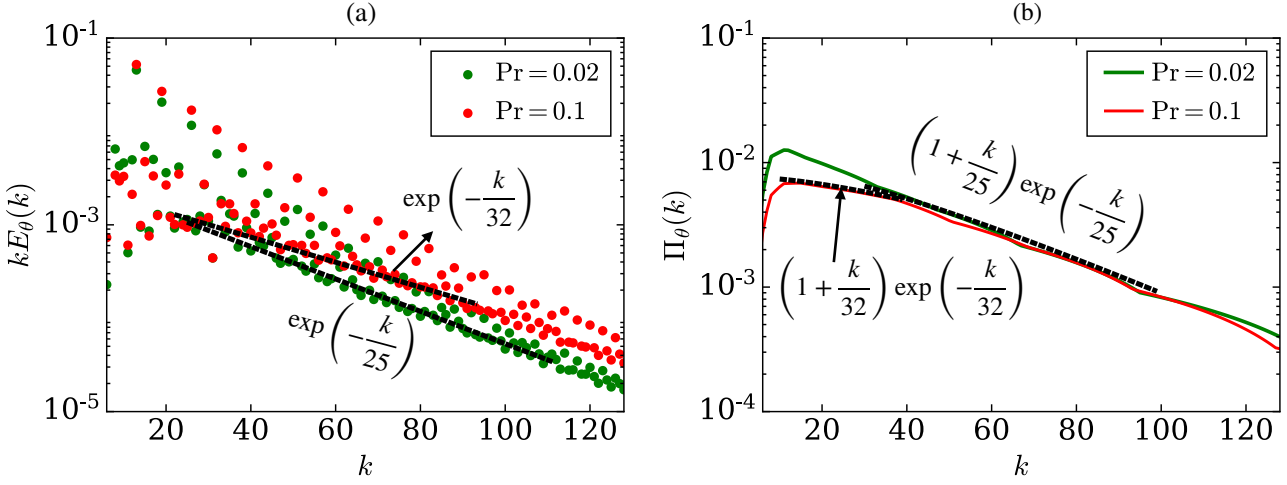


FIGURE 4.5: For $Ra = 10^7$ and $Pr = 0.02$ and 0.1 : Semi-log plots of (a) normalized entropy spectrum kE_θ and (b) entropy flux Π_θ vs. k . The lower branch of the entropy spectrum and the entropy flux fit well with exponential function. The magnitudes of both the entropy spectra and the fluxes do not vary significantly with Pr for this regime.

Now, for a steady state, the entropy flux is related to entropy injection (\mathcal{F}_θ) and dissipation spectra ($2\kappa k^2 E_\theta$) by the variable entropy flux equation:

$$\frac{d\Pi_\theta}{dk} = \mathcal{F}_\theta(k) - 2\kappa k^2 E_\theta(k), \quad (4.2)$$

In the intermediate wavenumbers for small- Pr convection, the spectrum of entropy dissipation dominates that of the entropy injection rate; hence $2\kappa k^2 E_\theta(k) \gg \mathcal{F}_\theta(k)$. Using this condition and substituting the expression of Eq. (4.1) in Eq. (4.2), we obtain the following:

$$\frac{d\Pi_\theta}{dk} \sim k \exp(-k/k_c). \quad (4.3)$$

Integration of the above expression yields the following expression for the entropy flux:

$$\Pi_\theta(k) \sim (1 + k/k_c) \exp(-k/k_c). \quad (4.4)$$

Our above arguments closely resemble the derivation of the energy flux for small- Re flows (see [Verma et al., 2018](#)), and for quasi-static magnetohydrodynamic turbulence with strong interaction parameters (see [Verma and Reddy, 2015](#)).

Figure 4.5(a) shows that the lower branch of the entropy spectrum fits well with

Eq. (4.1) in the intermediate wavenumbers, with $k_c = 32$ for $\text{Pr} = 0.1$ and $k_c = 25$ for $\text{Pr} = 0.02$. Further, as evident from Fig. 4.5(b), the entropy fluxes for $\text{Pr} = 0.1$ and 0.02 obey Eq. (4.4). Our results are consistent with earlier studies that also obtained similar exponential scalings in the entropy spectrum and flux of small- Pr convection (Mishra and Verma, 2010; Verma, 2018, 2019b).

In the next section, we discuss the Pr dependence on the velocity structure functions of turbulent convection.

4.4 Structure functions

In the following discussion we examine the scaling as well as the relative strengths of velocity structure functions for Pr ranging from 0.02 to 100.

We compute the second, third, fifth, and seventh-order velocity structure functions using our numerical data (see Eq. (1.24)). We plot the second-order velocity structure function $S_2^u(l)$ versus l in Fig. 4.6(a), and the negative of third, fifth, and seventh-order velocity structure functions $[-S_3^u(l), -S_5^u(l), -S_7^u(l)]$ versus l in Fig. 4.6 (b,c,d). We also plot the respective best-fit curves in the same figures. We observe that for $\text{Pr} \lesssim 1$, the third-order structure function exhibits Kolmogorov's scaling of $S_3^u(l) \sim -l$ over a range of intermediate scales that corresponds to the inertial range over which $E_u(k) \sim k^{-5/3}$ (as reported in Sec. 4.3.1). In addition, for the above Prandtl numbers, the structure functions of orders $q = 2, 5, \text{ and } 7$ follow the predictions of She and Leveque (1994) [see Figs. 4.6(a,c,d) and 4.7], as in hydrodynamic turbulence. The errors in the exponents range from ± 0.01 for the third-order structure functions to ± 0.05 for the seventh-order structure functions. Our results are thus consistent with those of Sun et al. (2006) but contrary to the studies that report Bolgiano-Obukhov scaling of the structure functions (see, for example, Benzi et al., 1994a,b; Ching, 2000; Calzavarini et al., 2002; Kunnen et al., 2008).

Figure 4.6(a,b,c,d) also shows that the amplitudes of the velocity structure functions for all orders increase with decreasing Pr , similar to the amplitudes of the kinetic energy spectrum and flux. This is expected because the structure functions are directly related to the kinetic energy spectrum and flux, which show similar scaling as discussed in Sec. 4.3 (Frisch, 1995; Lesieur, 2008; Ching, 2013).

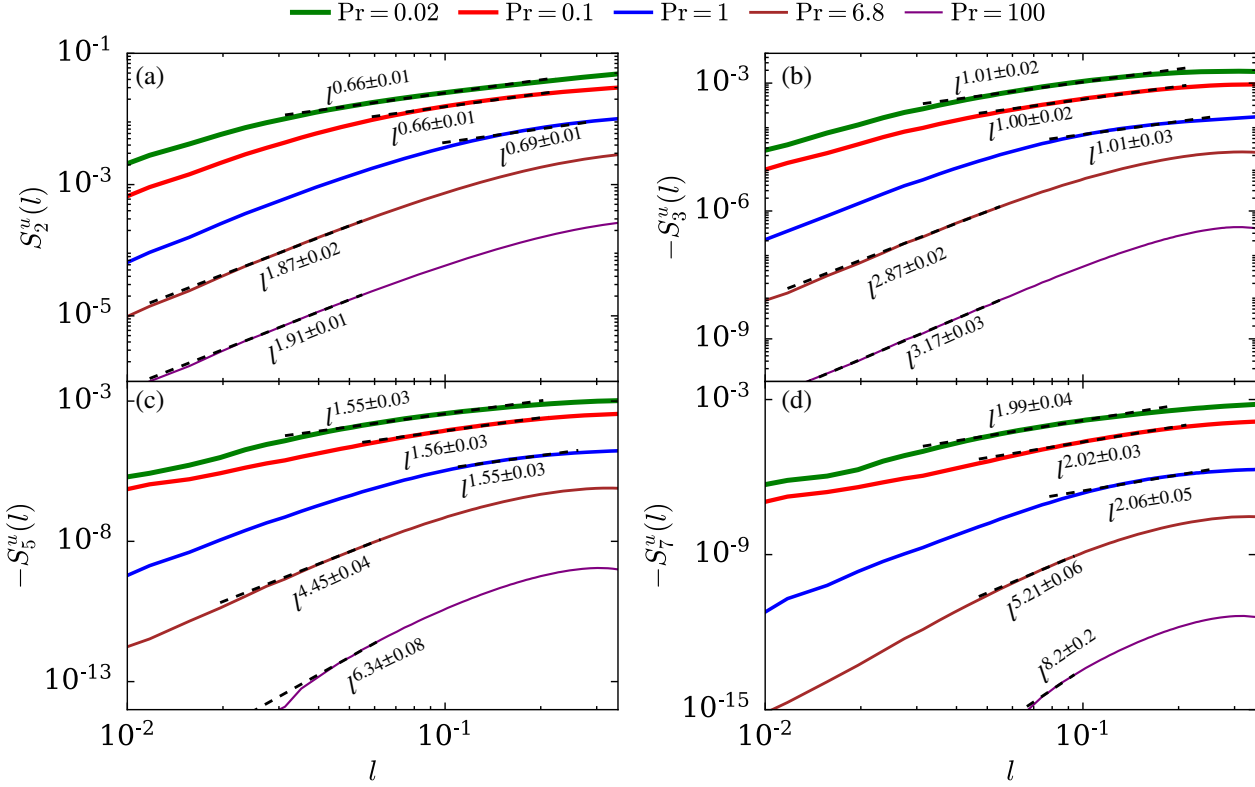


FIGURE 4.6: For $Pr = 0.02, 0.1, 1, 6.8,$ and 100 : longitudinal velocity structure functions of orders (a) 2, (b) 3, (c) 5, and (d) 7 vs. l . The amplitudes of the structure functions decrease with the increase of Pr .

The structure functions for $Pr = 6.8$ and 100 neither follow Kolmogorov's scaling nor She-Leveque's scaling; instead, they vary steeply at intermediate scales compared to those for $Pr \leq 1$ (see Fig. 4.6). For $Pr = 6.8$, the structure functions scale as $S_2^u(l) \sim l^{1.87}$, $S_3^u(l) \sim -l^{2.87}$, $S_5^u(l) \sim -l^{4.45}$, and $S_7^u(l) \sim -l^{5.21}$. For $Pr = 100$, the curves are even steeper, with the structure functions scaling as $S_2^u(l) \sim l^{1.91}$, $S_3^u(l) \sim -l^{3.47}$, $S_5^u(l) \sim -l^{6.34}$, and $S_7^u(l) \sim -l^{8.2}$. The errors in the above exponents range from ± 0.01 for $S_2^u(l)$ to ± 0.2 for $S_7^u(l)$. Recall that in the limit of infinite Pr , the energy spectrum scales as $E_u(k) \sim k^{-13/3}$ due to strong viscous dissipation in the intermediate scales. A simple extrapolation of the above to the second, third, fifth, and seventh-order structure functions lead to $S_2^u(l) \sim l^{10/3}$, $S_3^u(l) \sim -l^5$, $S_5^u(l) \sim -l^{25/3}$, and $S_7^u(l) \sim -l^{35/3}$ respectively [without intermittency effects (Frisch, 1995)]. The slopes of the structure functions computed using our data for $Pr = 6.8$ and 100 are not as steep as above predictions; this is possibly because the Prandtl numbers for our runs are finite and there are possible intermittency effects. Nevertheless, it is evident that the

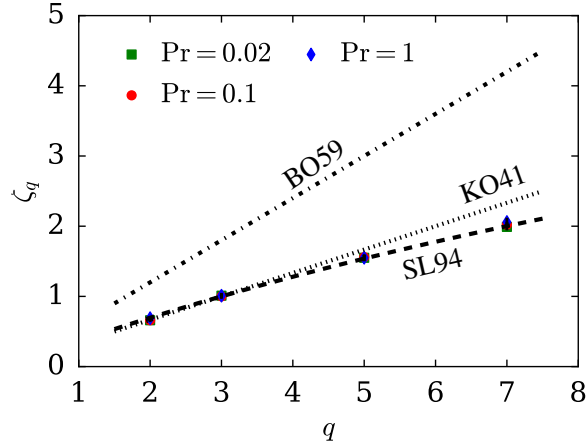


FIGURE 4.7: For $Pr = 0.02, 0.1,$ and 1 : The scaling exponents ζ_q for the velocity structure functions vs. order q . The exponents match closely with the predictions of She and Leveque (SL94). The figure also exhibits the extrapolated ζ_q 's for K41 ($q/3$) and Bolgiano-Obukhov (BO59) ($3q/5$).

slopes of the structure functions for larger Prandtl numbers are significantly steeper than those for smaller Prandtl numbers.

In the next section, we discuss the Prandtl number effects on the probability distribution functions of convective heat flux.

4.5 Prandtl number dependence of local heat flux

In RBC, the Nusselt number is always positive, but the local vertical heat flux, given by $u_z T$, exhibits strong fluctuations (Shang et al., 2003; Shishkina and Wagner, 2007; Kaczorowski and Xia, 2013; Pharasi et al., 2016). It has been observed that $u_z T$ take both positive and negative values, but the positive $u_z T$ dominates the negative ones leading to a net vertical heat flux. In this section, we present the variations of the probability distribution function (PDF) of $u_z T$ with the Prandtl number. In addition, we also study the horizontal heat fluxes, $u_x T$ and $u_y T$, which are expected to be symmetric so as to yield a zero net flux along the horizontal directions.

We compute the PDFs of the heat fluxes using our simulation data. The PDFs are averaged over 31 to 101 time frames depending on the Prandtl numbers (see Table 4.2). We plot the PDFs of the horizontal heat fluxes $u_x T$ and $u_y T$, normalized by

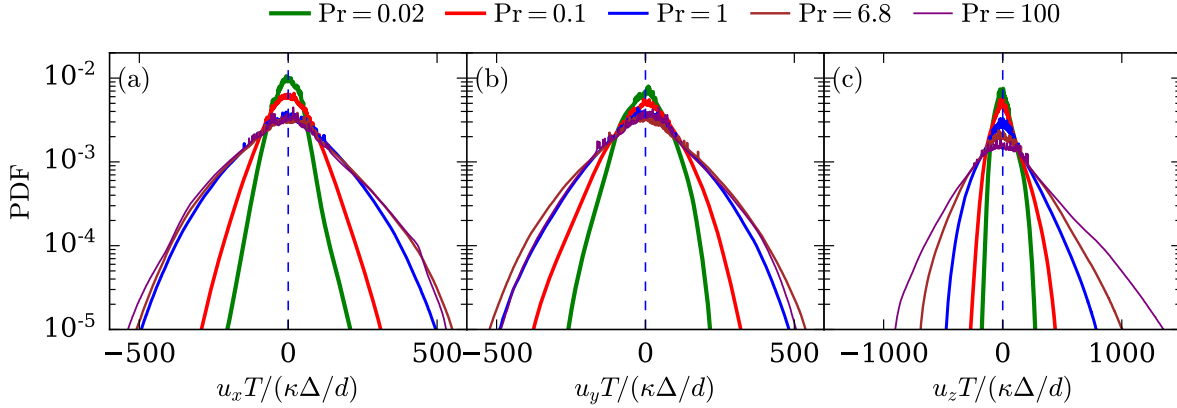


FIGURE 4.8: For $Ra = 10^7$: The probability distribution functions (PDFs) of normalized local convective heat flux in the (a) x direction, (b) y direction, and (c) z direction for different Pr . The fluctuations of the local heat flux increase with Pr .

TABLE 4.2: For $Pr = 0.02$ to 100 and $Ra = 10^7$: Standard deviations (σ_x , σ_y , and σ_z) of the local heat fluxes $u_x T$, $u_y T$, and $u_z T$ respectively, and the number of snapshots over which the PDFs of the above quantities are averaged. The standard deviations increase with Pr .

Pr	σ_x	σ_y	σ_z	Snapshots
0.02	35 ± 2	62 ± 1	66 ± 2	31
0.1	62 ± 5	87 ± 8	99 ± 7	87
1	125 ± 11	125 ± 11	173 ± 7	101
6.8	139 ± 16	138 ± 14	231 ± 13	101
100	140 ± 18	124 ± 16	296 ± 21	101

$\kappa\Delta/d$, in Fig. 4.8(a,b) respectively, and the vertical heat flux $u_z T$, normalized by $\kappa\Delta/d$, in Fig. 4.8(c). Note that $\kappa = (RaPr)^{-1/2}$ according to our nondimensionalization. For all Prandtl numbers, the horizontal and vertical heat fluxes peak at zero. However, the horizontal heat fluxes are symmetric about their peaks, but the vertical heat fluxes show clear asymmetry with long tails in the positive direction. The asymmetry in the vertical flux yields a net vertical heat transport, but the symmetric horizontal fluxes sum to zero, as expected. These results are consistent with earlier studies (Shang et al., 2003; Shishkina and Wagner, 2007; Kaczorowski and Xia, 2013; Pharasi et al., 2016). Both horizontal and vertical heat fluxes exhibit strong fluctuations near their most probable value of zero, causing noise-like ripples near the peaks of their PDFs.

A careful observation of the PDFs of Fig. 4.8 show an interesting feature: the fluc-

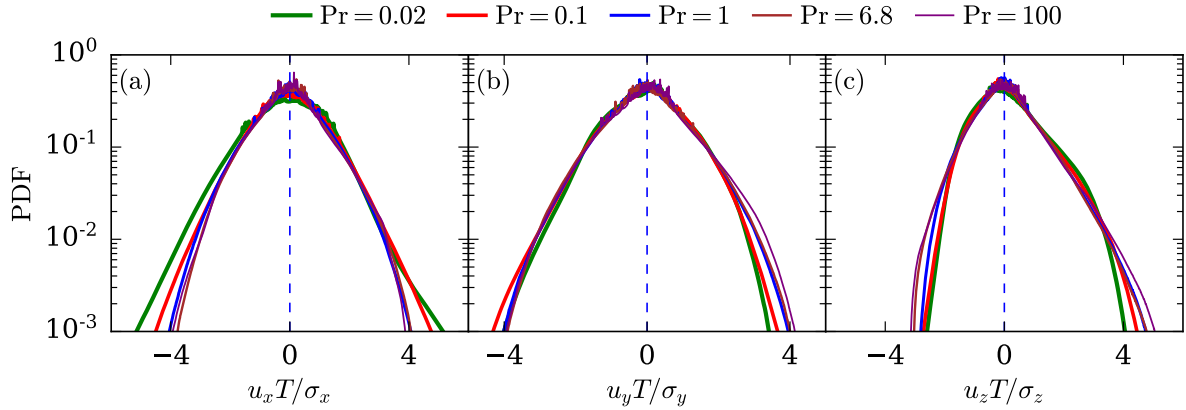


FIGURE 4.9: For $Ra = 10^7$: The probability distribution functions (PDFs) of the local convective heat flux normalized with their respective standard deviations (σ_x , σ_y , σ_z) in the (a) x direction, (b) y direction, and (c) z direction. The normalized PDFs for different Prandtl numbers collapse into one curve.

tuations in the local heat fluxes increase with the Prandtl numbers, which is evident from the long tails for $Pr \geq 1$. For small Prandtl numbers, thermal diffusion due to large κ and large thermal plumes is dominant. However, large-Pr convection takes place via thin thermal plumes that induces strong thermal fluctuations and inhomogeneity in the heat flux (Silano et al., 2010; Pandey et al., 2014, 2016b).

Interestingly, the PDFs of Fig. 4.8(a,b,c) can be collapsed into one curve each by normalizing the curves using the corresponding standard deviations. We present the collapsed curves in Fig. 4.9(a,b,c). The standard deviations are computed for every time frame and then averaged. The computed standard deviations for different Prandtl numbers are tabulated in Table 4.2. As expected, the standard deviations along with their respective errors increase with Prandtl number. There is, however, an anomaly in σ_y for $Pr = 100$ in that it is less than that for $Pr = 6.8$. However, we believe that this is a minor aberration that can be resolved by averaging over more time frames.

We conclude in the next section.

4.6 Summary and conclusions

In this paper, using detailed numerical simulations of turbulent convection, we analyzed the Prandtl number dependence of the kinetic energy spectrum, flux, and the spectra of buoyant energy injection and viscous dissipation rates. Additionally, we examined the variations of velocity structure functions and the local heat flux with Pr. For our analysis, we varied Pr from 0.02 to 100, keeping the Rayleigh number fixed at $Ra = 10^7$.

Consistent with earlier works, the kinetic energy spectrum exhibits Kolmogorov scaling of $\sim k^{-5/3}$ for $Pr \leq 1$ and a steeper scaling of $\sim k^{-2.5}$ for $Pr \geq 1$ (Mishra and Verma, 2010; Kumar et al., 2014; Pandey et al., 2014; Kumar and Verma, 2015; Pandey et al., 2016b; Verma et al., 2017; Kumar and Verma, 2018). The inertial range is widest for $Pr = 0.02$, and it gets narrower as Pr is increased. The magnitudes of the kinetic energy spectrum and flux decrease with Pr, implying that flows with small Prandtl number have stronger nonlinear interactions among the velocity modes. The amplitudes of kinetic energy injection and dissipation rates follow a similar pattern as energy flux and spectrum. For $Pr \ll 1$, kinetic energy injection by buoyancy occurs mostly at large scales, causing the kinetic energy flux in the inertial range to be approximately equal to the viscous dissipation rate, similar to hydrodynamic turbulence. On the other hand, for $Pr \gg 1$, significant kinetic energy is injected at small scales as well, causing the energy flux to be a small fraction of the viscous dissipation rate.

We showed that although the entropy does not change significantly with Pr, the entropy flux increases with Pr. The entropy spectrum exhibits dual branches with the upper branch scaling as k^{-2} , consistent with earlier works (Mishra and Verma, 2010; Pandey et al., 2014; Kumar et al., 2014). The entropy flux and the lower branch of the entropy spectrum follow an exponential curve for $Pr \ll 1$.

The amplitudes of the velocity structure functions increase with the decrease of Pr, consistent with the results on energy spectrum. The velocity structure functions for $Pr \leq 1$ were shown to be in agreement with She-Leveque's model, similar to hydrodynamic turbulence and consistent with earlier results (Sun et al., 2006). The structure functions exhibit steeper curves for $Pr = 6.8$ and 100 and are in agreement with the scaling of the energy spectrum for large Prandtl numbers.

The strength of fluctuations of the local convective heat flux increases with Pr.

This is because the thick thermal plumes for small-Pr flows transfer heat efficiently throughout the flow, but thin thermal plumes for large-Pr flows create strong inhomogeneity in the heat flux.

Thus, our present study provides valuable insights into the variations of turbulent velocity and thermal fluctuations with Pr. Although we worked on a small set of parameters, we expect these patterns to be valid over a wide range of Ra and Pr, with the possible exception of the ultimate regime ([Kraichnan, 1962](#)).

In the next chapter, we present our results on scaling and spatial intermittency of viscous dissipation in turbulent convection.

Chapter 5

Scaling and spatial distribution of viscous dissipation

5.1 Introduction

In Rayleigh Bénard convection, the buoyancy, walls, and their associated boundary layers modify the scaling of the viscous dissipation rate compared to homogeneous isotropic turbulence. This issue has been introduced in Chapter 1, Sec. 1.6. To better understand the effect of walls, it is important to analyze and quantify the scaling of viscous dissipation rate in the boundary layers and in the bulk of RBC. Although there has been some work on the bulk and boundary layer dissipation rates before, these studies either did not consider the entire bulk volume for their analysis or took the boundary layer thicknesses to be constant for all Ra and Pr , which could have affected the accuracy of the results (see Chapter 1, Sec. 1.6 for a detailed discussion and the relevant references). In this chapter, we address these limitations by analyzing the scaling and relative strengths of the dissipation rates in the entire volume of the bulk and boundary layers of RBC. We compute the boundary layer thicknesses for every set of governing parameters and hence determine the bulk and boundary layer subvolumes in which we compute the dissipation rates (see Sec 2.2.5 for a detailed procedure).

The results presented in this chapter have been published in *Physics of Fluids* (Bhattacharya et al., 2018). A summary of the results is as follows.

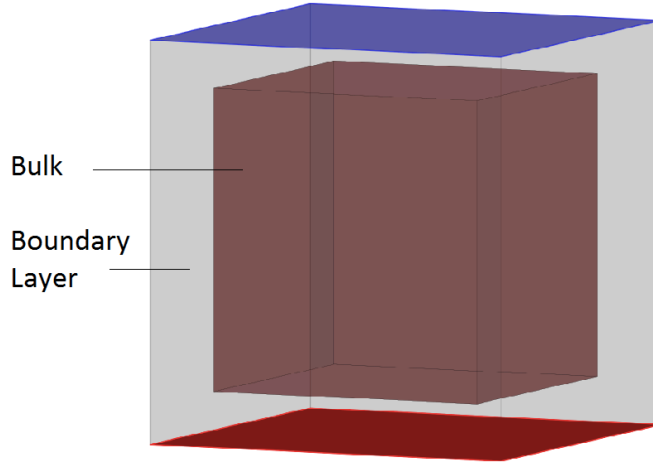


FIGURE 5.1: Schematic of a cubical RBC cell with no-slip boundaries depicting the bulk (brown) and the viscous boundary layer (gray) regions. This figure is adapted from [Bhattacharya et al. \(2018\)](#).

5.2 A summary of our results

We simulate RBC for Rayleigh number (Ra) ranging from 10^6 to 10^8 and for $Pr = 1$ and 6.8 . The simulations were conducted on 256^3 grid using the finite-volume solver OpenFOAM.

Using our numerical data, we compute the viscous boundary layer thickness and divide the convection cell into bulk and boundary layer subvolumes (Fig. 5.1). We observe that the viscous boundary layer thickness scales as $\delta_u \sim Re^{-0.44}$ instead of $Re^{-1/2}$ given by Prandtl-Blasius's relation. We compute the dissipation rates in the bulk and boundary layers, and show that the total viscous dissipation in the bulk is larger, albeit marginally, than that in the boundary layers. This is contrary to the general belief that most of the dissipation occurs in the boundary layers. The viscous dissipation rate in the bulk scales as

$$\epsilon_{u,\text{bulk}} \sim \frac{U^3}{d} Ra^{-0.18}$$

instead of U^3/d as predicted by [Grossmann and Lohse \(2000, 2001\)](#). Hence, the viscous dissipation rate in the bulk scales similar to that in the entire volume [$\epsilon_u \sim (U^3/d)Ra^{-0.2}$ as shown by [Pandey and Verma \(2016\)](#) and [Pandey et al. \(2016a\)](#)], implying that the bulk has a significant contribution to the total viscous dissipation.

The viscous dissipation rate is much more intense in the boundary layers than in the bulk; this is because the boundary layers occupy only a small fraction of the total volume. The probability distribution of the viscous dissipation rate in the boundary layers is stretched exponential, consistent with the fact that extreme events of viscous dissipation occur in the boundary layers. The probability distribution of the viscous dissipation rate in the bulk, on the other hand, is log-normal, similar to homogeneous isotropic turbulence ([Obukhov, 1962](#)).

5.3 Published manuscript

The details of our numerical simulations and the results are presented in the attached published manuscript ([Bhattacharya et al., 2018](#)). The manuscript consists of the analysis of the viscous dissipation rates for $Pr = 1$. The analysis for $Pr = 6.8$ is provided in the supplementary material.

Complexity of viscous dissipation in turbulent thermal convection

Shashwat Bhattacharya,^{1,a)} Amrish Pandey,^{2,b)} Abhishek Kumar,^{3,c)}
 and Mahendra K. Verma^{4,d)}

¹Department of Mechanical Engineering, Indian Institute of Technology Kanpur, Kanpur 208016, India

²Institut für Thermo- und Fluidodynamik, Technische Universität Ilmenau, Ilmenau 98684, Germany

³Applied Mathematics Research Centre, Coventry University, Coventry CV1 5FB, United Kingdom

⁴Department of Physics, Indian Institute of Technology Kanpur, Kanpur 208016, India

(Received 13 January 2018; accepted 14 March 2018; published online 29 March 2018)

Using direct numerical simulations of turbulent thermal convection for the Rayleigh number between 10^6 and 10^8 and unit Prandtl number, we derive scaling relations for viscous dissipation in the bulk and in the boundary layers. We show that contrary to the general belief, the total viscous dissipation in the bulk is larger, albeit marginally, than that in the boundary layers. The bulk dissipation rate is similar to that in hydrodynamic turbulence with log-normal distribution, but it differs from (U^3/d) by a factor of $\text{Ra}^{-0.18}$. Viscous dissipation in the boundary layers is rarer but more intense with a stretched-exponential distribution. *Published by AIP Publishing.* <https://doi.org/10.1063/1.5022316>

Physics of hydrodynamic turbulence is quite complex, involving strong nonlinearity and boundary effects. To simplify, researchers have considered hydrodynamic turbulence in a box away from the walls. The turbulence in such a geometry is statistically homogeneous and isotropic. The physics of even such idealised flows remain primarily unsolved, yet their energetics are reasonably well understood. Here, the energy supplied at large length scales cascades to intermediate scales and then to dissipative scales.^{1,2} Thus, under steady state, the energy supplied by the external force equals the energy cascade rate, Π_u , and the viscous dissipation rate, ϵ_u . From dimensional analysis, it has been deduced that $\epsilon_u \approx U^3/L$, where U is the large-scale velocity, L is the large length scale, and the prefactor is approximately unity.^{3,4}

Thermal convection is a very important problem of science and engineering. Here too researchers have considered an idealised system called *Rayleigh–Bénard convection* (RBC) in which a fluid is confined between two horizontal thermal plates separated by a vertical distance of d ; the bottom plate is hotter than the top one.^{5–7} The kinematic viscosity (ν) and thermal diffusivity (κ) are treated as constants. Additionally, the density of the fluid is considered to be a constant except for the buoyancy term of the fluid equation. The governing equations of RBC are as follows:

$$\partial_t \mathbf{u} + (\mathbf{u} \cdot \nabla) \mathbf{u} = -\nabla \sigma / \rho_0 + \alpha g \theta \hat{z} + \nu \nabla^2 \mathbf{u}, \quad (1)$$

$$\partial_t \theta + (\mathbf{u} \cdot \nabla) \theta = (\Delta/d) u_z + \kappa \nabla^2 \theta, \quad (2)$$

$$\nabla \cdot \mathbf{u} = 0, \quad (3)$$

where \mathbf{u} and σ are the velocity and pressure fields, respectively, θ is the temperature fluctuation over the conduction state, ρ_0 and α are, respectively, the mean density and thermal expansion coefficient of the fluid, g is the acceleration due to gravity, and Δ is the temperature difference between the

hot and cold plates. RBC is specified by two nondimensional parameters—Rayleigh number $\text{Ra} = (\alpha g \Delta d^3)/(\nu \kappa)$, which is a measure of buoyancy, and the Prandtl number $\text{Pr} = \nu/\kappa$ (see the [supplementary material](#)).

For thermal convection, walls and their associated boundary layers play an important role; hence, turbulence in thermal convection is more complex than hydrodynamic turbulence. In this letter, we focus on the properties of the viscous dissipation in RBC. Verzicco and Camussi⁸ and Zhang, Zhou, and Sun⁹ computed the viscous dissipation rates in the bulk and in the boundary layers in RBC and found them to be of the same order. Here, we perform a detailed analysis of these quantities and their probability distributions, both numerically and phenomenologically. We will show that the walls of thermally driven turbulence introduce interesting and generic features in the viscous dissipation.

Shraiman and Siggia¹⁰ derived an interesting exact relation that relates the viscous dissipation rate, ϵ_u , to the heat flux,

$$\begin{aligned} \epsilon_u &= \langle \epsilon_u(\mathbf{r}) \rangle = \left\langle \frac{\nu}{2} \left(\frac{\partial u_i}{\partial x_j} + \frac{\partial u_j}{\partial x_i} \right)^2 \right\rangle \\ &= \frac{\nu^3 (\text{Nu}-1) \text{Ra}}{d^4 \text{Pr}^2} = \frac{U^3 (\text{Nu}-1) \text{Ra}}{d \text{Re}^3 \text{Pr}^2}, \end{aligned} \quad (4)$$

where $\langle \cdot \rangle$ denotes the volume average over the entire domain and u_i with $i = (x, y, z)$ is the i th component of the velocity field. The Nusselt number, Nu , is the ratio of the total heat flux and the conductive heat flux, and $\text{Re} = UL/\nu$ is the Reynolds number. When the boundary layer is either absent (as in a periodic box) or weak (as in the ultimate regime proposed by Kraichnan¹¹), $\text{Nu} \sim (\text{RaPr})^{1/2}$ and $\text{Re} \sim (\text{Ra}/\text{Pr})^{1/2}$ (see Refs. 7 and 12–14). Substitution of these relations into Eq. (4) yields $\epsilon_u \sim U^3/d$, similar to hydrodynamic turbulence. In this letter, we focus on $\text{Pr} \sim 1$ and hence we ignore the Prandtl number dependence.

The scaling however is different for realistic RBC for which boundary layers near the plates play an important role.

^{a)}Electronic mail: shabhata@iitk.ac.in

^{b)}Electronic mail: amrish.pandey@tu-ilmenau.de

^{c)}Electronic mail: abhishek.kir@gmail.com

^{d)}Electronic mail: mkv@iitk.ac.in

Scaling arguments,^{12,15–17} experiments,^{5,16,18–21} and numerical simulations^{8,22–26} reveal that $\text{Re} \sim \text{Ra}^{1/2}$ and $\text{Nu} \sim \text{Ra}^{0.3}$, substitution of which in Eq. (4) yields $\epsilon_u \neq U^3/d$, rather

$$\epsilon_u \sim \frac{U^3}{d} \text{Ra}^{-0.2} \sim \frac{\nu^3}{d^4} \text{Ra}^{1.3}, \quad (5)$$

because $U \sim \text{Re} \sim \text{Ra}^{1/2}$. This is due to the relative suppression of the nonlinear interactions in RBC, as Pandey *et al.*,²⁵ Pandey and Verma,²⁶ and Verma, Kumar, and Pandey⁷ showed that in RBC, the ratio of the nonlinear term and viscous term scales as $(UL/\nu)\text{Ra}^{-0.15}$. The aforementioned suppression of nonlinear interactions leads to weaker energy cascade $\Pi(k)$ and hence lower viscous dissipation than the corresponding hydrodynamic turbulence.

In RBC, the viscous dissipation rates in the bulk and in the boundary layers are very different. In the following discussion, using scaling arguments and the exact relation given by Eq. (4), we will quantify the total viscous dissipation rates in the bulk and boundary layers, $\tilde{D}_{u,\text{bulk}}$ and $\tilde{D}_{u,\text{BL}}$, as well as the corresponding average viscous dissipation rates, $\epsilon_{u,\text{bulk}}$ and $\epsilon_{u,\text{BL}}$, which are obtained by dividing the total dissipation rates by their respective volumes.

Grossmann and Lohse's model^{12,13} assumes that $\epsilon_{u,\text{bulk}} \sim U^3/d \sim \text{Ra}^{3/2}$. We find that the average viscous dissipation in the bulk scales similar to the viscous dissipation rate in the entire volume, i.e.,

$$\epsilon_{u,\text{bulk}} \sim \frac{U^3}{d} \text{Ra}^{-0.18}. \quad (6)$$

Since the fluid flow in the boundary layers is laminar, we expect $\epsilon_{u,\text{BL}} \sim \nu U^2/\delta_u^2$, where δ_u is the thickness of the viscous boundary layer. Hence, the ratio of the two dissipation rates is

$$\begin{aligned} \frac{\epsilon_{u,\text{BL}}}{\epsilon_{u,\text{bulk}}} &\sim \text{Ra}^{0.18} \left(\frac{\nu U^2}{\delta_u^2} \right) / \left(\frac{U^3}{d} \right) \\ &\sim \frac{1}{\text{Re}} \left(\frac{d}{\delta_u} \right)^2 \text{Ra}^{0.18} \sim \left(\frac{d}{\delta_u} \right)^2 \text{Ra}^{-0.32}. \end{aligned} \quad (7)$$

Note, however, that the volume of the boundary layers is much less than that of the bulk. For simplicity, we assume that the fluid is contained in a cube of dimension d , then the ratio of the volumes of the boundary layer and bulk is

$$\frac{V_{\text{BL}}}{V_{\text{bulk}}} \sim \frac{\delta_u d^2}{(d - \delta_u)^3} \sim \frac{\delta_u}{d} \quad (8)$$

because $\delta_u \ll d$ for $\text{Pr} \sim 1$. Using the above relations, we can deduce the scaling of the ratio of the total viscous dissipation rates in the boundary layer and in the bulk as

$$\frac{\tilde{D}_{u,\text{BL}}}{\tilde{D}_{u,\text{bulk}}} \sim \frac{\epsilon_{u,\text{BL}}}{\epsilon_{u,\text{bulk}}} \times \frac{V_{\text{BL}}}{V_{\text{bulk}}} \sim \frac{d}{\delta_u} \text{Ra}^{-0.32}. \quad (9)$$

According to the Prandtl–Blassius theory,²⁷

$$\frac{\delta_u}{d} \sim \text{Re}^{-1/2} \sim \text{Ra}^{-1/4} \quad (10)$$

which yields $\tilde{D}_{u,\text{BL}}/\tilde{D}_{u,\text{bulk}} \sim \text{Ra}^{-0.07}$. Thus, in RBC, the total viscous dissipation in the boundary layer and bulk is comparable to each other. For very large Ra , the bulk dissipation

outweighs the dissipation in the boundary layer. This is contrary to the general belief that the viscous dissipation occurs primarily in the plumes of the boundary layers.

In this letter, using numerical simulations we show that δ_u/d differs slightly from Eq. (10) and

$$\frac{\delta_u}{d} \sim \text{Re}^{-0.44} \sim (\text{Ra}^{1/2})^{-0.44} \sim \text{Ra}^{-0.22}, \quad (11)$$

using which we find

$$\frac{\tilde{D}_{u,\text{BL}}}{\tilde{D}_{u,\text{bulk}}} \sim \text{Ra}^{-0.10}. \quad (12)$$

Thus,

$$\epsilon_{u,\text{BL}} \sim \frac{\nu U^2}{\delta_u^2} \sim \frac{\nu^3}{d^4} \text{Ra}^{1.44}, \quad (13)$$

$$\tilde{D}_{u,\text{BL}} \sim \epsilon_{u,\text{BL}} \delta_u d^2 \sim \frac{\nu^3}{d} \text{Ra}^{1.22}, \quad (14)$$

$$\tilde{D}_{u,\text{bulk}} \sim \epsilon_{u,\text{bulk}} d^3 \sim \frac{\nu^3}{d} \text{Ra}^{1.32}. \quad (15)$$

Interestingly, $\tilde{D}_{u,\text{BL}} \sim d^2 \nu U^2/\delta_u \sim (\nu^3/d)\text{Ra}^{5/4}$, as assumed in Grossmann and Lohse's model.^{12,13}

We perform direct numerical simulations of RBC and verify the aforementioned scaling. The simulations were performed using a finite volume code OpenFOAM²⁸ for $\text{Pr} = 1$ and Ra between 10^6 and 10^8 in a three-dimensional cube of unit dimension. We impose no-slip boundary condition at all the walls, isothermal condition at the top and bottom walls, and adiabatic condition at the sidewalls (see the [supplementary material](#)). A second-order Crank–Nicolson scheme is used for time-stepping. The values of ν and κ used in the simulations are shown in Table I, while keeping the temperature difference between the horizontal plates $\Delta = 1$ for all the runs.

We employ 256^3 non-uniform grid points and solve the governing equations of RBC. The grid is finer near the walls so as to adequately resolve the boundary layer. We ensure that minimum 4 grid points are in the boundary layer, thereby satisfying the criterion set by Grötzbach.²⁹ The ratio of the Kolmogorov length scale η to the average mesh width Δx_{avg} remains greater than unity for each simulation run implying that the smallest length scales are being adequately resolved in our simulations. We observe that the Nusselt numbers computed numerically using $\langle u_z \theta \rangle$ match quite closely with those computed using ϵ_u and Eq. (4). See Table I for the comparison of these two Nusselt numbers. Also, to validate our code, we compute Nu for $\text{Pr} = 6.8$ fluid and verify that it matches quite well with the experimental value of Nu .³⁰ We further remark that our simulations capture the large-scale quantities—volume-averaged viscous dissipation and Nusselt number—quite well; such quantities are not affected significantly by discretization errors at very small scales. Note that spectral method is more accurate but more complex than a finite volume method; yet a sufficiently resolved finite volume code is quite appropriate for studying large-scale quantities.

First we compute the thickness of the boundary layer, δ_u , for all our runs. For the same, we compute the root mean square horizontal velocity in each horizontal plane and estimate δ_u as the vertical height of the intersection of the tangent to the

TABLE I. Details of our direct numerical simulations performed in a unit box for $Pr = 1$: the Rayleigh Number (Ra), the kinematic viscosity (ν), the Reynolds Number (Re), the ratio of the Kolmogorov length scale (η) to the average mesh width Δx_{avg} , the Nusselt Number (Nu), the Nusselt number deduced from ϵ_u using Eq. (4) (Nu_S), the number of mesh points in the viscous boundary layer (N_{BL}), the volume fraction of the boundary layer region (V_{BL}/V), and the ratio $\tilde{D}_{u,BL}/\tilde{D}_{u,bulk}$.

Ra	$\nu (= \kappa)$	Re	$\eta/\Delta x_{avg}$	Nu	Nu_S	N_{BL}	V_{BL}/V	$\tilde{D}_{u,BL}/\tilde{D}_{u,bulk}$
1×10^6	0.001	150	4.92	8.40	8.34	10	0.14	0.81
2×10^6	0.0007071	212	3.89	10.1	10.3	8	0.12	0.67
5×10^6	0.0004472	342	2.87	13.3	13.5	7	0.099	0.65
1×10^7	0.00032	460	2.32	16.0	15.9	6	0.086	0.63
2×10^7	0.0002236	654	1.84	20.0	20.0	5	0.074	0.61
5×10^7	0.0001414	1080	1.36	25.5	26.0	4	0.062	0.57
1×10^8	0.0001	1540	1.09	32.8	32.0	4	0.054	0.56

profile at its local maximum with the slope of the profile at the plates.^{23,31,32} Similar computations are performed for the sidewalls. In Fig. 1, we plot δ_u for the horizontal walls and sidewalls. The best fit curves of the data yield

$$\text{at thermal plates: } \delta_u/d = 0.35Ra^{-0.20}, \quad (16)$$

$$\text{at sidewalls: } \delta_u/d = 0.62Ra^{-0.23}, \quad (17)$$

$$\text{average: } \delta_u/d = 0.52Ra^{-0.22}, \quad (18)$$

with the errors in the exponents and prefactors being ≈ 0.002 and 0.01 , respectively. In Fig. 1, we plot the horizontal and sidewall boundary layer thicknesses against Ra . These results, a key ingredient of our scaling arguments [see Eq. (11)], are consistent with earlier studies.^{8,23,33} As shown in the inset of Fig. 1, near the wall, the velocity profiles differ slightly from the Prandtl–Blasius profile, a result consistent with those of Scheel, Kim, and White²³ and Shi, Emran, and Schumacher;³² such deviations are attributed to the perpetual emission of plumes from the thermal boundary layers.

We compute the ratio V_{BL}/V , where V is the total volume, using δ_u and Eq. (8). In Table I, we list this ratio for various Ra 's. Clearly, the boundary layer occupies much less volume than the bulk, and the ratio decreases with Ra as $\delta_u/d \propto Ra^{-0.22}$ [see Eq. (11)].

After this, from the numerical data we compute the total dissipation rates in the bulk and in the boundary layer by

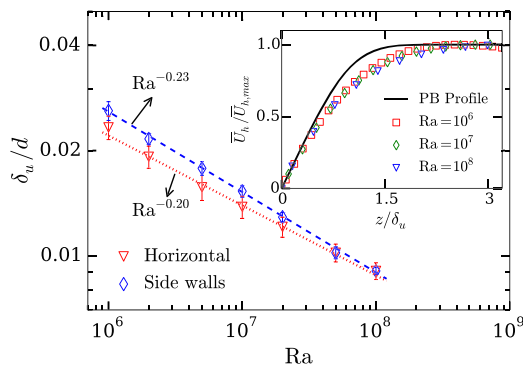


FIG. 1. Plot of normalized boundary layer thickness δ_u/d vs. Ra for horizontal and vertical plates. Best fits are depicted as dashed and dotted lines. Inset shows the comparison of horizontal velocity profiles near the bottom plate with the Prandtl–Blasius profile (solid black line).

computing $\int d\tau \epsilon_u(\mathbf{r})$ over the respective volumes. In Fig. 2(a), we plot these values for various Ra 's. Best fit curves for these data sets yield

$$\tilde{D}_{u,bulk} \approx 0.05 \frac{\nu^3}{d} Ra^{1.33}, \quad (19)$$

$$\tilde{D}_{u,BL} \approx 0.2 \frac{\nu^3}{d} Ra^{1.22} \quad (20)$$

which are consistent with the scaling arguments presented in Eqs. (14) and (15). The ratio of the above quantities, plotted in Fig. 2(b) and listed in Table I, is

$$\frac{\tilde{D}_{u,BL}}{\tilde{D}_{u,bulk}} \approx 4Ra^{-0.11} \quad (21)$$

which is consistent with the scaling of Eq. (12). Note that the above ratio, listed in Table I, decreases from 0.81 to 0.56 as

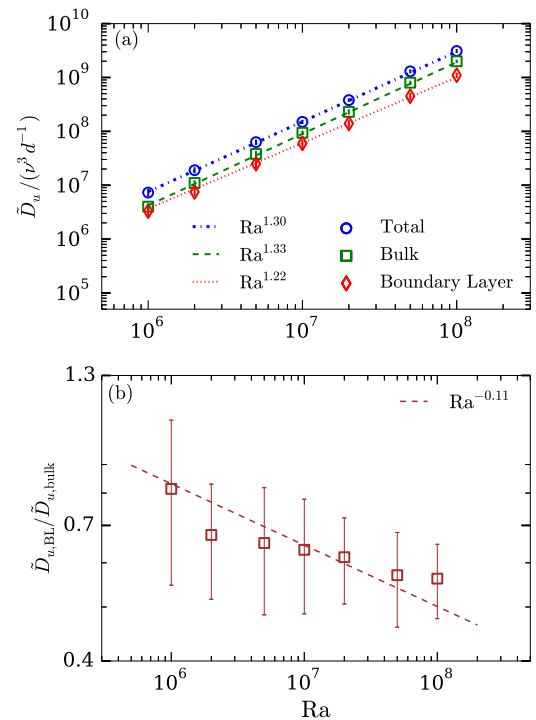


FIG. 2. (a) Plots of the viscous dissipation rates \tilde{D}_u —total, bulk, and in the boundary layer—vs. Ra . (b) Plot of the dissipation rate ratio, $\tilde{D}_{u,BL}/\tilde{D}_{u,bulk}$, vs. Ra that varies as $Ra^{-0.11}$.

Ra is increased from 10^6 to 10^8 . Thus, bulk dissipation dominates the dissipation in the boundary layer, which is contrary to the belief that viscous dissipation primarily takes place in the boundary layer. It is, however, important to keep in mind that the scaling arguments take inputs from numerical simulations, such as Eq. (18) and Nusselt number scaling.

Thus, both scaling arguments and numerical simulations show that the bulk dissipation is weaker than that in hydrodynamic turbulence, for which $\bar{D}_{u,\text{bulk}} \sim U^3/d \sim \text{Ra}^{3/2}$. We also compute the total dissipation rate in volume $V_i = (1/4)^3 V$ located deep inside the bulk and observe similar weak scaling with Ra (see the [supplementary material](#)). Furthermore, the viscous dissipation in the bulk dominates that in the boundary layer, albeit marginally. The boundary layer, however, occupies much smaller volume than the bulk. Hence, $\epsilon_u(\mathbf{r})$ in the boundary layer is much more intense than in the bulk, which is illustrated in Fig. 3. Here we show density plots of normalized viscous dissipation rate $\epsilon_u(\mathbf{r})/(\nu^3 d^{-4})$ for three planes—in the bottom and a side boundary layer, and in the bulk.

To quantify the asymmetry of the dissipation rate in the bulk and in the boundary layer, for $\text{Ra} = 10^8$, we compute the probability distribution function (PDF) of local viscous dissipation, $\epsilon_u(\mathbf{r})$, over the full volume, the bulk, and the boundary layer. These PDFs, plotted in Fig. 4, reveal many important features. Note that $\epsilon_u(\mathbf{r}) = d\tilde{D}_u/d\tau$ with $d\tau$ as the local volume. For $\epsilon_u(\mathbf{r})/\epsilon_u < 20$, we observe that $\epsilon_{u,\text{bulk}}(\mathbf{r}) \gg \epsilon_{u,\text{BL}}(\mathbf{r})$, and thus, the average dissipation rate in the bulk is relatively weak. But for $\epsilon_u(\mathbf{r})/\epsilon_u > 20$, the viscous dissipation in the boundary layer dominates the bulk dissipation.

In addition, the PDF of $\epsilon_{u,\text{bulk}}$ is log-normal, similar to Obukhov's predictions³⁴ for the hydrodynamic turbulence. See Fig. 4(a) for an illustration. This is consistent with the results

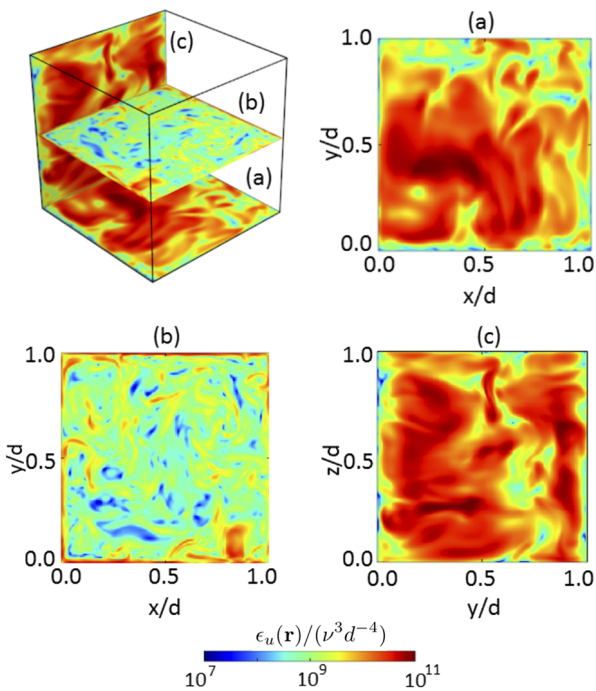


FIG. 3. For $\text{Ra} = 10^8$: Spatial distribution of normalized viscous dissipation rate $\epsilon_u(\mathbf{r})/(\nu^3 d^{-4})$ in planes (a) in the bottom boundary layer at $z = 2\delta_u/3$, (b) in the bulk at $z = 0.5d$, and (c) in one of the sidewall boundary layers at $x = 2\delta_u/3$.

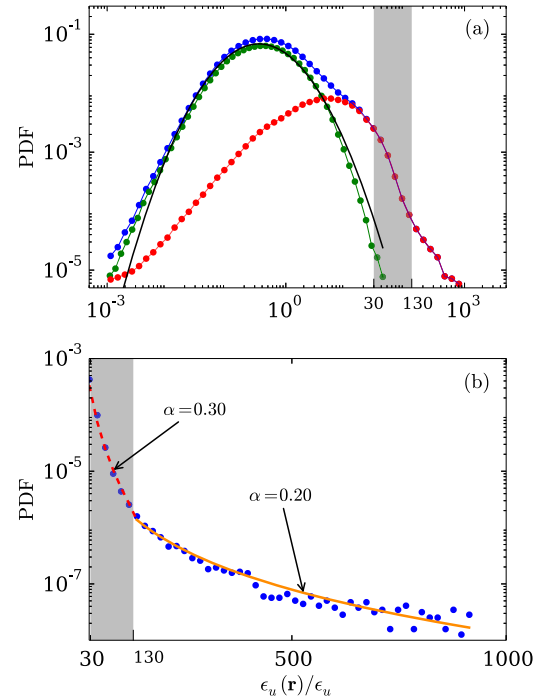


FIG. 4. For $\text{Ra} = 10^8$ and $\text{Pr} = 1$: (a) Probability distribution functions (PDFs) of normalized local dissipation rate ϵ_u in the bulk (green), in the boundary layer (red), and in the entire volume (blue). The bulk ϵ_u has a log-normal distribution (solid black line) with $\sigma = 1.2$ and $\mu = 0.4$. (b) Semilog plot of the PDF of ϵ_u indicates a strong tail for $\epsilon_{u,\text{BL}}$ that fits well with a stretched exponential curve with $\alpha = 0.30$ (dashed red line) in the shaded region and with $\alpha = 0.20$ (solid orange line) outside the region. The shaded region is also shown in (a) for comparison.

of Kumar, Chatterjee, and Verma³⁵ and Verma, Kumar, and Pandey,⁷ who showed similarities between turbulence in RBC and in hydrodynamics. The PDF of $\epsilon_{u,\text{BL}}$, however, is given by a stretched exponential— $P(\epsilon_u) \sim \beta \exp(-m\epsilon_u^{\alpha})/\sqrt{\epsilon_u^*}$ with $\alpha \approx 0.20$ for $\epsilon_u(\mathbf{r})/\epsilon_u > 130$ and $\alpha \approx 0.30$ for $30 < \epsilon_u(\mathbf{r})/\epsilon_u < 130$ [see Fig. 4(b)]. Here ϵ_u^* correspond to those values of ϵ_u , which are larger than the abscissa of the most probable value. This result indicates that the extreme dissipation takes place inside the boundary layer. We also carry out the PDF analysis of $\epsilon_{u,\text{BL}}$ for $\text{Ra} = 10^6$ and 10^7 and observe similar findings (see the [supplementary material](#)). Our detailed work is consistent with earlier results.^{8,9} Emran and Schumacher³⁶ reported similar PDF for the thermal dissipation rate.

We remark that by conducting a similar analysis for $\text{Pr} = 6.8$ and moderate Rayleigh numbers, we observe nearly identical scaling behaviour and distribution of the viscous dissipation rate (see the [supplementary material](#)). Thus, it can be inferred that our findings are robust.

A combination of scaling and PDF results reveals that the local viscous dissipation in the bulk, $\epsilon_{u,\text{bulk}}(\mathbf{r})$, is weak, but they add up to a significant sum due to a larger volume. On the contrary, the boundary layer exhibits extreme dissipation in a smaller volume. Interestingly, the total dissipation rate in the bulk and in the boundary layers is comparable, with the bulk dominating the boundary layer marginally.

Our findings clearly contrast the homogeneous-isotropic hydrodynamic turbulence and thermally driven turbulence. The dissipation in thermal convection has two components— $\epsilon_{u,\text{bulk}}$, similar to hydrodynamic turbulence, but distinctly

weaker by a factor of $\text{Ra}^{-0.18}$, and $\epsilon_{u, \text{BL}}$, which is unique to the flows with walls. We believe that a similar approach could be employed to analyse the thermal dissipation rate and heat transport.

See [supplementary material](#) for a similar analysis of viscous dissipation for a larger Prandtl number $\text{Pr} = 6.8$ and the Rayleigh number dependence of the probability distribution function.

We thank S. Fauve, R. Lakkaraju, M. Anas, and R. Samuel for useful discussions. Our numerical simulations were performed on Shaheen II at KAUST Supercomputing Laboratory, Saudi Arabia, under the Project No. k1052. This work was supported by the research Grant No. PLANEX/PHY/2015239 from Indian Space Research Organisation, India, and by the Department of Science and Technology, India (No. INT/RUS/RSF/P-03) and Russian Science Foundation Russia (No. RSF-16-41-02012) for the Indo-Russian project.

- ¹A. N. Kolmogorov, "The local structure of turbulence in incompressible viscous fluid for very large Reynolds numbers," *Proc. R. Soc. Lond. A* **434**, 9–13 (1991).
- ²A. N. Kolmogorov, "Dissipation of energy in the locally isotropic turbulence," *Proc. R. Soc. Lond. A* **434**, 15–17 (1991).
- ³W. D. McComb, *The Physics of Fluid Turbulence*, Oxford Engineering Science Series (Clarendon Press, Oxford, 1990).
- ⁴M. Lesieur, *Turbulence in Fluids* (Springer-Verlag, Dordrecht, 2008).
- ⁵G. Ahlers, S. Grossmann, and D. Lohse, "Heat transfer and large scale dynamics in turbulent Rayleigh-Bénard convection," *Rev. Mod. Phys.* **81**, 503–537 (2009).
- ⁶D. Lohse and K. Q. Xia, "Small-scale properties of turbulent Rayleigh-Bénard convection," *Annu. Rev. Fluid Mech.* **42**, 335–364 (2010).
- ⁷M. K. Verma, A. Kumar, and A. Pandey, "Phenomenology of buoyancy-driven turbulence: Recent results," *New J. Phys.* **19**, 025012 (2017).
- ⁸R. Verzicco and R. Camussi, "Numerical experiments on strongly turbulent thermal convection in a slender cylindrical cell," *J. Fluid Mech.* **477**, 19–49 (2003).
- ⁹Y. Zhang, Q. Zhou, and C. Sun, "Statistics of kinetic and thermal energy dissipation rates in two-dimensional turbulent Rayleigh-Bénard convection," *J. Fluid Mech.* **814**, 165–184 (2017).
- ¹⁰B. I. Shraiman and E. D. Siggia, "Heat transport in high-Rayleigh-number convection," *Phys. Rev. A* **42**, 3650–3653 (1990).
- ¹¹R. H. Kraichnan, "Turbulent thermal convection at arbitrary Prandtl number," *Phys. Fluids* **5**, 1374–1389 (1962).
- ¹²S. Grossmann and D. Lohse, "Scaling in thermal convection: A unifying theory," *J. Fluid Mech.* **407**, 27–56 (2000).
- ¹³S. Grossmann and D. Lohse, "Thermal convection for large Prandtl numbers," *Phys. Rev. Lett.* **86**, 3316–3319 (2001).
- ¹⁴M. K. Verma, P. K. Mishra, A. Pandey, and S. Paul, "Scalings of field correlations and heat transport in turbulent convection," *Phys. Rev. E* **85**, 016310 (2012).
- ¹⁵W. V. R. Malkus, "The heat transport and spectrum of thermal turbulence," *Proc. R. Soc. A* **225**, 196–212 (1954).
- ¹⁶B. Castaing, G. Gunaratne, L. P. Kadanoff, A. Libchaber, and F. Heslot, "Scaling of hard thermal turbulence in Rayleigh-Bénard convection," *J. Fluid Mech.* **204**, 1–30 (1989).
- ¹⁷S. Grossmann and D. Lohse, "Prandtl and Rayleigh number dependence of the Reynolds number in turbulent thermal convection," *Phys. Rev. E* **66**, 016305 (2002).
- ¹⁸X. Qiu and P. Tong, "Temperature oscillations in turbulent Rayleigh-Bénard convection," *Phys. Rev. E* **66**, 026308 (2002).
- ¹⁹E. Brown, D. Funfschilling, and G. Ahlers, "Anomalous Reynolds-number scaling in turbulent Rayleigh-Bénard convection," *J. Stat. Mech.: Theory Exp.* **2007**, P10005.
- ²⁰D. Funfschilling, E. Brown, A. Nikolaenko, and G. Ahlers, "Heat transport by turbulent Rayleigh-Bénard convection in cylindrical samples with aspect ratio one and larger," *J. Fluid Mech.* **536**, 145–154 (2005).
- ²¹A. Nikolaenko, E. Brown, D. Funfschilling, and G. Ahlers, "Heat transport by turbulent Rayleigh-Bénard convection in cylindrical cells with aspect ratio one and less," *J. Fluid Mech.* **523**, 251–260 (2005).
- ²²G. Stringano and R. Verzicco, "Mean flow structure in thermal convection in a cylindrical cell of aspect ratio one half," *J. Fluid Mech.* **548**, 1–16 (2006).
- ²³J. D. Scheel, E. Kim, and K. R. White, "Thermal and viscous boundary layers in turbulent Rayleigh-Bénard convection," *J. Fluid Mech.* **711**, 281–305 (2012).
- ²⁴J. D. Scheel and J. Schumacher, "Local boundary layer scales in turbulent Rayleigh-Bénard convection," *J. Fluid Mech.* **758**, 344–373 (2014).
- ²⁵A. Pandey, A. Kumar, A. G. Chatterjee, and M. K. Verma, "Dynamics of large-scale quantities in Rayleigh-Bénard convection," *Phys. Rev. E* **94**, 053106 (2016).
- ²⁶A. Pandey and M. K. Verma, "Scaling of large-scale quantities in Rayleigh-Bénard convection," *Phys. Fluids* **28**, 095105 (2016).
- ²⁷H. Schlichting and K. Gersten, *Boundary-Layer Theory*, 8th ed. (Springer-Verlag, Berlin, Heidelberg, 2000).
- ²⁸H. Jasak, A. Jemcov, Z. Tukovic *et al.*, "Openfoam: A C++ library for complex physics simulations," in *International Workshop on Coupled Methods in Numerical Dynamics* (IUC Dubrovnik, Croatia, 2007), Vol. 1000, pp. 1–20.
- ²⁹G. Grötzbach, "Spatial resolution requirements for direct numerical simulation of the Rayleigh-Bénard convection," *J. Comput. Phys.* **49**, 241–264 (1983).
- ³⁰Q. Zhou, B.-F. Liu, C.-M. Li, and B.-C. Zhong, "Aspect ratio dependence of heat transport by turbulent Rayleigh-Bénard convection in rectangular cells," *J. Fluid Mech.* **710**, 260–276 (2012).
- ³¹X. L. Qiu and K. Q. Xia, "Spatial structure of the viscous boundary layer in turbulent convection," *Phys. Rev. E* **58**, 5816 (1998).
- ³²N. Shi, M. S. Emran, and J. Schumacher, "Boundary layer structure in turbulent Rayleigh-Bénard convection," *J. Fluid Mech.* **706**, 5–33 (2012).
- ³³R. Verzicco and R. Camussi, "Prandtl number effects in convective turbulence," *J. Fluid Mech.* **383**, 55–73 (1999).
- ³⁴A. M. Obukhov, "Some specific features of atmospheric turbulence," *J. Geophys. Res.* **67**, 3011, <https://doi.org/10.1029/jz067i008p03011> (1962).
- ³⁵A. Kumar, A. G. Chatterjee, and M. K. Verma, "Energy spectrum of buoyancy-driven turbulence," *Phys. Rev. E* **90**, 023016 (2014).
- ³⁶M. S. Emran and J. Schumacher, "Fine-scale statistics of temperature and its derivatives in convective turbulence," *J. Fluid Mech.* **611**, 13–34 (2008).

Supplementary Material: Complexity of viscous dissipation rate in turbulent thermal convection

Shashwat Bhattacharya,^{1, a)} Amrish Pandey,^{2, b)} Abhishek Kumar,^{3, c)} and Mahendra K. Verma^{4, d)}

¹⁾Department of Mechanical Engineering, Indian Institute of Technology Kanpur, Kanpur 208016, India

²⁾Institut für Thermo- und Fluidodynamik, Technische Universität Ilmenau, Ilmenau 98684, Germany

³⁾Applied Mathematics Research Centre, Coventry University, Coventry, CV15FB, The United Kingdom

⁴⁾Department of Physics, Indian Institute of Technology Kanpur, Kanpur 208016, India

I. NON-DIMENSIONALIZATION OF THE GOVERNING EQUATIONS

In the Letter, we described the governing equations of Rayleigh-Bénard Convection. We nondimensionalize the governing equations by choosing d as the length scale, $\sqrt{\alpha g \Delta d}$ as the velocity scale, Δ as the temperature scale, and $d/\sqrt{\alpha g \Delta d}$ as the time scale. The resulting nondimensional equations are:

$$\partial_t \mathbf{u} + \mathbf{u} \cdot \nabla \mathbf{u} = -\nabla \sigma + \theta \hat{z} + \sqrt{\frac{\text{Pr}}{\text{Ra}}} \nabla^2 \mathbf{u}, \quad (1)$$

$$\partial_t \theta + \mathbf{u} \cdot \nabla \theta = u_z + \frac{1}{\sqrt{\text{RaPr}}} \nabla^2 \theta, \quad (2)$$

$$\nabla \cdot \mathbf{u} = 0, \quad (3)$$

where $\text{Ra} = \alpha g \Delta d^3 / (\nu \kappa)$ is the Rayleigh number and $\text{Pr} = \nu / \kappa$ is the Prandtl number. The Rayleigh and Prandtl numbers are the main governing parameters parameters of RBC.

II. SIMULATION GEOMETRY, AND REGIONS OF BULK AND BOUNDARY LAYERS

We simulate RBC in a cube with no-slip walls on all sides. In Fig. 1 we illustrate the box, the bulk region, and the boundary-layers. We compute the viscous dissipation rates in the bulk and in the boundary layers. We also compute the viscous dissipation rate inside the innermost cube V_i , which is $(1/4)^3$ of the cube.

The scaling of \tilde{D}_u in these regions are as follows:

$$\tilde{D}_{u, \text{BL}} = 0.2 \frac{\nu^3}{d} \text{Ra}^{1.22}, \quad (4)$$

$$\tilde{D}_{u, \text{bulk}} = 0.05 \frac{\nu^3}{d} \text{Ra}^{1.33}, \quad (5)$$

$$\tilde{D}_{u, V_i} = 0.002 \frac{\nu^3}{d} \text{Ra}^{1.25}. \quad (6)$$

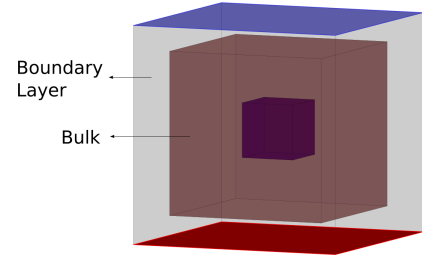


FIG. 1. Schematic of a cubical RBC cell with no-slip boundaries depicting the bulk (brown) and the boundary layer (gray) regions. Also shown is a cubical subvolume (purple) of length $0.25d$ deep inside the cube.

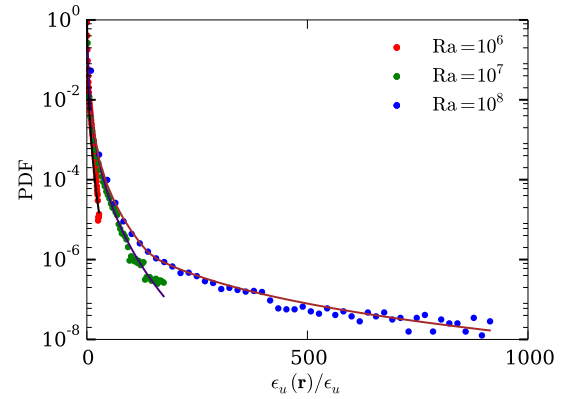


FIG. 2. PDFs of viscous dissipation rates for $\text{Ra} = 10^6, 10^7, 10^8$ and $\text{Pr} = 1$. Tails exhibit a stretched exponential behaviour. The brown, indigo and black curves represent the fits for $\text{Ra} = 10^8, \text{Ra} = 10^7$ and $\text{Ra} = 10^6$ respectively.

III. RAYLEIGH-NUMBER-DEPENDENCE OF PROBABILITY DISTRIBUTION FUNCTIONS (PDF) OF VISCOUS DISSIPATION

In the Letter, we discussed the PDF of viscous dissipation rate, ϵ_u , for $\text{Ra} = 10^8$. In this section we briefly describe the PDF of ϵ_u for various Ra 's in the turbulent regime. As shown in Fig. 2, the tail of the PDFs for all the three Rayleigh numbers exhibit stretched-exponential

^{a)}Electronic mail: shabhattach@iitk.ac.in

^{b)}Electronic mail: amrish.pandey@tu-ilmenau.de

^{c)}Electronic mail: abhishek.kir@gmail.com

^{d)}Electronic mail: mkv@iitk.ac.in

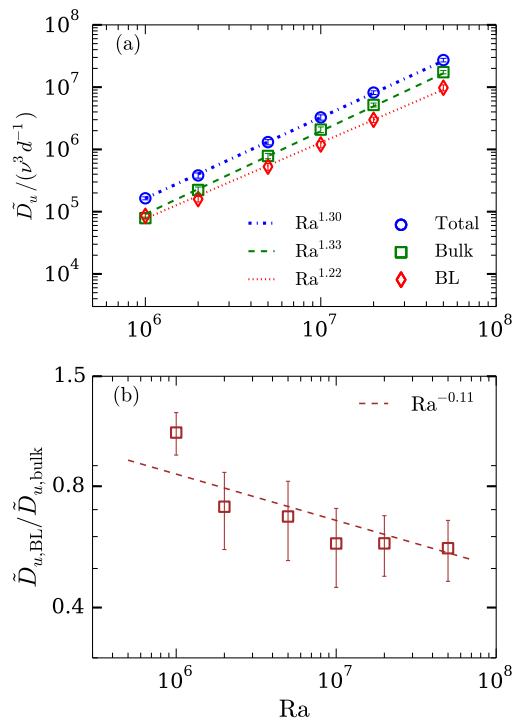


FIG. 3. (a) Plots of the viscous dissipation rates \tilde{D}_u —total, bulk, and in the boundary layer—vs. Ra . (b) Plot of the dissipation rate ratio, $\tilde{D}_{u,BL} / \tilde{D}_{u,bulk}$, vs. Ra that varies as $Ra^{-0.11}$.

behavior, i.e.,

$$P(\epsilon_u) \sim \frac{\beta}{\sqrt{\epsilon_u^*}} \exp(-m\epsilon_u^{*\alpha}), \quad (7)$$

with $\alpha = 0.20 - 0.30$, 0.32 and 0.38 for $Ra = 10^8$, 10^7 and 10^6 respectively. Clearly the tails are stretched more for larger Ra 's. This is expected because we expect stronger dissipation for larger Ra .

IV. VISCOUS DISSIPATION FOR $Pr = 6.8$

The Letter contains the description of viscous dissipation for $Pr = 1$ and $Ra = 10^6$ to 10^8 . To show that the results described in the letter are generic, we compute the dissipation rates in the bulk and boundary layer for $Pr = 6.8$ and $Ra = 10^6$ to 5×10^7 . We observe that

$$\tilde{D}_{u,bulk} \approx 0.001 \frac{\nu^3}{d} Ra^{1.33}, \quad (8)$$

$$\tilde{D}_{u,BL} \approx 0.004 \frac{\nu^3}{d} Ra^{1.22}, \quad (9)$$

$$\frac{\tilde{D}_{u,BL}}{\tilde{D}_{u,bulk}} \approx 4Ra^{-0.11}. \quad (10)$$

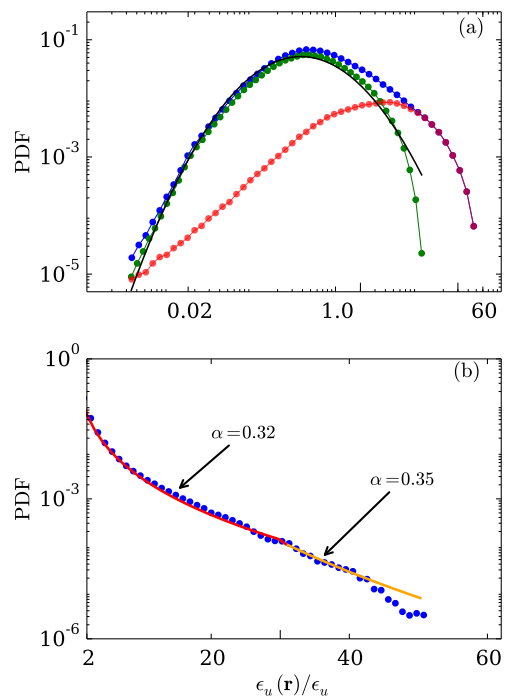


FIG. 4. For $Ra = 5 \times 10^7$ and $Pr = 6.8$: (a) PDF of local dissipation rates in the bulk (green), in the boundary layer (red), and in the entire volume (blue). The bulk ϵ_u has a log-normal distribution (solid black line). (b) Semilog plot of the PDF of ϵ_u indicates strong tail for $\epsilon_{u,BL}$ that fits well with a stretched exponential curve with $\alpha = 0.32$ (red line) - 0.35 (orange line).

Clearly, the exponents for $Pr = 6.8$ are very close to those for $Pr = 1$, thus showing that the results of the Letter are generic [see Figs. 3(a) and (b)]. The prefactors for $\tilde{D}_{u,bulk}$ and $\tilde{D}_{u,BL}$ are an order of magnitude lower than those for $Pr = 1$ case, which is due to lower nonlinearity of energy flux for $Pr = 6.8$.

We also compute the PDF of $\epsilon_u(\mathbf{r})$ for $Pr = 6.8$ and $Ra = 5 \times 10^7$ case. The behaviour for $Pr = 6.8$ is very similar to that for $Pr = 1$ case, where the PDF for the bulk dissipation rate exhibits log-normal behaviour, and the PDF for the dissipation rate in the boundary layer is stretched-exponential [see Figs. 4(a) and (b)]. The exponent α for $Ra = 5 \times 10^7$ is larger than that for $Ra = 1 \times 10^8$ ($Pr = 1$) indicating that the latter has longer tail in the PDF.

Chapter 6

Scaling and spatial distribution of thermal dissipation

6.1 Introduction

In Chapter 5, we discussed the effects of walls on the properties of the viscous dissipation rates in RBC. The walls and their associated boundary layers have a similar effect on the thermal dissipation rates in RBC as well (see Chapter 1, Sec. 1.6 for an introductory discussion). To better understand the effects of walls on the thermal dissipation rate, we compare and quantify the thermal dissipation rate separately in the thermal boundary layers and in the bulk. As discussed in Chapter 1, Sec. 1.6, there have been several studies on the thermal dissipation rates in the bulk and boundary layers before. However, these studies either did not take into account the entire bulk volume for their analysis or took the boundary layer thicknesses to be constant for all Ra and Pr , which could have affected the accuracy of the results. In this chapter, we address these limitations by analyzing the scaling and relative strengths of the thermal dissipation rates in the entire volume of the bulk and thermal boundary layers of RBC, similar to that done for the viscous dissipation rates in the previous chapter. We compute the thermal boundary layer thicknesses for every set of governing parameters and hence determine the bulk and boundary layer subvolumes in which we compute the dissipation rates (see Chapter 2, Sec 2.2.5 for a detailed procedure).

The results presented in this chapter have been published in *Physics of Fluids* (Bhattacharya et al., 2019b). A summary of our results is as follows.

6.2 A summary of our results

We employ the simulation data of RBC for $\text{Pr} = 1$ obtained in Chapter 5 for conducting our analysis on the thermal dissipation rates. Further, we conduct additional simulations of RBC for $\text{Pr} = 100$ using OpenFOAM.

Using our numerical data, we show that the thermal dissipation rate in the bulk scales as

$$\epsilon_{T,\text{bulk}} \sim \begin{cases} \frac{U\Delta^2}{d} \text{Ra}^{-0.22}, & \text{Pr} = 1, \\ \frac{U\Delta^2}{d} \text{Ra}^{-0.25}, & \text{Pr} = 100, \end{cases}$$

instead of $U\Delta^2/d$ as in homogeneous isotropic turbulence. We further observe that unlike viscous dissipation, the total thermal dissipation in the boundary layers is stronger than that in the bulk (by approximately a factor of 3). The ratio of the boundary layer and the bulk dissipation is roughly constant for $\text{Pr} = 1$ but decreases weakly with Ra for $\text{Pr} = 100$.

The probability distribution functions of thermal dissipation rate, both in the bulk and in the boundary layers, are stretched exponential, similar to passive scalar dissipation in homogeneous isotropic turbulence. The tail of the PDFs of boundary layer dissipation is wider than that of bulk dissipation, implying that extreme events occur more frequently in the boundary layers than in the bulk. This is expected because the gradient of temperature is very steep in the boundary layers due to which the thermal dissipation rate is expected to be large. We also show that the spatial intermittency of thermal dissipation is stronger for $\text{Pr} = 1$ compared to that for $\text{Pr} = 100$.

6.3 Published manuscript

The details of our numerical simulations and the results are presented in the attached published manuscript (Bhattacharya et al., 2019b).

Scaling and spatial intermittency of thermal dissipation in turbulent convection

Cite as: *Phys. Fluids* **31**, 075104 (2019); doi: 10.1063/1.5098073

Submitted: 31 March 2019 • Accepted: 17 June 2019 •

Published Online: 16 July 2019



Shashwat Bhattacharya,^{1,a)} Ravi Samtaney,² and Mahendra K. Verma³

AFFILIATIONS

¹Department of Mechanical Engineering, Indian Institute of Technology Kanpur, Kanpur 208016, India

²Mechanical Engineering, Division of Physical Science and Engineering, King Abdullah University of Science and Technology, Thuwal 23955, Saudi Arabia

³Department of Physics, Indian Institute of Technology Kanpur, Kanpur 208016, India

^{a)}Electronic mail: shabhatt@iitk.ac.in

ABSTRACT

We derive scaling relations for the thermal dissipation rate in the bulk and in the boundary layers for moderate and large Prandtl number (Pr) convection. Using direct numerical simulations of Rayleigh–Bénard convection, we show that the thermal dissipation in the bulk is suppressed compared to passive scalar dissipation. The suppression is stronger for large Pr. We further show that the dissipation in the boundary layers dominates that in the bulk for both moderate and large Pr. The probability distribution functions of thermal dissipation rate, both in the bulk and in the boundary layers, are stretched exponential, similar to passive scalar dissipation.

Published under license by AIP Publishing. <https://doi.org/10.1063/1.5098073>

I. INTRODUCTION

Scalar fields, such as temperature and concentration, are often carried along by turbulent flows. Flows with scalars are ubiquitous and frequently encountered in engineering and atmospheric applications. In general, these scalar fields influence the dynamics of fluid flow. The resulting coupling between the momentum and the scalar equations, along with strong nonlinearities, makes such flows very complex. Obukhov¹ and Corrsin² described the energetics of a simplified system consisting of homogeneous isotropic turbulence with passive scalar fields; such scalars do not affect the velocity field. In passive scalar turbulence, both kinetic energy [defined as $(1/2)\langle|\mathbf{u}|^2\rangle$] and scalar energy [defined as $(1/2)\langle\theta^2\rangle$] are supplied at large scales. Here, θ and \mathbf{u} are scalar and velocity fields, respectively, and $\langle \rangle$ denotes volume average. The supplied kinetic and scalar energies cascade to intermediate scales and then to dissipative scales. Similar to kinetic energy in homogeneous turbulence, the rate of scalar energy supply equals the scalar energy cascade rate Π_θ and the scalar dissipation rate ϵ_θ .^{3,4} Dimensional analysis gives $\epsilon_\theta \approx U\Theta^2/L$, where L , U , and Θ are large-scale length, velocity, and scalar, respectively.

In the present work, we consider turbulence in buoyancy-driven convection, which is an example of active scalar turbulence

where the scalar field (temperature) influences the flow-dynamics. We focus on an idealized system called *Rayleigh–Bénard convection* (RBC) in which a fluid is enclosed between two horizontal walls, with the bottom wall being hotter than the top one.^{5–7} Each horizontal wall is isothermal. RBC is specified by two nondimensional parameters—Rayleigh number (Ra) and Prandtl number (Pr). These parameters are defined as

$$\text{Ra} = \frac{\alpha g \Delta d^3}{\nu \kappa}, \quad \text{Pr} = \frac{\nu}{\kappa},$$

where α , ν , and κ , respectively, are the thermal expansion coefficient, kinematic viscosity, and thermal diffusivity of the fluid, g is the gravitational acceleration, and Δ and d , respectively, are the temperature difference and the distance between the top and bottom plates.

The energetics of thermally driven convection is more complex than that of passive scalar turbulence; this is due to the two-way coupling between the governing equations of momentum and thermal energy (see Sec. II), along with the presence of thermal boundary layers. Presently, we focus on the properties of thermal dissipation rate $\epsilon_T(\mathbf{r}) = \kappa(\nabla T)^2$, where T is the temperature field. In RBC, the volume-averaged thermal dissipation rate is related to the Nusselt number (Nu) by the following relation derived by Shraiman and

Siggia:⁸

$$\epsilon_T = \langle \kappa (\nabla T)^2 \rangle = \frac{\kappa \Delta^2}{d^2} \text{Nu} = \frac{U \Delta^2}{d} \frac{\text{Nu}}{\text{Pe}}. \quad (1)$$

The Nusselt number is the ratio of the total heat flux and the conductive heat flux, and $\text{Pe} = Ud/\kappa$ is the Péclet number. When the thermal boundary layers are less significant than the bulk (as in the ultimate regime proposed by Kraichnan⁹), or absent (as in a periodic box¹⁰), both Nu and Pe are proportional to $\sqrt{\text{RaPr}}$ (see Refs. 7, 11, and 12). These relations, when substituted in Eq. (1), yield $\epsilon_T \sim U\Delta^2/d$, similar to passive scalar turbulence.

In RBC, the thermal boundary layers near the conducting walls play an important role in the scaling of thermal dissipation rate. In our present work, we focus on the Ra dependence of thermal dissipation rate and other quantities. For moderate Prandtl numbers (of order 1), it has been shown via scaling arguments,^{11,13–15} experiments,^{14,16–23} and numerical simulations^{24–31} that

$$\text{Pe} \sim \text{Ra}^{0.5}, \quad \text{Nu} \sim \text{Ra}^{0.3}.$$

Note that the exponents in the above expressions shown here are approximate. Substitution of these expressions into Eq. (1) yields

$$\epsilon_T \sim \frac{\kappa \Delta^2}{d^2} \text{Ra}^{0.3} \sim \frac{U \Delta^2}{d} \text{Ra}^{-0.2}. \quad (2)$$

When compared to passive scalar flow, the additional term $\text{Ra}^{-0.2}$ in RBC accounts for suppression of nonlinear interactions due to the presence of walls; Pandey and Verma³⁰ and Pandey *et al.*³¹ showed that in RBC, the ratio of the nonlinear term to the diffusive term in the equation for thermal energy is proportional to $\text{PeRa}^{-0.30}$ instead of Pe . The walls truncate some of the Fourier modes, resulting in several channels of nonlinear interactions and energy cascades to be blocked (see Ref. 4 for details). Consequently, thermal dissipation in RBC is weakened compared to free passive scalar turbulence. For large Pr , Pandey and Verma³⁰ and Pandey *et al.*³¹ have shown that $\epsilon_T \sim (U\Delta^2/d)\text{Ra}^{-0.25}$ instead of $U\Delta^2/d$.

To better understand the effects of walls, we need to study the behavior of thermal dissipation separately in the boundary layers and in the bulk. It is generally believed that dissipation (thermal or viscous) occurs predominantly in the boundary layers.^{32,33} However, phenomenological arguments and numerical results presented by Verma, Kumar, and Pandey⁷ imply that significant dissipation occurs also at large scales, i.e., in the bulk. Motivated by this, Bhattacharya *et al.*³⁴ computed the viscous dissipation rate separately in the bulk and in the boundary layers for moderate Pr . Interestingly, they found the bulk dissipation to be greater, albeit marginally, than the boundary layer dissipation. On the other hand, the thermal dissipation for moderate Pr convection was shown to be dominant in the boundary layers; refer to the work of Verzicco and Camussi²⁴ and Zhang, Zhou, and Sun.³⁵

In this paper, we conduct a more detailed analysis of thermal dissipation rate in the bulk and boundary layers not only for moderate Pr but also for large Pr convection. Note that the statistics of thermal dissipation for large Pr is less explored in the literature. We compare and quantify the total and average thermal dissipation rates in the bulk and in the boundary layers using scaling arguments and numerical simulations. We also examine the probability distribution functions (PDFs) of the thermal dissipation in these regions.

Our analysis is similar to that conducted by Bhattacharya *et al.*³⁴ on viscous dissipation rate.

The outline of the paper is as follows. In Sec. II, we present the governing equations of RBC along with their nondimensionalization. We discuss the numerical method in Sec. III. In Sec. IV, we compute the thermal boundary layer thickness and present scaling arguments for the thermal dissipation rate in the bulk and in the boundary layers. We verify these scaling relations using our numerical results. We also study the spatial intermittency of thermal dissipation rate. Finally, we conclude in Sec. V.

II. GOVERNING EQUATIONS

In RBC, under the Boussinesq approximation, the thermal diffusivity (κ) and the kinematic viscosity (ν) are treated as constants. The density of the fluid is considered to be a constant except for the buoyancy term in the governing equations. Furthermore, the viscous dissipation term is considered to be small and is therefore dropped from the temperature equation. The governing equations of RBC are as follows:^{4,36}

$$\frac{\partial \mathbf{u}}{\partial t} + (\mathbf{u} \cdot \nabla) \mathbf{u} = -\nabla p / \rho_0 + \alpha g T \hat{z} + \nu \nabla^2 \mathbf{u}, \quad (3)$$

$$\frac{\partial T}{\partial t} + (\mathbf{u} \cdot \nabla) T = \kappa \nabla^2 T, \quad (4)$$

$$\nabla \cdot \mathbf{u} = 0, \quad (5)$$

where \mathbf{u} and p are the velocity and pressure fields, respectively, T is the temperature field with respect to a reference temperature, α is the thermal expansion coefficient, ρ_0 is the mean density of the fluid, and g is acceleration due to gravity.

Using d as the length scale, $\sqrt{\alpha g \Delta d}$ as the velocity scale, and Δ as the temperature scale, we nondimensionalize Eqs. (3)–(5), which yields

$$\frac{\partial \mathbf{u}}{\partial t} + \mathbf{u} \cdot \nabla \mathbf{u} = -\nabla p + T \hat{z} + \sqrt{\frac{\text{Ra}}{\text{Pr}}} \nabla^2 \mathbf{u}, \quad (6)$$

$$\frac{\partial T}{\partial t} + \mathbf{u} \cdot \nabla T = \frac{1}{\sqrt{\text{Ra Pr}}} \nabla^2 T, \quad (7)$$

$$\nabla \cdot \mathbf{u} = 0. \quad (8)$$

In Sec. III, we describe the numerical method used for our simulations.

III. NUMERICAL METHOD

We conduct our numerical analysis for (i) $\text{Pr} = 1$ and (ii) $\text{Pr} = 100$ fluids. For $\text{Pr} = 1$, we use the simulation data of Bhattacharya *et al.*³⁴ and Kumar and Verma,³⁷ which were obtained using the finite volume code OpenFOAM.³⁸ The simulations were conducted on a 256^3 grid for Ra ranging from 10^6 to 10^8 . No-slip boundary conditions were imposed at all the walls, isothermal boundary conditions at the top and bottom walls, and adiabatic boundary conditions at the sidewalls. For time marching, second-order Crank-Nicholson scheme was used. For $\text{Pr} = 100$, we conduct fresh simulations following the aforementioned schemes, boundary conditions, and grid

TABLE I. Details of our numerical data obtained using direct numerical simulations performed in a cubical box: the Prandtl number (Pr), the Rayleigh number (Ra), the Péclet number (Pe), the time step (Δt), the ratio of the Batchelor length scale⁴¹ (η_θ) to the maximum mesh width Δx_{\max} , the Nusselt number (Nu), the Nusselt number (Nu_S) deduced from ϵ_T using Eq. (1), the ratio of the thermal boundary layer thickness δ_T to the cell height d , the number of grid points in the thermal boundary layer (N_{BL}), and the number of snapshots over which the quantities are averaged.

Pr	Ra	Pe	Δt	$\eta_\theta/\Delta x_{\max}$	Nu	Nu_S	δ_T/d	N_{BL}	Snapshots
1	1×10^6	150	1×10^{-3}	3.6	8.40	8.26	0.061	23	56
1	2×10^6	212	1×10^{-3}	2.8	10.1	10.1	0.050	19	56
1	5×10^6	342	1×10^{-3}	2.1	13.3	13.4	0.037	14	55
1	1×10^7	460	1×10^{-3}	1.7	16.0	16.1	0.031	12	100
1	2×10^7	654	1×10^{-3}	1.3	20.0	19.7	0.025	10	100
1	5×10^7	1080	1×10^{-3}	1.0	25.5	25.7	0.019	8	101
1	1×10^8	1540	1×10^{-3}	0.8	32.8	32.0	0.016	7	86
100	2×10^6	277	5×10^{-4}	2.8	11.1	11.1	0.045	17	41
100	5×10^6	496	1×10^{-3}	2.0	14.5	14.4	0.034	13	50
100	1×10^7	698	1×10^{-3}	1.6	17.2	17.1	0.029	12	52
100	2×10^7	1036	1×10^{-3}	1.3	20.1	20.3	0.025	10	99
100	5×10^7	1772	1×10^{-3}	1.0	26.0	26.0	0.019	8	101

resolution for Ra's ranging from 2×10^6 to 5×10^7 . A constant time step was chosen, with $\Delta t = 10^{-3}$ and 5×10^{-4} , depending on the parameters (see Table I for details). Here, $t = 1$ corresponds to $d/\sqrt{\alpha g \Delta d}$.

We ensure that a minimum of 8 grid points is in the thermal boundary layers, thereby satisfying the resolution criterion set by Grötzbach³⁹ and Verzicco and Camussi.²⁴ In RBC, the thermal boundary layer thickness δ_T is defined as the distance between the wall and the point where the tangent to the planar-averaged temperature profile near the wall intersects with the average bulk temperature line.^{5,25,26,40} To ensure that the smallest length scales are resolved, we note that the ratio of the Batchelor length scale⁴¹ $\eta_\theta = (\nu \kappa^2 / \epsilon_u)^{1/4}$ to the maximum mesh width Δx_{\max} remains greater than unity for all runs. The only exception is for the $Ra = 10^8$, $Pr = 1$ case where $\eta_\theta = 0.8$, which is marginally less than unity. The Nusselt numbers computed using our data are consistent with those obtained in other simulations of RBC for the same geometry;^{30,31,42} this is how we validate our data. Furthermore, the Nusselt numbers computed numerically using $\langle u_z T \rangle$ match closely with those computed using ϵ_T and Eq. (1). This further validates our simulations. See Table I for the comparison of these two Nusselt numbers. All the quantities analyzed in this work are time-averaged over 40–100 snapshots after attaining a steady-state (see Table I).

In Sec. IV, we discuss the numerical results, focusing on the scaling of the thermal dissipation rate in the bulk and in the boundary layers, their relative contributions to the total thermal dissipation rate, and their spatial intermittency.

IV. NUMERICAL RESULTS

A. Boundary layer thickness

Using the simulation results, we first compute the thickness of the thermal boundary layers. Theoretically, boundary layer thickness (δ_T) is related to the Nusselt number as⁵

$$\frac{\delta_T}{d} = \frac{1}{2Nu}. \tag{9}$$

Now, as discussed in Sec. I, $Nu \sim Ra^{0.3}$ for Pr of order 1. Numerical simulations^{30,31,43} reveal that $Nu \sim Ra^{0.3}$ for large Pr as well. Therefore, for both $Pr = 1$ and 100, we expect

$$\frac{\delta_T}{d} \sim Ra^{-0.3}. \tag{10}$$

We numerically compute δ_T 's using the planar averaged temperature profile and list them in Table I. Furthermore, we plot them vs Ra in Figs. 1(a) and 1(b) for both $Pr = 1$ and 100. The best-fit curves of the data yield

$$\frac{\delta_T}{d} = \begin{cases} 3.6Ra^{-0.30}, & Pr = 1, \\ 2.4Ra^{-0.28}, & Pr = 100, \end{cases} \tag{11}$$

with the error in the exponents being approximately 0.01. The obtained fit is reasonably consistent with Eq. (10).

B. Scaling of thermal dissipation rate

In this subsection, we study the scaling of average thermal dissipation rate in the bulk ($\epsilon_{T,bulk}$) and in the boundary layers ($\epsilon_{T,BL}$) using our numerical data. These quantities are dissipation per unit volume. Based on these, using scaling arguments, we predict the relations for the total dissipation rate in the bulk ($\bar{D}_{T,bulk}$) and in the boundary layers ($\bar{D}_{T,BL}$), which are the products of average thermal dissipation rates in these regions and their corresponding volumes. We verify their scaling relations using our simulation data and analyze the relative strength of the bulk and the boundary layer dissipation.

1. Bulk dissipation

Using our simulation data, we numerically compute $\epsilon_{T,bulk} = \langle \kappa |\nabla T(\mathbf{r})|^2 \rangle_{bulk}$ and the large-scale mean flow $U = \sqrt{\langle |\mathbf{u}(\mathbf{r})|^2 \rangle}$.

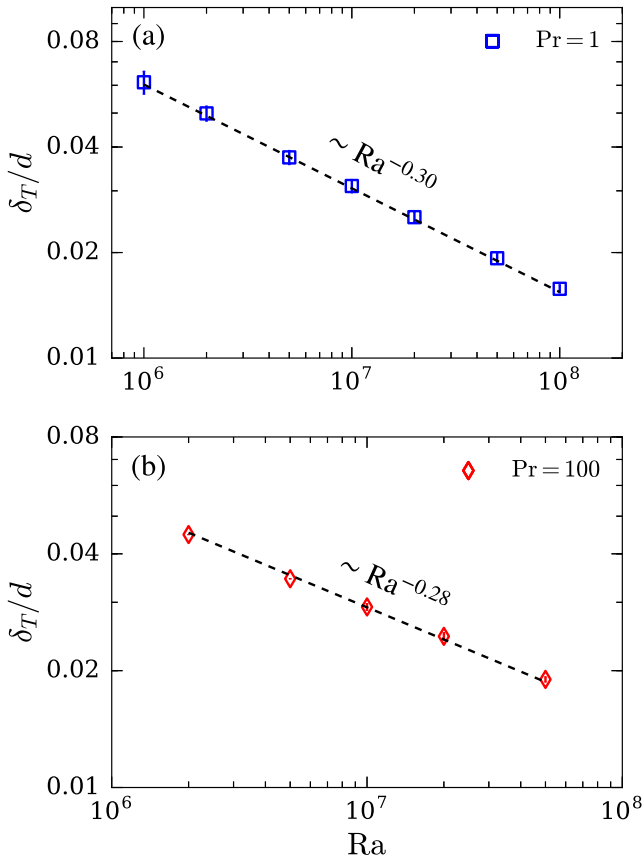


FIG. 1. For (a) $Pr = 1$ and (b) $Pr = 100$: plots of normalized thermal boundary layer thickness δ_T/d vs Ra , along with $Ra^{-0.30}$ and $Ra^{-0.28}$ fits (dashed curves). The error-bars represent the standard deviation of the dataset with respect to the temporal average.

In deriving their unifying scaling theory, Grossmann and Lohse^{11,12} argued that $\epsilon_{T,\text{bulk}} \sim U\Delta^2/d$. However, from our numerical data, we observe that

$$\epsilon_{T,\text{bulk}} \sim \begin{cases} (U\Delta^2/d)Ra^{-0.22}, & Pr = 1, \\ (U\Delta^2/d)Ra^{-0.25}, & Pr = 100, \end{cases} \quad (12)$$

instead of $U\Delta^2/d$ (see Fig. 2). The errors in the exponents are 0.02 and 0.01 for $Pr = 1$ and 100, respectively. Thus, the thermal dissipation in the bulk in RBC scales similar to the dissipation in the entire volume and is distinctly weaker than that in passive scalar turbulence. For moderate Pr fluids, the decrease in $\epsilon_{T,\text{bulk}}/(U\Delta^2/d)$ with Ra has also been observed by Emran and Schumacher⁴⁴ and Verzicco and Camussi²⁴ for convection in a cylindrical cell and by Zhang, Zhou, and Sun³⁵ for two-dimensional RBC. As discussed in Sec. I, the walls suppress nonlinear interactions in RBC,^{30,31} consequently weakening the thermal dissipation rate at large scales. Note that Bhattacharya *et al.*³⁴ observed similar suppression of viscous dissipation in the bulk, where $\epsilon_{u,\text{bulk}} \sim (U^3/d)Ra^{-0.18}$ instead of U^3/d for $Pr = 1$.

The aforementioned suppression has an important implication in the scaling of the total thermal dissipation in the bulk ($\tilde{D}_{T,\text{bulk}}$).

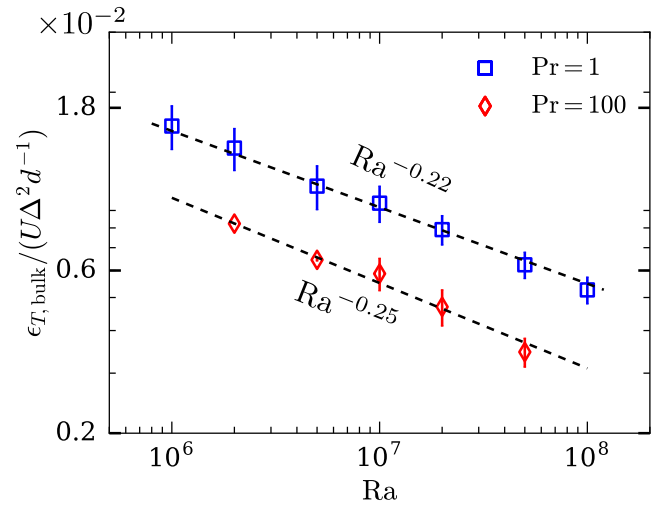


FIG. 2. Plots of average thermal dissipation rate in the bulk, normalized with $U\Delta^2/d$, vs Ra . The bulk dissipation is distinctly weaker than $U\Delta^2/d$. The error bars represent the standard deviation of the dataset with respect to the temporal average.

The bulk volume can be approximated as

$$V_{\text{bulk}} = (d - 2\delta_T)d^2 \approx d^3, \quad (13)$$

because $\delta_T \ll d$ (see Table I). We will now derive the scaling relations for $\tilde{D}_{T,\text{bulk}}$ separately for $Pr = 1$ and 100.

1. $Pr = 1$: Using Eqs. (12) and (13), we write the following for the bulk dissipation:

$$\tilde{D}_{T,\text{bulk}} = \epsilon_{T,\text{bulk}} V_{\text{bulk}} \sim \left(\frac{U\Delta^2}{d} Ra^{-0.22} \right) d^3. \quad (14)$$

By multiplying the numerator and the denominator of the rightmost expression in Eq. (14) by d/κ , we rewrite $\tilde{D}_{T,\text{bulk}}$ as

$$\left(\frac{U\Delta^2}{d} Ra^{-0.22} \right) d^3 = (\kappa\Delta^2 d) Pe Ra^{-0.22}, \quad (15)$$

where $Pe = Ud/\kappa$ is the Péclet number. As discussed in Sec. I, $Pe \sim Ra^{0.5}$ for moderate Pr . Substituting this relation in Eqs. (14) and (15), we obtain

$$\tilde{D}_{T,\text{bulk}} \sim (\kappa\Delta^2 d) Ra^{0.28}. \quad (16)$$

2. $Pr = 100$: Applying a similar procedure, we can write the total dissipation in the bulk for $Pr = 100$ as

$$\tilde{D}_{T,\text{bulk}} \sim (\kappa\Delta^2 d) Pe Ra^{-0.25}, \quad (17)$$

because $\epsilon_{T,\text{bulk}} \sim (U\Delta^2/d)Ra^{-0.25}$ in this case. Now, according to the predictions of Grossmann and Lohse¹² and Shishkina *et al.*⁴⁵ for large Pr convection, $Pe \sim Ra^{3/5}$. Pandey, Verma, and Mishra,⁴³ Pandey and Verma,³⁰ and Pandey *et al.*³¹ have also shown that for large Pr , $Pe \sim Ra^{0.6}$. Substituting this relation in

Eq. (17), we obtain

$$\tilde{D}_{T,\text{bulk}} \sim (\kappa\Delta^2 d)\text{Ra}^{0.35}. \quad (18)$$

Thus, the suppression of thermal dissipation in the bulk leads to a weaker dependence of the total thermal dissipation with Ra. Note that in the absence of this suppression, $\tilde{D}_{T,\text{bulk}} \sim (\kappa\Delta^2 d)\text{Pe}$. Had this been the case, $\tilde{D}_{T,\text{bulk}}$, normalized with $\kappa\Delta^2 d$, would have been proportional to $\text{Ra}^{0.5}$ for $\text{Pr} = 1$ and $\text{Ra}^{0.6}$ for $\text{Pr} = 100$.

2. Boundary layer dissipation

The heat transport in the boundary layers is primarily diffusive due to steep temperature gradients. Thus, we expect the thermal dissipation in the boundary layers to be given by

$$\epsilon_{T,\text{BL}} \sim \kappa\Delta^2/\delta_T^2. \quad (19)$$

We verify this by plotting the numerically computed $\epsilon_{T,\text{BL}}/(\kappa\Delta^2/\delta_T^2)$ vs Ra in Fig. 3, where we observe the slope to be flat. For $\text{Pr} = 100$ and at lower Ra, however, there is a very slight decrease in $\epsilon_{T,\text{BL}}/(\kappa\Delta^2/\delta_T^2)$ with Ra. However, we will ignore this in our scaling analysis.

The total thermal dissipation in the boundary layers is given by $\tilde{D}_{T,\text{BL}} = \epsilon_{T,\text{BL}}V_{\text{BL}}$. Substituting Eq. (19) in the above relation and noting that $V_{\text{BL}} = 2\delta_T d^2$, we obtain

$$\tilde{D}_{T,\text{BL}} \sim \left(\frac{\kappa\Delta^2}{\delta_T^2}\right)\delta_T d^2 \sim \kappa\Delta^2 d \left(\frac{d}{\delta_T}\right). \quad (20)$$

As discussed in Sec. IV A, $\delta_T/d \sim \text{Ra}^{-0.30}$ for $\text{Pr} = 1$ and $\sim \text{Ra}^{-0.28}$ for $\text{Pr} = 100$. Substituting these relations in Eq. (20), we obtain

$$\tilde{D}_{T,\text{BL}} \sim \begin{cases} (\kappa\Delta^2 d)\text{Ra}^{0.30}, & \text{Pr} = 1, \\ (\kappa\Delta^2 d)\text{Ra}^{0.28}, & \text{Pr} = 100. \end{cases} \quad (21)$$

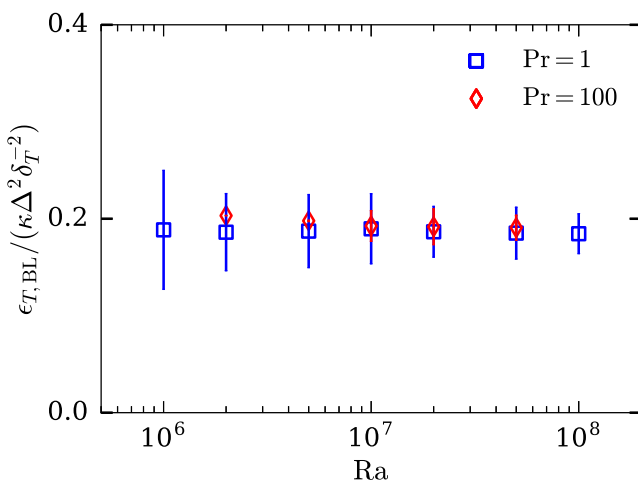


FIG. 3. Plots of average thermal dissipation in the boundary layers, normalized with $\kappa\Delta^2/\delta_T^2$, vs Ra. The error bars represent the standard deviation of the dataset with respect to the temporal average.

3. Ratio of the boundary layer and the bulk dissipation

To analyze the relative strengths of the thermal dissipation in the bulk and in the boundary layers, we divide Eq. (21) with Eqs. (16) and (18) to obtain the ratio of the total dissipation in the boundary layers and the bulk for $\text{Pr} = 1$ and 100, respectively. The predicted ratio is

$$\frac{\tilde{D}_{T,\text{BL}}}{\tilde{D}_{T,\text{bulk}}} \sim \begin{cases} \text{Ra}^{0.02}, & \text{Pr} = 1, \\ \text{Ra}^{-0.07}, & \text{Pr} = 100. \end{cases} \quad (22)$$

Thus, we expect the ratio of the boundary layer and bulk dissipation to have a weak dependence on Ra. For $\text{Pr} = 1$, this ratio remains approximately constant, implying that the relative strengths of the bulk and the boundary layer dissipation remain roughly invariant with Ra. However, for $\text{Pr} = 100$, the above ratio decreases weakly with Ra; this implies that the relative strength of the boundary layer dissipation decreases with Ra and that of the bulk dissipation increases with Ra. The magnitudes of the prefactors in Eq. (22) determine whether the bulk or the boundary layer dissipation is dominant. These prefactors are obtained using numerical simulations.

4. Numerical verification of the scaling arguments

We numerically verify the scaling relations predicted by Eqs. (16), (18), (21), and (22). We compute \tilde{D}_T (the total dissipation in the entire volume), $\tilde{D}_{T,\text{bulk}}$, and $\tilde{D}_{T,\text{BL}}$ using our simulation data and plot them vs Ra in Fig. 4(a) for $\text{Pr} = 1$ and in Fig. 4(b) for $\text{Pr} = 100$. Our data fit well with the following expressions:

$$\tilde{D}_T = 0.16c\text{Ra}^{0.29}, \quad \text{Pr} = 1, 100, \quad (23)$$

$$\tilde{D}_{T,\text{bulk}} = \begin{cases} 0.041c\text{Ra}^{0.29}, & \text{Pr} = 1, \\ 0.015c\text{Ra}^{0.34}, & \text{Pr} = 100, \end{cases} \quad (24)$$

$$\tilde{D}_{T,\text{BL}} = \begin{cases} 0.12c\text{Ra}^{0.29}, & \text{Pr} = 1, \\ 0.15c\text{Ra}^{0.28}, & \text{Pr} = 100, \end{cases} \quad (25)$$

where $c = \kappa\Delta^2 d$. The errors in the exponents in the above expressions range from 0.001 to 0.02. The above expressions match with the scaling arguments presented in Eqs. (21), (16), and (18) within the fitting error.

The computed ratio of the boundary layer and the bulk dissipation is

$$\frac{\tilde{D}_{T,\text{BL}}}{\tilde{D}_{T,\text{bulk}}} \approx \begin{cases} 3.0, & \text{Pr} = 1, \\ 10\text{Ra}^{-0.06}, & \text{Pr} = 100, \end{cases} \quad (26)$$

which agrees well with Eq. (22). We plot this ratio in Fig. 4(c) for $\text{Pr} = 1$ and Fig. 4(d) for $\text{Pr} = 100$.

Because of the prefactors in Eq. (26), the ratio of the boundary layer and the bulk dissipation remains above unity, implying that the boundary layer dissipation is larger than the bulk dissipation, although they are of the same order. As shown in Figs. 4(c) and 4(d), the boundary layer dissipation is approximately 3–4 times greater than the bulk dissipation. This is unlike viscous dissipation for $\text{Pr} = 1$, where the dissipation in the bulk is greater, albeit marginally, than that in the boundary layers.³⁴ This is because while the temperature is fairly constant in the bulk (except for a few regions of localized plumes), the velocity in the bulk is not so, as illustrated in

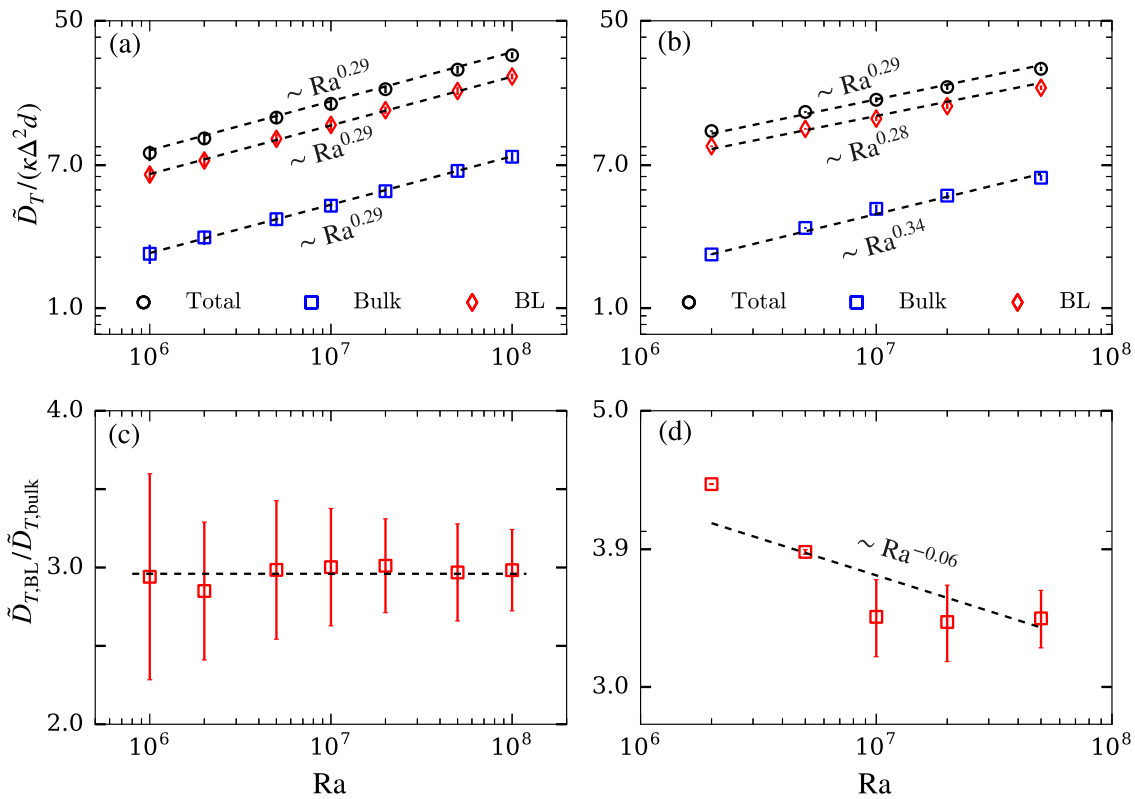


FIG. 4. For (a) $Pr = 1$ and (b) $Pr = 100$: plots of thermal dissipation rates \tilde{D}_T —total, bulk, and in the boundary layers (BL)—vs Ra. For (c) $Pr = 1$ and (d) $Pr = 100$: plots of the dissipation rate ratio, $\tilde{D}_{T,BL} / \tilde{D}_{T,bulk}$, vs Ra. The error bars represent the standard deviation of the dataset with respect to the temporal average.

Fig. 5. Here, we show the temperature density plot superimposed with velocity vector plot on the x - z plane at $y = d/2$, for $Ra = 10^8$, $Pr = 1$. Clearly, the velocity fluctuations are large near the walls (just outside the viscous boundary layers) but small near the center. On the other hand, $T \approx 0.5$ in the bulk. Thus, the velocity gradients in

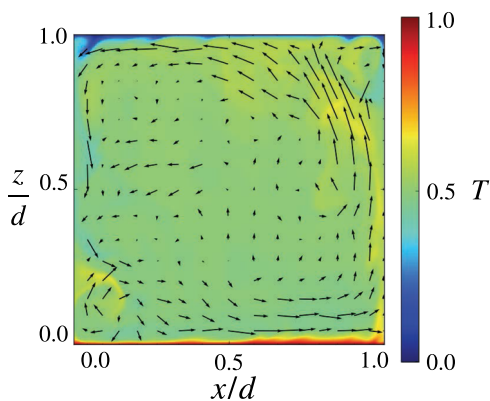


FIG. 5. For $Ra = 10^8$, $Pr = 1$: Density plot of temperature field, superimposed with velocity vector plot, on the x - z plane at $y = d/2$. The temperature is approximately constant in the bulk, unlike the velocity fluctuations.

the bulk are more pronounced than the temperature gradients; this results in stronger viscous dissipation compared to thermal dissipation in the bulk. However, one must note that for $Pr = 100$, the viscous boundary layers will occupy almost the entire volume; thus, the viscous dissipation in the boundary layers will be dominant. Also, we need to carefully simulate low Pr convection to find out whether bulk or boundary layer dissipation dominates in this regime.

The dominance of the total thermal dissipation in the boundary layers has been reported previously for convection in a slender cylindrical cell²⁴ and for two-dimensional convection.³⁵

C. Spatial intermittency of thermal dissipation rate

In this subsection, we will study the intermittency of the local thermal dissipation rate $\epsilon_T(\mathbf{r})$. Since $\delta_T/d \ll 1$ (see Fig. 1), the boundary layers occupy a much smaller volume than the bulk. Therefore, $\epsilon_T(\mathbf{r})$ is much stronger in the boundary layers than in the bulk.

We compute the probability distribution functions (PDFs) of $\epsilon_T^*(\mathbf{r}) = \epsilon_T(\mathbf{r})/\epsilon_T$ in the entire volume, bulk and boundary layers to quantify the spatial intermittency of thermal dissipation rate. The PDFs are computed for $Ra = 5 \times 10^7$ for both $Pr = 1$ and 100. We plot these quantities in Fig. 6(a) for $Pr = 1$ and in Fig. 6(b) for $Pr = 100$. From the inset of Fig. 6(a), we observe that for $Pr = 1$, $P(\epsilon_{T,bulk}^*) \gg P(\epsilon_{T,BL}^*)$ for $\epsilon_T^* < 10$, while $P(\epsilon_{T,bulk}^*) \ll P(\epsilon_{T,BL}^*)$ for $\epsilon_T^* > 10$.

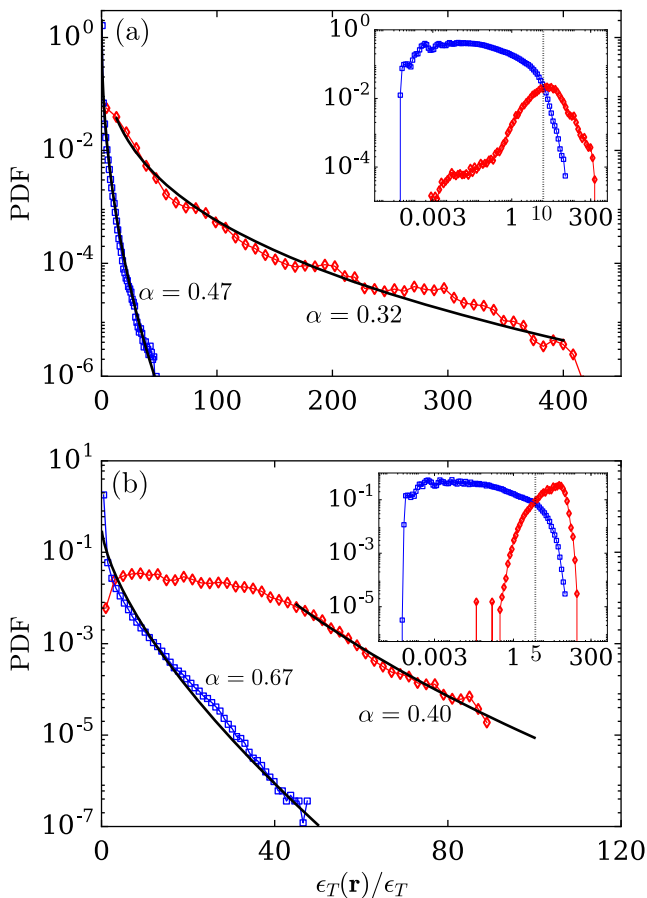


FIG. 6. For $Ra = 5 \times 10^7$ and (a) $Pr = 1$ and (b) $Pr = 100$: probability distribution functions (PDF) of normalized local dissipation rate $\epsilon_T(\mathbf{r})/\epsilon_T$ in the bulk (blue squares) and in the boundary layers (red diamonds). The PDFs of both $\epsilon_{T,BL}$ and $\epsilon_{T,bulk}$ fit well with stretched exponential curves (black solid lines). The insets in (a) and (b) show the log-log plots of the PDFs of $\epsilon_T(\mathbf{r})$ in the bulk and the boundary layers.

This clearly shows that thermal dissipation is weak in the bulk and strong in the boundary layers. We observe a similar behavior for $Pr = 100$, but with cutoff $\epsilon_T^* \approx 5$ [see the inset of Fig. 6(b)].

It has been analytically shown by Chertkov, Falkovich, and Kolokolov⁴⁶ that the passive scalar dissipation has a stretched exponential distribution. This profile is given by $P(\epsilon_T) \sim \beta \exp(-m\epsilon_T^*)$ for $\epsilon_T^* \gg 1$. Interestingly, the PDFs of thermal dissipation for RBC are also stretched exponential for both bulk and boundary layers. Our observation is consistent with earlier studies.^{35,44,47} For bulk dissipation, the stretching exponent $\alpha = 0.47$ for $Pr = 1$ and $\alpha = 0.67$ for $Pr = 100$. The corresponding exponents for the boundary layers are 0.32 and 0.40, respectively.

Clearly, for both Pr , the tails of the PDFs are stretched more for the boundary layer dissipation. This is expected because extreme events are more frequent in the boundary layers than in the bulk; note that $\epsilon_T(\mathbf{r})$ is stronger in the boundary layers. Furthermore, for both bulk and boundary layer dissipation, α 's are smaller for $Pr = 1$. Thus, the tails of the PDFs are stretched more for $Pr = 1$, implying

stronger spatial intermittency of thermal dissipation for the lower Pr fluid. This is because for $Pr = 1$, convection is more turbulent than that for $Pr = 100$, causing the temperature fluctuations to be more pronounced for the former.

V. CONCLUSIONS

In this paper, we present scaling relations for the thermal dissipation rate in the bulk and in the boundary layers in turbulent convection. Using numerical simulations of RBC, we show that compared to passive scalar turbulence, the thermal dissipation rate in the bulk is suppressed by a factor of $Ra^{-0.22}$ for $Pr = 1$ and $Ra^{-0.25}$ for $Pr = 100$. Furthermore, unlike viscous dissipation, the total thermal dissipation in the boundary layers is greater than that in the bulk. The ratio of the boundary layer and the bulk dissipation is roughly constant for $Pr = 1$ and decreases weakly with Ra for $Pr = 100$.

We also show that the probability distribution functions of thermal dissipation rate, both in the bulk and in the boundary layers, are stretched exponential, similar to passive scalar dissipation. The stretching exponent for the PDFs of boundary layer dissipation is lower than that of bulk dissipation, implying that extreme events occur more often in the boundary layers than in the bulk. We also show that the spatial intermittency of thermal dissipation is stronger for lower Pr fluids.

The results presented in this paper are important for modeling thermal convection. For example, we may need to incorporate the suppression of thermal dissipation in the bulk in the scaling analysis for Pe and Nu . Thus far, our analysis has been for $Pr \geq 1$. We need to extend them to low Pr convection for a comprehensive modeling of thermal convection.

ACKNOWLEDGMENTS

We thank A. Pandey, A. Guha, and R. Samuel for useful discussions. Our numerical simulations were performed on Shaheen II at KAUST Supercomputing Laboratory, Saudi Arabia, under the Project No. k1052. This work was supported by the research Grant No. PLANEX/PHY/2015239 from Indian Space Research Organisation, India, and by the Department of Science and Technology, India (Grant No. INT/RUS/RSF/P-03), and the Russian Science Foundation, Russia (Grant No. RSF-16-41-02012), for the Indo-Russian project.

REFERENCES

- A. M. Obukhov, "Structure of the temperature field in a turbulent flow," *Izv. Geogr. Geophys. Ser.* **13**, 58–69 (1949).
- S. Corrsin, "On the spectrum of isotropic temperature fluctuations in an isotropic turbulence," *J. Appl. Phys.* **22**, 469–473 (1951).
- M. Lesieur, *Turbulence in Fluids* (Springer-Verlag, Dordrecht, 2008).
- M. K. Verma, *Physics of Buoyant Flows* (World Scientific, Singapore, 2018).
- G. Ahlers, S. Grossmann, and D. Lohse, "Heat transfer and large scale dynamics in turbulent Rayleigh-Bénard convection," *Rev. Mod. Phys.* **81**, 503–537 (2009).
- D. Lohse and K.-Q. Xia, "Small-scale properties of turbulent Rayleigh-Bénard convection," *Annu. Rev. Fluid Mech.* **42**, 335–364 (2010).
- M. K. Verma, A. Kumar, and A. Pandey, "Phenomenology of buoyancy-driven turbulence: Recent results," *New J. Phys.* **19**, 025012 (2017).
- B. I. Shraiman and E. D. Siggia, "Heat transport in high-Rayleigh-number convection," *Phys. Rev. A* **42**, 3650–3653 (1990).

- ⁹R. H. Kraichnan, "Turbulent thermal convection at arbitrary Prandtl number," *Phys. Fluids* **5**, 1374–1389 (1962).
- ¹⁰M. K. Verma, P. K. Mishra, A. Pandey, and S. Paul, "Scalings of field correlations and heat transport in turbulent convection," *Phys. Rev. E* **85**, 016310 (2012).
- ¹¹S. Grossmann and D. Lohse, "Scaling in thermal convection: A unifying theory," *J. Fluid Mech.* **407**, 27–56 (2000).
- ¹²S. Grossmann and D. Lohse, "Thermal convection for large Prandtl numbers," *Phys. Rev. Lett.* **86**, 3316–3319 (2001).
- ¹³W. V. R. Malkus, "The heat transport and spectrum of thermal turbulence," *Proc. R. Soc. London, Ser. A* **225**, 196–212 (1954).
- ¹⁴B. Castaing, G. Gunaratne, L. P. Kadanoff, A. Libchaber, and F. Heslot, "Scaling of hard thermal turbulence in Rayleigh-Bénard convection," *J. Fluid Mech.* **204**, 1–30 (1989).
- ¹⁵S. Grossmann and D. Lohse, "Prandtl and Rayleigh number dependence of the Reynolds number in turbulent thermal convection," *Phys. Rev. E* **66**, 016305 (2002).
- ¹⁶X.-L. Qiu and P. Tong, "Temperature oscillations in turbulent Rayleigh-Bénard convection," *Phys. Rev. E* **66**, 026308 (2002).
- ¹⁷X.-L. Qiu, X.-D. Shang, P. Tong, and K.-Q. Xia, "Velocity oscillations in turbulent Rayleigh-Bénard convection," *Phys. Fluids* **16**, 412–423 (2004).
- ¹⁸E. Brown, D. Funfschilling, and G. Ahlers, "Anomalous Reynolds-number scaling in turbulent Rayleigh-Bénard convection," *J. Stat. Mech.: Theory Exp.* **2007**, P10005.
- ¹⁹D. Funfschilling, E. Brown, A. Nikolaenko, and G. Ahlers, "Heat transport by turbulent Rayleigh-Bénard convection in cylindrical samples with aspect ratio one and larger," *J. Fluid Mech.* **536**, 145–154 (2005).
- ²⁰A. Nikolaenko, E. Brown, D. Funfschilling, and G. Ahlers, "Heat transport by turbulent Rayleigh-Bénard convection in cylindrical cells with aspect ratio one and less," *J. Fluid Mech.* **523**, 251–260 (2005).
- ²¹X. He, D. Funfschilling, E. Bodenschadtz, and G. Ahlers, "Heat transport by turbulent Rayleigh-Bénard convection for $Pr \approx 0.8$ and $4 \times 10^{11} \lesssim Ra \lesssim 2 \times 10^{14}$: Ultimate-state transition for aspect ratio $\Gamma = 1.00$," *New J. Phys.* **14**, 063030 (2012).
- ²²G. Ahlers, X. He, D. Funfschilling, and E. Bodenschadtz, "Heat transport by turbulent Rayleigh-Bénard convection for $Pr \approx 0.8$ and $3 \times 10^{12} \lesssim Ra \lesssim 10^{15}$: Aspect ratio $\Gamma = 0.50$," *New J. Phys.* **14**, 103012 (2012).
- ²³M. Vial and R. H. Hernández, "Feedback control and heat transfer measurements in a Rayleigh-Bénard convection cell," *Phys. Fluids* **29**, 074103 (2017).
- ²⁴R. Verzicco and R. Camussi, "Numerical experiments on strongly turbulent thermal convection in a slender cylindrical cell," *J. Fluid Mech.* **477**, 19–49 (2003).
- ²⁵J. D. Scheel, E. Kim, and K. R. White, "Thermal and viscous boundary layers in turbulent Rayleigh-Bénard convection," *J. Fluid Mech.* **711**, 281–305 (2012).
- ²⁶J. D. Scheel and J. Schumacher, "Local boundary layer scales in turbulent Rayleigh-Bénard convection," *J. Fluid Mech.* **758**, 344–373 (2014).
- ²⁷F. Waleffe, A. Boonkasame, and L. M. Smith, "Heat transport by coherent Rayleigh-Bénard convection," *Phys. Fluids* **27**, 051702 (2015).
- ²⁸M. K. Verma, S. C. Ambhire, and A. Pandey, "Flow reversals in turbulent convection with free-slip walls," *Phys. Fluids* **27**, 047102 (2015).
- ²⁹W.-F. Zhou and J. Chen, "Letter: Similarity model for corner roll in turbulent Rayleigh-Bénard convection," *Phys. Fluids* **30**, 111705 (2018).
- ³⁰A. Pandey and M. K. Verma, "Scaling of large-scale quantities in Rayleigh-Bénard convection," *Phys. Fluids* **28**, 095105 (2016).
- ³¹A. Pandey, A. Kumar, A. G. Chatterjee, and M. K. Verma, "Dynamics of large-scale quantities in Rayleigh-Bénard convection," *Phys. Rev. E* **94**, 053106 (2016).
- ³²B. A. Puthenveetil and J. H. Arakeri, "Plume structure in high-Rayleigh-number convection," *J. Fluid Mech.* **542**, 217–249 (2005).
- ³³B. A. Puthenveetil, G. Ananthakrishna, and J. H. Arakeri, "The multifractal nature of plume structure in high-Rayleigh-number convection," *J. Fluid Mech.* **526**, 245–256 (2005).
- ³⁴S. Bhattacharya, A. Pandey, A. Kumar, and M. K. Verma, "Complexity of viscous dissipation in turbulent thermal convection," *Phys. Fluids* **30**, 031702 (2018).
- ³⁵Y. Zhang, Q. Zhou, and C. Sun, "Statistics of kinetic and thermal energy dissipation rates in two-dimensional turbulent Rayleigh-Bénard convection," *J. Fluid Mech.* **814**, 165–184 (2017).
- ³⁶S. Chandrasekhar, *Hydrodynamic and Hydromagnetic Stability* (Oxford University Press, Oxford, 2013).
- ³⁷A. Kumar and M. K. Verma, "Applicability of Taylor's hypothesis in thermally driven turbulence," *R. Soc. Open Sci.* **5**, 172152 (2018).
- ³⁸H. Jasak, A. Jemcov, Z. Tukovic *et al.*, "OpenFOAM: A C++ library for complex physics simulations," in *International Workshop on Coupled Methods in Numerical Dynamics* (IUC Dubrovnik, Croatia, 2007), Vol. 1000, pp. 1–20.
- ³⁹G. Grötzbach, "Spatial resolution requirements for direct numerical simulation of the Rayleigh-Bénard convection," *J. Comput. Phys.* **49**, 241–264 (1983).
- ⁴⁰N. Shi, M. S. Emran, and J. Schumacher, "Boundary layer structure in turbulent Rayleigh-Bénard convection," *J. Fluid Mech.* **706**, 5–33 (2012).
- ⁴¹G. K. Batchelor, "Small-scale variation of convected quantities like temperature in turbulent fluid Part I. General discussion and the case of small conductivity," *J. Fluid Mech.* **5**, 113–133 (1959).
- ⁴²S. Wagner and O. Shishkina, "Aspect-ratio dependency of Rayleigh-Bénard convection in box-shaped containers," *Phys. Fluids* **25**, 085110 (2013).
- ⁴³A. Pandey, M. K. Verma, and P. K. Mishra, "Scaling of heat flux and energy spectrum for very large Prandtl number convection," *Phys. Rev. E* **89**, 023006 (2014).
- ⁴⁴M. S. Emran and J. Schumacher, "Fine-scale statistics of temperature and its derivatives in convective turbulence," *J. Fluid Mech.* **611**, 13–34 (2008).
- ⁴⁵O. Shishkina, M. S. Emran, S. Grossmann, and D. Lohse, "Scaling relations in large-Prandtl-number natural thermal convection," *Phys. Rev. Fluids* **2**, 103502 (2017).
- ⁴⁶M. Chertkov, G. Falkovich, and I. Kolokolov, "Intermittent dissipation of a passive scalar in turbulence," *Phys. Rev. Lett.* **80**, 2121–2124 (1998).
- ⁴⁷X. He and P. Tong, "Measurements of the thermal dissipation field in turbulent Rayleigh-Bénard convection," *Phys. Rev. E* **79**, 026306 (2009).

Chapter 7

Revisiting Reynolds and Nusselt numbers in turbulent thermal convection

7.1 Introduction

A well-known model to predict the Reynolds and Nusselt numbers in RBC for a given set of governing parameters was developed by [Grossmann and Lohse \(2000, 2001, 2002, 2003\)](#). This model, referred to as the GL model, has been quite successful in predicting large scale velocity and heat transport in many experiments and simulations. However, the GL model is based on the following assumptions: (i) the viscous boundary layer thickness follows Prandtl-Blasius relation of $\delta_u \sim \text{Re}^{-1/2}$, and (ii) the viscous and thermal dissipation rates in the bulk scale as U^3/d and $U\Delta^2/d$ respectively, similar to homogeneous isotropic turbulence away from the walls. However, as shown in Chapters 5 and 6, the viscous and the thermal dissipation rates in the bulk for moderate-Pr RBC get additional correction factors, respectively, of approximately $\text{Ra}^{-0.18}$ and $\text{Ra}^{-0.21}$. Further, in RBC, the viscous boundary layer thickness, δ_u , deviates marginally from $\sim \text{Re}^{-1/2}$, as shown in Chapter 5 and also in earlier works ([Breuer et al., 2004](#); [Scheel et al., 2012](#); [Shi et al., 2012](#)).

In this chapter, we significantly enhance the GL model by incorporating the additional Ra dependence on the bulk viscous and thermal dissipation rates. We also take into account the deviation in the scaling of the viscous boundary layer thickness. The

results presented in this chapter are published in *Physics of Fluids* (Bhattacharya et al., 2021b).

A summary of our results is as follows.

7.2 A summary of our results

Grossmann and Lohse (2000, 2001) derived their predictive model by substituting the bulk and the boundary layer contributions of viscous and thermal dissipation rates in the exact relations of Shraiman and Siggia (1990). The bulk and the boundary layer contributions were written in terms of Re , Nu , Ra , and Pr and thus a system of equations for Re and Nu in terms of Ra and Pr were obtained. The prefactors of the bulk and boundary layer dissipation rates in these equations were considered to be constants. We extend the GL model by writing these prefactors as functions, instead of constants, in these equations. The functional forms of the prefactors arise due to the additional Ra dependence in the scaling of the bulk dissipation rates and the deviation of the viscous boundary layer thickness from Prandtl-Blasius theory. Using these revised equations, we arrive at a cubic polynomial equation for Re and Nu that reduces to power-law expressions in the limit of viscous dissipation rate dominating in the bulk.

We perform 60 direct numerical simulations of RBC covering a wide range of Ra and Pr and compute the prefactors of the bulk and boundary layer dissipation rates. As expected, we find the prefactors to be functions of Ra . Additionally, these prefactors are found to be weakly dependent on Pr as well. The functional forms of these prefactors are determined using machine learning algorithm (regression analysis) and were then plugged into the aforementioned cubic polynomial equation for Re and Nu . The revised predictions are in better agreement with the past numerical and experimental results than those of the GL model. We observe significant improvements in the predictions of Re , which is important because Re is more sensitive to modeling parameters compared to Nu . The improvement in the predictions of Nu is more pronounced for extreme Pr regimes ($Pr \leq 0.02$ and ≥ 100).

Our results underscore the importance of applying data-driven methods to improve existing models, a practice that has recently been picking up pace in research on turbulence (Parish and Duraisamy, 2016; Pandey et al., 2020). Our work presently takes inputs from data that are restricted to $Ra < 10^{10}$ and unit aspect ratio. Our pre-

dictions can be further enhanced after taking inputs from simulations or experiments for $Ra > 10^{10}$ and for different aspect ratios.

7.3 Published manuscript

The details of our numerical simulations and the results are presented in the attached published manuscript ([Bhattacharya et al., 2021b](#)).

Revisiting Reynolds and Nusselt numbers in turbulent thermal convection

Cite as: Phys. Fluids 33, 015113 (2021); doi: 10.1063/5.0032498

Submitted: 8 October 2020 • Accepted: 19 December 2020 •

Published Online: 11 January 2021



Shashwat Bhattacharya,^{1,a)} Mahendra K. Verma,² and Ravi Samtaney³

AFFILIATIONS

¹Department of Mechanical Engineering, Indian Institute of Technology Kanpur, Kanpur 208016, India

²Department of Physics, Indian Institute of Technology Kanpur, Kanpur 208016, India

³Mechanical Engineering, Division of Physical Science and Engineering, King Abdullah University of Science and Technology, Thuwal 23955, Saudi Arabia

^{a)} Author to whom correspondence should be addressed: shabhatt@iitk.ac.in

ABSTRACT

In this paper, we extend Grossmann and Lohse's (GL) model [S. Grossmann and D. Lohse, "Thermal convection for large Prandtl numbers," Phys. Rev. Lett. **86**, 3316 (2001)] for the predictions of Reynolds number (Re) and Nusselt number (Nu) in turbulent Rayleigh–Bénard convection. Toward this objective, we use functional forms for the prefactors of the dissipation rates in the bulk and boundary layers. The functional forms arise due to inhibition of nonlinear interactions in the presence of walls and buoyancy compared to free turbulence, along with a deviation of the viscous boundary layer profile from Prandtl–Blasius theory. We perform 60 numerical runs on a three-dimensional unit box for a range of Rayleigh numbers (Ra) and Prandtl numbers (Pr) and determine the aforementioned functional forms using machine learning. The revised predictions are in better agreement with the past numerical and experimental results than those of the GL model, especially for extreme Prandtl numbers.

Published under license by AIP Publishing. <https://doi.org/10.1063/5.0032498>

I. INTRODUCTION

A classical problem in fluid dynamics is Rayleigh–Bénard convection (RBC), where a fluid is enclosed between two horizontal walls with the bottom wall kept at a higher temperature than the top wall. RBC serves as a paradigm for many types of convective flows occurring in nature and in engineering applications. RBC is primarily governed by two parameters: the Rayleigh number, Ra, which is the ratio of the buoyancy and the dissipative force, and the Prandtl number, Pr, which is the ratio of kinematic viscosity and thermal diffusivity of the fluid. In this paper, we derive a relation to predict two important quantities—the Nusselt number, Nu, and the Reynolds number, Re, which are respective measures of large-scale heat transport and velocity in turbulent RBC.

The dependence of Nu and Re on RBC's governing parameters (Ra and Pr) has been extensively studied in the literature.^{1–5} Malkus⁶ proposed $Nu \sim Ra^{1/3}$ based on marginal stability theory. For very large Ra called the ultimate regime, Kraichnan⁷ deduced $Nu \sim \sqrt{RaPr}$, $Re \sim \sqrt{Ra/Pr}$ for $Pr \leq 0.15$ and $Nu \sim \sqrt{RaPr^{-1/2}}$, $Re \sim \sqrt{Ra/Pr^{3/2}}$ for $0.15 < Pr \leq 1$, with logarithmic corrections. Subsequently, Castaing *et al.*⁸ argued that $Nu \sim Ra^{2/7}$ and $Re \sim Ra^{3/7}$

based on the existence of a mixing zone in the central region of the RBC cell, where hot rising plumes meet the mildly warm fluid. Castaing *et al.*⁸ also deduced that $Re^\omega \sim Ra^{1/2}$, where Re^ω is the Reynolds number based on the frequency ω of torsional azimuthal oscillations of the large-scale wind in RBC. Later, Shraiman and Siggia⁹ derived that $Nu \sim Ra^{2/7} Pr^{-1/7}$ and $Re \sim Ra^{3/7} Pr^{-5/7}$ (with logarithmic corrections) using the properties of boundary layers. They also derived exact relations between Nu and the viscous and thermal dissipation rates.

Many experiments and simulations of RBC have been performed to obtain the scaling of Nu and Re. These studies also revealed a power-law scaling of Nu and Re as $Nu \sim Ra^\alpha Pr^\beta$ and $Re \sim Ra^\gamma Pr^\delta$. For the scaling of Nu, the exponent α ranges from 1/4 for $Pr \ll 1$ to approximately 1/3 for $Pr \gtrsim 1$ ^{8,10–29} and β from approximately zero for $Pr \gtrsim 1$ to 0.14 for $Pr \ll 1$.^{30,31} Thus, Nu has a relatively weaker dependence on Pr. For the scaling of Re, the exponent γ was observed to be approximately 2/5 for $Pr \ll 1$, 1/2 for $Pr \sim 1$, and 3/5 for $Pr \gg 1$,^{8,10,11,15–18,22–24,32–35} and δ has been observed to range from -0.7 for $Pr \lesssim 1$ to -0.95 for $Pr \gg 1$.^{30,36} A careful examination of the results of the above references reveals that the above exponents also depend on the regime of Ra as well. The

ultimate regime, characterized by $Nu \sim \sqrt{Ra}$, has been observed in simulations of RBC with periodic boundary conditions,^{34,37} in free convection with the density gradient,^{38–40} and in convection with only lateral walls.⁴¹ Using numerical simulations, Calzavarini *et al.*⁴² showed that $Re \sim Pr^{1/2}$ and $Nu \sim Pr^{1/2}$ for convection with periodic walls. However, some doubts have been raised on the ultimate scaling observed in RBC with periodic walls because of the presence of elevator modes in the system.^{43,44} Some experiments and simulations of RBC with non-periodic walls and very large Ra ($\sim 10^{15}$) have reported a possible transition to the ultimate regime;^{15,38,45,46} however, some others^{47,48} argue against such transition.

The above studies show that the scaling of Re and Nu depends on the regime of Ra and Pr , highlighting the need for a unified model that encompasses all the regimes. Grossmann and Lohse^{49–52} constructed one such model, henceforth referred to as the GL model. To derive this model, Grossmann and Lohse^{49,50} substituted the bulk and boundary layer contributions of viscous and thermal dissipation rates in the exact relations of Shraiman and Siggia.⁹ The bulk and boundary layer contributions were written in terms of Re , Nu , Ra , and Pr using the properties of boundary layers (Prandtl–Blasius theory)⁵³ and those of hydrodynamic and passive scalar turbulence in the bulk. Finally, using additional crossover functions, Grossmann and Lohse⁵⁰ obtained a system of equations for Re and Nu in terms of Ra , Pr , and four coefficients that were determined using inputs from experimental data.⁵⁴ Using the momentum equation of RBC, Pandey *et al.*^{22,23} constructed a model to predict the Reynolds number as a function of Ra and Pr . The predictions of Kraichnan,⁷ Castaing *et al.*,⁸ and Shraiman and Siggia⁹ are limiting cases of the GL model.

The GL model has been quite successful in predicting large-scale velocity and heat transport in many experiments and simulations. However, it does not capture large Pr convection very accurately⁵ and has been reported to under-predict the Reynolds number.¹ Note that the scaling exponent for Re has a longer range (0.40–0.60) compared to that for Nu (0.25–0.33); hence, the predictions for Re are more sensitive to modeling parameters. Furthermore, the GL model is based on certain assumptions that are not valid for RBC. For example, the model assumes the viscous and the thermal dissipation rate in the bulk scale as U^3/d and $U\Delta^2/d$ (for $Pr \lesssim 1$), respectively, as in passive scalar turbulence with open boundaries.^{55,56} Here, U is the large-scale velocity, and Δ and d are, respectively, the temperature difference and distance between the top and bottom walls. However, subsequent studies of RBC have shown that the aforementioned viscous and thermal dissipation rates in the bulk are suppressed by approximately $Ra^{-0.2}$ for $Pr \sim 1$.^{11,17,22,23,57–59} The above suppression is due to the inhibition of nonlinear interactions because of walls^{22,23} and buoyancy.⁶⁰ Moreover, recent studies have revealed that the viscous boundary layer thickness in RBC considerably deviate from $Re^{-1/2}$ as assumed in the GL model.^{58,61,62}

In the present work, we address the above limitations of the GL model and propose a new relation for the Reynolds and Nusselt numbers involving a cubic polynomial equation for Re and Nu . For implementation of the viscous and thermal dissipation rates in the bulk and boundary layers, we employ machine-learning tools on 60 datasets that were obtained using numerical simulations of RBC. The new relation rectifies some of the limitations of the GL model, especially for small and large Prandtl numbers.

The outline of the paper is as follows: In Sec. II, we discuss the governing equations of RBC and briefly explain the GL model. Then, we extend the GL framework by using functional forms for the prefactors of the dissipation rates in the bulk and boundary layers and incorporate the deviation in the scaling of viscous boundary layer thickness described earlier. Simulation details are provided in Sec. III. In Sec. IV, we report the scaling of boundary layer thicknesses and dissipation rates using our data, following which we describe the machine-learning tools used to determine the aforementioned functional forms. We also test the revised predictions with experiments and numerical simulations, and compare them with those of the GL model. We conclude in Sec. V.

II. RBC EQUATIONS AND THE GL MODEL

We consider RBC under the Boussinesq approximation, whose governing equations are as follows:^{5,63}

$$\frac{\partial \mathbf{u}}{\partial t} + (\mathbf{u} \cdot \nabla) \mathbf{u} = -\nabla p / \rho_0 + \alpha g T \hat{z} + \nu \nabla^2 \mathbf{u}, \quad (1)$$

$$\frac{\partial T}{\partial t} + (\mathbf{u} \cdot \nabla) T = \kappa \nabla^2 T, \quad (2)$$

$$\nabla \cdot \mathbf{u} = 0, \quad (3)$$

where \mathbf{u} and p are the velocity and pressure fields, respectively, T is the temperature field, ν is the kinematic viscosity, κ is the thermal diffusivity, α is the thermal expansion coefficient, ρ_0 is the mean density of the fluid, and g is the acceleration due to gravity.

Using d as the length scale, $\sqrt{\alpha g \Delta d}$ as the velocity scale, and Δ as the temperature scale, we non-dimensionalize Eqs. (1)–(3) that yield

$$\frac{\partial \mathbf{u}}{\partial t} + \mathbf{u} \cdot \nabla \mathbf{u} = -\nabla p + T \hat{z} + \sqrt{\frac{Pr}{Ra}} \nabla^2 \mathbf{u}, \quad (4)$$

$$\frac{\partial T}{\partial t} + \mathbf{u} \cdot \nabla T = \frac{1}{\sqrt{RaPr}} \nabla^2 T, \quad (5)$$

$$\nabla \cdot \mathbf{u} = 0, \quad (6)$$

where $Ra = \alpha g \Delta d^3 / (\nu \kappa)$ is the Rayleigh number and $Pr = \nu / \kappa$ is the Prandtl number. The large-scale velocity and heat transfer are quantified by two important non-dimensional quantities, namely, the Reynolds number (Re) and the Nusselt number (Nu). The Nusselt number, Nu , is the ratio of the total heat flux to the conductive heat flux and is defined as $Nu = 1 + \langle u_z T \rangle / (\kappa \Delta / d)$. The Reynolds number Re is defined as $Re = Ud / \nu$, where U is the large-scale velocity. In our work, we will consider U to be the root mean square (rms) velocity, that is, $U = \sqrt{\langle u_x^2 + u_y^2 + u_z^2 \rangle}$, where $\langle \cdot \rangle$ represents the volume average.

The dissipation rates of kinetic and thermal energies, represented as ϵ_u and ϵ_T , respectively, are important quantities in our study. These are defined as $\epsilon_u = 2\nu \langle S_{ij} S_{ij} \rangle$ and $\epsilon_T = \kappa \langle |\nabla T|^2 \rangle$, where S_{ij} is the strain rate tensor. Shraiman and Siggia⁹ derived two exact relations between Nu and the dissipation rates; these are

$$\epsilon_u = \frac{\nu^3}{d^4} (Nu - 1) \frac{Ra}{Pr^2}, \quad (7)$$

$$\epsilon_T = \frac{\kappa\Delta^2}{d^2} \text{Nu}. \quad (8)$$

The above relations will be the backbone of our present work.

Now, we will briefly summarize the GL model to predict Nu and Re. Grossmann and Lohse^{49,50} split the total viscous and thermal dissipation rates ($\tilde{D}_u = \epsilon_u V$ and $\tilde{D}_T = \epsilon_T V$, respectively, V being the domain volume) into their bulk and boundary layer contributions. Thus,

$$\tilde{D}_u = \tilde{D}_{u,\text{bulk}} + \tilde{D}_{u,\text{BL}}, \quad (9)$$

$$\tilde{D}_T = \tilde{D}_{T,\text{bulk}} + \tilde{D}_{T,\text{BL}}. \quad (10)$$

The GL model assumes the Prandtl-Blasius relation of $\delta_u \sim \text{Re}^{-1/2}$ above a critical Reynolds number Re_c for viscous boundary layers and $\delta_T = d/2\text{Nu}$ for thermal boundary layers. Here, δ_u and δ_T are the viscous and thermal boundary layer thicknesses, respectively. For $\text{Re} < \text{Re}_c$, the viscous boundary layer is assumed to occupy the entire RBC cell. Using the above relations and the properties of hydrodynamic and passive scalar turbulence in the bulk (see Sec. IV A), Grossmann and Lohse^{49,50} deduced that

$$\frac{1}{V} \tilde{D}_{u,\text{bulk}} \sim \frac{U^3}{d} = c_1 \frac{v^3}{d^4} \text{Re}^3, \quad (11)$$

$$\frac{1}{V} \tilde{D}_{u,\text{BL}} \sim \frac{\nu U^2}{\delta_u^2} \frac{\delta_u}{d} = c_2 \frac{v^3}{d^4} \text{Re}^{2.5}, \quad (12)$$

$$\frac{1}{V} \tilde{D}_{T,\text{bulk}} \sim \frac{U\Delta^2}{d} = c_3 \frac{\kappa\Delta^2}{d^2} \text{RePr}, \quad (13)$$

$$\frac{1}{V} \tilde{D}_{T,\text{BL}} \sim \frac{\kappa\Delta^2}{\delta_T^2} \frac{\delta_T}{d} = c_4 \frac{\kappa\Delta^2}{d^2} \text{Nu}, \quad (14)$$

where c_1, c_2, c_3 , and c_4 are constants. Note that for $\delta_u > \delta_T$ ($\text{Pr} \gg 1$), Grossmann and Lohse⁴⁹ modified Eq. (13) as

$$\frac{1}{V} \tilde{D}_{T,\text{bulk}} \sim \frac{\delta_T}{\delta_u} \frac{U\Delta^2}{d} = c_3 \frac{\kappa\Delta^2}{d} \text{Re}^{3/2} \text{PrNu}^{-1}. \quad (15)$$

By approximating the dominant terms of Eq. (2) in the thermal boundary layers, Grossmann and Lohse^{49,50} further deduced that $\text{Nu} \sim \text{Re}^{1/2} \text{Pr}^{1/2}$ for $\delta_u < \delta_T$ and $\text{Nu} \sim \text{Re}^{1/2} \text{Pr}^{1/3}$ for $\delta_u > \delta_T$. To ensure smooth transition through different regimes of boundary layer thicknesses and Reynolds number, Grossmann and Lohse⁵⁰ introduced two crossover functions, $f(x) = (1 + x^4)^{-1/4}$ and $g(x) = x(1 + x^4)^{-1/4}$, and applied them in the RHS of Eqs. (12)–(15). Finally, Grossmann and Lohse⁵⁰ put the modeling and splitting assumptions [Eqs. (9)–(15)] together with the exact relations given by Eqs. (7) and (8) to obtain the following set of equations for Nu and Re:

$$(\text{Nu} - 1) \frac{\text{Ra}}{\text{Pr}^2} = c_1 \text{Re}^3 + c_2 \frac{\text{Re}^2}{g(\sqrt{\text{Re}_c/\text{Re}})}, \quad (16)$$

$$\text{Nu} = c_3 \text{PrRe} f \left[\frac{2a\text{Nu}}{\sqrt{\text{Re}_c}} g \left(\sqrt{\frac{\text{Re}_c}{\text{Re}}} \right) \right] + c_4 \sqrt{\text{RePr}} \left\{ f \left[\frac{2a\text{Nu}}{\sqrt{\text{Re}_c}} g \left(\sqrt{\frac{\text{Re}_c}{\text{Re}}} \right) \right] \right\}^{1/2}. \quad (17)$$

The values of the constants, obtained from experiments, are $c_1 = 1.38$, $c_2 = 8.05$, $c_3 = 0.0252$, $c_4 = 0.487$, $a = 0.922$, and $\text{Re}_c = 3.401$.⁵⁴ The above equations can be solved iteratively to obtain Re and Nu for given Ra and Pr.

Although the GL model has been quite successful in predicting Re and Nu, it has certain deficiencies due to some assumptions that are invalid for RBC. First, recent studies reveal that the relation $\delta_u \sim \text{Re}^{-1/2}$ for the viscous boundary layers is not strictly valid for RBC.^{58,61,62} The viscous boundary layer thickness becomes a progressively weaker function of Re as Pr is increased.⁶⁴ Thus, the relation given by Eq. (12) is not accurate. Second, as discussed earlier, studies have shown that for $\text{Pr} \sim 1$, the thermal and viscous dissipation rates in the bulk are suppressed relative to free turbulence,^{17,57–59}

$$\frac{1}{V} \tilde{D}_{u,\text{bulk}} \sim \frac{U^3}{d} \text{Ra}^{-0.18}, \quad \frac{1}{V} \tilde{D}_{T,\text{bulk}} \sim \frac{U\Delta^2}{d} \text{Ra}^{-0.20}.$$

Contrast the above relations with Eqs. (11) and (13)^{58,59} used in the GL model. This clearly signifies that c_1 and c_3 from Eqs. (11) and (13) cannot be treated as constants. Thus, it becomes imperative to study how c_i varies with Ra and Pr in different regimes of RBC.

We propose a modified relation for Re and Nu by incorporating the aforementioned suppression of the total dissipation rates, as well as the modified law for the viscous boundary layers. Toward this objective, we make the following modifications to Eqs. (11)–(14),

$$\frac{1}{V} \tilde{D}_{u,\text{bulk}} = f_1(\text{Ra}, \text{Pr}) \frac{U^3}{d} = f_1(\text{Ra}, \text{Pr}) \frac{v^3}{d^4} \text{Re}^3, \quad (18)$$

$$\frac{1}{V} \tilde{D}_{u,\text{BL}} = f_2(\text{Ra}, \text{Pr}) \frac{\nu U^2}{\delta_u^2} \frac{\delta_u}{d} = f_2(\text{Ra}, \text{Pr}) \frac{v^3}{d^4} \frac{d}{\delta_u} \text{Re}^2, \quad (19)$$

$$\frac{1}{V} \tilde{D}_{T,\text{bulk}} = f_3(\text{Ra}, \text{Pr}) \frac{U\Delta^2}{d} = f_3(\text{Ra}, \text{Pr}) \frac{\kappa\Delta^2}{d^2} \text{RePr}, \quad (20)$$

$$\frac{1}{V} \tilde{D}_{T,\text{BL}} = f_4(\text{Ra}, \text{Pr}) \frac{\kappa\Delta^2}{\delta_T^2} \frac{\delta_T}{d} = f_4(\text{Ra}, \text{Pr}) \frac{\kappa\Delta^2}{d^2} \text{Nu}. \quad (21)$$

Note that we replaced the coefficients c_i with functions $f_i(\text{Ra}, \text{Pr})$. Furthermore, we do not express d/δ_u in terms of Re in Eq. (19). The above modified formulas are inserted in the exact relations of Shraiman and Siggia⁹ that lead to

$$(\text{Nu} - 1) \frac{\text{Ra}}{\text{Pr}^2} = f_1(\text{Ra}, \text{Pr}) \text{Re}^3 + f_2(\text{Ra}, \text{Pr}) \frac{d}{\delta_u} \text{Re}^2, \quad (22)$$

$$\text{Nu} = f_3(\text{Ra}, \text{Pr}) \text{RePr} + 2f_4(\text{Ra}, \text{Pr}) \text{Nu}. \quad (23)$$

The functions $f_i(\text{Ra}, \text{Pr})$ will be later determined using our simulation results. For the sake of brevity, we will skip the arguments within the parenthesis of f_i 's henceforth.

Equations (22) and (23) constitute a system of two equations with two unknowns (Re and Nu). To solve these equations, we will now reduce them to a cubic polynomial equation for Re by eliminating Nu. We rearrange Eq. (23) to obtain

$$\text{Nu} = \frac{f_3}{1 - 2f_4} \text{RePr}. \quad (24)$$

Substitution of Eq. (24) in Eq. (22) yields the following cubic equation for Re:

$$f_1 \text{Re}^3 + f_2 \frac{d}{\delta_u} \text{Re}^2 - \frac{f_3}{1 - 2f_4} \frac{\text{Ra}}{\text{Pr}} \text{Re} + \frac{\text{Ra}}{\text{Pr}^2} = 0. \quad (25)$$

The above equation for Re can be solved for a given Ra and Pr once f_i and δ_u have been determined. We determine Nu using Eq. (24) once Re has been computed.

Now, we will show that in the limit of the viscous dissipation rate dominating in the bulk or in the boundary layers ($\tilde{D}_{u,\text{bulk}} \gg \tilde{D}_{u,\text{BL}}$ or vice versa), Eqs. (22) and (23) are reduced to power-law expressions for Re and Nu. In the following discussion, we consider scaling for these limiting cases.

Case 1: $\tilde{D}_{u,\text{bulk}} \gg \tilde{D}_{u,\text{BL}}$

First, let us consider the case where the viscous dissipation rate in the bulk is dominant. This regime is expected for large Ra ($\gg 10^8$) or for small Pr ($\ll 1$), where the boundary layers are thin. In this regime, $f_2(d/\delta_u)\text{Re}^2 \ll f_1\text{Re}^3$. Assuming $\text{Nu} \gg 1$, Eq. (22) reduces to

$$\text{Nu} \frac{\text{Ra}}{\text{Pr}^2} \approx f_1 \text{Re}^3. \quad (26)$$

Using Eqs. (24) and (26), we arrive at

$$\text{Re} = \sqrt{\frac{f_3}{f_1(1 - 2f_4)} \frac{\text{Ra}}{\text{Pr}}}, \quad (27)$$

$$\text{Nu} = \sqrt{\frac{1}{f_1} \left(\frac{f_3}{1 - 2f_4} \right)^3 \text{RaPr}}. \quad (28)$$

Note that f_1 and f_3 are expected to be constants and $f_4 \approx 0$ when the boundary layers are absent (as in a periodic box) or weak (as in the ultimate regime proposed by Kraichnan⁷). For this case, $\text{Re} \sim \sqrt{\text{Ra}/\text{Pr}}$ and $\text{Nu} \sim \sqrt{\text{RaPr}}$, consistent with the arguments of Kraichnan⁷ for large Ra and small Pr. However, for RBC with walls, the relations for Re and Nu will deviate from the above relations because f_1 and f_3 are functions of Ra and Pr.

Case 2: $\tilde{D}_{u,\text{BL}} \gg \tilde{D}_{u,\text{bulk}}$

Now, we consider the other extreme when the viscous dissipation rates in the boundary layers are dominant, which is expected for small Ra ($\ll 10^5$) or for large Pr ($\gg 7$).^{49,50,57} In this regime, again assuming $\text{Nu} \gg 1$, Eq. (22) reduces to

$$\text{Nu} \frac{\text{Ra}}{\text{Pr}^2} \approx f_2 \frac{d}{\delta_u} \text{Re}^2. \quad (29)$$

Using Eqs. (24) and (29), we obtain

$$\text{Re} = \left\{ \frac{f_3}{f_2(1 - 2f_4)} \frac{\delta_u}{d} \right\} \frac{\text{Ra}}{\text{Pr}}, \quad (30)$$

$$\text{Nu} = \frac{1}{f_2} \frac{\delta_u}{d} \left(\frac{f_3}{1 - 2f_4} \right)^2 \text{Ra}. \quad (31)$$

We will examine these cases once we deduce the forms of f_i using our numerical simulations.

We remark that the aspect ratio of the RBC cell also influences the scaling of Ra and Pr.⁵² In the current work, we do not consider the effect of aspect ratio. We intend to include the aspect ratio dependence in a future work.

In Sec. III, we will discuss the simulation method.

III. SIMULATION DETAILS

We perform direct numerical simulations of RBC by solving Eqs. (4)–(6) in a cubical box of unit dimensions using the finite difference code SARAS.^{66,67} We carry out 60 runs for Pr ranging from 0.02 to 100 and Ra ranging from 5×10^5 to 5×10^9 . The grid size was varied from 257^3 to 1025^3 depending on parameters. Refer to Tables I and II for the simulation details.

We impose isothermal boundary conditions on the horizontal walls and adiabatic boundary conditions on the sidewalls. No-slip boundary conditions were imposed on all the walls. A second-order Crank–Nicholson scheme was used for time-advancement, with the maximum Courant number kept at 0.2. The solver uses a multi-grid method for solving the pressure–Poisson equations. We ensure a minimum of five points in the viscous and thermal boundary layers (see Tables I and II); this satisfies the resolution criterion of Grötzbach,⁶⁸ and Verzicco and Camussi.⁵⁷ The simulations are run up to 3–263 non-dimensional time units (t_{ND}) after attaining a steady state. For post-processing, we employ a central difference method for spatial differentiation and Simpson’s method for computing the volume average.

In order to resolve the smallest scales of the flow, we ensure that the grid spacing Δx is smaller than the Kolmogorov length scale $\eta = (\nu^3 \epsilon_u^{-1})^{1/4}$ for $\text{Pr} \leq 1$ and the Batchelor length scale $\eta_T = (\nu \kappa^2 \epsilon_u^{-1})^{1/4}$ for $\text{Pr} > 1$. We numerically compute ϵ_u and ϵ_T and use these values to compute Nu_u and Nu_T employing Shraiman and Siggia’s exact relations⁹ [see Eqs. (7) and (8)]. The Nusselt numbers computed using $\langle u_z T \rangle$ match with Nu_u and Nu_T within two percent on an average; this further confirms that our runs are well-resolved (see Tables I and II). All the above quantities are averaged over 12 to 259 snapshots taken at equal time intervals after attaining a steady state.

In Sec. IV, we analyze our numerical results, construct the cubic polynomial relation for Re and Nu using the data from our simulations, and compare our revised predictions with those of the GL model.

IV. RESULTS

Using our numerical data, we determine the scaling of dissipation rates, boundary layer thicknesses, and the functional forms of f_i . We construct the relations for Re and Nu given by Eqs. (22) and (23) using these inputs and compare the revised predictions with those of the original GL model. We also analyze how the proposed relation performs in the limit of $\tilde{D}_{u,\text{bulk}} \gg \tilde{D}_{u,\text{BL}}$ and vice versa.

A. Viscous and thermal dissipation rates

Here, we examine the scaling of viscous and thermal dissipation rates and explore how their scaling deviates from that of free turbulence. First, we present theoretical arguments on the above scaling, following which we verify our arguments with our numerical results.

TABLE I. Details of our direct numerical simulations performed in a cubical box for $Pr \leq 1$: the Prandtl number (Pr), the Rayleigh Number (Ra), the grid size, the ratio of the Kolmogorov length scale⁶⁵ (η) to the mesh width Δx , the number of grid points in viscous and thermal boundary layers (N_{VBL} and N_{TBL} , respectively), the Reynolds number (Re), the Nusselt number computed using $\langle u_z T \rangle$ and the exact relations given by Eqs. (7) and (8) (Nu , Nu_u , and Nu_T , respectively), the ratio of the total viscous dissipation rate in the boundary layer ($\bar{D}_{u,BL}$) and that in the bulk ($\bar{D}_{u,bulk}$), the ratio of the total thermal dissipation rate in the boundary layer ($\bar{D}_{T,BL}$) and that in the bulk ($\bar{D}_{T,bulk}$), and the number of non-dimensional time units (t_{ND}) and snapshots over which the quantities are averaged.

Pr	Ra	Grid size	$\eta/\Delta x$	N_{VBL}	N_{TBL}	Re	Nu	Nu_u	Nu_T	$\frac{\bar{D}_{u,BL}}{\bar{D}_{u,bulk}}$	$\frac{\bar{D}_{T,BL}}{\bar{D}_{T,bulk}}$	t_{ND}	Snapshots
0.02	5×10^5	513^3	1.99	7	58	2440	4.48	4.54	4.49	0.751	2.90	95	95
0.02	1×10^6	513^3	1.55	6	46	3200	5.78	5.79	5.78	0.564	2.89	41	41
0.02	2×10^6	513^3	1.24	5	38	4290	6.90	6.88	6.91	0.468	2.72	30	30
0.02	5×10^6	1025^3	1.81	7	59	6650	8.85	9.18	8.89	0.381	2.68	7	71
0.02	1×10^7	1025^3	1.45	7	48	9420	10.3	11.0	10.8	0.357	2.62	3	31
0.1	5×10^5	513^3	4.06	11	43	749	6.11	6.11	6.11	0.911	2.89	107	107
0.1	1×10^6	513^3	3.23	9	36	1030	7.34	7.39	7.35	0.787	2.71	66	66
0.1	2×10^6	513^3	2.58	7	30	1380	8.85	8.83	8.86	0.646	2.66	88	88
0.1	5×10^6	513^3	1.91	6	24	2090	11.3	11.4	11.3	0.539	2.63	83	83
0.1	1×10^7	513^3	1.52	6	20	2870	13.9	14.0	13.9	0.474	2.63	33	66
0.1	2×10^7	513^3	1.22	5	17	3870	16.4	16.4	16.4	0.389	2.41	37	73
0.1	5×10^7	1025^3	1.83	7	25	6020	20.8	20.8	21.3	0.337	2.22	12	12
0.1	1×10^8	1025^3	1.45	6	21	8140	26.7	26.1	26.3	0.288	2.28	5	26
0.5	1×10^6	513^3	6.96	13	32	285	8.38	8.36	8.37	1.01	3.25	71	71
0.5	3×10^6	513^3	4.85	10	24	482	11.4	11.4	11.4	0.745	2.94	140	140
0.5	1×10^7	513^3	3.28	8	17	874	15.9	16.0	16.0	0.682	2.95	91	91
0.5	3×10^7	513^3	2.30	7	13	1480	21.6	21.8	21.6	0.550	2.73	48	48
0.5	1×10^8	513^3	1.55	5	9	2610	30.6	30.8	30.6	0.475	2.58	37	37
1	1×10^6	257^3	4.92	7	17	147	8.18	8.45	8.48	0.765	2.83	101	101
1	2×10^6	257^3	3.94	7	14	213	10.1	10.1	10.2	0.791	2.98	101	101
1	5×10^6	257^3	2.90	6	11	340	13.3	13.3	13.4	0.709	2.97	101	101
1	1×10^7	257^3	2.31	5	9	491	16.3	16.3	16.4	0.679	2.93	101	101
1	2×10^7	257^3	1.85	5	7	702	19.8	19.7	19.9	0.682	2.91	91	91
1	5×10^7	513^3	2.73	7	11	1100	26.0	26.0	26.1	0.561	2.81	103	103
1	1×10^8	513^3	2.19	6	9	1530	31.4	31.3	31.5	0.512	2.69	101	101
1	2×10^8	513^3	1.75	6	8	2170	38.6	38.3	38.7	0.490	2.68	101	101
1	5×10^8	513^3	1.30	5	6	3330	49.2	49.6	49.2	0.437	2.51	101	101
1	1×10^9	1025^3	2.06	7	9	4700	61.2	61.6	61.4	0.426	2.35	15	30
1	2×10^9	1025^3	1.62	7	8	6580	76.8	81.1	76.7	0.392	2.47	13	26

In free turbulence, the viscous and scalar dissipation rates are estimated as follows:

$$\epsilon_u \sim \frac{U^3}{d}, \quad \epsilon_T \sim \frac{U\Delta^2}{d}. \quad (32)$$

However, in wall-bounded convection, the scaling of the dissipation rates is different. To understand this, let us rewrite the exact relations of Shraiman and Siggia⁹ given by Eqs. (7) and (8) as

$$\epsilon_u = \frac{U^3}{d} \frac{1}{Re^3} (Nu - 1) \frac{Ra}{Pr^2}, \quad (33)$$

$$\epsilon_T = \frac{U\Delta^2}{d} \frac{1}{RePr} Nu. \quad (34)$$

Recall from Sec. I that the Reynolds number scales as $Re \sim Ra^{1/2}$ for $Pr \sim 1$ and $Re \sim Ra^{0.6}$ for $Pr \gg 1$, and the Nusselt number scales as

$Nu \sim Ra^{0.3}$ for $Pr \gtrsim 1$. Substituting the above relations in Eqs. (33) and (34) yields

$$\epsilon_u \sim \begin{cases} \frac{U^3}{d} Ra^{-0.2}, & Pr \sim 1, \\ \frac{U^3}{d} Ra^{-0.5}, & Pr \gg 1, \end{cases} \quad (35)$$

instead of U^3/d , and

$$\epsilon_T \sim \begin{cases} \frac{U\Delta^2}{d} Ra^{-0.2}, & Pr \sim 1, \\ \frac{U\Delta^2}{d} Ra^{-0.3}, & Pr \gg 1, \end{cases} \quad (36)$$

instead of $U\Delta^2/d$. Pandey and Verma²² and Pandey *et al.*²³ argued that the additional Ra dependence is due to the suppression of nonlinear interactions due to the presence of walls. Some Fourier

TABLE II. Details of our direct numerical simulations performed in a cubical box for $Pr > 1$: the Prandtl number (Pr), the Rayleigh Number (Ra), the grid size, the ratio of the Batchelor length scale⁶⁵ (η_T) to the mesh width Δx , the number of grid points in viscous and thermal boundary layers (N_{VBL} and N_{TBL} , respectively), the Reynolds number (Re), the Nusselt number computed using $\langle u_z T \rangle$ and the exact relations given by Eqs. (7) and (8) (Nu , Nu_u , and Nu_T , respectively), the ratio of the total viscous dissipation rate in the boundary layer ($\bar{D}_{u,BL}$) and that in the bulk ($\bar{D}_{u,bulk}$), the ratio of the total thermal dissipation rate in the boundary layer ($\bar{D}_{T,BL}$) and that in the bulk ($\bar{D}_{T,bulk}$), and the number of non-dimensional time units (t_{ND}) and snapshots over which the quantities are averaged.

Pr	Ra	Grid size	$\eta_T/\Delta x$	N_{VBL}	N_{TBL}	Re	Nu	Nu_u	Nu_T	$\frac{\bar{D}_{u,BL}}{\bar{D}_{u,bulk}}$	$\frac{\bar{D}_{T,BL}}{\bar{D}_{T,bulk}}$	t_{ND}	Snapshots
6.8	1×10^6	257^3	5.02	9	17	24.9	7.90	7.87	7.87	0.822	3.08	101	101
6.8	2×10^6	257^3	4.01	8	15	35.6	9.46	9.43	9.48	0.744	2.94	101	101
6.8	5×10^6	257^3	2.93	7	11	59.7	12.9	12.9	13.0	0.646	2.97	101	101
6.8	1×10^7	257^3	2.33	6	9	89.2	15.9	15.8	16.0	0.605	2.93	101	101
6.8	2×10^7	257^3	1.85	6	8	128	19.5	19.4	19.3	0.579	2.97	107	101
6.8	5×10^7	257^3	1.37	5	6	217	26.1	25.7	25.9	0.588	2.99	101	101
6.8	1×10^8	513^3	2.18	8	9	314	31.6	31.6	31.7	0.614	2.85	56	56
6.8	2×10^8	513^3	1.75	7	8	452	38.5	37.7	39.3	0.529	2.84	26	51
6.8	5×10^8	513^3	1.29	7	6	729	50.5	50.4	50.8	0.521	2.83	58	58
6.8	1×10^9	1025^3	2.06	11	9	1070	65.7	61.9	62.0	0.518	2.69	14	28
6.8	2×10^9	1025^3	1.64	10	8	1520	77.0	77.6	77.5	0.463	2.83	20	40
6.8	5×10^9	1025^3	1.22	9	6	2400	101	101	101	0.440	2.72	17	33
50	1×10^6	513^3	9.92	17	33	3.53	8.17	8.16	7.99	0.815	3.23	131	131
50	2×10^6	513^3	7.96	16	27	5.19	9.66	9.60	9.61	0.722	3.42	51	51
50	5×10^6	513^3	5.74	14	20	9.38	13.8	13.7	13.5	0.627	3.19	130	130
50	1×10^7	513^3	4.58	13	17	14.0	16.7	16.7	16.2	0.581	3.12	65	65
50	2×10^7	513^3	3.67	12	14	21.1	20.2	20.1	20.0	0.525	3.13	55	55
50	5×10^7	513^3	2.72	11	11	35.2	26.4	26.2	26.0	0.489	3.07	57	57
50	1×10^8	513^3	2.18	10	9	50.8	31.8	31.6	31.6	0.436	2.92	111	111
50	2×10^8	513^3	1.74	9	8	76.4	38.7	38.8	38.7	0.433	3.10	101	101
50	5×10^8	513^3	1.29	9	6	137	51.8	51.6	50.4	0.481	2.88	62	62
50	1×10^9	513^3	1.03	8	5	202	61.5	63.0	69.3	0.599	2.79	101	101
100	1×10^6	257^3	5.01	10	17	1.80	7.94	7.93	7.94	1.04	3.41	259	259
100	2×10^6	257^3	3.91	9	14	2.78	10.4	10.3	10.2	0.862	3.42	263	263
100	5×10^6	257^3	2.87	8	10	4.90	13.9	13.9	14.0	0.731	3.36	153	153
100	1×10^7	257^3	2.30	7	9	7.02	16.8	16.7	16.6	0.585	3.30	101	101
100	2×10^7	257^3	1.84	7	7	9.91	20.1	20.0	19.9	0.485	3.00	101	101
100	5×10^7	257^3	1.37	6	6	17.1	26.1	25.9	26.1	0.467	3.20	101	101
100	1×10^8	513^3	2.18	10	9	26.0	31.8	31.7	31.7	0.433	2.96	107	107
100	2×10^8	513^3	1.74	9	8	37.5	39.1	38.8	38.8	0.373	3.08	108	108
100	5×10^8	513^3	1.30	10	6	71.4	49.7	49.2	50.3	0.429	2.95	86	86

modes that are otherwise present in free turbulence are absent in wall-bounded RBC; this results in several channels of nonlinear interactions and energy cascades to be blocked.⁵ Note that the horizontal walls seem to have a more pronounced effect on the aforementioned suppression than the lateral walls, as Schmidt *et al.*⁴¹ observed passive scalar scaling for homogeneous laterally confined RBC. In addition, buoyancy also appears to suppress the energy cascade rate,⁶⁰ similar to the role played by the magnetic field in magnetohydrodynamic turbulence.⁶⁹

Now, for $Pr \ll 1$, recall that $Re \sim Ra^{0.42}$ and $Nu \sim Ra^{0.25}$ (see Sec. I). Substitution of these expressions in Eqs. (33) and (34) yields

$$\epsilon_u \sim \frac{U^3}{d}, \quad \epsilon_T \sim \frac{U\Delta^2}{d} Ra^{-0.17}. \quad (37)$$

Thus, the viscous dissipation rate scales similar to free turbulence for small Pr . However, the additional Ra dependence is still present in the scaling of thermal dissipation rates because of the presence of thick thermal boundary layers.

Using our data, we numerically compute the viscous and thermal dissipation rates and normalize them with U^3/d and $U\Delta^2/d$, respectively. We plot the normalized dissipation rates vs Ra and exhibit these plots in Figs. 1(a) and 1(b). We observe that for small Pr , the normalized viscous dissipation rate is independent of Ra , whereas for larger Pr , the aforementioned quantity decreases with Ra . The decrease becomes steeper as Pr increases, with $\epsilon_u/(U^3 d^{-1}) \sim Ra^{-0.21}$ for $Pr = 1$ and $\sim Ra^{-0.45}$ for $Pr = 100$. The normalized thermal dissipation rate decreases with Ra for all Pr values, with $\epsilon_T/(U\Delta^2 d^{-1}) \sim Ra^{-0.15}$ for $Pr = 0.02$ to $\sim Ra^{-0.28}$ for $Pr = 100$, which are consistent with the earlier estimates.

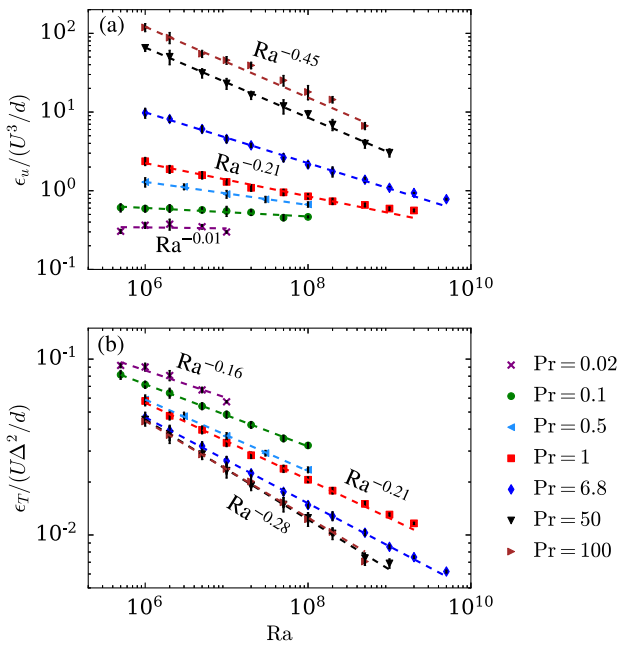


FIG. 1. Plots of (a) normalized viscous dissipation rate vs Ra and (b) normalized thermal dissipation rate vs Ra. The error bars represent the standard deviation of the dataset with respect to the temporal average. Both the viscous and thermal dissipation rates exhibit additional Ra dependence.

In Subsection IV B, we discuss the computations of the boundary layer thicknesses and their dependence on Re and Nu for different Pr.

B. Boundary layer thicknesses

There are several ways to define the viscous and thermal boundary layer thicknesses in RBC.^{1,61} In our paper, the viscous boundary layer thickness δ_u is defined as the depth where a linear fit of the velocity profile near the wall intersects with the tangent to the velocity profile at its local maximum. Similarly, the thermal boundary layer thickness δ_T is defined as the depth where a linear fit of the temperature profile near the wall intersects with the mean temperature $T = 0.5$. The above methods are described in detail in Refs. 1, 61, and 64.

Using the data generated from our simulations, we first compute the thicknesses of the thermal and viscous boundary layers. We report the average thicknesses of the viscous boundary layers near all the six walls and the thermal boundary layers near the top and bottom walls. We examine the validity of the Prandtl–Blasius relation of $\delta_u \sim \text{Re}^{-0.5}$ for the viscous boundary layers and $\delta_T = 0.5\text{Nu}^{-1}$ for the thermal boundary layers. Toward this objective, we plot $\delta_T\text{Nu}$ vs Nu in Fig. 2(a) and $\delta_u\text{Re}^{1/2}$ vs Re in Fig. 2(b).

We observe from Fig. 2(a) that $\delta_T\text{Nu} \approx 1/2$, independent of Nu, which is consistent with the definition. On the other hand, from Fig. 2(b), it is evident that $\delta_u\text{Re}^{1/2}$ is constant in Re only for Pr = 0.5 and 0.1. However, $\delta_u\text{Re}^{1/2}$ increases as $\sim \text{Re}^{0.31}$ for large Pr and decreases marginally as $\sim \text{Re}^{-0.07}$ for Pr = 0.02. This shows that for large Pr, δ_u becomes a weak function of Re; this is consistent with the observation of Breuer *et al.*⁶⁴ We also plot Grossmann

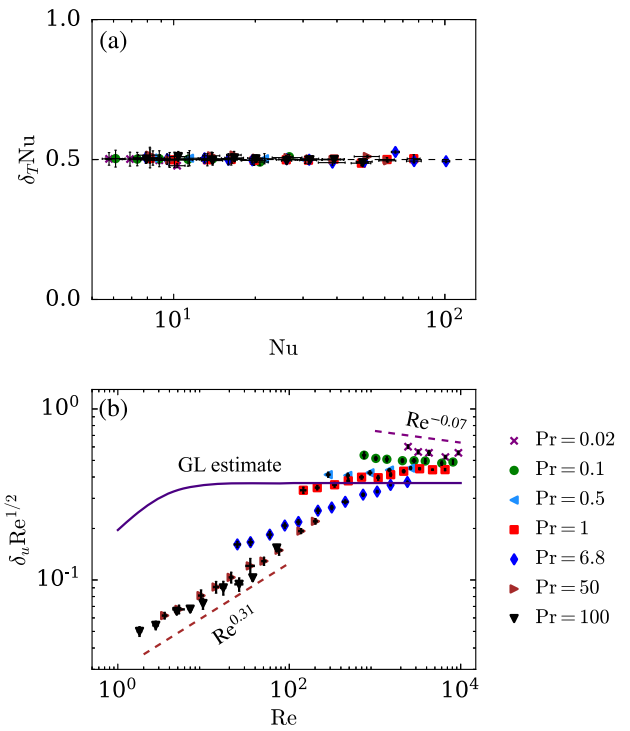


FIG. 2. Plots of (a) normalized thermal boundary layer thickness vs Nu and (b) normalized viscous boundary layer thickness vs Re. The error bars represent the standard deviation of the dataset with respect to the temporal average. The viscous boundary layer thickness deviates from the Prandtl–Blasius relation of $\delta_u \sim \text{Re}^{-1/2}$, as well as from Grossmann and Lohse’s estimate of $g(\sqrt{\text{Re}_c/\text{Re}})$.

and Lohse’s⁵⁰ estimate of viscous boundary layer thickness, which is given by $g(\sqrt{\text{Re}_c/\text{Re}})$; here, $g(x) = x(1+x^4)^{-1/4}$ and $\text{Re}_c = 3.401$. It is clear that Grossmann and Lohse’s estimate deviates significantly from the actual values.

Therefore, we cannot assume $\delta_u \sim g(\text{Re}^{-1/2})$ for viscous boundary layers in RBC, and it is more prudent to obtain the scaling of $f_2\delta_u^{-1}$ with Ra, where f_2 is the function from Eq. (19). The above deviation from the Prandtl–Blasius profile has also been observed in previous studies.^{58,61,62} This is because $\delta_u \sim \text{Re}^{-1/2}$ is valid asymptotically for very large Reynolds numbers.⁵³

C. f_i vs Ra for different Pr

In this subsection, we numerically compute f_i using our simulation data and discuss how these quantities vary with Ra for different Pr. We also obtain the limiting cases for the scaling of f_i with Ra.

We numerically compute the total viscous and thermal dissipation rates in the bulk and in the boundary layers for all the simulation runs. Using these values and boundary layer thicknesses, we compute f_1 , f_2 , f_3 , and f_4 and plot them vs Ra in Fig. 3. We observe that f_1 and f_3 are, in general, not constants as in free turbulence. f_1 decreases with Ra except for Pr = 0.1 and 0.02, where it is nearly constant. The above decrease is more prominent for large Pr (≥ 50), where $f_1 \sim \text{Ra}^{-0.35}$. In a similar fashion, f_3 also decreases with Ra for

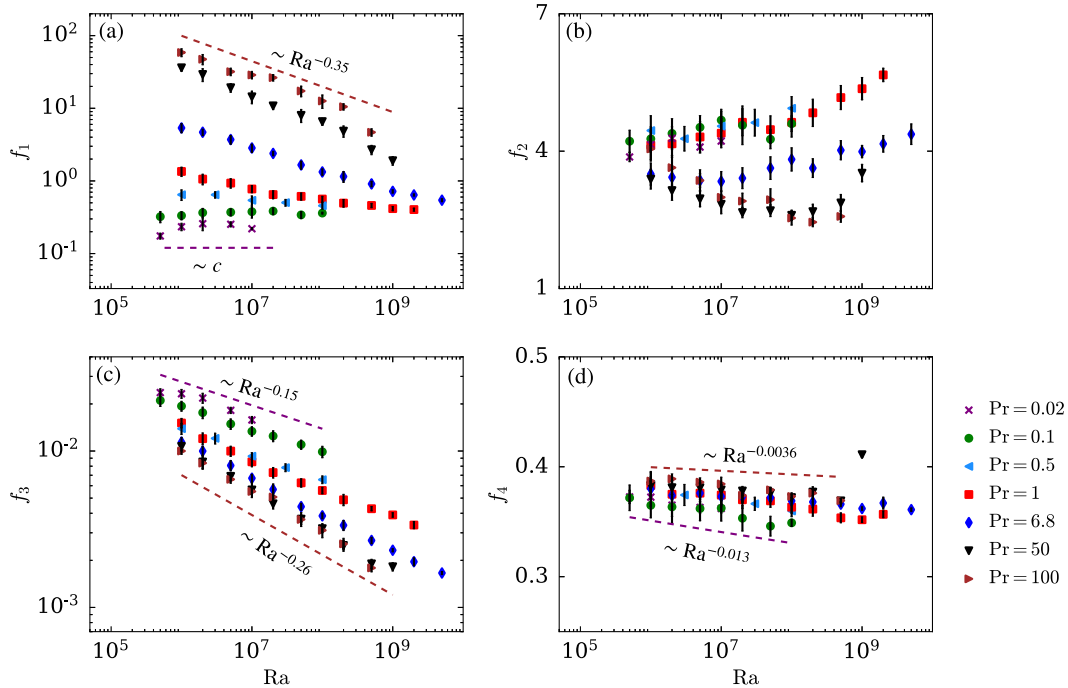


FIG. 3. Plots of (a) f_1 , (b) f_2 , (c) f_3 , and (d) f_4 vs Ra . The error bars represent the standard deviation of the dataset with respect to the temporal average. f_2 remains roughly independent of Ra and Pr , albeit with fluctuations; however, f_1 , f_3 , and f_4 decrease with Ra .

all Pr values and is more pronounced for large Pr ($f_3 \sim Ra^{-0.26}$) and less pronounced for small Pr ($f_3 \sim Ra^{-0.15}$). The above observations imply that the scaling of the dissipation rates in the bulk is similar to that in the entire volume^{58,59} (see Sec. IV A). This is because the bulk occupies a large fraction of the total volume, and its contribution to the total dissipation is significant.^{58,59}

The Ra and Pr dependences of f_2 cannot be clearly established from Fig. 3(b); we can only infer that f_2 is independent of Ra and Pr , albeit with significant fluctuations. This is consistent with $\epsilon_{u,BL} \sim \nu U^2 / \delta_u^2$ as predicted by Grossmann and Lohse.^{49,50} The function f_4 of Fig. 3(d) appears flat, but a careful examination shows that f_4 decreases weakly with Ra , with $f_4 \sim Ra^{-0.013}$ for small Pr and $f_4 \sim Ra^{-0.0036}$ for large Pr . The reason for the marginal decrease of f_4 with Ra needs investigation and is not in the scope of this paper.

As discussed earlier, the solution of Eq. (25) for Re and Nu depends on the quantity $f_2 \delta_u^{-1}$. Hence, we plot this quantity vs Ra for different Pr in Fig. 4. Since f_2 is nearly constant, $f_2 \delta_u^{-1}$ is inversely proportional to the viscous boundary layer thickness. Thus, $f_2 \delta_u^{-1}$ increases marginally for large Pr ($\sim Ra^{0.052}$) and steeply for small Pr ($\sim Ra^{0.26}$), which is in agreement with the scaling of viscous boundary layer thickness discussed in Sec. IV B.

In Subsection IV D, we describe the machine-learning tools used to determine the functional forms of f_i .

D. Machine-learning algorithm to obtain $f_i(Ra, Pr)$

So far, we have examined the variation of f_i with only Ra for different Prandtl numbers and obtained the limiting cases. Now, using

machine-learning and matching functions, we will combine these scalings to determine f_i as functions of both Ra and Pr . We make use of the machine-learning software WEKA⁷⁰ for obtaining the functional forms of f_i . The values of f_i computed for every Ra and Pr using our simulation data serve as training sets for our machine-learning algorithm. For simplicity, we will look for a power-law relation of the form $f_i = A Ra^\alpha Pr^\beta$, take logarithms of this expression, and employ *linear regression* to obtain A , α , and β . The linear regression algorithm works by estimating coefficients for a hyperplane that best fits the training data using the least squares method.

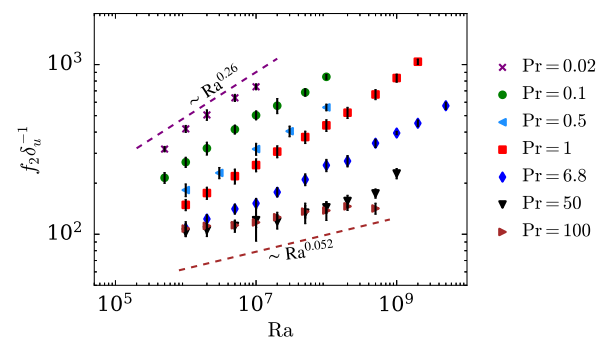


FIG. 4. Plot of $f_2 \delta_u^{-1}$ vs Ra . The error bars represent the standard deviation of the dataset with respect to the temporal average. The dependence of $f_2 \delta_u^{-1}$ on Ra is stronger for small Pr and becomes weaker as Pr increases.

Since the dependence of f_i on Ra is not uniform (see Sec. IV C), we split our parameter space into three regimes such that for each regime, the scaling of f_i with Ra is approximately the same. We choose the regimes as follows:

$$\begin{aligned} \text{Small Pr : } & \text{Pr} \leq 0.5, \\ \text{Moderate Pr : } & 0.5 \leq \text{Pr} \leq 6.8, \\ \text{Large Pr : } & \text{Pr} \geq 6.8. \end{aligned}$$

We then determine the prefactor A and the exponents α and β for each regime. To ensure continuity between the regimes, we introduce the following matching functions:

$$H_1(\text{Pr}) = \frac{1}{1 + e^{-k_1(0.5-\text{Pr})}}, \quad (38)$$

$$H_2(\text{Pr}) = \frac{1}{1 + e^{-k_1(\text{Pr}-0.5)}} - \frac{1}{1 + e^{-k_2(\text{Pr}-6.8)}}, \quad (39)$$

$$H_3(\text{Pr}) = \frac{1}{1 + e^{-k_2(\text{Pr}-6.8)}}, \quad (40)$$

where k_1 and k_2 are taken to be 10 and 0.75, respectively. The functions H_1 , H_2 , and H_3 become unity inside the regimes given by $\text{Pr} < 0.5$, $0.5 < \text{Pr} < 6.8$, and $\text{Pr} > 6.8$, respectively, and become negligible outside their regimes. The value of these functions is 1/2 in the boundaries of their respective regimes. See Fig. 5 for an illustration of the behavior of the matching functions. Using these functions and employing regression for each regime, we obtain the following fits for f_i :

$$f_1 = 0.67H_1\text{Pr}^{0.28} + 27H_2\text{Ra}^{-0.21}\text{Pr}^{0.55} + 170H_3\text{Ra}^{-0.34}\text{Pr}^{0.78}, \quad (41)$$

$$\frac{f_2}{\delta_u} = 4.4H_1\text{Ra}^{0.25}\text{Pr}^{-0.26} + 7.4H_2\text{Ra}^{0.22}\text{Pr}^{-0.29} + 27H_3\text{Ra}^{0.14}\text{Pr}^{-0.18}, \quad (42)$$

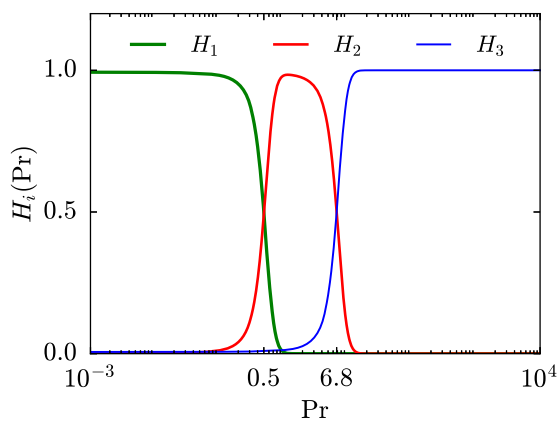


FIG. 5. Plot of the matching functions $H_i(\text{Pr})$ vs Pr . H_1 , H_2 , and H_3 become unity in the regimes given by $\text{Pr} < 0.5$, $0.5 < \text{Pr} < 6.8$, and $\text{Pr} > 6.8$, respectively. They attain the value of 1/2 at the regime boundaries and become negligible outside their respective regimes.

$$f_3 = 0.095H_1\text{Ra}^{-0.15}\text{Pr}^{-0.17} + 0.25H_2\text{Ra}^{-0.21}\text{Pr}^{-0.17} + 0.45H_3\text{Ra}^{-0.25}\text{Pr}^{-0.093}, \quad (43)$$

$$f_4 = 0.46H_1\text{Ra}^{-0.013}\text{Pr}^{0.010} + 0.43H_2\text{Ra}^{-0.0081}\text{Pr}^{0.0053} + 0.39H_3\text{Ra}^{-0.0036}\text{Pr}^{0.0093}. \quad (44)$$

The average deviation between the f_i 's predicted by the fits and the actual values are 24%, 19%, 12%, and 58% for f_1 , f_2/δ_u , f_3 , and f_4 , respectively. As we will see later, incorporation of the aforementioned functional forms results in more accurate predictions than the GL model; thus, the above uncertainty in f_i is acceptable. In the Appendix, we employ the same regression algorithm over a reduced training set consisting of half of our data points and show that the fits so obtained are close to Eqs. (41)–(44). Thus, the estimated parameter values are reasonably robust.

Having obtained the functional forms of f_i , we can plug them in Eqs. (25) and (24) to complete the relation for Re and Nu. We remark that f_i obtained above are valid for RBC cells with a unit aspect ratio. We suspect that they are weak functions of the aspect ratio; this study will be taken up in the future work. Furthermore, efforts are ongoing to make the functional forms of $f_i(\text{Ra}, \text{Pr})$ more compact.

E. Enhancement of the GL model

In this subsection, we will examine the enhancement of the GL model brought about by using the obtained functional forms for the prefactors of the dissipation rates. We will test both, the original GL model and the revised estimates with our numerical results, as well as those of Scheel and Schumacher¹¹ ($\text{Pr} = 0.005$ and 0.02), Wagner and Shishkina¹⁸ ($\text{Pr} = 0.7$), Emran and Schumacher¹⁷ ($\text{Pr} = 0.7$), Kaczorowski and Xia¹⁹ ($\text{Pr} = 4.38$), and Horn, Shishkina, and Wagner¹⁶ ($\text{Pr} = 2547.9$). We also include the experimental results of Cioni, Ciliberto, and Sommeria¹⁰ ($\text{Pr} = 0.02$), and Niemela *et al.*³² ($\text{Pr} = 0.7$) for our comparisons. The simulations of Wagner and Shishkina¹⁸ and Kaczorowski and Xia¹⁹ involved a cubical cell such as ours, whereas the rest of the above simulations and experiments involved a cylindrical cell. All the above work involve RBC cells with a unit aspect ratio. We compute the percentage deviations (\mathcal{D}_{Re} and \mathcal{D}_{Nu}) between the estimated and actual values according to the following formula:

$$\mathcal{D} = \left| \frac{\text{Predicted value} - \text{Actual value}}{\text{Actual value}} \right| \times 100. \quad (45)$$

In Table III, we list the average of the deviations computed for all the points for every Pr.

In Figs. 6(a) and 6(b), we plot the normalized Reynolds number, $\text{ReRa}^{-0.5}$, computed using our simulation data and those of Refs. 10, 11, 16–18, and 32, vs Ra. To avoid clutter, we exhibit the results for $\text{Pr} < 1$ in Fig. 6(a) and those for $\text{Pr} \geq 1$ in Fig. 6(b). The dashed and solid curves in Fig. 6 denote Re predicted by the GL model and our revised estimates, respectively. From Fig. 6 and Table III, it is clear that the revised estimates of Re are in better agreement with the observed results compared to the original GL model, especially for extreme Prandtl numbers. Furthermore, the trend of estimated Re is also in better agreement with the numerical and experimental

TABLE III. Quantitative comparison between the predictions the GL model and the revised estimates of Nu and Re for different sets of simulation and experimental data. \mathcal{D}_{Re} is the percentage difference between the observed and predicted values of Re, and \mathcal{D}_{Nu} is the percentage difference between the observed and predicted values of Nu [see Eq. (45)]. Note that no data on Re are available for $Pr = 4.38$.¹⁹

Pr	Range of Ra (Re)	\mathcal{D}_{Re} (Revised estimate) (%)	\mathcal{D}_{Re} (GL Model) (%)	Range of Ra (Nu)	\mathcal{D}_{Nu} (Revised estimate) (%)	\mathcal{D}_{Nu} (GL Model) (%)
0.005	$3 \times 10^5 - 10^7$	11	48	$3 \times 10^5 - 10^7$	9.6	17
0.02	$3 \times 10^5 - 3 \times 10^9$	9.1	62	$3 \times 10^5 - 3 \times 10^9$	10	15
0.1	$5 \times 10^5 - 10^8$	1.3	30	$5 \times 10^5 - 10^8$	3.1	5.0
0.5	$10^6 - 10^8$	1.9	14	$10^6 - 10^8$	1.4	5.4
0.7	$10^5 - 10^{13}$	6.8	25	$10^5 - 10^9$	3.8	9.9
1.0	$10^6 - 2 \times 10^9$	2.8	20	$10^6 - 2 \times 10^9$	3.6	5.8
4.38	$10^6 - 3 \times 10^9$	5.7	6.3
6.8	$10^6 - 5 \times 10^9$	3.4	27	$10^6 - 5 \times 10^9$	5.6	6.5
50	$10^6 - 10^9$	6.0	84	$10^6 - 10^9$	3.2	7.2
100	$10^6 - 5 \times 10^8$	3.4	150	$10^6 - 5 \times 10^8$	2.7	3.9
2547.9	$10^5 - 10^9$	85	560	$10^5 - 10^9$	2.3	17

results (note that the trend of Re computed based on different large-scale velocities does not change even though there may be minor differences in absolute values¹). This improvement in the estimation of Re is crucial because the predictions of Re are more sensitive to modeling parameters compared to Nu due to a larger range of the scaling exponent.

In Figs. 7(a) and 7(b), we plot the normalized Nusselt number, $NuGr^{-0.3}$, computed using our simulation data along with those

of Refs. 10, 11, and 16–19, vs Ra. We employ the Grashof number $Gr = Ra/Pr$ in the y axis to avoid clutter; this is because $Nu \sim Ra^{0.3}$ (with a weak dependence on Pr). These figures, along with Table III, indicate that the revised estimates of Nu (solid curves) are more accurate compared to those predicted by the original GL model (dashed curves). It is interesting to note that for extreme

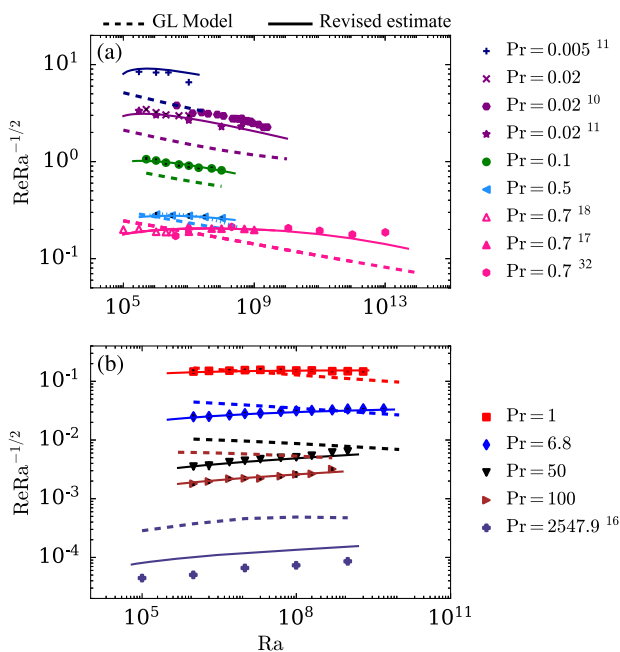


FIG. 6. Comparison between the predictions of Re vs Ra using the original GL model (dashed curves) and our proposed modifications (solid curves) with the results from our work and from the literature^{10,11,16–18,32} for (a) $Pr < 1$ and (b) $Pr \geq 1$. The error bars (shown only for our datasets) represent the standard deviation of the dataset with respect to the temporal average.

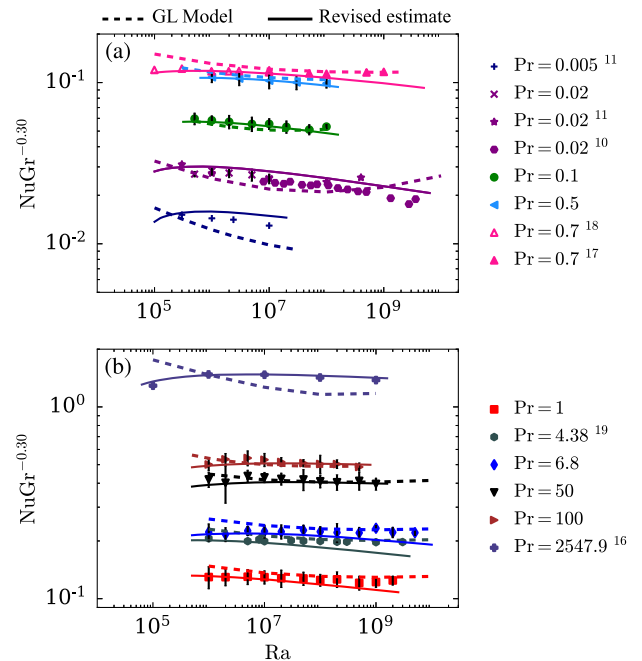


FIG. 7. Comparison between the predictions of Nu vs Ra using the original GL model (dashed curves) and our proposed modifications (solid curves) with the results from our work and from the literature^{10,11,16–19} for (a) $Pr < 1$ and (b) $Pr \geq 1$. The error bars (shown only for our datasets) represent the standard deviation of the dataset with respect to the temporal average.

Prandtl numbers ($Pr = 0.005, 2547.9$), the accuracy of the revised estimates of Nu is significantly improved with only 2.3% deviation from the actual values for $Pr = 2547.9$ and 9.6% deviation for $Pr = 0.005$. Contrast this with the GL model, where we observe 17% deviation for both $Pr = 2547.9$ and 0.005 . For $Pr \sim 1$, the accuracy of the revised estimates of Nu and those predicted by the GL model are comparable, with the former being more accurate for $Ra < 10^8$ but marginally less for larger Ra . Thus, we observe an overall improvement in the predictions of Nu , though it is not as significant as it was for Re .

In Figs. 8(a) and 8(b), we contrast the Pr dependence on our estimates of Re and Nu and those of the GL model. Here, we plot the predictions of $Re(Pr)$ and $Nu(Pr)$ along with the actual values computed using our data and those of Refs. 11 and 16–19. We choose four Rayleigh numbers for our comparisons: $10^6, 10^7, 10^8$, and 10^9 . As expected based on our earlier discussions, the revised estimates of $Re(Pr)$ are more accurate than those of the GL model [see Fig. 8(a)]. We also observe improvements in the predictions of Nu , especially for $Pr \ll 1$ and $Pr \gg 1$ [see Fig. 8(b)]. This is again consistent with our earlier discussions.

The improvements, thus, in the predictions of Re and Pr underscore the importance of considering the additional Ra and Pr dependences on the scaling of the dissipation rates and the viscous boundary layers in convection.

F. Limiting cases: Power-law expressions

Recall from Sec. II that Eqs. (22) and (23) reduce to power-law scaling in the limiting cases: $\tilde{D}_{u,bulk} \gg \tilde{D}_{u,BL}$ and $\tilde{D}_{u,bulk} \ll \tilde{D}_{u,BL}$.

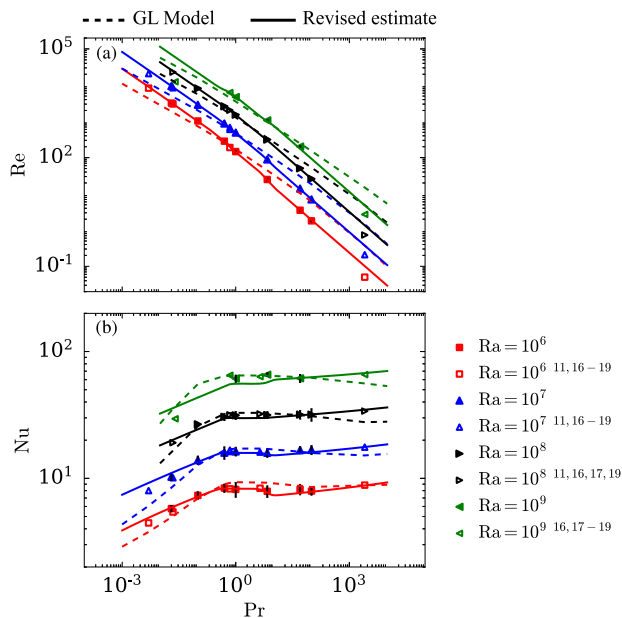


FIG. 8. Comparison between the predictions of (a) Re and (b) Nu vs Pr using the original GL model (dashed curves) and our proposed modifications (solid curves) with the results from our work (filled markers) and from Refs. 11, and 16–19 (unfilled markers). The error bars (shown only for our datasets) represent the standard deviation of the dataset with respect to the temporal average.

First, we will estimate the regimes of Ra and Pr , where the viscous and thermal dissipation rates dominate in the bulk or in the boundary layers. Using f_i 's and Eqs. (11)–(14), we deduce that

$$\frac{\tilde{D}_{u,BL}}{\tilde{D}_{u,bulk}} = \frac{f_2}{f_1} \frac{d}{\delta_u} \frac{1}{Re}, \quad (46)$$

$$\frac{\tilde{D}_{T,BL}}{\tilde{D}_{T,bulk}} = \frac{2f_4}{f_3} \frac{Nu}{RePr}. \quad (47)$$

In Figs. 9(a) and 9(b), we exhibit the plots of the above estimates for $Pr = 0.02, 1$, and 50 . We also exhibit the numerically computed points in Fig. 9; these points are consistent with the estimates given by Eqs. (46) and (47). On the other hand, the ratio of the dissipation rates estimated using the GL model [by employing the bulk and the boundary layer terms of Eqs. (16) and (17)] deviates significantly from the numerically computed points.

The plots show that the thermal dissipation rate in the boundary layers exceeds that in the bulk by a factor of two to four for all Pr values. On the other hand, the viscous dissipation rate in the bulk exceeds that in the boundary layers for $Ra \gtrsim 10^5$. These observations are in agreement with previous studies.^{58,59} The plots imply that $\tilde{D}_{u,BL}$ dominates $\tilde{D}_{u,bulk}$ only for $Ra \ll 10^5$, where $Nu \approx 1$. However, recall that the power-law relations for this limiting case, given by Eqs. (30) and (31), are invalid for small Nu . Thus, we do not examine this limiting case further.

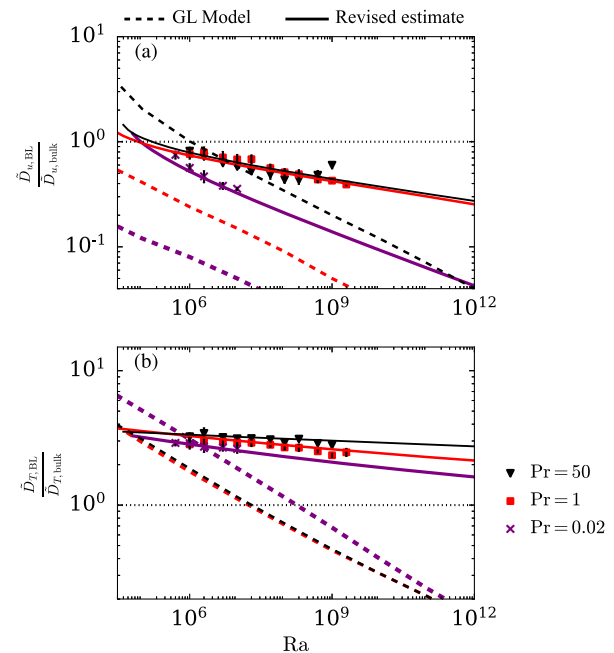


FIG. 9. Estimates of (a) $\tilde{D}_{u,BL}/\tilde{D}_{u,bulk}$ and (b) $\tilde{D}_{T,BL}/\tilde{D}_{T,bulk}$ using Eqs. (46) and (47) (solid curves) and the GL model (dashed curves) for $Pr = 0.02$ (purple), $Pr = 1$ (red), and $Pr = 50$ (black). Points obtained from our simulation data are also displayed. The dotted horizontal lines in (a) and (b) represent $\tilde{D}_{u,BL}/\tilde{D}_{u,bulk} = 1$ and $\tilde{D}_{T,BL}/\tilde{D}_{T,bulk} = 1$, respectively. The error bars represent the standard deviation of the dataset with respect to the temporal average.

For the regimes characterized by $\tilde{D}_{u,bulk} \gg \tilde{D}_{u,BL}$, we plug the best-fit relation for f_i in Eqs. (27) and (28) to obtain the following:

$$Re = \begin{cases} 0.76Ra^{0.42}Pr^{-0.72}, & \text{Small Pr,} \\ 0.20Ra^{0.50}Pr^{-0.86}, & \text{Moderate Pr,} \\ 0.11Ra^{0.55}Pr^{-0.94}, & \text{Large Pr,} \end{cases} \quad (48)$$

$$Nu = \begin{cases} 0.30Ra^{0.27}Pr^{0.11}, & \text{Small Pr,} \\ 0.21Ra^{0.29}Pr^{-0.03}, & \text{Moderate Pr,} \\ 0.21Ra^{0.30}Pr^{-0.03}, & \text{Large Pr.} \end{cases} \quad (49)$$

Since f_4 is a very weak function of Ra and Pr, we assume it to be a constant (≈ 0.37). The Ra dependence described by Eqs. (48) and (49) is consistent with the scaling observed for large Rayleigh numbers ($10^8 \ll Ra \ll 10^{12}$) in the literature.^{8,11,16–18,22,23,36,57,61,71–73} Furthermore, the above relation for Re and Nu in the small Pr regime is not very far from GL's predictions of $Re \sim Ra^{2/5}Pr^{-3/5}$ and $Nu \sim Ra^{1/5}Pr^{1/5}$. The derived relation for Nu is also in agreement with analytically derived upper bounds of $Nu \lesssim Ra^{1/3} \ln(Ra^{2/3})$ ⁷⁴ and $Nu \leq 0.644Ra^{1/3} \ln(Ra^{1/3})$.⁷⁵ Equation (49) also suggests that Nu is a weak function of Pr for moderate and large Pr [see Fig. 8(b)].

For very large Ra ($\gg 10^{12}$), some recent works^{48,76} reveal that the Nusselt number scales in the band from $Ra^{0.33}$ to $Ra^{0.35}$. Unfortunately, our predictions are not very accurate in this regime; this is because the functional forms of f_i are constructed using data from simulations with $Ra \lesssim 10^{10}$. Note that for larger Ra, we expect the suppression of viscous and thermal dissipation rates to weaken because of the thin boundary layers. This can, in turn, cause the scaling exponent for Nu to increase. For example, f_1 and f_3 may scale as

$$f_1 \sim Ra^{-0.14}, \quad f_3 \sim Ra^{-0.16}, \quad (50)$$

instead of $Ra^{-0.21}$ as per Eqs. (41) and (43). Plugging the above expressions for f_1 and f_3 in Eq. (28) gives

$$Nu \sim Ra^{0.33},$$

which is consistent with the results of Iyer *et al.*⁴⁸ However, the scalings for f_1 and f_3 , given by Eq. (50), are conjectures that need to be verified using simulations with large Ra's. In a future work, we plan to upgrade our present work by taking inputs from large Ra simulations.

We conclude in Sec. V.

V. CONCLUSIONS

In this paper, we enhance Grossmann and Lohse's model to provide improved predictions of Reynolds and Nusselt numbers in turbulent Rayleigh–Bénard convection. The process of obtaining this relation involves Grossman and Lohse's idea of splitting the total viscous and thermal dissipation rates into bulk and boundary layer contributions and using the exact relations of Shraiman and Siggia. In the present work, we address the additional Ra and Pr dependences on the viscous and thermal dissipation rates in the bulk compared to free turbulence, as well as the deviation of viscous boundary layer thickness from Prandtl–Blasius theory.

The Reynolds and Nusselt numbers are obtained by solving a cubic polynomial equation consisting of four functions $f_i(Ra, Pr)$ that are prefactors for the dissipation rates in the bulk and boundary layers. Note that these prefactors were constants in the original GL model. The aforementioned functions are determined using machine learning (regression analysis) on 60 datasets obtained from direct numerical simulations of RBC. The cubic polynomial equation reduces to power-law expressions in the limit of the viscous dissipation rate dominating in the bulk.

Using functional forms for the prefactors for the dissipation rates improves the predictions for both Re and Nu compared to the GL model. We observe significant improvements in the predictions of Re, which is important because Re is more sensitive to modeling parameters compared to Nu. The improvement in the predictions of Nu is more pronounced for extreme Pr regimes ($Pr \leq 0.02$ and ≥ 100). Our results underscore the importance of applying data-driven methods to improve existing models, a practice that has recently been picking up pace in research on turbulence.^{77,78} Presently, our work takes inputs from data that are restricted to $Ra < 10^{10}$ and unit aspect ratio. Our predictions can be further enhanced after determining f_i for $Ra > 10^{10}$ and for different aspect ratios. Moreover, our work can be extended to convection with magnetic fields following the approach of Zürner *et al.*^{79,80}

We believe that our results will be valuable to the scientific and engineering community, especially where flows with extreme Prandtl numbers are involved. For example, they will help understand the fluid dynamics and heat transport in liquid metal batteries that involve small Pr convection.⁸¹ On the other end, our analysis will help strengthen our knowledge on mantle convection, which involves a large Pr flow.^{1,2,82} This will, in turn, enable us to make better predictions of seismic disturbances and the earth's magnetic field. Apart from this, our present work should also aid in expanding our knowledge on oceanic and atmospheric flows and, thus, enable us to make improved weather predictions.

ACKNOWLEDGMENTS

The authors thank Arnab Bhattacharya, K. R. Sreenivasan, Jörg Schumacher, and Amrish Pandey for useful discussions. The authors thank Roshan Samuel, Ali Asad, Soumyadeep Chatterjee, and Syed Fahad Anwer for their contributions to the development of the finite-difference solver SARAS. Our numerical simulations were performed on Shaheen II of KAUST supercomputing laboratory, Saudi Arabia (Project No. k1416) and on HPC2013 of IIT Kanpur, India.

APPENDIX: ROBUSTNESS OF THE ESTIMATED PARAMETER VALUES FOR $f_i(Ra, Pr)$

In this section, we check the robustness of the parameter values for $f_i(Ra, Pr)$ estimated in Sec. IV D. Toward this objective, we employ the regression algorithm, used in Sec. IV D, on a reduced training set consisting of 30 data points, which is half of the total number of data points, and test the algorithm on the remaining 30 data points. Starting from the point corresponding to $Pr = 0.02$ and $Ra = 5 \times 10^5$, we take alternate data points from Tables I and II for training and the remaining data points for testing. We obtain the

following fits for f_i for the reduced training set:

$$f_1 = 0.72H_1\text{Pr}^{0.30} + 28H_2\text{Ra}^{-0.21}\text{Pr}^{0.52} + 150H_3\text{Ra}^{-0.33}\text{Pr}^{0.79}, \quad (\text{A1})$$

$$\frac{f_2}{\delta_u} = 4.1H_1\text{Ra}^{0.26}\text{Pr}^{-0.27} + 6.9H_2\text{Ra}^{0.23}\text{Pr}^{-0.30} + 21H_3\text{Ra}^{0.15}\text{Pr}^{-0.18}, \quad (\text{A2})$$

$$f_3 = 0.087H_1\text{Ra}^{-0.14}\text{Pr}^{-0.16} + 0.26H_2\text{Ra}^{-0.21}\text{Pr}^{-0.17} + 0.40H_3\text{Ra}^{-0.24}\text{Pr}^{-0.095}, \quad (\text{A3})$$

$$f_4 = 0.45H_1\text{Ra}^{-0.012}\text{Pr}^{0.0075} + 0.42H_2\text{Ra}^{-0.0078}\text{Pr}^{0.0050} + 0.36H_3\text{Pr}^{0.0161}. \quad (\text{A4})$$

We observe that the fits given by Eqs. (A1)–(A4) are similar to those of Eqs. (41)–(44), which correspond to the fits obtained when all the data points were used as training sets. The average deviation between the f_i 's predicted by the fits and the actual values of the test set are 25%, 20%, 13%, and 71% for f_1 , f_2/δ_u , f_3 , and f_4 , respectively. These deviations are almost the same as those observed when all the datasets were used for training and testing. Furthermore, if we train our algorithm using only 15 datasets (every fourth set from Tables I and II), we obtain

$$f_1 = 0.68H_1\text{Pr}^{0.31} + 25H_2\text{Ra}^{-0.20}\text{Pr}^{0.47} + 238H_3\text{Ra}^{-0.37}\text{Pr}^{0.81}, \quad (\text{A5})$$

$$\frac{f_2}{\delta_u} = 3.7H_1\text{Ra}^{0.26}\text{Pr}^{-0.27} + 5.8H_2\text{Ra}^{0.24}\text{Pr}^{-0.33} + 23H_3\text{Ra}^{0.15}\text{Pr}^{-0.19}, \quad (\text{A6})$$

$$f_3 = 0.060H_1\text{Ra}^{-0.12}\text{Pr}^{-0.17} + 0.23H_2\text{Ra}^{-0.20}\text{Pr}^{-0.19} + 0.40H_3\text{Ra}^{-0.24}\text{Pr}^{-0.090}, \quad (\text{A7})$$

$$f_4 = 0.42H_1\text{Ra}^{-0.0099} + 0.41H_2\text{Ra}^{-0.0069}\text{Pr}^{0.0059} + 0.38H_3, \quad (\text{A8})$$

with the average deviation between the f_i 's predicted by the fits and the actual values of the test set being 26%, 21%, 16%, and 71% for f_1 , f_2/δ_u , f_3 , and f_4 , respectively. We observe that there are visible changes in the parameter values estimated using 15 datasets. Thus, we infer that the parameter values estimated using more than 30 datasets are reasonably robust.

DATA AVAILABILITY

The data that support the findings of this study are available from the corresponding author upon reasonable request.

REFERENCES

- ¹G. Ahlers, S. Grossmann, and D. Lohse, "Heat transfer and large scale dynamics in turbulent Rayleigh-Bénard convection," *Rev. Mod. Phys.* **81**, 503–537 (2009).
- ²F. Chillà and J. Schumacher, "New perspectives in turbulent Rayleigh-Bénard convection," *Eur. Phys. J. E* **35**, 58 (2012).
- ³E. D. Siggia, "High Rayleigh number convection," *Annu. Rev. Fluid Mech.* **26**, 137–168 (1994).
- ⁴K.-Q. Xia, "Current trends and future directions in turbulent thermal convection," *Theor. Appl. Mech. Lett.* **3**, 052001 (2013).
- ⁵M. K. Verma, *Physics of Buoyant Flows: From Instabilities to Turbulence* (World Scientific, Singapore, 2018).
- ⁶W. V. R. Malkus, "The heat transport and spectrum of thermal turbulence," *Proc. R. Soc. London, Ser. A* **225**, 196–212 (1954).
- ⁷R. H. Kraichnan, "Turbulent thermal convection at arbitrary Prandtl number," *Phys. Fluids* **5**, 1374–1389 (1962).
- ⁸B. Castaing, G. Gunaratne, F. Heslot, L. Kadanoff, A. Libchaber, S. Thomae, X.-Z. Wu, S. Zaleski, and G. Zanetti, "Scaling of hard thermal turbulence in Rayleigh-Bénard convection," *J. Fluid Mech.* **204**, 1–30 (1989).
- ⁹B. I. Shraiman and E. D. Siggia, "Heat transport in high-Rayleigh-number convection," *Phys. Rev. A* **42**, 3650–3653 (1990).
- ¹⁰S. Cioni, S. Ciliberto, and J. Sommeria, "Strongly turbulent Rayleigh-Bénard convection in mercury: Comparison with results at moderate Prandtl number," *J. Fluid Mech.* **335**, 111–140 (1997).
- ¹¹J. D. Scheel and J. Schumacher, "Predicting transition ranges to fully turbulent viscous boundary layers in low Prandtl number convection flows," *Phys. Rev. Fluids* **2**, 123501 (2017).
- ¹²H. T. Rossby, "A study of Bénard convection with and without rotation," *J. Fluid Mech.* **36**, 309–335 (1969).
- ¹³T. Takeshita, T. Segawa, J. A. Glazier, and M. Sano, "Thermal turbulence in mercury," *Phys. Rev. Lett.* **76**, 1465–1468 (1996).
- ¹⁴S. Ashkenazi and V. Steinberg, "High Rayleigh number turbulent convection in a gas near the gas-liquid critical point," *Phys. Rev. Lett.* **83**, 3641–3645 (1999).
- ¹⁵X. Chavanne, F. Chillà, B. Castaing, B. Hébral, B. Chabaud, and J. Chassigny, "Observation of the ultimate regime in Rayleigh-Bénard convection," *Phys. Rev. Lett.* **79**, 3648–3651 (1997).
- ¹⁶S. Horn, O. Shishkina, and C. Wagner, "On non-Oberbeck-Boussinesq effects in three-dimensional Rayleigh-Bénard convection in glycerol," *J. Fluid Mech.* **724**, 175–202 (2013).
- ¹⁷M. S. Emran and J. Schumacher, "Fine-scale statistics of temperature and its derivatives in convective turbulence," *J. Fluid Mech.* **611**, 13–34 (2008).
- ¹⁸S. Wagner and O. Shishkina, "Aspect-ratio dependency of Rayleigh-Bénard convection in box-shaped containers," *Phys. Fluids* **25**, 085110 (2013).
- ¹⁹M. Kaczorowski and K.-Q. Xia, "Turbulent flow in the bulk of Rayleigh-Bénard convection: Small-scale properties in a cubic cell," *J. Fluid Mech.* **722**, 596–617 (2013).
- ²⁰J. Niemela and K. R. Sreenivasan, "Confined turbulent convection," *J. Fluid Mech.* **481**, 355–384 (2003).
- ²¹D. Funfschilling, E. Brown, A. Nikolaenko, and G. Ahlers, "Heat transport by turbulent Rayleigh-Bénard convection in cylindrical samples with aspect ratio one and larger," *J. Fluid Mech.* **536**, 145–154 (2005).
- ²²A. Pandey and M. K. Verma, "Scaling of large-scale quantities in Rayleigh-Bénard convection," *Phys. Fluids* **28**, 095105 (2016).
- ²³A. Pandey, A. Kumar, A. G. Chatterjee, and M. K. Verma, "Dynamics of large-scale quantities in Rayleigh-Bénard convection," *Phys. Rev. E* **94**, 053106 (2016).
- ²⁴A. Pandey, M. K. Verma, and P. K. Mishra, "Scaling of heat flux and energy spectrum for very large Prandtl number convection," *Phys. Rev. E* **89**, 023006 (2014).
- ²⁵R. J. A. M. Stevens, R. Verzicco, and D. Lohse, "Radial boundary layer structure and Nusselt number in Rayleigh-Bénard convection," *J. Fluid Mech.* **643**, 495–507 (2010).
- ²⁶A. Xu, L. She, and H.-D. Xi, "Statistics of temperature and thermal energy dissipation rate in low-Prandtl number turbulent thermal convection," *Phys. Fluids* **31**, 125101 (2019).
- ²⁷D.-L. Dong, B.-F. Wang, Y.-H. Dong, Y.-X. Huang, N. Jiang, Y.-L. Liu, Z.-M. Lu, X. Qiu, Z.-Q. Tang, and Q. Zhou, "Influence of spatial arrangements of roughness elements on turbulent Rayleigh-Bénard convection," *Phys. Fluids* **32**, 045114 (2020).
- ²⁸U. Madanan and R. J. Goldstein, "High-Rayleigh-number thermal convection of compressed gases in inclined rectangular enclosures," *Phys. Fluids* **32**, 017103 (2020).

- ²⁹M. Vial and R. H. Hernández, “Feedback control and heat transfer measurements in a Rayleigh–Bénard convection cell,” *Phys. Fluids* **29**, 074103 (2017).
- ³⁰K.-Q. Xia, S. Lam, and S.-Q. Zhou, “Heat-flux measurement in high-Prandtl-number turbulent Rayleigh–Bénard convection,” *Phys. Rev. Lett.* **88**, 064501 (2002).
- ³¹R. Verzicco and R. Camussi, “Prandtl number effects in convective turbulence,” *J. Fluid Mech.* **383**, 55–73 (1999).
- ³²J. J. Niemela, L. Skrbek, K. R. Sreenivasan, and R. J. Donnelly, “The wind in confined thermal convection,” *J. Fluid Mech.* **449**, 169–178 (2001).
- ³³S. Lam, X.-D. Shang, S.-Q. Zhou, and K.-Q. Xia, “Prandtl number dependence of the viscous boundary layer and the Reynolds numbers in Rayleigh–Bénard convection,” *Phys. Rev. E* **65**, 066306 (2002).
- ³⁴M. K. Verma, P. K. Mishra, A. Pandey, and S. Paul, “Scalings of field correlations and heat transport in turbulent convection,” *Phys. Rev. E* **85**, 016310 (2012).
- ³⁵G. Silano, K. R. Sreenivasan, and R. Verzicco, “Numerical simulations of Rayleigh–Bénard convection for Prandtl numbers between 10^{-1} and 10^4 and Rayleigh numbers between 10^5 and 10^9 ,” *J. Fluid Mech.* **662**, 409–446 (2010).
- ³⁶E. Brown, D. Funfschilling, and G. Ahlers, “Anomalous Reynolds-number scaling in turbulent Rayleigh–Bénard convection,” *J. Stat. Mech.: Theory Exp.* **2007**, P10005.
- ³⁷D. Lohse and F. Toschi, “Ultimate state of thermal convection,” *Phys. Rev. Lett.* **90**, 034502 (2003).
- ³⁸X. He, D. Funfschilling, E. Bodenschatz, and G. Ahlers, “Heat transport by turbulent Rayleigh–Bénard convection for $Pr \approx 0.8$ and $4 \times 10^{11} \leq Ra \leq 2 \times 10^{14}$: Ultimate-state transition for aspect ratio $T = 1.00$,” *New J. Phys.* **14**, 063030 (2012).
- ³⁹S. S. Pawar and J. H. Arakeri, “Kinetic energy and scalar spectra in high Rayleigh number axially homogeneous buoyancy driven turbulence,” *Phys. Fluids* **28**, 065103 (2016).
- ⁴⁰S. S. Pawar and J. H. Arakeri, “Two regimes of flux scaling in axially homogeneous turbulent convection in vertical tube,” *Phys. Rev. Fluids* **1**, 042401(R) (2016).
- ⁴¹L. E. Schmidt, E. Calzavarini, D. Lohse, and F. Toschi, “Axially homogeneous Rayleigh–Bénard convection in a cylindrical cell,” *J. Fluid Mech.* **691**, 52–68 (2012).
- ⁴²E. Calzavarini, D. Lohse, F. Toschi, and R. Tripiccion, “Rayleigh and Prandtl number scaling in the bulk of Rayleigh–Bénard turbulence,” *Phys. Fluids* **17**, 055107 (2005).
- ⁴³E. Calzavarini, C. R. Doering, J. D. Gibbon, D. Lohse, A. Tanabe, and F. Toschi, “Exponentially growing solutions in homogeneous Rayleigh–Bénard convection,” *Phys. Rev. E* **73**, 035301 (2006).
- ⁴⁴C. R. Doering, “Thermal forcing and ‘classical’ and ‘ultimate’ regimes of Rayleigh–Bénard convection,” *J. Fluid Mech.* **868**, 1–4 (2019).
- ⁴⁵P.-E. Roche, B. Castaing, B. Chabaud, and B. Hebral, “Observation of the 1/2 power law in Rayleigh–Bénard convection,” *Phys. Rev. E* **63**, 045303(R) (2001).
- ⁴⁶G. Ahlers, D. Funfschilling, and E. Bodenschatz, “Transitions in heat transport by turbulent convection at Rayleigh numbers up to 10^{15} ,” *New J. Phys.* **11**, 123001 (2009).
- ⁴⁷J. J. Niemela, L. Skrbek, K. R. Sreenivasan, and R. J. Donnelly, “Turbulent convection at very high Rayleigh numbers,” *Nature* **404**, 837–840 (2000).
- ⁴⁸K. P. Iyer, J. D. Scheel, J. Schumacher, and K. R. Sreenivasan, “Classical 1/3 scaling of convection holds up to $Ra = 10^{15}$,” *Proc. Natl. Acad. Sci. U. S. A.* **117**, 7594–7598 (2020).
- ⁴⁹S. Grossmann and D. Lohse, “Scaling in thermal convection: A unifying theory,” *J. Fluid Mech.* **407**, 27–56 (2000).
- ⁵⁰S. Grossmann and D. Lohse, “Thermal convection for large Prandtl numbers,” *Phys. Rev. Lett.* **86**, 3316–3319 (2001).
- ⁵¹S. Grossmann and D. Lohse, “Prandtl and Rayleigh number dependence of the Reynolds number in turbulent thermal convection,” *Phys. Rev. E* **66**, 016305 (2002).
- ⁵²S. Grossmann and D. Lohse, “On geometry effects in Rayleigh–Bénard convection,” *J. Fluid Mech.* **486**, 105–114 (2003).
- ⁵³L. D. Landau and E. M. Lifshitz, *Fluid Mechanics*, 2nd ed., Course of Theoretical Physics (Elsevier, Oxford, 1987).
- ⁵⁴R. J. A. M. Stevens, E. P. van der Poel, S. Grossmann, and D. Lohse, “The unifying theory of scaling in thermal convection: The updated prefactors,” *J. Fluid Mech.* **730**, 295–308 (2013).
- ⁵⁵M. Lesieur, *Turbulence in Fluids* (Springer-Verlag, Dordrecht, 2008).
- ⁵⁶M. K. Verma, *Energy Transfers in Fluid Flows: Multiscale and Spectral Perspectives* (Cambridge University Press, Cambridge, 2019).
- ⁵⁷R. Verzicco and R. Camussi, “Numerical experiments on strongly turbulent thermal convection in a slender cylindrical cell,” *J. Fluid Mech.* **477**, 19–49 (2003).
- ⁵⁸S. Bhattacharya, A. Pandey, A. Kumar, and M. K. Verma, “Complexity of viscous dissipation in turbulent thermal convection,” *Phys. Fluids* **30**, 031702 (2018).
- ⁵⁹S. Bhattacharya, R. Samtaney, and M. K. Verma, “Scaling and spatial intermittency of thermal dissipation in turbulent convection,” *Phys. Fluids* **31**, 075104 (2019).
- ⁶⁰S. Bhattacharya, S. Sathukhan, A. Guha, and M. K. Verma, “Similarities between the structure functions of thermal convection and hydrodynamic turbulence,” *Phys. Fluids* **31**, 115107 (2019).
- ⁶¹J. D. Scheel, E. Kim, and K. R. White, “Thermal and viscous boundary layers in turbulent Rayleigh–Bénard convection,” *J. Fluid Mech.* **711**, 281–305 (2012).
- ⁶²N. Shi, M. S. Emran, and J. Schumacher, “Boundary layer structure in turbulent Rayleigh–Bénard convection,” *J. Fluid Mech.* **706**, 5–33 (2012).
- ⁶³S. Chandrasekhar, *Hydrodynamic and Hydromagnetic Stability* (Dover Publications, Oxford, 1981).
- ⁶⁴M. Breuer, S. Wessling, J. Schmalzl, and U. Hansen, “Effect of inertia in Rayleigh–Bénard convection,” *Phys. Rev. E* **69**, 026302 (2004).
- ⁶⁵G. K. Batchelor, “Small-scale variation of convected quantities like temperature in turbulent fluid. Part 1. General discussion and the case of small conductivity,” *J. Fluid Mech.* **5**, 113–133 (1959).
- ⁶⁶M. K. Verma, R. J. Samuel, S. Chatterjee, S. Bhattacharya, and A. Asad, “Challenges in fluid flow simulations using exascale computing,” *SN Comput. Sci.* **1**, 178 (2020).
- ⁶⁷R. J. Samuel, S. Bhattacharya, A. Asad, S. Chatterjee, M. K. Verma, R. Samtaney, and S. F. Anwer, “SARAS: A general-purpose PDE solver for fluid dynamics,” J. Open Source Software (unpublished) (2020).
- ⁶⁸G. Grötzbach, “Spatial resolution requirements for direct numerical simulation of the Rayleigh–Bénard convection,” *J. Comput. Phys.* **49**, 241–264 (1983).
- ⁶⁹M. K. Verma, S. Alam, and S. Chatterjee, “Turbulent drag reduction in magnetohydrodynamic and quasi-static magnetohydrodynamic turbulence,” *Phys. Plasmas* **27**, 052301 (2020).
- ⁷⁰E. Frank, M. Hall, G. Holmes, R. Kirkby, B. Pfahringer, I. H. Witten, and L. Trigg, “Weka—A machine learning workbench for data mining,” in *Data Mining and Knowledge Discovery Handbook* (Springer, 2009), pp. 1269–1277.
- ⁷¹X.-L. Qiu and P. Tong, “Temperature oscillations in turbulent Rayleigh–Bénard convection,” *Phys. Rev. E* **66**, 026308 (2002).
- ⁷²A. Nikolaenko, E. Brown, D. Funfschilling, and G. Ahlers, “Heat transport by turbulent Rayleigh–Bénard convection in cylindrical cells with aspect ratio one and less,” *J. Fluid Mech.* **523**, 251–260 (2005).
- ⁷³J. D. Scheel and J. Schumacher, “Local boundary layer scales in turbulent Rayleigh–Bénard convection,” *J. Fluid Mech.* **758**, 344–373 (2014).
- ⁷⁴P. Constantin and C. R. Doering, “Infinite Prandtl number convection,” *J. Stat. Phys.* **94**, 159–172 (1999).
- ⁷⁵C. R. Doering, F. Otto, and M. G. Reznikoff, “Bounds on vertical heat transport for infinite-Prandtl-number Rayleigh–Bénard convection,” *J. Fluid Mech.* **560**, 229–241 (2006).
- ⁷⁶X. Zhu, V. Mathai, R. J. A. M. Stevens, R. Verzicco, and D. Lohse, “Transition to the ultimate regime in two-dimensional Rayleigh–Bénard convection,” *Phys. Rev. Lett.* **120**, 144502 (2018).
- ⁷⁷S. Pandey, J. Schumacher, and K. R. Sreenivasan, “A perspective on machine learning in turbulent flows,” *J. Turbul.* **21**, 567–584 (2020).
- ⁷⁸E. J. Parish and K. Duraisamy, “A paradigm for data-driven predictive modeling using field inversion and machine learning,” *J. Comput. Phys.* **305**, 758–774 (2016).

⁷⁹T. Zürner, W. Liu, D. Krasnov, and J. Schumacher, “Heat and momentum transfer for magnetoconvection in a vertical external magnetic field,” *Phys. Rev. E* **94**, 043108 (2016).

⁸⁰T. Zürner, “Refined mean field model of heat and momentum transfer in magnetoconvection,” *Phys. Fluids* **32**, 107101 (2020).

⁸¹D. H. Kelley and T. Weier, “Fluid mechanics of liquid metal batteries,” *Appl. Mech. Rev.* **70**, 020801 (2018).

⁸²V. N. Prakash, K. R. Sreenivas, and J. H. Arakeri, “The role of viscosity contrast on plume structure in laboratory modeling of mantle convection,” *Chem. Eng. Sci.* **158**, 245–256 (2017).

Chapter 8

Conclusions and scope for future work

8.1 Conclusions of the thesis

Rayleigh-Bénard convection (RBC) is a classical problem and a paradigm for different convective flows occurring in nature and in engineering applications. Despite its simplicity, its dynamics is very rich and has been explored by researchers for decades. In this thesis, we studied turbulent RBC over a wide range of Rayleigh and Prandtl numbers and comprehensively analyzed the characteristics of viscous and thermal dissipation rates, structure functions, the spectra and fluxes of kinetic energy and entropy, the local and global heat fluxes, and the large-scale velocity.

We simulated turbulent RBC in a three-dimensional cubical box with rigid walls on all sides. We employed a finite difference code, SARAS, and a finite volume code, OpenFOAM, for our simulations. The Rayleigh number ranged from 5×10^5 to 5×10^9 , and the Prandtl number from 0.02 to 100. Additionally, we also used highly-resolved simulation data of [Verma et al. \(2017\)](#) with free-slip walls ($Ra = 1.1 \times 10^{11}$ and $Pr = 1$) and of [Kumar and Verma \(2018\)](#) with no-slip walls ($Ra = 1 \times 10^8$ and $Pr = 1$). The former dataset was used for the analysis of structure functions only.

We computed the longitudinal velocity structure functions of turbulent convection using our simulation data. We obtained a wide inertial range and showed conclusively that for $Pr \leq 1$, the third-order velocity structure functions obey Kolmogorov scaling of $S_3^u(l) \sim -l$ in this range, which is similar to that of homogeneous isotropic

turbulence. For $q \neq 3$, the structure functions of turbulent convection fit well with the hierarchy model of [She and Leveque \(1994\)](#) that was analytically derived for homogeneous isotropic turbulence. These results are in agreement with Kolmogorov's energy spectrum observed in turbulent convection for moderate and small Prandtl numbers ([Mishra and Verma, 2010](#); [Kumar et al., 2014](#); [Kumar and Verma, 2018](#); [Verma et al., 2017](#)). However, for large Prandtl numbers, the velocity structure functions exhibit steeper scaling due to strong viscous dissipation in the inertial range. Our results agree with the steeper kinetic energy spectrum observed for large Pr ([Pandey et al., 2014, 2016b](#)).

We also studied the probability distribution functions (PDFs) of the transverse velocity increments, given by $\delta u = \{\mathbf{u}(\mathbf{r} + \mathbf{l}) - \mathbf{u}(\mathbf{r})\} \cdot \hat{\mathbf{l}}$, for different values of the separation distance l . The PDFs are non-Gaussian with stretched-exponential tails for small l and become closer to Gaussian as l is increased, as has also been observed for homogeneous isotropic turbulence ([Donzis et al., 2008](#)).

We studied the Prandtl number (Pr) dependence of amplitudes of the spectra and fluxes of kinetic energy, as well as the energy injection rates and dissipation rates, of turbulent thermal convection using numerical data. We present novel results and showed that the amplitudes of the kinetic energy fluxes and spectra and those of structure functions increase with the decrease of Pr, thus exhibiting stronger nonlinearity for flows with small Prandtl numbers. Consistent with these observations, the kinetic energy injection rates and the dissipation rates too increase with the decrease of Pr. For small Prandtl numbers, kinetic energy injection by buoyancy occurs mostly at large scales. This results in the kinetic energy flux in the inertial range to be approximately equal to the viscous dissipation rate, similar to hydrodynamic turbulence. However, for moderate and large Prandtl numbers, significant kinetic energy is injected at small scales as well, causing the energy flux in the inertial range to be a fraction of the viscous dissipation rate.

We analyzed the statistics of local convective heat flux in thermal convection using our numerical data and studied their variations with Prandtl numbers. The fluctuations of the local heat flux were found to become stronger with the increase of Pr. This is because the plumes transferring heat become thinner as Pr is increased, thereby increasing inhomogeneity in the heat flux.

We studied the scaling and relative strengths of the viscous and thermal dissipa-

tion rates in the bulk and boundary layers of RBC cell. For this work, we determined the boundary layer thicknesses for each data and computed the scaling of the dissipation rates over the entire bulk and boundary layer volumes. We showed that for moderate and large Pr, the viscous dissipation rate in the bulk, $\epsilon_{u,\text{bulk}}$, does not scale as U^3/d as in homogeneous isotropic turbulence; instead, it gets a correction of approximately $\text{Ra}^{-0.18}$ for moderate Pr to $\text{Ra}^{-0.35}$ for large Pr. However, for small Pr, $\epsilon_{u,\text{bulk}}$ was found to scale as U^3/d without any additional Ra dependence. The thermal dissipation rate in the bulk also does not scale as $U\Delta^2/d$ as in homogeneous isotropic turbulence with passive scalar but gets an additional correction of approximately $\text{Ra}^{-0.15}$ for small Pr to $\text{Ra}^{-0.25}$ for large Pr. Further, the viscous boundary layer thickness was observed to deviate marginally from Prandtl-Blasius's relation of $\delta_u \sim \text{Re}^{-1/2}$.

We showed that the viscous dissipation rate is stronger, albeit marginally, in the bulk than in the boundary layers for all the Rayleigh numbers employed in our study. This is contrary to the general assumption that most of the viscous dissipation occurs near the walls. The thermal dissipation rate, on the other hand, was found to be stronger in the boundary layers by a factor of approximately three. We also showed that the velocity gradients in the bulk are more pronounced than the thermal gradients; thus, viscous dissipation rate is stronger in the bulk compared to the thermal dissipation rate.

The intensity of the dissipation rates was found to be more in the boundary layers than in the bulk because the former occupy much less volume than the bulk. The probability distribution function (PDF) of the viscous dissipation rates was observed to be log normal in the bulk (as in homogeneous isotropic turbulence) but stretched exponential in the boundary layers. This implies that extreme events occur in the boundary layers. We also showed the PDF of the thermal dissipation rates to be stretched exponentials both in the bulk and in the boundary layers. However, the tails of the PDFs were observed to be much wider in the boundary layers, again implying that the extreme events of thermal dissipation occur in the boundary layers. Further, the fluctuations of both viscous and thermal dissipation rates become stronger as the intensity of turbulence is increased by increasing Ra or decreasing Pr.

Finally, we used our results to extend Grossmann and Lohse's model ([Grossmann and Lohse, 2000, 2001](#)) for predicting the Nusselt and Reynolds numbers for arbitrary sets of governing parameters. Towards this objective, we derived a cubic polynomial equation for Re and Nu that consists of four functions $f_i(\text{Ra}, \text{Pr})$; these functions are

prefactors for the dissipation rates in the bulk and boundary layers. These functional forms arise due to the modification of the scaling of bulk dissipation rates and the viscous boundary-layer thickness, as discussed earlier. The aforementioned functions were determined using a regression algorithm on 60 datasets obtained from our numerical simulations. The revised predictions were observed to be in better agreement with the past numerical and experimental results compared the GL model, especially for very large and very small Prandtl numbers.

We believe that our work will be valuable to the scientific and engineering community. The enhancement in the predictions of Re and Nu will be of significant importance for flows with extreme Prandtl numbers. For example, our results will be useful for modeling the heat transfer in liquid metal batteries, a promising technology for energy storage because of its long cycle life (Kelley and Weier, 2018). In addition, our analysis should help understand mantle convection involving large Pr flow, which may enable us to make better predictions of seismic disturbances and the earth's magnetic fields. Further, our analysis on small-scale statistics in RBC will be important for modeling flows in stars and bubbly turbulence. Our results should also help in developing accurate subgrid models for convection; these subgrid models can be used to simulate more complex convective flows such as heat sinks, combustion chambers, and building interiors.

8.2 Scope of future work

In the present thesis, we numerically analyzed the velocity structure functions and studied the Prandtl number dependence of the local heat fluxes and the spectra of kinetic energy and entropy in Rayleigh-Bénard convection. We also studied the scaling and spatial intermittency of viscous and thermal dissipation rates, and using these results, enhanced Grossmann and Lohse's model for predicting the Reynolds and Nusselt numbers.

Based on the above results, we discuss some possible projects which may be investigated in the future.

1. We studied the scaling of velocity structure functions in detail in this work. It would be useful to study the structure functions of the temperature fluctuations (θ) and relate them to the dual branches observed in the spectrum of entropy (θ^2).

2. The boundary layers exhibit different physics than the bulk. It would be instructive to study the spectra and fluxes of kinetic energy and entropy in the boundary layers. The structure functions of velocity and temperature inside the boundary layers would also be interesting to analyze.
3. For large Prandtl number RBC, the flow becomes anisotropic (Nath et al., 2016). It would thus be instructive to study the structure functions and the spectral quantities in terms of horizontal and vertical length scales in this regime to understand the small-scale dynamics of the system better.
4. Presently, we studied the scaling of the dissipation rates using data that are restricted to $Ra < 10^{10}$. For larger Rayleigh numbers, we expect weaker dependence of Ra and Pr for the prefactors for the dissipation rates due to thin boundary layers. Thus, it is suggested to test this out by conducting high-resolution simulations for $Ra \gg 10^{10}$. However, with the current computational resources, it is difficult to achieve such large Rayleigh numbers for 3D simulations. Large-eddy simulation (LES) is a promising technique to achieve this goal.
5. In the current thesis, we enhanced the GL model by considering the prefactors for the dissipation rates, f_i , to be functions of Ra and Pr . However, we believe that these prefactors also weakly depend on the aspect ratio of the convective cell. It would be instructive to perform simulations of RBC for different aspect ratios to ascertain their dependence of the above prefactors, and hence of Reynolds and Nusselt numbers.
6. It would also be interesting to study convection under the influence of rotation. Rotation introduces interesting dynamics such as inertial waves (Ranjan and Davidson, 2021), and it would be instructive to study their effects on heat transfer and small-scale dynamics.

Rayleigh-Bénard convection is an important topic exhibiting a rich set of dynamics. Our work is a small attempt to uncover some of these mysteries.

Bibliography

- Ahlers, G., Bodenschatz, E., and He, X. (2017). Ultimate-state transition of turbulent Rayleigh-Bénard convection. *Phys. Rev. Fluids*, 2(5):054603.
- Ahlers, G., Funfschilling, D., and Bodenschatz, E. (2009a). Transitions in heat transport by turbulent convection at rayleigh numbers up to 10^{15} . *New J. Phys.*, 11(12):123001.
- Ahlers, G., Grossmann, S., and Lohse, D. (2009b). Heat transfer and large scale dynamics in turbulent Rayleigh-Bénard convection. *Rev. Mod. Phys.*, 81(2):503–537.
- Ahlers, G. and Xu, X. (2001). Prandtl-number dependence of heat transport in turbulent Rayleigh-Bénard convection. *Phys. Rev. Lett.*, 86(1):3320–3323.
- Anderson, J. D. (1995). *Computational Fluid Dynamics: The Basics With Applications*. McGraw-Hill, New York.
- Ashkenazi, S. and Steinberg, V. (1999a). High Rayleigh number turbulent convection in a gas near the gas-liquid critical point. *Phys. Rev. Lett.*, 83(18):3641–3645.
- Ashkenazi, S. and Steinberg, V. (1999b). Spectra and statistics of velocity and temperature fluctuations in turbulent convection. *Phys. Rev. Lett.*, 83(23):4760–4763.
- Bartello, P. and Tobias, S. M. (2013). Sensitivity of stratified turbulence to the buoyancy Reynolds number. *J. Fluid Mech.*, 725:1–22.
- Bejan, A. (2013). *Convection Heat Transfer*. John Wiley & Sons, New Jersey, 4th edition.

BIBLIOGRAPHY

- Benzi, R., Massaioli, F., Succi, S., and Tripicciono, R. (1994a). Scaling behaviour of the velocity and temperature correlation functions in 3D convective turbulence. *EPL*, 28(4):231–236.
- Benzi, R., Tripicciono, R., Massaioli, F., Succi, S., and Ciliberto, S. (1994b). On the scaling of the velocity and temperature structure functions in Rayleigh-Bénard convection. *EPL*, 25(5):341–346.
- Bhattacharjee, J. K. (1987). *Convection and Chaos in Fluids*. World Scientific, Singapore.
- Bhattacharjee, J. K. (2015). Kolmogorov argument for the scaling of the energy spectrum in a stratified fluid. *Phys. Lett. A*, 379(7):696–699.
- Bhattacharya, S., Pandey, A., Kumar, A., and Verma, M. K. (2018). Complexity of viscous dissipation in turbulent thermal convection. *Phys. Fluids*, 30(3):031702.
- Bhattacharya, S., Sadhukhan, S., Guha, A., and Verma, M. K. (2019a). Similarities between the structure functions of thermal convection and hydrodynamic turbulence. *Phys. Fluids*, 31(11):115107.
- Bhattacharya, S., Samtaney, R., and Verma, M. K. (2019b). Scaling and spatial intermittency of thermal dissipation in turbulent convection. *Phys. Fluids*, 31(7):075104.
- Bhattacharya, S., Verma, M. K., and Samtaney, R. (2021a). Prandtl number dependence of the small-scale properties in Rayleigh-Bénard convection. *Phys. Rev. Fluids*, 6(6):063501.
- Bhattacharya, S., Verma, M. K., and Samtaney, R. (2021b). Revisiting Reynolds and Nusselt numbers in turbulent thermal convection. *Phys. Fluids*, 33(1):015113.
- Bolgiano, R. (1959). Turbulent spectra in a stably stratified atmosphere. *J. Geophys. Res.*, 64(12):2226–2229.
- Boyd, J. P. (2013). *Chebyshev and Fourier Spectral Methods*. Dover (NY).
- Brethouwer, G., Billant, P., Lindborg, E., and Chomaz, J.-M. (2007). Scaling analysis and simulation of strongly stratified turbulent flows. *J. Fluid Mech.*, 585:343–368.
- Breuer, M., Wessling, S., Schmalzl, J., and Hansen, U. (2004). Effect of inertia in Rayleigh-Bénard convection. *Phys. Rev. E*, 69(2):026302.

BIBLIOGRAPHY

- Brown, E., Nikolaenko, A., and Ahlers, G. (2005). Reorientation of the Large-Scale Circulation in Turbulent Rayleigh-Bénard Convection. *Phys. Rev. Lett.*, 95(8):84503.
- Calzavarini, E., Doering, C. R., Gibbon, J. D., Lohse, D., Tanabe, A., and Toschi, F. (2006). Exponentially growing solutions in homogeneous Rayleigh-Bénard convection. *Phys. Rev. E*, 73(3):035301.
- Calzavarini, E., Lohse, D., and Toschi, F. (2005). Rayleigh and Prandtl number scaling in the bulk of Rayleigh-Bénard turbulence. *Phys. Fluids*, 17(5):055107.
- Calzavarini, E., Toschi, F., and Tripicciono, R. (2002). Evidences of Bolgiano-Obukhov scaling in three-dimensional Rayleigh-Bénard convection. *Phys. Rev. E*, 66(1):016304.
- Camussi, R. and Verzicco, R. (1998). Convective turbulence in mercury: scaling laws and spectra. *Phys. Fluids*, 10(2):516–527.
- Canuto, C., Hussaini, M. Y., Quarteroni, A., and Zang, T. A. (1988). *Spectral Methods in Fluid Dynamics*. Springer-Verlag, Berlin Heidelberg.
- Castaing, B., Gunaratne, G., Heslot, F., Kadanoff, L., Libchaber, A., Thomae, A., Wu, X. Z., Zaleski, S., and Zannetti, G. (1989). Scaling of hard thermal turbulence in Rayleigh-Bénard convection. *J. Fluid Mech.*, 204:1–30.
- Chandrasekhar, S. (1981). *Hydrodynamic and Hydromagnetic Stability*. Dover publications, Oxford, 1st edition.
- Chatterjee, A. G., Verma, M. K., Kumar, A., Samtaney, R., Hadri, B., and Khurram, R. (2018). Scaling of a Fast Fourier Transform and a pseudo-spectral fluid solver up to 196608 cores. *J. Parallel Distrib. Comput.*, 113:77–91.
- Chavanne, X., Chillà, F., Castaing, B., Hebral, B., Chabaud, B., and Chaussy, J. (1997). Observation of the ultimate regime in Rayleigh-Bénard convection. *Phys. Rev. Lett.*, 79(19):3648–3651.
- Chertkov, M., Falkovich, G., and Kolokolov, I. (1998). Intermittent Dissipation of a Passive Scalar in Turbulence. *Phys. Rev. Lett.*, 80(10):2121–2124.
- Chillà, F., Ciliberto, S., Innocenti, C., and Pampaloni, E. (1993). Spectra of Local and Averaged Scalar Fields in Turbulence. *EPL*, 22(1):23–28.
- Chillà, F. and Schumacher, J. (2012). New perspectives in turbulent Rayleigh-Bénard convection. *Eur. Phys. J. E*, 35(7):58.

BIBLIOGRAPHY

- Ching, E. S. C. (2000). Intermittency of temperature field in turbulent convection. *Phys. Rev. E*, 61(1):R33.
- Ching, E. S. C. (2007). Scaling laws in the central region of confined turbulent thermal convection. *Phys. Rev. E*, 75(5):056302.
- Ching, E. S. C. (2013). *Statistics and Scaling in Turbulent Rayleigh-Bénard Convection*. Springer, Berlin.
- Ching, E. S. C. and Cheng, W. C. (2008). Anomalous scaling and refined similarity of an active scalar in a shell model of homogeneous turbulent convection. *Phys. Rev. E*, 77(1):015303.
- Ching, E. S. C., Tsang, Y.-K., Fok, T. N., He, X., and Tong, P. (2013). Scaling behavior in turbulent Rayleigh-Bénard convection revealed by conditional structure functions. *Phys. Rev. E*, 87(1):013005.
- Cioni, S., Ciliberto, S., and Sommeria, J. (1995). Temperature structure functions in turbulent convection at low prandtl number. *EPL*, 32(5):413–418.
- Cioni, S., Ciliberto, S., and Sommeria, J. (1997). Strongly turbulent Rayleigh-Bénard convection in mercury: comparison with results at moderate Prandtl number. *J. Fluid Mech.*, 335:111–140.
- Constantin, P. and Doering, C. R. (1999). Infinite Prandtl number convection. *J. Stat. Phys.*, 94(1):159–172.
- Corrsin, S. (1951). On the spectrum of isotropic temperature fluctuations in an isotropic turbulence. *J. Appl. Phys.*, 22(4):469–473.
- Coulson, J. M. and Richardson, J. F. (1999). *Chemical Engineering Volume 1*. Elsevier, 6th edition.
- Crank, J. and Nicolson, P. (1947). A practical method for numerical evaluation of solutions of partial differential equations of the heat conduction type. *Proc. Camb. Phil. Soc.*, 43:50–67.
- Dar, G., Verma, M. K., and Eswaran, V. (2001). Energy transfer in two-dimensional magnetohydrodynamic turbulence: formalism and numerical results. *Physica D*, 157(3):207–225.

BIBLIOGRAPHY

- Davidson, P. A. (2004). *Turbulence: An Introduction for Scientists and Engineers*. Oxford University Press, Oxford.
- Davis, A. (1922a). Natural convective cooling in fluids. *The London, Edinburgh, and Dublin Philosophical Magazine and Journal of Science*, 44(263):920–940.
- Davis, A. (1922b). Natural convective cooling of wires. *The London, Edinburgh, and Dublin Philosophical Magazine and Journal of Science*, 43(254):329–339.
- Doering, C. R. (2019). Thermal forcing and classical and ultimate regimes of Rayleigh-Bénard convection. *J. Fluid Mech.*, 868:1–4.
- Donzis, D. A., Yeung, P. K., and Sreenivasan, K. R. (2008). Dissipation and enstrophy in isotropic turbulence: Resolution effects and scaling in direct numerical simulations. *Phys. Fluids*, 20(4):045108.
- Ecke, R. E., Mainieri, R., and Sullivan, T. S. (1991). Universality in quasiperiodic Rayleigh-Bénard convection. *Phys. Rev. A*, 44(12):8103–8118.
- Emran, M. S. and Schumacher, J. (2008). Fine-scale statistics of temperature and its derivatives in convective turbulence. *J. Fluid Mech.*, 611:13–34.
- Falcon, E., Aumaitre, S., Falcon, C., Laroche, C., and Fauve, S. (2008). Fluctuations of energy flux in wave turbulence. *Phys. Rev. Lett.*, 100(6):064503.
- Falkovich, G., Gawędzki, K., and Vergassola, M. (2001). Particles and fields in fluid turbulence. *Rev. Mod. Phys.*, 73:913–975.
- Ferziger, J. H. and Peric, M. (2001). *Computational Methods for Fluid Dynamics*. Springer-Verlag, Berlin Heidelberg, 3 edition.
- Frick, P., Khalilov, R., Kolesnichenko, I., Mamykin, A., Pakholkov, V., Pavlinov, A., and Rogozhkin, S. (2015). Turbulent convective heat transfer in a long cylinder with liquid sodium. *EPL*, 109(1):14002.
- Frisch, U. (1995). *Turbulence: The Legacy of A. N. Kolmogorov*. Cambridge University Press, Cambridge.
- Funfschilling, D., Brown, E., Nikolaenko, A., and Ahlers, G. (2005). Heat transport in turbulent Rayleigh-Bénard convection in cylindrical samples with aspect ratio one and larger. *J. Fluid Mech.*, 536:145–154.

BIBLIOGRAPHY

- Glazier, J. A., Segawa, T., Naert, A., and Sano, M. (1999). Evidence against ‘ultrahard’ thermal turbulence at very high Rayleigh numbers. *Nature*, 398:307–310.
- Grossmann, S. and Lohse, D. (2000). Scaling in thermal convection: a unifying theory. *J. Fluid Mech.*, 407:27–56.
- Grossmann, S. and Lohse, D. (2001). Thermal convection for large Prandtl numbers. *Phys. Rev. Lett.*, 86(1):3316–3319.
- Grossmann, S. and Lohse, D. (2002). Prandtl and Rayleigh number dependence of the Reynolds number in turbulent thermal convection. *Phys. Rev. E*, 66(1):016305.
- Grossmann, S. and Lohse, D. (2003). On geometry effects in Rayleigh-Bénard convection. *J. Fluid Mech.*, 486:105–114.
- Grötzbach, G. (1983). Spatial resolution requirements for direct numerical simulation of the Rayleigh-Bénard convection. *J. Comput. Phys*, 49(2):241–264.
- Gupta, A., Jayaram, R., Chatterjee, A. G., Sadhukhan, S., Samtaney, R., and Verma, M. K. (2019). Energy and enstrophy spectra and fluxes for the inertial-dissipation range of two-dimensional turbulence. *Phys. Rev. E*, 100(5):053101.
- He, X., Ching, E. S. C., and Tong, P. (2011). Locally averaged thermal dissipation rate in turbulent thermal convection: A decomposition into contributions from different temperature gradient components. *Phys. Fluids*, 23(2):025106.
- He, X., Funfschilling, D., Bodenschatz, E., and Ahlers, G. (2012). Heat transport by turbulent Rayleigh-Bénard convection for $\text{Pr} \approx 0.8$ and $4 \times 10^{11} \leq \text{Ra} \leq 2 \times 10^4$: ultimate state transition for aspect ratio $T = 1.00$. *New J. Phys.*, 14:063030.
- He, X. and Tong, P. (2009). Measurements of the thermal dissipation field in turbulent Rayleigh-Bénard convection. *Phys. Rev. E*, 79(2):026306.
- He, X., Tong, P., and Xia, K. Q. (2007). Measured Thermal Dissipation Field in Turbulent Rayleigh-Bénard Convection. *Phys. Rev. Lett.*, 98(14):144501.
- Heslot, F., Castaing, B., and Libchaber, A. (1987). Transitions to turbulence in helium gas. *Phys. Rev. A*, 36(12):5870–5873.
- Horanyi, S., Krebs, L., and Müller, U. (1999). Turbulent rayleigh-bénard convection in low prandtl-number fluids. *Int. J. Heat Mass Transf.*, 42(21):3983 – 4003.

BIBLIOGRAPHY

- Horn, S., Shishkina, O., and Wagner, C. (2013). On non-Oberbeck–Boussinesq effects in three-dimensional Rayleigh–Bénard convection in glycerol. *J. Fluid Mech.*, 724:175–202.
- Ierley, G. R. and Kerswell, R. R. (2006). Infinite-Prandtl-number convection. Part 2. A singular limit of upper bound theory. *J. Fluid Mech.*, 560:159–227.
- Issa, R. I. (1985). Solution of the Implicitly Discretized Fluid Flow Equations by Operator-Splitting. *J. Comput. Phys.*, 62(1):40–65.
- Iyer, K. P., Scheel, J. D., Schumacher, J., and Sreenivasan, K. R. (2020). Classical $1/3$ scaling of convection holds up to $Ra=10^{15}$. *Proc. Natl. Acad. Sci. U.S.A.*, 117(14):7594–7598.
- Jasak, H., Jemcov, A., Tukovic, Z., et al. (2007). OpenFOAM: A C++ library for complex physics simulations. In *International workshop on coupled methods in numerical dynamics*, volume 1000, pages 1–20. IUC Dubrovnik, Croatia.
- Kaczorowski, M. and Xia, K.-Q. (2013). Turbulent flow in the bulk of Rayleigh–Bénard convection: small-scale properties in a cubic cell. *J. Fluid Mech.*, 722:596–617.
- Kays, W. M. and Crawford, M. E. (1993). *Convective Heat and Mass Transfer*. McGraw Hill, Singapore, 3rd edition.
- Kelley, D. H. and Weier, T. (2018). Fluid Mechanics of Liquid Metal Batteries. *Appl. Mech. Rev.*, 70(2):020801.
- Kerr, R. M. (1996). Rayleigh number scaling in numerical convection. *J. Fluid Mech.*, 310:139–179.
- Kerr, R. M. and Herring, J. R. (2000). Prandtl number dependence of Nusselt number in direct numerical simulations. *J. Fluid Mech.*, 419:325–344.
- Khatri, H., Sukhatme, J., Kumar, A., and Verma, M. K. (2018). Surface Ocean Enstrophy, Kinetic Energy Fluxes, and Spectra From Satellite Altimetry. *J. Geophys. Res. Oceans*, 123(5):3875–3892.
- Kimura, Y. and Herring, J. R. (1996). Diffusion in stably stratified turbulence. *J. Fluid Mech.*, 328:253–269.
- Kolmogorov, A. N. (1941a). Dissipation of Energy in Locally Isotropic Turbulence. *Dokl Acad Nauk SSSR*, 32:16–18.

BIBLIOGRAPHY

- Kolmogorov, A. N. (1941b). The local structure of turbulence in incompressible viscous fluid for very large Reynolds numbers. *Dokl Acad Nauk SSSR*, 30:301–305.
- Kraichnan, R. H. (1959). The structure of isotropic turbulence at very high Reynolds numbers. *J. Fluid Mech.*, 5:497–543.
- Kraichnan, R. H. (1962). Turbulent thermal convection at arbitrary prandtl number. *Phys. Fluids*, 5(11):1374–1389.
- Kreyszig, E. (2011). *Advanced Engineering Mathematics*. Wiley, New York, 10th edition.
- Kumar, A., Chatterjee, A. G., and Verma, M. K. (2014). Energy spectrum of buoyancy-driven turbulence. *Phys. Rev. E*, 90(2):023016.
- Kumar, A. and Verma, M. K. (2015). Shell model for buoyancy-driven turbulence. *Phys. Rev. E*, 91(4):043014.
- Kumar, A. and Verma, M. K. (2018). Applicability of Taylor’s hypothesis in thermally driven turbulence. *R. Soc. open sci.*, 5(4):172152.
- Kunnen, R. P. J., Clercx, H. J. H., Geurts, B. J., van Bokhoven, L. J. A., Akkermans, R. A. D., and Verzicco, R. (2008). Numerical and experimental investigation of structure-function scaling in turbulent Rayleigh–Bénard convection. *Phys. Rev. E*, 77(1):016302.
- Lam, S., Shang, X.-D., Zhou, S.-Q., and Xia, K.-Q. (2002). Prandtl number dependence of the viscous boundary layer and the Reynolds numbers in Rayleigh–Bénard convection. *Phys. Rev. E*, 65(6):066306.
- Landau, L. D. and Lifshitz, E. M. (1987). *Fluid Mechanics*. Course of Theoretical Physics. Elsevier, Oxford, 2nd edition.
- Lesieur, M. (2008). *Turbulence in Fluids*. Springer-Verlag, Dordrecht.
- Lindborg, E. (2006). The energy cascade in a strongly stratified fluid. *J. Fluid Mech.*, 550:207–242.
- Lohse, D. and Toschi, F. (2003). Ultimate state of thermal convection. *Phys. Rev. Lett.*, 90(3):034502.
- Lohse, D. and Xia, K.-Q. (2010). Small-scale properties of turbulent Rayleigh–Bénard convection. *Annu. Rev. Fluid Mech.*, 42(1):335–364.

BIBLIOGRAPHY

- L'vov, V. S. (1991). Spectra of velocity and temperature-fluctuations with constant entropy flux of fully-developed free-convective turbulence. *Phys. Rev. Lett.*, 67(6):687–690.
- L'vov, V. S. and Falkovich, G. (1992). Conservation laws and two-flux spectra of hydrodynamic convective turbulence. *Physica D*, 57:85–95.
- Malkus, W. V. R. (1954). The Heat Transport and Spectrum of Thermal Turbulence. *Proceedings of the Royal Society of London. Series A*, 225(1):196–212.
- Martínez, D. O., Chen, S., Doolen, G. D., Kraichnan, R. H., Wang, L.-P., and Zhou, Y. (1997). Energy spectrum in the dissipation range of fluid turbulence. *J. Plasma Phys.*, 57(1):195–201.
- McComb, W. D. (1990). *The physics of fluid turbulence*. Clarendon Press, Oxford.
- Mishra, P. K. and Verma, M. K. (2010). Energy spectra and fluxes for Rayleigh-Bénard convection. *Phys. Rev. E*, 81(5):056316.
- Mishra, P. K., Wahi, P., and Verma, M. K. (2010). Patterns and bifurcations in low-Prandtl-number Rayleigh-Bénard convection. *EPL*, 89(4):44003.
- Moukalled, F., Mangani, L., and Darwish, M. (2016). *The Finite Volume Method in Computational Fluid Dynamics*. Springer, Cham, 1st edition.
- Nandukumar, Y. and Pal, P. (2016). Instabilities and chaos in low-Prandtl number rayleigh-Bénard convection. *Computers & Fluids*, 138(C):61–66.
- Nath, D., Pandey, A., Kumar, A., and Verma, M. K. (2016). Near isotropic behavior of turbulent thermal convection. *Phys. Rev. Fluids*, 1(6):064302.
- Niemela, J. J., Skrbek, L., Sreenivasan, K. R., and Donnelly, R. J. (2000). Turbulent convection at very high Rayleigh numbers. *Nature*, 404:837–840.
- Niemela, J. J., Skrbek, L., Sreenivasan, K. R., and Donnelly, R. J. (2001). The wind in confined thermal convection. *J. Fluid Mech.*, 449:169–178.
- Obukhov, A. M. (1949). Structure of the temperature field in a turbulent flow. *Izv. Geogr. Geophys. Ser.*, 13:58–69.
- Obukhov, A. M. (1959). On influence of buoyancy forces on the structure of temperature field in a turbulent flow. *Dokl Acad Nauk SSSR*, 125:1246.

BIBLIOGRAPHY

- Obukhov, A. M. (1962). Some Specific Features of Atmospheric Turbulence. *J. Fluid Mech.*, 13(1):77–81.
- Pal, P., Wahi, P., Paul, S., Verma, M. K., Kumar, K., and Mishra, P. K. (2009). Bifurcation and chaos in zero-Prandtl-number convection. *EPL*, 87(5):54003.
- Pandey, A., Kumar, A., Chatterjee, A. G., and Verma, M. K. (2016a). Dynamics of large-scale quantities in Rayleigh-Bénard convection. *Phys. Rev. E*, 94(5):053106.
- Pandey, A. and Verma, M. K. (2016). Scaling of large-scale quantities in Rayleigh-Bénard convection. *Phys. Fluids*, 28(9):095105.
- Pandey, A., Verma, M. K., Chatterjee, A. G., and Dutta, B. (2016b). Similarities between 2D and 3D convection for large Prandtl number. *Pramana-J. Phys.*, 87(1):13.
- Pandey, A., Verma, M. K., and Mishra, P. K. (2014). Scaling of heat flux and energy spectrum for very large Prandtl number convection. *Phys. Rev. E*, 89(2):023006.
- Pandey, S., Schumacher, J., and Sreenivasan, K. R. (2020). A perspective on machine learning in turbulent flows. *J. of Turbulence*, 21(9 – 10):567–584.
- Parish, E. J. and Duraisamy, K. (2016). A paradigm for data-driven predictive modeling using field inversion and machine learning. *J. Comput. Phys.*, 305:758–774.
- Patankar, S. V. (1980). *Numerical Heat Transfer and Fluid Flow*. Taylor and Francis, London, 1st edition.
- Patankar, S. V. and Spalding, D. B. (1972). A calculation procedure for heat, mass and momentum transfer in three-dimensional parabolic flows. *Int. J. Heat Mass Transf.*, 15(10):1787–1806.
- Paul, S., Pal, P., Wahi, P., and Verma, M. K. (2011). Dynamics of zero-Prandtl number convection near onset. *Chaos*, 21(2):023118.
- Pawar, S. S. and Arakeri, J. H. (2016a). Kinetic energy and scalar spectra in high Rayleigh number axially homogeneous buoyancy driven turbulence. *Phys. Fluids*, 28(6):065103.
- Pawar, S. S. and Arakeri, J. H. (2016b). Two regimes of flux scaling in axially homogeneous turbulent convection in vertical tube. *Phys. Rev. Fluids*, 1(8):042401(R).

BIBLIOGRAPHY

- Petschel, K., Stellmach, S., Wilczek, M., Lülff, J., and Hansen, U. (2013). Dissipation Layers in Rayleigh-Bénard Convection: A Unifying View. *Phys. Rev. Lett.*, 110(11):114502.
- Pharasi, H. K., Kumar, D., Kumar, K., and Bhattacharjee, J. K. (2016). Spectra and probability distributions of thermal flux in turbulent Rayleigh-Bénard convection. *Phys. Fluids*, 28(5):055103.
- Pope, S. B. (2000). *Turbulent Flows*. Cambridge University Press, Cambridge.
- Procaccia, I. and Zeitak, R. (1989). Scaling exponents in nonisotropic convective turbulence. *Phys. Rev. Lett.*, 62(18):2128–2131.
- Puthenveettil, B. A., Ananthakrishna, G., and Arakeri, J. H. (2005). The multifractal nature of plume structure in high-Rayleigh-number convection. *J. Fluid Mech.*, 526:245–256.
- Puthenveettil, B. A. and Arakeri, J. H. (2005). Plume structure in high-Rayleigh-number convection. *J. Fluid Mech.*, 542:217–249.
- Ranjan, A. and Davidson, P. A. (2021). Columnar heat transport via advection induced by inertial waves. *Int. J. Heat Fluid Flow*, 87:108703.
- Roche, P.-E., Castaing, B., Chabaud, B., and Hebral, B. (2001). Observation of the $1/2$ power law in Rayleigh-Bénard convection. *Phys. Rev. E*, 63(4):045303(R).
- Rossby, H. T. (1969). A study of Bénard convection with and without rotation. *J. Fluid Mech.*, 36:309–335.
- Rubinstein, R. (1994). Renormalization group theory of Bolgiano scaling in Boussinesq turbulence. Technical Report ICOM-94-8; CMOTT-94-2.
- Sadhukhan, S., Bhattacharya, S., and Verma, M. K. (2021). fastSF: A parallel code for computing the structure functions of turbulence. *J. Open Source Softw.*, 6(57):2185.
- Sadhukhan, S., Verma, M. K., Stepanov, R., Plunian, F., and Samtaney, R. (2019). Kinetic helicity and enstrophy transfers in helical hydrodynamic turbulence. *Phys. Rev. Fluids*, 4:84607.
- Sameen, A., Verzicco, R., and Sreenivasan, K. R. (2008). Non-Boussinesq convection at moderate Rayleigh numbers in low temperature gaseous helium. *Phys. Scr.*, T132:014053.

BIBLIOGRAPHY

- Sameen, A., Verzicco, R., and Sreenivasan, K. R. (2009). Specific roles of fluid properties in non-Boussinesq thermal convection at the Rayleigh number of 2×10^8 . *EPL*, 86(1):14006.
- Samuel, R. J., Bhattacharya, S., Asad, A., Chatterjee, S., Verma, M. K., Samtaney, R., and Anwer, S. F. (2020). SARAS: A general-purpose PDE solver for fluid dynamics. *under review in J. Open Source Softw.*
- Sano, M., Wu, X.-Z., and Libchaber, A. (1989). Turbulence in helium-gas free convection. *Phys. Rev. A*, 40(11):6421–6430.
- Scheel, J. D., Emran, M. S., and Schumacher, J. (2013). Resolving the fine-scale structure in turbulent Rayleigh–Bénard convection. *New J. Phys.*, 15(11):113063.
- Scheel, J. D., Kim, E., and White, K. R. (2012). Thermal and viscous boundary layers in turbulent Rayleigh–Bénard convection. *J. Fluid Mech.*, 711:281–305.
- Scheel, J. D. and Schumacher, J. (2016). Global and local statistics in turbulent convection at low Prandtl numbers. *J. Fluid Mech.*, 802:147–173.
- Scheel, J. D. and Schumacher, J. (2017). Predicting transition ranges to fully turbulent viscous boundary layers in low Prandtl number convection flows. *Phys. Rev. Fluids*, 2(12):123501.
- Schmalzl, J., Breuer, M., and Hansen, U. (2002). The influence of the Prandtl number on the style of vigorous thermal convection. *Geophys. Astrophys. Fluid Dyn.*, 96(5):381–403.
- Schmidt, L. E., Calzavarini, E., Lohse, D., and Toschi, F. (2012). Axially homogeneous Rayleigh–Bénard convection in a cylindrical cell. *J. Fluid Mech.*, 691:52–68.
- Schumacher, J., Götzfried, P., and Scheel, J. D. (2015). Enhanced enstrophy generation for turbulent convection in low-Prandtl-number fluids. *PNAS*, 112(31):201505111.
- Schumacher, J. and Sreenivasan, K. R. (2020). Colloquium: Unusual dynamics of convection in the Sun. *Rev. Mod. Phys.*, 92(4):041001.
- Shang, X.-D., Qiu, X.-L., Tong, P., and Xia, K.-Q. (2003). Measured local heat transport in turbulent Rayleigh–Bénard convection. *Phys. Rev. Lett.*, 90(7):074501.
- Shang, X.-D. and Xia, K.-Q. (2001). Scaling of the velocity power spectra in turbulent thermal convection. *Phys. Rev. E*, 64(6):65301.

BIBLIOGRAPHY

- Sharma, M. K., Verma, M. K., and Chakraborty, S. (2019). Anisotropic energy transfers in rapidly rotating turbulence. *Phys. Fluids*, 31(8):085117.
- She, Z.-S. and Leveque, E. (1994). Universal scaling laws in fully developed turbulence. *Phys. Rev. Lett.*, 72(3):336–339.
- Shestakov, A., Stepanov, R., and Frick, P. (2017). On cascade energy transfer in convective turbulence. *J. Appl. Mech. Tech. Phy.*, 58(12):1171.
- Shi, N., Emran, M. S., and Schumacher, J. (2012). Boundary layer structure in turbulent Rayleigh–Bénard convection. *J. Fluid Mech.*, 706:5–33.
- Shishkina, O., Emran, M. S., Grossmann, S., and Lohse, D. (2017). Scaling relations in large-Prandtl-number natural thermal convection. *Phys. Rev. Fluids*, 2(10):103502.
- Shishkina, O., Horn, S., and Wagner, S. (2013). Falkner–Skan boundary layer approximation in Rayleigh–Bénard convection. *J. Fluid Mech.*, 730:442–463.
- Shishkina, O., Stevens, R. J. A. M., Grossmann, S., and Lohse, D. (2010). Boundary layer structure in turbulent thermal convection and its consequences for the required numerical resolution. *New J. Phys.*, 12:075022.
- Shishkina, O. and Wagner, C. (2005). Analysis of thermal dissipation rates in turbulent Rayleigh–Bénard convection. *J. Fluid Mech.*, 546:51–60.
- Shishkina, O. and Wagner, C. (2007). Local heat fluxes in turbulent Rayleigh–Bénard convection. *Phys. Fluids*, 19(8):085107.
- Shraiman, B. I. and Siggia, E. D. (1990). Heat transport in high-Rayleigh-number convection. *Phys. Rev. A*, 42(6):3650–3653.
- Siggia, E. D. (1994). High Rayleigh number convection. *Annu. Rev. Fluid Mech.*, 26(1):137–168.
- Silano, G., Sreenivasan, K. R., and Verzicco, R. (2010). Numerical simulations of Rayleigh–Bénard convection for Prandtl numbers between 10^{-1} and 10^4 and Rayleigh numbers between 10^5 and 10^9 . *J. Fluid Mech.*, 662:409–446.
- Spiegel, E. A. (1971). Convection in stars: I. Basic Boussinesq convection. *Annu. Rev. Astron. Astrophys.*, 9:323–352.

BIBLIOGRAPHY

- Sreenivasan, K. R. (1991). Fractals and multifractals in fluid turbulence. *Annu. Rev. Fluid Mech.*, 23(1):539–600.
- Sreenivasan, K. R. and Antonia, R. A. (1997). The phenomenology of small-scale turbulence. *Annu. Rev. Fluid Mech.*, 29(1):435–472.
- Stepanov, R., Plunian, F., Kessar, M., and Balarac, G. (2014). Systematic bias in the calculation of spectral density from a three-dimensional spatial grid. *Phys. Rev. E*, 90(5):053309.
- Stevens, R. J. A. M., van der Poel, E. P., Grossmann, S., and Lohse, D. (2013). The unifying theory of scaling in thermal convection: the updated prefactors. *J. Fluid Mech.*, 730:295–308.
- Sun, C., Zhou, Q., and Xia, K.-Q. (2006). Cascades of velocity and temperature fluctuations in buoyancy-driven thermal turbulence. *Phys. Rev. Lett.*, 97(1):144504.
- Takeshita, T., Segawa, T., Glazier, J. A., and Sano, M. (1996). Thermal turbulence in mercury. *Phys. Rev. Lett.*, 76(9):1465–1468.
- van der Walt, S., Colbert, S. C., and Varoquaux, G. (2011). The NumPy Array: A Structure for Efficient Numerical Computation. *Comput. Sci. Eng.*, 13(2):22.
- Verma, M. K. (2004). Statistical theory of magnetohydrodynamic turbulence: recent results. *Phys. Rep.*, 401(5):229–380.
- Verma, M. K. (2005). Introduction to Statistical Theory of Fluid Turbulence. *arXiv*.
- Verma, M. K. (2018). *Physics of Buoyant Flows: From Instabilities to Turbulence*. World Scientific, Singapore.
- Verma, M. K. (2019a). Contrasting turbulence in stably stratified flows and thermal convection. *Phys. Scr.*, 94(6):1–10.
- Verma, M. K. (2019b). *Energy transfers in Fluid Flows: Multiscale and Spectral Perspectives*. Cambridge University Press, Cambridge.
- Verma, M. K., Chatterjee, A. G., Yadav, R. K., Paul, S., Chandra, M., and Samtaney, R. (2013). Benchmarking and scaling studies of pseudospectral code Tarang for turbulence simulations. *Pramana-J. Phys.*, 81(4):617–629.

BIBLIOGRAPHY

- Verma, M. K., Kumar, A., Kumar, P., Barman, S., Chatterjee, A. G., Samtaney, R., and Stepanov, R. (2018). Energy Spectra and Fluxes in Dissipation Range of Turbulent and Laminar Flows. *Fluid Dyn.*, 53:728–739.
- Verma, M. K., Kumar, A., and Pandey, A. (2017). Phenomenology of buoyancy-driven turbulence: recent results. *New J. Phys.*, 19:025012.
- Verma, M. K., Mishra, P. K., Pandey, A., and Paul, S. (2012). Scalings of field correlations and heat transport in turbulent convection. *Phys. Rev. E*, 85(1):016310.
- Verma, M. K. and Reddy, K. S. (2015). Modeling quasi-static magnetohydrodynamic turbulence with variable energy flux. *Phys. Fluids*, 27(2):025114.
- Verma, M. K., Samuel, R. J., Chatterjee, S., Bhattacharya, S., and Asad, A. (2020). Challenges in fluid flow simulations using exascale computing. *S.N. Comput. Sci.*, 1(178):178.
- Verzicco, R. and Camussi, R. (1999). Prandtl number effects in convective turbulence. *J. Fluid Mech.*, 383:55–73.
- Verzicco, R. and Camussi, R. (2003). Numerical experiments on strongly turbulent thermal convection in a slender cylindrical cell. *J. Fluid Mech.*, 477:19–49.
- Verzicco, R. and Camussi, V. (1997). Transitional regimes of low-Prandtl thermal convection in a cylindrical cell. *Phys. Fluids*, 9(5):1287.
- Virtanen, P., Gommers, R., Oliphant, T. E., A., B., C, D., E, F., and G, H. (2020). SciPy 1.0: fundamental algorithms for scientific computing in Python. *Nat. Methods*, 17:261–272.
- Vishnu, R. and Sameen, A. (2020). Heat transfer scaling in natural convection with shear due to rotation. *Phys. Rev. Fluids*, 5(11):113504.
- Wagner, S., Shishkina, O., and Wagner, C. (2012). Boundary layers and wind in cylindrical Rayleigh–Bénard cells. *J. Fluid Mech.*, 697:336–366.
- Warhaft, Z. (2000). Passive Scalars in Turbulent Flows. *Annu. Rev. Fluid Mech.*, 32(1):203–240.
- Wesseling, P. (1992). *An Introduction to Multigrid Methods*. John Wiley & Sons, Chichester, 1st edition.

BIBLIOGRAPHY

- Whitehead, J. and Doering, C. R. (2011). Ultimate state of two-dimensional Rayleigh-Bénard convection between free-slip fixed-temperature boundaries. *Phys. Rev. Lett.*, 106(24):244501.
- Whitehead, J. P. and Doering, C. R. (2012). Rigid bounds on heat transport by a fluid between slippery boundaries. *J. Fluid Mech.*, 707:241–259.
- Wu, X.-Z., Kadanoff, L. P., Libchaber, A., and Sano, M. (1990). Frequency power spectrum of temperature fluctuations in free convection. *Phys. Rev. Lett.*, 64(18):2140–2143.
- Xia, K.-Q., Lam, S., and Zhou, S.-Q. (2002). Heat-flux measurement in high-Prandtl-number turbulent Rayleigh-Bénard convection. *Phys. Rev. Lett.*, 88(6):064501.
- Xin, Y.-B. and Xia, K.-Q. (1997). Boundary layer length scales in convective turbulence. *Phys. Rev. E*, 56(3):3010–3015.
- Yeung, P. K. (2002). Lagrangian investigations of turbulence. *Annu. Rev. Fluid Mech.*, 34(1):115–142.
- Zhang, Y., Zhou, Q., and Sun, C. (2017). Statistics of kinetic and thermal energy dissipation rates in two-dimensional turbulent Rayleigh-Bénard convection. *J. Fluid Mech.*, 814:165–184.
- Zhou, S.-Q. and Xia, K.-Q. (2001). Scaling properties of the temperature field in convective turbulence. *Phys. Rev. Lett.*, 87(6):064501.
- Zhu, X., Mathai, V., Stevens, R. J. A. M., Verzicco, R., and Lohse, D. (2018). Transition to the Ultimate Regime in Two-Dimensional Rayleigh-Bénard Convection. *Phys. Rev. Lett.*, 120(14):144502.

AIP PUBLISHING LICENSE TERMS AND CONDITIONS

Feb 26, 2021

This Agreement between Mr. Shashwat Bhattacharya ("You") and AIP Publishing ("AIP Publishing") consists of your license details and the terms and conditions provided by AIP Publishing and Copyright Clearance Center.

License Number 5016331421988

License date Feb 26, 2021

Licensed Content Publisher AIP Publishing

Licensed Content Publication Physics of Fluids

Licensed Content Title Complexity of viscous dissipation in turbulent thermal convection

Licensed Content Author Shashwat Bhattacharya, Ambrish Pandey, Abhishek Kumar, et al

Licensed Content Date Mar 1, 2018

Licensed Content Volume 30

Licensed Content Issue 3

Type of Use Thesis/Dissertation

Requestor type Author (original article)

Format Electronic

Portion Excerpt (> 800 words)

Will you be translating? No

Title Properties of small-scale turbulence in Rayleigh-Bénard convection

Institution name Indian Institute of Technology Kanpur

Expected presentation date Feb 2021

Portions The entire manuscript.

Requestor Location Mr. Shashwat Bhattacharya
C-112, Hall of Residence X
Indian Institute of Technology Kanpur

Kanpur, Uttar Pradesh 208016
India
Attn: Mr. Shashwat Bhattacharya

Total 0.00 USD

Terms and Conditions

AIP Publishing -- Terms and Conditions: Permissions Uses

AIP Publishing hereby grants to you the non-exclusive right and license to use and/or distribute the Material according to the use specified in your order, on a one-time basis, for the specified term, with a maximum distribution equal to the number that you have ordered. Any links or other content accompanying the Material are not the subject of this license.

1. You agree to include the following copyright and permission notice with the reproduction of the Material: "Reprinted from [FULL CITATION], with the permission of AIP Publishing." For an article, the credit line and permission notice must be printed on the first page of the article or book chapter. For photographs, covers, or tables, the notice may appear with the Material, in a footnote, or in the reference list.
2. If you have licensed reuse of a figure, photograph, cover, or table, it is your responsibility to ensure that the material is original to AIP Publishing and does not contain the copyright of another entity, and that the copyright notice of the figure, photograph, cover, or table does not indicate that it was reprinted by AIP Publishing, with permission, from another source. Under no circumstances does AIP Publishing purport or intend to grant permission to reuse material to which it does not hold appropriate rights.
You may not alter or modify the Material in any manner. You may translate the Material into another language only if you have licensed translation rights. You may not use the Material for promotional purposes.
3. The foregoing license shall not take effect unless and until AIP Publishing or its agent, Copyright Clearance Center, receives the Payment in accordance with Copyright Clearance Center Billing and Payment Terms and Conditions, which are incorporated herein by reference.

4. AIP Publishing or Copyright Clearance Center may, within two business days of granting this license, revoke the license for any reason whatsoever, with a full refund payable to you. Should you violate the terms of this license at any time, AIP Publishing, or Copyright Clearance Center may revoke the license with no refund to you. Notice of such revocation will be made using the contact information provided by you. Failure to receive such notice will not nullify the revocation.
5. AIP Publishing makes no representations or warranties with respect to the Material. You agree to indemnify and hold harmless AIP Publishing, and their officers, directors, employees or agents from and against any and all claims arising out of your use of the Material other than as specifically authorized herein.
6. The permission granted herein is personal to you and is not transferable or assignable without the prior written permission of AIP Publishing. This license may not be amended except in a writing signed by the party to be charged.
7. If purchase orders, acknowledgments or check endorsements are issued on any forms containing terms and conditions which are inconsistent with these provisions, such inconsistent terms and conditions shall be of no force and effect. This document, including the CCC Billing and Payment Terms and Conditions, shall be the entire agreement between the parties relating to the subject matter hereof.

This Agreement shall be governed by and construed in accordance with the laws of the State of New York. Both parties hereby submit to the jurisdiction of the courts of New York County for purposes of resolving any disputes that may arise hereunder.

V1.2

Questions? customercare@copyright.com or +1-855-239-3415 (toll free in the US) or +1-978-646-2777.

AIP PUBLISHING LICENSE TERMS AND CONDITIONS

Feb 26, 2021

This Agreement between Mr. Shashwat Bhattacharya ("You") and AIP Publishing ("AIP Publishing") consists of your license details and the terms and conditions provided by AIP Publishing and Copyright Clearance Center.

License Number	5016340155524
License date	Feb 26, 2021
Licensed Content Publisher	AIP Publishing
Licensed Content Publication	Physics of Fluids
Licensed Content Title	Scaling and spatial intermittency of thermal dissipation in turbulent convection
Licensed Content Author	Shashwat Bhattacharya, Ravi Samtaney, Mahendra K. Verma
Licensed Content Date	Jul 1, 2019
Licensed Content Volume	31
Licensed Content Issue	7
Type of Use	Thesis/Dissertation
Requestor type	Author (original article)
Format	Electronic
Portion	Excerpt (> 800 words)

Will you be translating? No

Title Properties of small-scale turbulence in Rayleigh-Bénard convection

Institution name Indian Institute of Technology Kanpur

Expected presentation date Feb 2021

Portions The entire manuscript

Requestor Location Mr. Shashwat Bhattacharya
C-112, Hall of Residence X
Indian Institute of Technology Kanpur

Kanpur, Uttar Pradesh 208016
India
Attn: Mr. Shashwat Bhattacharya

Total 0.00 USD

Terms and Conditions

AIP Publishing -- Terms and Conditions: Permissions Uses

AIP Publishing hereby grants to you the non-exclusive right and license to use and/or distribute the Material according to the use specified in your order, on a one-time basis, for the specified term, with a maximum distribution equal to the number that you have ordered. Any links or other content accompanying the Material are not the subject of this license.

1. You agree to include the following copyright and permission notice with the reproduction of the Material: "Reprinted from [FULL CITATION], with the permission of AIP Publishing." For an article, the credit line and permission notice must be printed on the first page of the article or book chapter. For photographs, covers, or tables, the notice may appear with the Material, in a footnote, or in the reference list.
2. If you have licensed reuse of a figure, photograph, cover, or table, it is your responsibility to ensure that the material is original to AIP Publishing and does not contain the copyright of another entity, and that the copyright notice of the figure, photograph, cover, or table does not indicate that it was reprinted by AIP Publishing, with permission, from another source. Under no circumstances does AIP Publishing purport or intend to grant permission to reuse material to which it does not hold appropriate rights.
You may not alter or modify the Material in any manner. You may translate the Material into another language only if you have licensed translation rights. You may not use the Material for promotional purposes.
3. The foregoing license shall not take effect unless and until AIP Publishing or its agent, Copyright Clearance Center, receives the Payment in accordance with Copyright

Clearance Center Billing and Payment Terms and Conditions, which are incorporated herein by reference.

4. AIP Publishing or Copyright Clearance Center may, within two business days of granting this license, revoke the license for any reason whatsoever, with a full refund payable to you. Should you violate the terms of this license at any time, AIP Publishing, or Copyright Clearance Center may revoke the license with no refund to you. Notice of such revocation will be made using the contact information provided by you. Failure to receive such notice will not nullify the revocation.
5. AIP Publishing makes no representations or warranties with respect to the Material. You agree to indemnify and hold harmless AIP Publishing, and their officers, directors, employees or agents from and against any and all claims arising out of your use of the Material other than as specifically authorized herein.
6. The permission granted herein is personal to you and is not transferable or assignable without the prior written permission of AIP Publishing. This license may not be amended except in a writing signed by the party to be charged.
7. If purchase orders, acknowledgments or check endorsements are issued on any forms containing terms and conditions which are inconsistent with these provisions, such inconsistent terms and conditions shall be of no force and effect. This document, including the CCC Billing and Payment Terms and Conditions, shall be the entire agreement between the parties relating to the subject matter hereof.

This Agreement shall be governed by and construed in accordance with the laws of the State of New York. Both parties hereby submit to the jurisdiction of the courts of New York County for purposes of resolving any disputes that may arise hereunder.

V1.2

Questions? customercare@copyright.com or +1-855-239-3415 (toll free in the US) or +1-978-646-2777.

AIP PUBLISHING LICENSE TERMS AND CONDITIONS

Feb 26, 2021

This Agreement between Mr. Shashwat Bhattacharya ("You") and AIP Publishing ("AIP Publishing") consists of your license details and the terms and conditions provided by AIP Publishing and Copyright Clearance Center.

License Number	5016340378512
License date	Feb 26, 2021
Licensed Content Publisher	AIP Publishing
Licensed Content Publication	Physics of Fluids
Licensed Content Title	Similarities between the structure functions of thermal convection and hydrodynamic turbulence
Licensed Content Author	Shashwat Bhattacharya, Shubhadeep Sadhukhan, Anirban Guha, et al
Licensed Content Date	Nov 1, 2019
Licensed Content Volume	31
Licensed Content Issue	11
Type of Use	Thesis/Dissertation
Requestor type	Author (original article)
Format	Electronic

Portion	Excerpt (> 800 words)
Will you be translating?	No
Title	Properties of small-scale turbulence in Rayleigh-Bénard convection
Institution name	Indian Institute of Technology Kanpur
Expected presentation date	Feb 2021
Portions	The entire manuscript
Requestor Location	Mr. Shashwat Bhattacharya C-112, Hall of Residence X Indian Institute of Technology Kanpur Kanpur, Uttar Pradesh 208016 India Attn: Mr. Shashwat Bhattacharya
Total	0.00 USD

Terms and Conditions

AIP Publishing -- Terms and Conditions: Permissions Uses

AIP Publishing hereby grants to you the non-exclusive right and license to use and/or distribute the Material according to the use specified in your order, on a one-time basis, for the specified term, with a maximum distribution equal to the number that you have ordered. Any links or other content accompanying the Material are not the subject of this license.

1. You agree to include the following copyright and permission notice with the reproduction of the Material: "Reprinted from [FULL CITATION], with the permission of AIP Publishing." For an article, the credit line and permission notice must be printed on the first page of the article or book chapter. For photographs, covers, or tables, the notice may appear with the Material, in a footnote, or in the reference list.
2. If you have licensed reuse of a figure, photograph, cover, or table, it is your responsibility to ensure that the material is original to AIP Publishing and does not contain the copyright of another entity, and that the copyright notice of the figure, photograph, cover, or table does not indicate that it was reprinted by AIP Publishing, with permission, from another source. Under no circumstances does AIP Publishing purport or intend to grant permission to reuse material to which it does not hold appropriate rights.
You may not alter or modify the Material in any manner. You may translate the Material into another language only if you have licensed translation rights. You may not use the Material for promotional purposes.

3. The foregoing license shall not take effect unless and until AIP Publishing or its agent, Copyright Clearance Center, receives the Payment in accordance with Copyright Clearance Center Billing and Payment Terms and Conditions, which are incorporated herein by reference.
4. AIP Publishing or Copyright Clearance Center may, within two business days of granting this license, revoke the license for any reason whatsoever, with a full refund payable to you. Should you violate the terms of this license at any time, AIP Publishing, or Copyright Clearance Center may revoke the license with no refund to you. Notice of such revocation will be made using the contact information provided by you. Failure to receive such notice will not nullify the revocation.
5. AIP Publishing makes no representations or warranties with respect to the Material. You agree to indemnify and hold harmless AIP Publishing, and their officers, directors, employees or agents from and against any and all claims arising out of your use of the Material other than as specifically authorized herein.
6. The permission granted herein is personal to you and is not transferable or assignable without the prior written permission of AIP Publishing. This license may not be amended except in a writing signed by the party to be charged.
7. If purchase orders, acknowledgments or check endorsements are issued on any forms containing terms and conditions which are inconsistent with these provisions, such inconsistent terms and conditions shall be of no force and effect. This document, including the CCC Billing and Payment Terms and Conditions, shall be the entire agreement between the parties relating to the subject matter hereof.

This Agreement shall be governed by and construed in accordance with the laws of the State of New York. Both parties hereby submit to the jurisdiction of the courts of New York County for purposes of resolving any disputes that may arise hereunder.

V1.2

Questions? customercare@copyright.com or +1-855-239-3415 (toll free in the US) or +1-978-646-2777.

AIP PUBLISHING LICENSE TERMS AND CONDITIONS

Feb 26, 2021

This Agreement between Mr. Shashwat Bhattacharya ("You") and AIP Publishing ("AIP Publishing") consists of your license details and the terms and conditions provided by AIP Publishing and Copyright Clearance Center.

License Number	5016340648615
License date	Feb 26, 2021
Licensed Content Publisher	AIP Publishing
Licensed Content Publication	Physics of Fluids
Licensed Content Title	Revisiting Reynolds and Nusselt numbers in turbulent thermal convection
Licensed Content Author	Shashwat Bhattacharya, Mahendra K. Verma, Ravi Samtaney
Licensed Content Date	Jan 1, 2021
Licensed Content Volume	33
Licensed Content Issue	1
Type of Use	Thesis/Dissertation
Requestor type	Author (original article)
Format	Electronic
Portion	Excerpt (> 800 words)

Will you be translating? No

Title Properties of small-scale turbulence in Rayleigh-Bénard convection

Institution name Indian Institute of Technology Kanpur

Expected presentation date Feb 2021

Portions The entire manuscript

Requestor Location
Mr. Shashwat Bhattacharya
C-112, Hall of Residence X
Indian Institute of Technology Kanpur
Kanpur, Uttar Pradesh 208016
India
Attn: Mr. Shashwat Bhattacharya

Total 0.00 USD

Terms and Conditions

AIP Publishing -- Terms and Conditions: Permissions Uses

AIP Publishing hereby grants to you the non-exclusive right and license to use and/or distribute the Material according to the use specified in your order, on a one-time basis, for the specified term, with a maximum distribution equal to the number that you have ordered. Any links or other content accompanying the Material are not the subject of this license.

1. You agree to include the following copyright and permission notice with the reproduction of the Material: "Reprinted from [FULL CITATION], with the permission of AIP Publishing." For an article, the credit line and permission notice must be printed on the first page of the article or book chapter. For photographs, covers, or tables, the notice may appear with the Material, in a footnote, or in the reference list.
2. If you have licensed reuse of a figure, photograph, cover, or table, it is your responsibility to ensure that the material is original to AIP Publishing and does not contain the copyright of another entity, and that the copyright notice of the figure, photograph, cover, or table does not indicate that it was reprinted by AIP Publishing, with permission, from another source. Under no circumstances does AIP Publishing purport or intend to grant permission to reuse material to which it does not hold appropriate rights.
You may not alter or modify the Material in any manner. You may translate the Material into another language only if you have licensed translation rights. You may not use the Material for promotional purposes.
3. The foregoing license shall not take effect unless and until AIP Publishing or its agent, Copyright Clearance Center, receives the Payment in accordance with Copyright Clearance Center Billing and Payment Terms and Conditions, which are incorporated herein by reference.

4. AIP Publishing or Copyright Clearance Center may, within two business days of granting this license, revoke the license for any reason whatsoever, with a full refund payable to you. Should you violate the terms of this license at any time, AIP Publishing, or Copyright Clearance Center may revoke the license with no refund to you. Notice of such revocation will be made using the contact information provided by you. Failure to receive such notice will not nullify the revocation.
5. AIP Publishing makes no representations or warranties with respect to the Material. You agree to indemnify and hold harmless AIP Publishing, and their officers, directors, employees or agents from and against any and all claims arising out of your use of the Material other than as specifically authorized herein.
6. The permission granted herein is personal to you and is not transferable or assignable without the prior written permission of AIP Publishing. This license may not be amended except in a writing signed by the party to be charged.
7. If purchase orders, acknowledgments or check endorsements are issued on any forms containing terms and conditions which are inconsistent with these provisions, such inconsistent terms and conditions shall be of no force and effect. This document, including the CCC Billing and Payment Terms and Conditions, shall be the entire agreement between the parties relating to the subject matter hereof.

This Agreement shall be governed by and construed in accordance with the laws of the State of New York. Both parties hereby submit to the jurisdiction of the courts of New York County for purposes of resolving any disputes that may arise hereunder.

V1.2

Questions? customercare@copyright.com or +1-855-239-3415 (toll free in the US) or +1-978-646-2777.
